

University of Ioannina School of Sciences Department of Physics

Studies of signatures from theories beyond the Standard Model and development of new detector systems for the CMS experiment at the HL-LHC accelerator at CERN

PhD Dissertation

BY PANAGIOTIS KATSOULIS



Πανεπιστήμιο Ιωαννίνων Σχολή Θετικών Επιστημών Τμήμα Φυσικής

Μελέτες υπογραφών για θεωρίες πέραν του καθιερωμένου προτύπου και ανάπτυξη νέων ανιχνευτικών συστημάτων για το πείραμα CMS στον επιταχυντή HL-LHC του CERN

ΔΙΔΑΚΤΟΡΙΚΗ ΔΙΑΤΡΙΒΗ

ΤΟΥ ΠΑΝΑΓΙΩΤΗ ΚΑΤΣΟΥΛΗ

ΙΩΑΝΝΙΝΑ 2025

Three-Member Advisory Committee

- Konstantinos Fountas, Professor, Department of Physics, University of Ioannina, Greece (Supervisor)
- Ioannis Papadopoulos, Associate Professor, Department of Physics, University of Ioannina, Greece
- Ioannis Strologas, Associate Professor, Department of Physics, University of Ioannina, Greece

Seven-Member Select Committee

- Konstantinos Fountas, Professor, Department of Physics, University of Ioannina, Greece (Supervisor)
- Ioannis Papadopoulos, Associate Professor, Department of Physics, University of Ioannina, Greece
- Ioannis Strologas, Associate Professor, Department of Physics, University of Ioannina, Greece
- Panagiotis Kokkas, Professor, Department of Physics, University of Ioannina, Greece
- Paraskevas Sphicas, Professor, Department of Physics, National and Kapodistrian University of Athens,
 Greece
- Konstantinos Vellidis, Associate Professor, Department of Physics, National and Kapodistrian University of Athens, Greece
- Cristina Botta, Physicist, Experimental Physics Department, CERN

First and foremost, I am grateful to my supervisor - Costas Foudas. The opportunity he gave me during my early professional career, to meet and work and grow alongside bright people, built some of the most impactful cornerstones of my character. Very powerful and defining experiences.

Limitless important to me has been the support and endless confidence of specific significant people, who I will always foster with me down the next day. A doctorate, as long a chapter is, is constituted from more than one stage, and understandably people enter and depart. Without their presence, even partial, furnishing this dissertation would not be possible, thus I consider them also a piece of it. If not a piece of myself.

Special reference, even though the previous remarks are also credited to them too, I ought to make to my family. They, most of everyone, wanted me to show my best self, without settling for anything less.

Abstract

This PhD Thesis concerns high-energy physics studies based on exploration for new signatures of electroweakinos in the context of MSSM (Minimal Supersymmetric Standard Model) and Split SUSY (Split Supersymmetry). The studies are carried out on 138 fb⁻¹ of data with soft leptons and significant Missing Transverse Energy that are collected by the CMS experiment at CERN during the Run 2 period (2016-2018). This work focuses on suppressed phase-spaces, with very small mass-splitting ($\Delta M = m_{\chi^0_2} - m_{\chi^0_1}$) between the LSP (Lightest Supersymmetric Particle) and the next heavier particle. Such small ΔM introduces several challenges. It requires the reconstruction of very soft leptons, with the analysis excluding Neutralinos (χ^0_2) up to 120 (320) GeV and 100 (230) GeV at ΔM of 10 (1) GeV for Binos and Higgsinos respectively, profiting from the latest *LowPtElectron* reconstruction of the CMS. Also, for Neutralinos that become significantly long-lived, the analysis excludes up to 250-475 GeV and up to 200-350 GeV, depending on the $c\tau$ (up to 10 cm), at ΔM of 20 GeV for Binos and Higgsinos respectively. Additionally, we present HL-LHC projections of the study to 400 fb⁻¹, 3000 fb⁻¹, and 6000 fb⁻¹, together with 2 more CMS analyses (arxiv:2309.16823 and CMS-SUS-24-012), covering completely the phase-space in the Higgsino interpretation to exclude Higgsinos with mass up to 260 GeV.

Η παρούσα Διδακτορική Διατριβή αφορά μελέτες στη φυσική υψηλών ενεργειών, με επίκεντρο την αναζήτηση νέων υπογραφών υπερσυμμετρικών φερμιονίων ηλεκτρασθενούς αλληλεπίδρασης (electroweakinos) στο πλαίσιο του Minimal Supersymmetric Standard Model (MSSM) και του Split SUSY (Split Supersymmetry). Οι μελέτες βασίζονται σε σύνολο δεδομένων 138 fb- 1 με ανίχνευση λεπτονίων χαμηλής εγκάρσιας ορμής και σημαντικής ελλείπουσας εγκάρσιας ενέργειας, τα οποία συλλέχθηκαν από το πείραμα CMS του CERN κατά τη διάρκεια της περιόδου Run 2 (2016-2018). Η εργασία εστιάζει σε φασικούς χώρους με πολύ μικρή διαφορά μάζας ($\Delta M = m_{\chi_2^0} - m_{\chi_1^0}$) μεταξύ του ελαφρύτερου υπερσυμμετρικού σωματιδίου (LSP) και του επόμενου βαρύτερου. Η μικρή αυτή διαφορά ΔM δημιουργεί προκλήσεις: απαιτείται η ανακατασκευή λεπτονίων ιδιαίτερης χαμηλής ορμής, με την ανάλυση να αποκλείοντας Neutralinos (χ_2^0) μέχρι 120 (320) GeV και 100 (230) GeV σε ΔM =10(1) GeV για Binos και Higgsinos αντίστοιχα, εκμεταλλευόμενη την καινούργια μέθοδο ανακατασκευής LowPtElectron του CMS. Επίσης, για Neutralinos τα οποία είναι σημαντικά μακρόβια, η ανάλυση αποκλείει μάζες μέχρι 250-475 GeV και μέχρι 200-350 GeV, ανάλογα την Louphκης απόσταση διάσπασης Louphκης απόσταση διάσπασης Louphκης ανάλυση για το HL-LHC με φωτεινότητα 400 fb-Louph1, 3000 fb-Louph1 και 6000 fb-Louph1 μαζί με δύο ακόμη αναλύσεις του CMS (arxiv:2309.16823 και CMS-SUS-24-012), καλύπτοντας πλήρως τον φασικό χώρο για την ερμηνεία των αποτελεσμάτων στα Higgsinos αποκλείοντας μάζες έως και 260 GeV.

Summary

This PhD dissertation, carried out at CERN, discusses High Energy Particle Physics studies and engineering work about data collected by the CMS experiment. Data analysis was associated to CMS datasets that were collected during Run-2 era (2016-2018) and looking for final states with 2 (or 3) muons and electrons of low transverse momenta, together with significant amounts of missing transverse energy in each event. Furthermore, the software engineering and algorithm development work was associated to the Level-1 Trigger system of the CMS, which serves as a primary filter for the experiment, and regulates the volume of the data collected.

The dissertation is separated to 5 main sections: first chapters describe the accelerator complex at CERN that serves with collisions the CMS experiment, next chapters describe in detail the structure of the CMS experiment, following these is an in detail presentation of the work associated to the Level-1 Trigger, and the final half of the dissertation is dedicated to presenting the "Multilepton Analysis" (with Supersymmetry Bino/Wino and Higgsino interpretations of the results), together with projections of such results to data volumes that is expected to be collected during the High-Luminosity LHC era (2030-2041).

1. The Large Hadron Collider (LHC) and other accelerators at CERN

The Large Hadron Collider (LHC) at CERN stands as the world's most powerful particle accelerator, designed to probe the fundamental particles and study their interactions. Hosted in a 27-kilometer tunnel beneath the French-Swiss border near Geneva, the LHC accelerates protons to energies of 6.5 TeV per beam, providing collisions at a total energy of 13 TeV. These collisions are delivered to four experiments, ATLAS, CMS, ALICE, and LHCb, each optimized for different aspects of high-energy physics. The LHC's construction and operation involved decades of planning, engineering, and huge efforts of international collaboration.

The LHC's scientific achievements are profound, most importantly the discovery of the Higgs boson in 2012, which confirmed completely the Standard Model of Particle Physics. Beyond this, the LHC continues to enable precision measurements and searches for new physics, including phenomena beyond the Standard Model such as supersymmetry, extra dimensions, and dark matter candidates.

The Super Proton Synchrotron (SPS) serves as the last in chain pre-accelerator in the CERN accelerator complex, boosting proton energies to 450 GeV before injection into the LHC. Built in the 1970s, the SPS has played a pivotal role in both collider and fixed-target experiments, contributing to discoveries such as the W and Z bosons. Its flexible configuration allows it to deliver beams, except the LHC, to a variety of fixed-target experiments, including those for neutrino oscillation studies at the Gran Sasso Laboratory in Italy.

The Proton Synchrotron (PS) is a foundational component of CERN's accelerator infrastructure that was commissioned in the 60's, providing intermediate acceleration for protons and heavy ions. Operating at energies from 2 to 25 GeV, the PS acts as a bridge between the initial acceleration stages and the higher-energy SPS. The longevity of PS and its adaptability are proofs of its robust design and the insight of its creators. Over the decades, it has undergone numerous upgrades to accommodate new experimental requirements and to improve beam quality and stability.

The Proton Synchrotron Booster (PSB) marks the first synchrotron stage in the acceleration of protons at CERN, receiving low-energy beams from the linear accelerators and boosting them to 2 GeV. The PSB's design incorporates multiple rings to handle high-intensity beams and efficient injection into the PS. Its construction in the early 70s addressed the growing need for higher beam intensities and energies, laying the groundwork for subsequent advancements in accelerator technology. Beyond its primary role in proton acceleration, the PSB also serves specialized low-energy experiments, such as ISOLDE and MEDICS, which require precise control over beam parameters.

Linear accelerators (LINACs) at CERN provide the initial acceleration for both protons and heavy ions, delivering beams with energies up to 160 MeV. LINAC 4, which is commissioned in 2020, represents the latest generation of these machines, incorporating advanced technologies to improve beam quality and reliability. LINAC 3, operational since '94, specializes in heavy-ion acceleration.

Particle accelerator design is rooted in fundamental physical principles that govern the acceleration, the beam focus, and the collision of charged particles. Electric fields in radiofrequency (RF) cavities transmit energy to particles, while magnetic fields guide and focus the beams along their trajectories. The interplay between acceleration and beam stability is critical, with techniques such as stochastic and electron cooling employed to maintain beam quality.

Synchrotron radiation, a consequence of accelerating charged particles along curved paths, is one of the most significant challenges, particularly for lighter particles like electrons. Managing energy losses and optimizing the luminosity (the rate of collisions per unit area and time) are central to the accelerator performance too. High luminosity provides more rare interactions and enables the study of new physics.

2. The CMS Experiment, its sub-detectors, and systems

Following the accelerator chapters is the section that describes the CMS experiment and its sub-detectors. A detailed description of each component is made, and basic characteristics are discussed, which are essential for their performance.

The CMS Silicon Tracker is a sophisticated system designed to reconstruct the trajectories of charged particles with high precision. Combing an inner pixel detector and an outer silicon strip detector, the tracker provides very fine granularity, fast readout, and radiation hardness. Upgrades to the tracker, including the Phase-1 Pixel Upgrade and planned Phase-2 enhancements, ensure sustained performance in the high-luminosity environment of the HL-LHC.

The pixel detector, with its four layers and high-density pixel sensors, is positioned closest to the interaction point, enabling precise vertex reconstruction and impact parameter measurements. The silicon strip detector extends the tracker's coverage, ensuring multiple measurements per track and enhancing pattern recognition capabilities. The combined system achieves high spatial resolution that is essential for also identifying primary and secondary vertices and reconstructing full decay history.

The CMS calorimeter system is designed to measure the energy of electrons, photons, and hadrons with precision. The Electromagnetic Calorimeter (ECAL), constructed from lead tungstate crystals, provides fine granularity and fast response, enabling accurate energy measurements and efficient particle

identification. The ECAL is segmented into a barrel, endcaps, and a preshower detector, each optimized for different regions of the detector.

The Hadronic Calorimeter (HCAL) complements the ECAL by measuring the energy of hadrons and contributing to the calculation of missing transverse energy. The HCAL is also divided into sectors like barrel, endcap, forward, and outer sections, each covering specific pseudorapidity ranges. Together, the ECAL and HCAL provide nearly full coverage around the collision point, enabling extensive reconstruction of the events and supporting a wide range of physics analyses.

The CMS muon system is designed to identify and measure muons with high efficiency and precision, even in the challenging environment of high-luminosity collisions. The system combines Drift Tubes (DTs) in the barrel region, Cathode Strip Chambers (CSCs) in the endcaps, and Resistive Plate Chambers (RPCs) covering both regions. Recent upgrades have also introduced Gas Electron Multiplier (GEM) detectors to enhance performance in high pseudorapidity areas.

The muon detectors are optimized for specific pseudorapidity ranges and radiation-environment requirements, ensuring robust coverage and redundancy. The multilayered architecture allows for as precise as possible momentum measurements at higher distances (4-7 meters away from the beam), efficient triggering, and effective background suppression. Continuous upgrades and maintenance ensure that the system remains resistant to aging and capable of meeting the demands of future data-taking periods.

The CMS magnet is a central feature of the experiment, generating 4T axial magnetic field, which is designed to bend the trajectories of charged particles to facilitate measurements. The solenoid, constructed from superconducting material, is housed within a massive steel return yoke that also provides structural support for the detector.

The return yoke is segmented into barrel and endcap sections, each designed to guide the magnetic flux and support the installation of subdetectors. The operation at cryogenic temperatures and high currents requires efficient cooling and a sophisticated control system. The investment of the CMS in its magnet reflects its critical role in supporting the experiment's physics goals.

The CMS trigger system is a two-tiered architecture designed to reduce the data rate from 40 MHz to the manageable "few kHz" for permanent storage. The Level-1 Trigger (L1T) is designed on custom-made electronics using FPGAs, aiming to make rapid decisions based on coarse detector information, while the High-Level Trigger (HLT) uses software algorithms running on a computing farm to perform more refined event selection. Together, these systems ensure that only the most interesting data from collisions are recorded for analysis.

Upgrades to the trigger system, including the introduction of advanced algorithms and heterogeneous computing architectures, have enhanced its flexibility and performance throughout the years. The trigger menu, the list of algorithms evaluated together with "OR" logic, is continuously adapted to reflect the evolving physics program, incorporating new selection criteria and optimizing resource usage. The system's reliability and efficiency are vital, as lost events cannot be recovered, and its ongoing development is an important focus of the CMS collaboration.

3. The Barrel Muon Track Finder (BMTF) and The Condition DB

The BMTF is a specialized system within the CMS Level-1 Trigger architecture that is responsible for reconstructing muon candidates in the barrel region using data from DTs and RPCs. The BMTF employs a Kalman Filter algorithm to achieve high efficiency and momentum resolution. Upgrades since Run 2 have enabled the identification of displaced muons at Level-1, expanding the experiment's sensitivity to long-lived particles.

The Kalman Filter algorithm implemented is one significant advancement in real-time track reconstruction, which is featured by the Level-1 Trigger. Iteratively, appending data from subsequent muon stations and updating the state vector of the reconstructed muon (internal mathematical representation in algorithm's logic), the Kalman Filter achieves optimal estimates of the trajectories.

The implementation of the Kalman algorithm on FPGAs enables fast, parallel processing of multiple track candidates, ensuring the best possible outputs for the Level-1 Trigger. Validation of the Kalman Filter using cosmic data and simulation has demonstrated excellent agreement between hardware and software emulations, confirming the algorithm's accuracy and reliability. The success of the Kalman Filter in the BMTF opens the way for its broader adoption in future Level-1 Trigger upgrades.

The Conditions Database (CondDB) enables the reproducibility and consistency of CMS data analysis by managing non-event data such as calibrations, alignments, and hardware configurations. The Online-to-Offline (O2O) workflows ensures that the conditions used during data-taking are synchronized in the CMS internal instance of CondDB. These workflows bridge the gap between the online operational environment of the CMS detector and the offline reconstruction and analysis frameworks. By leveraging object-relational mapping and automated data synchronization, the O2O system ensures that all relevant conditions data are accurately transferred and validated.

Recent developments have focused on enhancing the immutability, idempotence, and concurrency of the O2O backend, aligning it with the latest requirements of the CMSSW software framework. Comprehensive unit and integration testing, along with explicit dependency declarations, have improved the system's robustness and maintainability even more.

4. The Soft Multilepton Analysis

The Soft Multilepton Analysis is a search for electroweakinos in compressed mass spectra, where new physics signatures manifest as low-momentum leptons and significant missing transverse energy. By requiring multiple soft leptons in the final state, the background components from bad quality reconstructions are suppressed, and the sensitivity is enhanced for signals predicted by supersymmetric models. The analysis uses datasets from the Run-2 period, which are reconstructed with the Ultra Legacy (UL) campaign of the CMS that incorporates the latest algorithms and calibrations for the period 2016-2018. Such algorithm is the novel LowPtElectron algorithm, extending the acceptance down to 1 GeV for the electron channels.

Supersymmetry (SUSY) extends the Standard Model by introducing a symmetry between bosons and fermions, predicting a spectrum of superpartners for known particles. The interpretations that are

included in this thesis are based on the Minimal Supersymmetric Standard Model (MSSM) and the Split SUSY frameworks, each offering solutions to theoretical challenges such as the hierarchy problem and providing viable dark matter candidates. The R-parity conservation in these frameworks ensures the stability of the lightest supersymmetric particle (LSP), making it a target for experimental searches.

Compressed mass scenarios, characterized by small mass differences between the LSP and next-to-lightest supersymmetric particle (NLSP), present unique experimental challenges. The resulting decay products are soft and often displaced, requiring specialized reconstruction and analysis techniques.

General Description of the Analysis Methodology

The analysis is structured into multiple categories and regions, each optimized for different final states and background compositions. Signal regions are defined for prompt and displaced leptons, with further subdivisions based on kinematic variables such as missing transverse energy and displacement significance.

Five distinct categories are defined based on the number and type of leptons in the final state, with each category associated with specific signal regions. Selection criteria are optimized to capture the kinematic features of the targeted decays, including requirements on lepton momentum, displacement, and isolation.

The background estimation combines simulation-based predictions with data-driven techniques. Control regions enriched in specific background processes are used to normalize simulations and extract systematic uncertainties. Application and validation regions support the estimation of non-prompt backgrounds, leveraging transfer factors and other validation techniques (like Closure Tests) to ensure the reliability of the predictions. The overall strategy is designed to provide robust statistical inference while maintaining sensitivity across a broad range of signal mass hypotheses.

Event Reconstruction

The event reconstruction in the analysis is a process involving the measurement and identification of objects like the primary and secondary vertices, leptons, jets, and missing transverse energy. Among them, the LowPtElectron reconstruction is a key innovation, which enables the identification of very soft electrons, critical for probing the very compressed part of the phase-space. The LowPtElectron reconstruction is combined with the nominal CMS Particle-Flow reconstruction as efficiently as possible, leading to special treatments of the resulting mixed reconstruction in many aspects of the analysis.

Both for muon and electrons, simulated samples are produced using the latest generators and detector simulations, ensuring accurate modelling of both signal and background processes. Trigger selection and identification performance are carefully matched between data and simulation, with scale factors applied to correct for differences in efficiency.

Data-Driven Background Estimation

Data-driven methods are central to the estimation of non-prompt backgrounds, particularly those arising from leptons within jets (fake leptons) and pile-up interactions. The Tight-to-Loose method, widely used in CMS, leverages orthogonal regions enriched in fake leptons to measure misidentification probabilities

(Fake Rates). These probabilities are then applied to data in application regions to predict the shape and yields of these background contributions in the signal regions.

The approaches that are followed account for correlations between close-by leptons, differences in isolation, and variations across kinematic regions. Closure tests are performed to validate the accuracy of the predictions, with systematic uncertainties assigned based on the level of accuracy achieved in these tests. The method is adapted for both prompt and displaced categories, ensuring comprehensive coverage of all relevant background sources.

Results & Interpretations

The results of the analysis are presented in terms of observed and expected exclusion limits on electroweakino masses and lifetimes, across a range of mass-splitting and displacement scenarios. The binning of each signal region is optimized for different interpretations, targeting for the pest possible sensitivity. The final post-fit yields and upper limits are calculated using a likelihood-based fit of the Signal and Control Regions to the data observed, resulting to exclusion limits at 95% Confidence Level for the mass hypothesis that the analysis includes. The analysis demonstrates sensitivity to both prompt and displaced signatures, with exclusion limits extending to previously unexplored regions of the parameter space.

Interpretations are provided within the context of simplified SUSY models, including Wino/Bino and Higgsino scenarios. The results are compared to simulated (theoretical) predictions and previous experimental searches, highlighting the analysis's contributions to the global effort to discover or constrain electroweakinos at the GeV scale.

5. Compressed SUSY Summary and projections to High Luminosity LHC (HL-LHC)

A dedicated summary chapter combines the results for compressed mass scenarios, focusing on the Higgsino pMSSM interpretation. The analysis combines the reach of three complementary CMS searches: (a) the soft multileptons analysis, (b) the soft isolated tracks analysis, and (c) the disappearing tracks analysis, providing a comprehensive exclusion of the phase-space by the CMS experiment.

Furthermore, projections for future data-taking periods, including Run-3 and the HL-LHC, are presented, illustrating what are the anticipated improvements in sensitivity. The projections are based on current results of the searches, accounting also for the surplus of luminosity that will be provided by the HL-LHC. On top of that, projections that account for the reduction of the systematic errors, because of the evolution of reconstruction techniques, have also been studied, however not presented due to little difference between reducing or not the systematic errors.

Περίληψη

Αυτή η διδακτορική διατριβή, η οποία εκπονήθηκε στο CERN, συζητά μελέτες Φυσικής Υψηλών Ενεργειών πάνω σε δεδομένα που συλλέχθηκαν από το πείραμα CMS. Η ανάλυση δεδομένων σχετίστηκε με δεδομένων του CMS που συλλέχθηκαν κατά την περίοδο Run-2 (2016–2018) και αναζητούσε τελικές καταστάσεις με 2 (ή 3) μιόνια και ηλεκτρόνια χαμηλής εγκάρσιας ορμής, μαζί με σημαντικές ποσότητες ελλείπουσας εγκάρσιας ενέργειας στα γεγονότα. Επιπλέον, η ανάπτυξη λογισμικού και αλγορίθμων σχετίστηκε με το σύστημα Level-1 Trigger του CMS, το οποίο λειτουργεί ως πρώτο φίλτρο επιλογής γεγονότων για το πείραμα, και ρυθμίζει τον όγκο των δεδομένων που συλλέγονται.

Η διατριβή χωρίζεται σε 5 κύριες ενότητες: τα πρώτα κεφάλαια περιγράφουν το σύμπλεγμα επιταχυντών στο CERN που παρέχει συγκρούσεις στο πείραμα CMS, τα επόμενα κεφάλαια περιγράφουν λεπτομερώς τη δομή του πειράματος CMS, ακολουθεί λεπτομερής παρουσίαση της εργασίας που σχετίζεται με το Level-1 Trigger, και το τελευταίο μισό της διατριβής είναι αφιερωμένο στην παρουσίαση της "Multilepton Analysis" (με ερμηνείες αποτελεσμάτων υπερσυμμετρίας Bino/Wino και Higgsino), μαζί με προβολές αυτών των αποτελεσμάτων σε όγκους δεδομένων που αναμένεται να συλλεχθούν κατά την εποχή του High-Luminosity LHC (2030–2041).

1. Ο Μεγάλος Επιταχυντής Αδρονίων (LHC) και άλλοι επιταχυντές στο CERN

Ο Μεγάλος Επιταχυντής Αδρονίων (LHC) στο CERN αποτελεί τον ισχυρότερο επιταχυντή σωματιδίων στον κόσμο, σχεδιασμένο για να διερευνήσει τα θεμελιώδη σωματίδια και να μελετήσει τις αλληλεπιδράσεις τους. Φιλοξενείται σε μια σήραγγα 27 χιλιομέτρων κάτω από τα σύνορα Γαλλίας—Ελβετίας κοντά στη Γενεύη και επιταχύνει δέσμες πρωτονίων με ενέργειες 6.5 TeV ανά δέσμη, προσφέροντας συγκρούσεις συνολικής ενέργειας 13 TeV. Οι συγκρούσεις αυτές παρέχονται σε τέσσερα πειράματα: ATLAS, CMS, ALICE και LHCb, καθένα από τα οποία είναι βελτιστοποιημένο για διαφορετικά είδη φυσικής υψηλών ενεργειών. Η κατασκευή και λειτουργία του LHC απαιτούσε δεκαετίες σχεδιασμού και μεγάλης κλίμακας διεθνή συνεργασία.

Τα επιστημονικά επιτεύγματα του LHC είναι σημαντικά, με σημαντικότερο την ανακάλυψη του μποζονίου Higgs το 2012, η οποία επιβεβαίωσε πλήρως το Καθιερωμένο Μοντέλο της Φυσικής Σωματιδίων. Πέραν αυτού, ο LHC συνεχίζει να επιτρέπει μετρήσεις ακριβείας και αναζητήσεις για νέα φυσική, συμπεριλαμβανομένων των φαινομένων πέραν του Καθιερωμένου Μοντέλου όπως η υπερσυμμετρία, οι επιπλέον διαστάσεις, και η διερεύνηση για σωματίδια σκοτεινής ύλης.

O Super Proton Synchrotron (SPS) λειτουργεί ως ο προτελευταίος επιταχυντής στην αλυσίδα επιταχυντών του CERN, αυξάνοντας την ενέργεια των πρωτονίων στα 450 GeV πριν την παραχώρησή τους στον LHC. Κατασκευασμένος τη δεκαετία του 1970, ο SPS έχει παίξει καθοριστικό ρόλο τόσο σε πειράματα σύγκρουσης δέσμεων όσο και σε πειράματα σταθερού στόχου, συμβάλλοντας σε ανακαλύψεις όπως τα μποζόνια W και Z. Η κατασκευή του τού επιτρέπει να παρέχει δέσμες, εκτός από τον LHC, σε διάφορα πειράματα σταθερού στόχου, συμπεριλαμβανομένων αυτών για μελέτες ταλαντώσεων νετρίνων στο εργαστήριο Gran Sasso στην Ιταλία.

O Proton Synchrotron (PS) αποτελεί θεμελιώδες κομμάτι της επιταχυντικής αλυσίδας του CERN και τέθηκε σε λειτουργία τη δεκαετία του '60, παρέχοντας επιτάχυνση για πρωτόνια και βαρέα ιόντα.

Λειτουργώντας σε ενέργειες από 2 έως 25 GeV, ο PS λειτουργεί ως γέφυρα μεταξύ των αρχικών σταδίων επιτάχυνσης και του υψηλότερης επιτάχυνσης στον SPS. Η μακροβιότητα του PS και η προσαρμοστικότητά του αποτελούν αποδείξεις του σχεδιασμού του και της διορατικότητας των σχεδιαστών του. Μέσα στα χρόνια, έχουν γίνει πολλές αναβαθμίσεις για να ανταποκριθεί στις νέες πειραματικές απαιτήσεις και να βελτιώσει την ποιότητα και σταθερότητα της δέσμης.

O Proton Synchrotron Booster (PSB) είναι το πρώτο σύγχροτρο στην επιτάχυνση των πρωτονίων στο CERN, λαμβάνοντας δέσμες χαμηλής ενέργειας από τους γραμμικούς επιταχυντές και φτάνοντας τις δέσμες στα 2 GeV. Ο σχεδιασμός του PSB ενσωματώνει πολλαπλούς δακτυλίους για να χειρίζεται δέσμες υψηλής έντασης και να επιτρέπει την αποτελεσματική παραχώρηση των πρωτονίων στον PS. Η κατασκευή του στις αρχές της δεκαετίας του '70 ήταν η απάντηση στην αυξανόμενη ανάγκη για υψηλότερες εντάσεις και ενέργειες δέσμης, βάζοντας τα θεμέλια για τις επόμενες τεχνολογίες επιταχυντών. Πέραν του βασικού του ρόλου στην επιτάχυνση πρωτονίων, ο PSB εξυπηρετεί επίσης εξειδικευμένα πειράματα χαμηλής ενέργειας, όπως τα ISOLDE και MEDICS, τα οποία απαιτούν ακριβή έλεγχο των παραμέτρων της δέσμης.

Οι γραμμικοί επιταχυντές (LINACs) στο CERN παρέχουν την αρχική επιτάχυνση τόσο για πρωτόνια όσο και για βαρέα ιόντα, προσφέροντας δέσμες με ενέργειες έως 160 MeV. Ο LINAC 4, που μπήκε σε λειτουργία το 2020, αντιπροσωπεύει τη νεότερη γενιά αυτών των μηχανών, με προηγμένες τεχνολογίες και λύσεις για τη βελτίωση της ποιότητας και αξιοπιστίας της δέσμης. Ο LINAC 3, που λειτουργεί από το '94, ειδικεύεται στην επιτάχυνση βαρέων ιόντων.

Η τεχνολογία των επιταχυντών βασίζεται σε θεμελιώδεις φυσικές αρχές που διέπουν την επιτάχυνση, την εστίαση της δέσμης, και τη σύγκρουση φορτισμένων σωματιδίων. Ηλεκτρικά πεδία σε κοιλότητες ραδιοσυχνοτήτων (RF) προσδίδουν ενέργεια στα σωματίδια, ενώ μαγνητικά πεδία καθοδηγούν και εστιάζουν τις δέσμες κατά μήκος των τροχιών τους. Η εξισορρόπηση μεταξύ επιτάχυνσης και σταθερότητας της δέσμης είναι ο κρίσιμος στόχος, με τεχνικές όπως η στοχαστική ψύξη και η ψύξη ηλεκτρονίων δέσμης να χρησιμοποιούνται για τη διατήρηση της ποιότητας της δέσμης.

Η ακτινοβολία του σύγχροτρου, που είναι μία συνέπεια της επιτάχυνσης φορτισμένων σωματιδίων κατά μήκος καμπυλωτών τροχιών, αποτελεί μία από τις σημαντικότερες προκλήσεις, ιδιαίτερα για ελαφρύτερα σωματίδια όπως τα ηλεκτρόνια. Η διαχείριση των απωλειών ενέργειας και η βελτιστοποίηση της φωτεινότητας (ο ρυθμός συγκρούσεων ανά μονάδα επιφάνειας και χρόνου) είναι εξίσου σημαντικά για την απόδοση των επιταχυντών. Η υψηλή φωτεινότητα προσφέρει περισσότερες σπάνιες αλληλεπιδράσεις και επιτρέπει τη μελέτη νέας φυσικής.

2. Το Πείραμα CMS, οι υπο-ανιχνευτές και τα συστήματά του

Μετά τα κεφάλαια για τους επιταχυντές ακολουθεί η ενότητα που περιγράφει το πείραμα CMS και τα ανιχνευτικά συστήματά του. Παρέχεται λεπτομερής περιγραφή κάθε κομματιού και συζητούνται τα βασικά τους χαρακτηριστικά, που είναι σημαντικά για την απόδοσή τους.

O CMS Silicon Tracker είναι ένα σύστημα «τροχογραφίας» σχεδιασμένο για την ανακατασκευή των τροχιών φορτισμένων σωματιδίων με υψηλή ακρίβεια. Συνδυάζοντας έναν εσωτερικό ανιχνευτή pixel και έναν εξωτερικό ανιχνευτή λωρίδων πυριτίου (strips), ο tracker προσφέρει πολύ υψηλή διακριτική

ικανότητα, γρήγορη εξαγωγή δεδομένων, και ανθεκτικότητα στην ακτινοβολία. Αναβαθμίσεις στον tracker, όπως η Phase-1 Pixel Upgrade και οι προγραμματισμένες βελτιώσεις για το Phase-2, εξασφαλίζουν τη διατήρηση της απόδοσης στο περιβάλλον υψηλής φωτεινότητας του HL-LHC.

Ο ανιχνευτής pixel, με τα τέσσερα στρώματα και τους υψηλής πυκνότητας αισθητήρες pixel, είναι τοποθετημένος πλησιέστερα στο σημείο σύγκρουσης, επιτρέποντας ακριβή ανακατασκευή κορυφών αλληλεπίδρασης (vertices) και μετρήσεις παραμέτρων των τροχιών σχετικές με τις κορυφές. Ο ανιχνευτής λωρίδων πυριτίου επεκτείνει την κάλυψη του tracker, εξασφαλίζοντας πολλαπλές μετρήσεις ανά τροχιά και ενισχύοντας τους αλγορίθμους αναγνώρισης μοτίβων. Το σύστημα επιτυγχάνει υψηλή χωρική ανάλυση, η οποία είναι σημαντική και για την ταυτοποίηση πρώτων και δεύτερων κορυφών και την ανακατασκευή του πλήρους ιστορικού των διασπάσεων.

Το σύστημα καλορίμετρων του CMS έχει σχεδιαστεί για να μετρά την ενέργεια ηλεκτρονίων, φωτονίων και αδρονίων με ακρίβεια. Το Ηλεκτρομαγνητικό Καλορίμετρο (ECAL), το οποίο είναι κατασκευασμένο από κρυστάλλους βολφραμίου-μολύβδου, προσφέρει υψηλή διακριτική ικανότητα και γρήγορη απόκριση, επιτρέποντας ακριβείς μετρήσεις ενέργειας και αποδοτική ταυτοποίηση σωματιδίων. Το ECAL χωρίζεται σε κυλινδρικό τμήμα (barrel), άκρα (endcaps), και έναν προ-ανιχνευτή (preshower), καθένα από τα οποία είναι βελτιστοποιημένο για τις διαφορετικές περιοχές ευθύνης του.

Το Αδρονικό Καλορίμετρο (HCAL) συμπληρώνει το ECAL μετρώντας την ενέργεια των αδρονίων και συμβάλλοντας στον υπολογισμό της ελλείπουσας εγκάρσιας ενέργειας. Το HCAL διαιρείται εξίσου σε τομείς κυλινδρικού τμήματος, των 2 άκρων, του εμπρόσθιου και του εξωτερικού τμήματος, όπου το καθένα καλύπτει συγκεκριμένες περιοχές ψευδοκύτητας. Μαζί, τα 2 καλορίμετρα προσφέρουν σχεδόν πλήρη κάλυψη γύρω από το σημείο σύγκρουσης, επιτρέποντας αναλυτική ανακατασκευή των γεγονότων και υποστηρίζοντας ένα ευρύ φάσμα αναλύσεων.

Το σύστημα μιονίων του CMS έχει σχεδιαστεί για να ανιχνεύει και να ταυτοποιεί μιόνια με υψηλή απόδοση και ακρίβεια, ακόμη και στο απαιτητικό περιβάλλον υψηλής φωτεινότητας. Το σύστημα συνδυάζει Drift Tubes (DTs) στην κυλινδρική περιοχή, Cathode Strip Chambers (CSCs) στα άκρα, και Resistive Plate Chambers (RPCs) που καλύπτουν και τις δύο περιοχές. Πρόσφατες αναβαθμίσεις έχουν επίσης εισάγει ανιχνευτές Gas Electron Multiplier (GEM) για την ενίσχυση της απόδοσης σε περιοχές με υψηλή ψευδοκύτητα.

Οι ανιχνευτές μιονίων είναι βελτιστοποιημένοι για συγκεκριμένες περιοχές ψευδοκύτητας λόγω της διαφορετικής ακτινοβολίας, εξασφαλίζοντας πλήρη γεωμετρική κάλυψη και ανοχή στις βλάβες μέσω πλεονασμού (redundancy). Ο πολυεπίπεδος σχεδιασμός του συστήματος μιονίων επιτρέπει όσο το δυνατόν ακριβέστερες μετρήσεις ορμής σε μεγαλύτερες αποστάσεις (4–7 μέτρα από τη δέσμη), αποδοτικό σκανδαλισμό (triggering), και αποτελεσματικό έλεγχο του υποβάθρου. Συνεχείς αναβαθμίσεις εξασφαλίζουν ότι το σύστημα παραμένει ανθεκτικό στα χρόνια και ικανό να ανταποκριθεί στις απαιτήσεις των μελλοντικών περιόδων του πειράματος.

Ο μαγνήτης του CMS είναι ένα σημαντικό κομμάτι του πειράματος, όπου δημιουργώντας αξονικό μαγνητικό πεδίο 4T, έχει σχεδιαστεί να κάμπτει τις τροχιές των φορτισμένων σωματιδίων ώστε να μετριέται αποτελεσματικά της ορμής τους. Ο σωληνοειδής μαγνήτης, κατασκευασμένος από υπεραγώγιμο υλικό, στεγάζεται μέσα σε έναν τεράστιο χαλύβδινο κάλυμμα (return yoke), το οποίος παρέχει επίσης δομική υποστήριξη στον ανιχνευτή.

Το κάλυμμα χωρίζεται σε κυλινδρικά και ακτινικά τμήματα, καθένα από τα οποία έχει σχεδιαστεί για να καθοδηγεί τη μαγνητική ροή και να υποστηρίζει την εγκατάσταση επιμέρους ανιχνευτών. Η λειτουργία σε κρυογονικές θερμοκρασίες και υψηλά ρεύματα απαιτεί αποδοτική ψύξη και εξελιγμένο σύστημα ελέγχου. Η επένδυση του CMS στον μαγνήτη του αντικατοπτρίζει τον κεντρικό ρόλο που έχει στην υποστήριξη των στόχων του πειράματος.

Το σύστημα σκανδαλισμού (trigger) του CMS είναι σχεδιασμένο με αρχιτεκτονική δύο επιπέδων και στοχεύει να μειώσει τον ρυθμό δεδομένων από 40 MHz στον διαχειρίσιμο ρυθμό των «λίγων kHz» για αποθήκευση. Ο Level-1 Trigger (L1T) βασίζεται σε ειδικά σχεδιασμένα ηλεκτρονικά με FPGAs, με στόχο τη λήψη γρήγορων αποφάσεων βασισμένων σε πρωτογενή δεδομένα από τους ανιχνευτές, ενώ ο High-Level Trigger (HLT) χρησιμοποιεί αλγορίθμους που εκτελούνται σε λογισμικό για πιο εξιδεικευμένη επιλογή γεγονότων. Μαζί, αυτά τα συστήματα εξασφαλίζουν ότι μόνο τα πιο ενδιαφέροντα δεδομένα από τις συγκρούσεις καταγράφονται για ανάλυση.

Οι αναβαθμίσεις στο σύστημα σκανδαλισμού, συμπεριλαμβανομένης της εισαγωγής προηγμένων αλγορίθμων και σύνθετων υπολογιστικών αρχιτεκτονικών, έχουν ενισχύσει την ευελιξία και την απόδοσή του συστήματος με την πάροδο των ετών. Το trigger menu, δηλαδή η λίστα των αλγορίθμων που εφαρμόζονται με λογική "OR", προσαρμόζεται συνεχώς ώστε να αντικατοπτρίζει το εξελισσόμενο ερευνητικό πρόγραμμα του πειράματος, ενσωματώνοντας νέα κριτήρια επιλογής και βελτιστοποιώντας τη χρήση πόρων. Η αξιοπιστία και η απόδοση του συστήματος είναι ζωτικής σημασίας, καθώς τα χαμένα γεγονότα δεν μπορούν να ανακτηθούν, και η συνεχής ανάπτυξή του αποτελεί σημαντική προτεραιότητα του CMS.

3. Το Barrel Muon Track Finder (BMTF) και η Βάση Δεδομένων Συνθηκών (CondDB)

Το BMTF είναι ένα εξειδικευμένο σύστημα εντός της αρχιτεκτονικής του Level-1 Trigger του CMS, το οποίο είναι υπεύθυνο για την ανακατασκευή υποψηφίων μιονίων στην κυλινδρική περιοχή χρησιμοποιώντας δεδομένα από DTs και RPCs. Το BMTF χρησιμοποιεί τον αλγόριθμο Kalman Filter για να επιτύχει υψηλή απόδοση και ακρίβεια στην μέτρηση της ορμής. Οι αναβαθμίσεις από την περίοδο Run 2 και μετά επέτρεψαν την αναγνώριση μιονίων μετατοπισμένης κορυφής στο Level-1, επεκτείνοντας την ευαισθησία του πειράματος σε μακρόβια σωματίδια.

Ο αλγόριθμος Kalman Filter που εφαρμόζεται αποτελεί μια σημαντική πρόοδο στην ανακατασκευή τροχιών σε πραγματικό χρόνο, η οποία χαρακτηρίζει τον Level-1 Trigger. Διαδοχικά, προσθέτοντας δεδομένα από διαφορετικούς σταθμούς ανίχνευσης μιονίων, το διανυσματικό μέγεθος κατάστασης (εσωτερική μαθηματική αναπαράσταση στη λογική του αλγορίθμου) του ανακατασκευασμένου μιονίου ενημερώνεται, και ο Kalman Filter επιτυγχάνει βέλτιστες εκτιμήσεις των τροχιών.

Η υλοποίηση του αλγορίθμου Kalman σε FPGAs επιτρέπει γρήγορη, παράλληλη επεξεργασία πολλαπλών υποψηφίων τροχιών, εξασφαλίζοντας τα καλύτερα δυνατά αποτελέσματα για τον Level-1 Trigger. Ο έλεγχος του Kalman Filter με χρήση δεδομένων από κοσμικά μιόνια και προσομοιώσεις έχει δείξει εξαιρετική συμφωνία μεταξύ υλοποιήσεων σε υλικό και λογισμικό, επιβεβαιώνοντας την ακρίβεια και αξιοπιστία του αλγορίθμου. Η επιτυχία του Kalman Filter στον BMTF ανοίγει το δρόμο για ευρύτερη υιοθέτησή του σε μελλοντικές αναβαθμίσεις του Level-1 Trigger.

Η Βάση Δεδομένων CondDB επιτρέπει την πιστή αναπαραγωγή «ρυθμίσεων λειτουργίας» με συνέπεια στην ανάλυση δεδομένων του CMS, καθώς αποθηκεύει δεδομένα που δεν σχετίζονται με φυσικές ποσότητες, αλλά με βαθμονομήσεις, ευθυγραμμίσεις, και ρυθμίσεις υλικολογισμικού. Το λογισμικό Online-to-Offline (O2O) εξασφαλίζει ότι οι συνθήκες που χρησιμοποιούνται κατά τη διάρκεια της συλλογής δεδομένων συγχρονίζονται με την εσωτερική εκδοχή της βάσης δεδομένων CondDB του CMS. Αυτό το σύστημα γεφυρώνει το κενό μεταξύ του online περιβάλλοντος λειτουργίας του ανιχνευτή CMS και των offline λογισμικών ανακατασκευής και ανάλυσης. Με την αξιοποίηση τεχνικών όπως το «object-relational mapping» και ο αυτόματος συγχρονισμός των βάσεων δεδομένων, το σύστημα O2O εξασφαλίζει ότι όλες οι «ρυθμίσεις λειτουργίας» κλωνοποιούνται με ακρίβεια.

Οι πρόσφατες αναβαθμίσεις ενίσχυσαν τον κώδικα του O2O ως προς την αμεταβλητότητά του (immutability), τη σταθερότητα σε αλλεπάλληλες εκτελέσεις ίδιων εντολών προς τη βάση δεδομένων (idempotency), και την ικανότητα ταυτόχρονης εκτέλεσης του backend (concurrency), ευθυγραμμίζοντάς το με τις τελευταίες απαιτήσεις του λογισμικού CMSSW. Νέες αυτόματες δοκιμές (unit tests) και ρητές δηλώσεις των απαιτήσεων στον κώδικα (dependency declaration), βελτίωσαν τη ακόμα περισσότερο σταθερότητα του συστήματος.

4. Η Ανάλυση Soft Multilepton

Η Ανάλυση Soft Multilepton ψάχνει για υπερσυμμετρικά φερμιόνια ηλεκτρασθενούς αλληλεπίδρασης σε φασικούς χώρους με εκφυλισμένες μάζες, όπου οι υπογραφές νέας φυσικής εκδηλώνονται ως λεπτόνια χαμηλής εγκάρσιας ορμής και σημαντική ελλείπουσα εγκάρσια ενέργεια. Με την απαίτηση πολλαπλών λεπτονίων χαμηλής εγκάρσιας ορμής στην τελική κατάσταση, μειώνεται το υπόβαθρο και ενισχύεται η ευαισθησία της ανάλυσης σε σήματα που προβλέπονται από υπερσυμμετρικά μοντέλα. Η ανάλυση χρησιμοποιεί δεδομένων από την περίοδο Run-2, τα οποία έχουν ανακατασκευαστεί με την έκδοση ανακατασκευής Ultra Legacy (UL) του CMS, η οποία ενσωματώνει τους πιο πρόσφατους αλγορίθμους και βαθμονομήσεις για την περίοδο 2016–2018. Τέτοιος αλγόριθμος είναι ο καινούριος LowPtElectron, ο οποίος επεκτείνει την ανακατασκευή μέχρι και 1 GeV για τα ηλεκτρόνια.

Η υπερσυμμετρία (SUSY) επεκτείνει το Καθιερωμένο Μοντέλο εισάγοντας μια συμμετρία μεταξύ μποζονίων και φερμιονίων, προβλέποντας υπερσυμμετρικά σωματίδια ως συμπληρωματικά στα ήδη γνωστά. Οι ερμηνείες αποτελεσμάτων που περιλαμβάνονται σε αυτήν τη διατριβή βασίζονται στο Minimal Supersymmetric Standard Model και στο Split SUSY, καθένα από τα οποία προσφέρει λύσεις σε ανοιχτά ερωτήματα όπως το πρόβλημα της ιεραρχίας και προβλέπουν υποψήφια σωματίδια για σκοτεινή ύλη. Η διατήρηση της R-parity σε αυτά τα μοντέλα εξασφαλίζει τη σταθερότητα του ελαυρύτερου υπερσυμμετρικού σωματιδίου, καθιστώντας το στόχο για τα πειράματα.

Τα σενάρια εκφυλισμένων μαζών, που χαρακτηρίζονται από μικρές διαφορές μάζας μεταξύ του LSP και του επόμενου ελαφρύτερου υπερσυμμετρικού σωματιδίου (NLSP), παρουσιάζουν ιδιαίτερες πειραματικές προκλήσεις. Τα προϊόντα της διάσπασης που προκύπτουν είναι χαμηλής εγκάρσιας ορμής και συχνά προέρχονται από δευτερογενείς κορυφές (secondary vertices), απαιτώντας ειδικές τεχνικές ανακατασκευής και ανάλυσης.

Γενική Περιγραφή της Μεθοδολογίας της Ανάλυσης

Η ανάλυση είναι χωρισμένη σε πολλαπλές κατηγορίες και περιοχές, καθεμία βελτιστοποιημένη για διαφορετικές τελικές καταστάσεις και συνδυασμούς υποβάθρου. Οι περιοχές σήματος ορίζονται για λεπτόνια από πρωτογενή και δευτερογενή κορυφές (vertex), με περαιτέρω υποδιαιρέσεις βασισμένες σε κινηματικά μεγέθη όπως η ελλείπουσα εγκάρσια ενέργεια και η μετατόπισης από την κορυφή.

Ορίζονται πέντε ξεχωριστές κατηγορίες με βάση τον αριθμό και τον τύπο των λεπτονίων στην τελική κατάσταση, με κάθε κατηγορία να σχετίζεται με συγκεκριμένες Signal Regions. Τα κριτήρια επιλογής είναι βελτιστοποιημένα ώστε να καταγράφουν τα κινηματικά χαρακτηριστικά των διασπάσεων, συμπεριλαμβανομένων απαιτήσεων στην ορμή των λεπτονίων, τη μετατόπιση από την κορυφή, και την απομόνωσή τους από άλλα σωματίδια.

Ο υπολογισμός του υπόβαθρου συνδυάζει προσομοιώσεις και υπολογισμούς βασισμένους σε πραγματικά δεδομένα. Control Regions επικεντρωμένες σε συγκεκριμένες διαδικασίες υποβάθρου χρησιμοποιούνται για τη διόρθωση των προσομοιώσεων και την εξαγωγή συστηματικών σφαλμάτων. Τα Application και Validation Regions χρησιμοποιούνται στον υπολογισμό υποβάθρων με λεπτόνια που δεν προέρχονται από την πρωτογενή κορυφή (non-prompt), αξιοποιώντας transfer factors και άλλες τεχνικές ελέγχου (όπως τα Closure Tests) για να εξασφαλιστεί η αξιοπιστία των υπολογισμών. Η συνολική στρατηγική έχει σχεδιαστεί ώστε να παρέχει καλά θεμελιωμένη στατιστική ανάλυση διατηρώντας παράλληλα την ευαισθησία σε ένα ευρύ φάσμα μαζών για το σήμα.

Ανακατασκευή Γεγονότων

Η ανακατασκευή γεγονότων στην ανάλυση είναι μια διαδικασία που περιλαμβάνει τη μέτρηση και ταυτοποίηση αντικειμένων όπως οι πρωτογενείς και δευτερογενείς κορυφές, λεπτόνια, πίδακες σωματιδίων (jets) και ελλείπουσα εγκάρσια ενέργεια. Μεταξύ αυτών, ο αλγόριθμος LowPtElectron αποτελεί βασική καινοτομία, η οποία επιτρέπει την ταυτοποίηση ηλεκτρονίων πολύ χαμηλής εγκάρσιας ορμής, κρίσιμη για τη μελέτη της «πολύ εκφυλισμένης» περιοχής του φασικού χώρου. Ο αλγόριθμος LowPtElectron συνδυάζεται με το βασικό αλγόριθμο CMS Particle-Flow όσο το δυνατόν πιο αποδοτικά, οδηγώντας σε ειδικές επεξεργασίες της μικτής συλλογής ηλεκτρονίων σε πολλές πτυχές της ανάλυσης.

Τόσο για τα μιόνια όσο και για τα ηλεκτρόνια, η προσομοίωση γίνεται χρησιμοποιώντας τους πιο πρόσφατους αλγορίθμους προσομοίωσης, εξασφαλίζοντας ακριβής μοντελοποίηση τόσο του σήματος όσο και υποβάθρου. Οι επιπτώσεις των αλγορίθμων επιλογής (triggers) και η επίδοση της ταυτοποίησης των σωματιδίων διορθώνονται στην προσομοίωση με χρήση πολλαπλασιαστικών παραγόντων, διορθώνοντας διαφορές απόδοσης των αλγορίθμων μεταξύ πειράματος και προσομοίωσης.

Υπολογισμός του Υποβάθρου από Πειραματικά Δεδομένα

Οι τεχνικές βασισμένες σε πειραματικά δεδομένα είναι σημαντικές για την εκτίμηση non-prompt υποβάθρων, ιδιαίτερα αυτών που προκύπτουν από λεπτόνια εντός πιδάκων σωματιδίων («fake» λεπτόνια) και από pile-up. Η μέθοδος Tight-to-Loose, η οποία χρησιμοποιείται ευρέως στο CMS, αξιοποιεί ορθογώνιες περιοχές επικεντρωμένες στα fake λεπτόνια για τη μέτρηση της πιθανότητας λάθους ταυτοποίησης (Fake Rates). Αυτές οι πιθανότητες εφαρμόζονται σε πειραματικά δεδομένα των Application Regions με σκοπό τον υπολογισμό των κατανομών του υποβάθρου στις Signal Regions.

Οι μέθοδοι που ακολουθούνται λαμβάνουν υπόψη συσχετίσεις μεταξύ κοντινών λεπτονίων, το επίπεδο απομόνωσης των λεπτονίων, και μεταβολές σε κινηματικές μεταβλητές. Το επίπεδο της ακρίβειας των

υπολογισμών ελέγχεται με τις δοκιμές «Closure Tests» και τα συστηματικά σφάλματα αποδίδονται βάσει του επιπέδου ακρίβειας που επιτυγχάνεται σε αυτές τις δοκιμές. Η μέθοδος προσαρμόζεται τόσο για κατηγορίες με λεπτόνια από τις πρωτογενή κορυφές όσο και για κατηγορίες με λεπτόνια από τις δευτερογενή, καλύπτοντας όλες τις σχετικές πηγές υποβάθρου.

Αποτελέσματα και Ερμηνείες

Τα αποτελέσματα της ανάλυσης παρουσιάζονται υπό μορφή παρατηρούμενων και αναμενόμενων ορίων απόρριψης σε μάζες και χρόνους ζωής των υπερσυμμετρικών φερμιονίων ηλεκτρασθενούς αλληλεπίδρασης, σε ένα εύρος σεναρίων διαφοράς μάζας και μετατόπισης. Η διακριτοποίηση (binning) σε κάθε Signal Region είναι βελτιστοποιημένη για τις διαφορετικές ερμηνείες αποτελεσμάτων, στοχεύοντας στην καλύτερη δυνατή ευαισθησία της ανάλυσης στο κάθε σενάριο. Τα τελικά (post-fit) αποτελέσματα και τα ανώτατα όρια απόρριψης υπολογίζονται μέσω fit των πιθανοτήτων πληθυσμού των Signal και Control Regions στα πειραματικά δεδομένα, οδηγώντας σε όρια αποκλεισμού για τις υποθέσεις μάζας που περιλαμβάνει η ανάλυση με 95% επίπεδο εμπιστοσύνης. Η ανάλυση δείχνει ευαισθησία τόσο σε σήματα από τις πρωτογενής κορυφές όσο και από δευτερογενή κορυφές, με όρια αποκλεισμού που πλέον καλύπτουν προηγουμένως ανεξερεύνητες περιοχές του φασικού χώρου.

Οι ερμηνείες αποτελεσμάτων παρέχονται στο πλαίσιο απλοποιημένων μοντέλων SUSY, συμπεριλαμβανομένων των σεναρίων Bino/Wino και Higgsino. Τα αποτελέσματα συγκρίνονται με θεωρητικές προβλέψεις και προηγούμενες πειραματικές αναλύσεις, αναδεικνύοντας τη συμβολή της ανάλυσης στη γενική προσπάθεια για την ανακάλυψη ή την απόρριψη των υπερσυμμετρικών φερμιονίων ηλεκτρασθενούς αλληλεπίδρασης στην περιοχή των GeV.

5. Σύνοψη Εκφυλισμένης Υπερσυμμετρίας και Προβολή Αποτελεσμάτων για το High Luminosity LHC (HL-LHC)

Ένα τελευταίο κεφάλαιο παρουσιάζει τα αποτελέσματα για σενάρια εκφυλισμένων μαζών, εστιάζοντας στο σενάριο Higgsino pMSSM. Η σύνοψη παρουσιάζει τα αποτελέσματα τριών συμπληρωματικών αναλύσεων του CMS: (α) την ανάλυση soft multileptons, (β) την ανάλυση soft isolated tracks και (γ) την ανάλυση disappearing tracks, παρέχοντας αποτελέσματα που καλύπτουν πλήρως το φασικό χώρο από το πείραμα CMS.

Επιπλέον, παρουσιάζονται προβολές για μελλοντικές περιόδους συλλογής δεδομένων, συμπεριλαμβανομένων του Run-3 και του HL-LHC, απεικονίζοντας τις αναμενόμενες βελτιώσεις στην ευαισθησία των αναλύσεων αυτών. Οι προβολές αυτές βασίζονται σε τωρινά αποτελέσματα των αναλύσεων, λαμβάνοντας υπόψη την αυξημένη φωτεινότητα που θα προσφέρει ο HL-LHC. Επίσης, εξετάστηκαν προβολές λαμβάνοντας υπόψη τη μείωση των συστηματικών σφαλμάτων λόγω βελτίωσης των διαφόρων αλγορίθμων ανακατασκευής, αλλά δεν παρουσιάζονται καθώς η διαφορά με και χωρίς τη μείωση των συστηματικών σφαλμάτων είναι ελάχιστη.

Table of Contents

| Abstr | ract | | 7 |
|-------|--------|---|-----|
| Sumr | mary | / | 8 |
| Περίλ | ληψ | η | 14 |
| Table | e of (| Contents | 21 |
| The A | Acce | lerator Complex at CERN | 23 |
| | 1. | The Large Hadron Collider (LHC): Particle Physics and High-Energy Collisions | 23 |
| 2 | 2. | Super Proton Synchrotron (SPS): Pre-Acceleration and Fixed-Target Experiments | 24 |
| 3 | 3. | Proton Synchrotron (PS): Intermediate Acceleration and Beam Distribution | 25 |
| 4 | 4. | Proton Synchrotron Booster (PSB): Initial Acceleration of Protons | 25 |
| į | 5. | LINACs at CERN: The Starting Point of Acceleration | 26 |
| (| 6. | Physical Principles of Accelerator Designs | 27 |
| The C | CMS | Experiment | 29 |
| - | 7. | The Silicon Tracker | 31 |
| 8 | 8. | The Calorimeter Detector | 33 |
| Ś | 9. | The Muon Detectors | 39 |
| : | 10. | The CMS Magnet | 42 |
| : | 11. | The Trigger System of the CMS | 44 |
| The B | Barre | el Muon Track Finder and The Condition DB | 49 |
| : | 12. | The Kalman Filter in BMTF (Run 3 and Phase-2) | 49 |
| : | 13. | Online-to-Offline (O2O) Workflows in CMS and L1 Trigger | 52 |
| The S | oft | Multilepton Analysis | 58 |
| • | 14. | Supersymmetry & Compress Mass Scenarios | 59 |
| | 15. | General Description of the Analysis Methodology | 63 |
| • | 16. | Event Reconstruction | 84 |
| | 17. | Data-Driven Background Estimation | 108 |
| | 18. | Results & Interpretations | 122 |
| Comp | pres | sed SUSY Summary | 128 |
| | 19. | THE ANALYSIS WITH SOFT MULTILEPTONS CMS-EXO-23-017 [36] | 128 |
| 2 | 20. | THE ANALYSIS WITH SOFT ISOLATED TRACKS CMS-SUS-24-012 [37] | 129 |
| : | 21. | THE ANALYSIS WITH DISAPPEARING TRACKS CMS-SUS-21-006, arXiv:2309.16823 [38] | 130 |
| 2 | 22. | Summary and Projections to Run3 and HL-LHC | 130 |
| Appe | ndix | C | 132 |

| References and Citations | | | 159 |
|--------------------------|-----|--|-----|
| | 27. | Prompt Rate Measurements for the Tight-to-Loose method | 158 |
| | 26. | Validation Regions for the Soft Multilepton Analysis | 153 |
| | 25. | Application Region for the Soft Multilepton Analysis | 143 |
| | 24. | Control Regions for the Soft Multilepton Analysis | 138 |
| | 23. | Signal Regions for the Soft Multilepton Analysis | 132 |

The Accelerator Complex at CERN

The European Organization for Nuclear Research, CERN (Conseil Européen pour la Recherche Nucléaire), hosts the most advanced particle accelerator complex in the world, a system of synchrotrons and linear accelerators that contribute to answering fundamental questions in physics and pushing the boundaries of technology [1, 2]. The accelerators operate as a chain, progressively increasing the energy of particles, and serve distinct experiments and research facilities. This chapter outlines CERN's accelerators, their contributions to physics, while also referring to the predecessors of these machines, and the principles that drive their design.

1. The Large Hadron Collider (LHC): Particle Physics and High-Energy Collisions

The Large Hadron Collider (LHC) is the flagship accelerating machine at CERN and is used to provide colliding beams at the 4 most advanced and famous experiments in the physics community, ATLAS, CMS, ALICE, and LHCb. Operating at the highest energy levels ever achieved ever in a collider, its central task is to receive the beams from the previous accelerator at 450 GeV and deliver them to the 4 points of collisions for the experiments at 6.5 TeV per beam (13 TeV total collision energy).

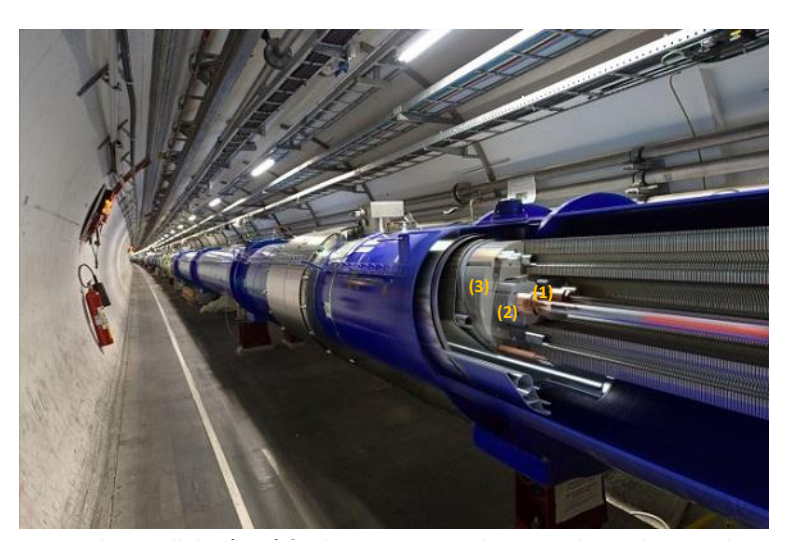


Figure 1: Picture of the Large Hadron Collider (LHC) facilities at CERN. The LHC is hosted in a 27 km tunnel that spans around several French villages between the Jura mountains and the Leman Lake in Geneva. In the image, there is a schematic of the accelerator apparatus featuring key components, like the beam pipes (1), the superconducting magnet (2), and the cooling system (3) that is responsible to keep the environment down to -271.3 °C.

The LHC is hosted in a 27 km tunnel that is located at the "Pay de Gex" region, spanning along several villages in France and close to Geneva. It took 10 years to be built, 1998-2008 and its designing phase lasted approximately 10 years in the 90s. Its contribution to Particle Physics is substantial, helping to discover the Higgs Boson in 2012 and nowadays it contributes to precision measurements for the Standard Model and searches for new physics beyond the Standard Model.

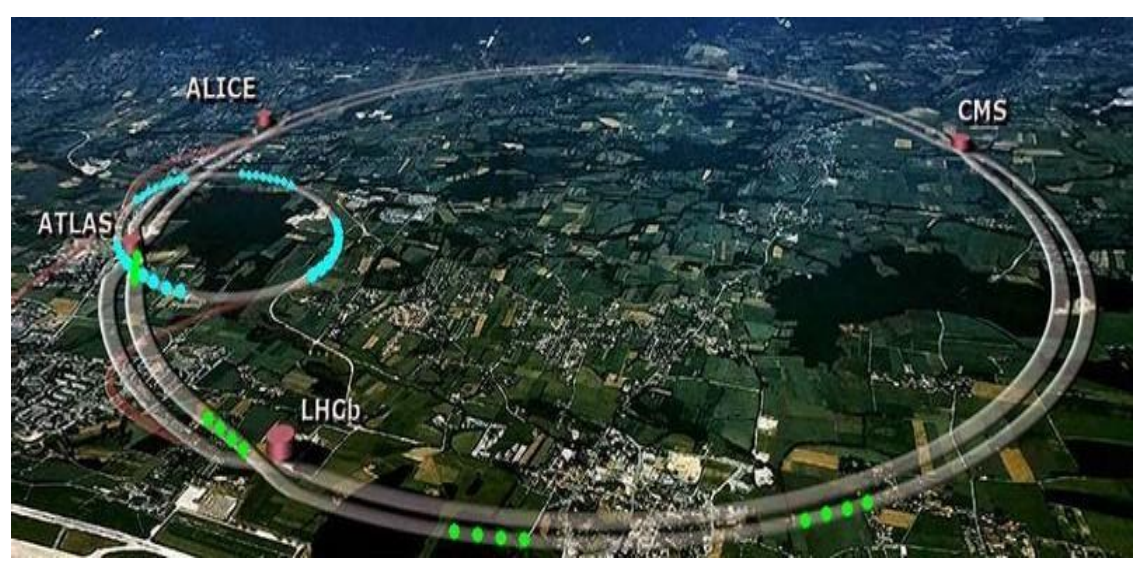


Figure 2: Aerial photo of the region that hosts the Large Hadron Collider. This is a representation of the circumference of the accelerator and protons traveling around the SPS and the 4 experiments, ATLAS, CMS, ALICE, and LHCb.

2. Super Proton Synchrotron (SPS): Pre-Acceleration and Fixed-Target Experiments

The **Super Proton Synchrotron (SPS)** serves today as a pre-accelerator before the LHC and delivers beams with energy of 450 GeV, to be further accelerated. Also, it contributes to fixed-target experiments and delivers test beams to the Gran Sasso Laboratory in Italy, which performs neutrino oscillation studies (known as CERN Neutrinos to Gran Sasso - CNGS). The machine was built in 1976 and designing it lasted approximately 6 years, a project that started in the beginning of the 70s.



Figure 3: The Super Proton Synchrotron (SPS) facilities at CERN. The SPS, like other accelerators except the LHC, is hosted in a tunnel in the Meyrin site of the CERN facilities. In the image, there are the accelerator machine and several structures that include the beam pipe, the magnets, and the cooling system like the LHC picture above.

3. Proton Synchrotron (PS): Intermediate Acceleration and Beam Distribution

The **Proton Synchrotron (PS)** is the previous step in the chain of accelerators that provide beams for the experiments at CERN, it operates as an intermediate step. It operates at the energy range of 2 to 25 GeV, before passing it through to the SPS. At the same time, the Proton Synchrotron is responsible to deliver protons, anti-protons, and heavy-ions to several medium-energy experiments, some of the most important are the Antiproton Decelerator complex and the n_TOF. This machine was built in 1959 and designing it lasted around 5 years, making it one of the oldest accelerators at CERN still in operation.



Figure 4: Picture of the Proton Synchrotron (PS) facilities at CERN. The PS, like other accelerators but the LHC, is hosted in a tunnel in the Meyrin site of the CERN facilities. In the image, there are the accelerator and several structures including the beam pipe, dipole and quadrapole magnets, and the cooling system.

4. Proton Synchrotron Booster (PSB): Initial Acceleration of Protons

The **Proton Synchrotron Booster (PBS)** is the first machine that handles protons stripped from their ions. This accelerator receives the beam at 160 MeV of energy and boosts it to 2 GeV before injecting it into the PS. The PBS is also responsible for delivering the beam to multiple low-energy experiments at CERN, such as ISOLDE and MEDICS. This machine was built in 1972, while it was under design in the second half of the 60s.

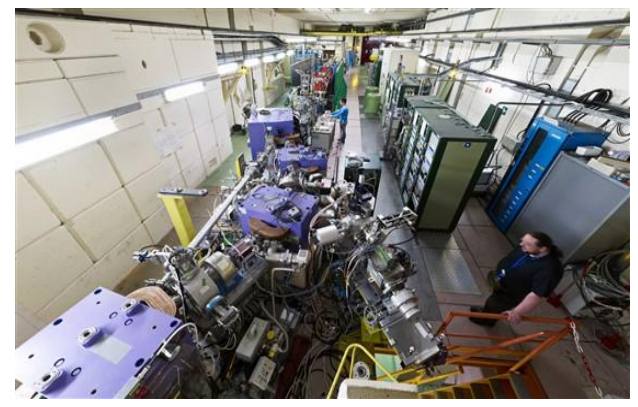


Figure 5: Picture of the Proton Synchrotron Booster (PSB) facilities at CERN. The PSB, like all other accelerators but the LHC, is hosted in a tunnel in the Meyrin site of the CERN facilities. In the image, there are the accelerator and several structures including dipole magnets (in orange), quadrapole magnets (in green), and the cooling system that all together keep the particles focused and moving on the right trajectory.

5. LINACs at CERN: The Starting Point of Acceleration

The linear accelerators (LINACs) at CERN are the machines that provide protons to the acceleration chain. Hydrogen-ions or heavy-ions are accelerated up to 50-160 MeV, depending on the LINAC generation and technology, they are stripped of their ions using a combination of electric and magnetic fields, and eventually they are injected to the PSB or the PS for further acceleration.

Today two of the LINACs are still operational, LINAC 4 that was commissioned in 2020 and LINAC 3 that was built in 1994. LINAC 4 delivers protons of 160 MeV to the PBS for the Proton-Proton Collision program. This machine is the latest one that was developed at CERN and was under the designing stage since the late 2000s. LINAC 3 delivers heavy-ions of 4.2 MeV/nucleon to the LEIR accelerator (Low Energy Ion Ring) that further accelerates the nucleons before passing them through to PS for the Heavy-Ion Collision program. The LINAC 3 was built in 1994.



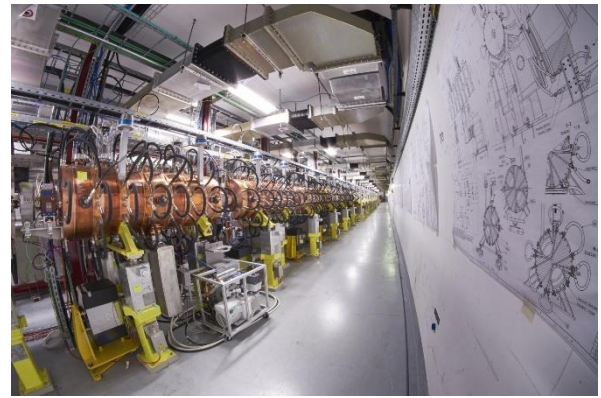


Figure 6: Pictures of LINAC 3 and 4 facilities at CERN, left and right respectively. The LINACs, like other accelerators except the LHC, is hosted in a tunnel in the Meyrin site of the CERN facilities.

6. Physical Principles of Accelerator Designs

The design of particle accelerators is based on several principles that allow the machines to efficiently boost the particles (or heavier nucleons) to high energies. Very important is also the task to keep the particles focused on a beam that follows a designated trajectory and allows for precise collisions and interactions.

Firstly, particle accelerators rely on electric fields that are generated in RF (radiofrequency) cavities to accelerate the charged particles. The oscillating electromagnetic fields transfer energy to the particles as they are crossing these fields. As an example, the LHC uses 400 MHz RF cavities to accelerate protons to 6.5 TeV.

Synchrotrons like the LHC and the SPS use magnetic fields to guide the particles in circular trajectories. **Dipole magnets** bend the trajectory of particles and **quadrupole magnets** focus the beam, preventing the beam from spreading. These magnets are highly strong, for reference a dipole magnet in the LHC generates a field of 8.3 Tesla.

Charged particles, while they are accelerated in a curved trajectory, emit radiation known as "synchrotron radiation" and this leads to energy loss. This effect is more significant when accelerating lighter particles like electrons (e.g. at LEP) and subsequently this requires energy refilling in parallel with acceleration. Also important, in terms of beam quality, is the optimization of the accelerated beams using techniques like **stochastic cooling** and **electron cooling** to stabilize the beams by controlling their trajectories and spread energy, respectively.

In colliders, luminosity is a crucial parameter and measures the number of collisions per area and time that the collider can deliver. It depends on the number of particles in the beams, their spread area, and the frequency of operation. High luminosity increases the probability of particle interactions and leads to larger volumes of data to be analyzed. As an example, the LHC is designed to operate with a luminosity of $10^{34} cm^{-2} s^{-1}$.

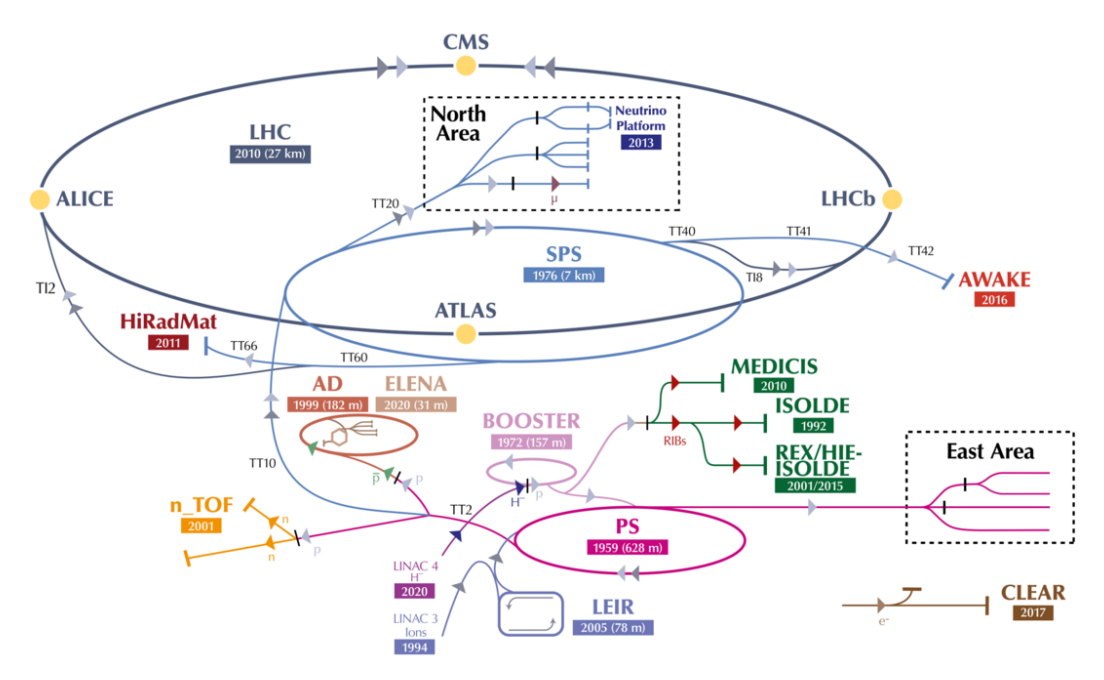


Figure 7: A schematic of the Acceleration Complex at CERN and the experiments that the accelerators deliver beams to. Together with their names, the frames also include the year of commissioning for each machine.

The CMS Experiment

The following chapters are dedicated to describing the CMS Experiment, one of the most advanced and collaborative modern experiments of High Energy Physics. The CMS Experiment is located at CERN and its purpose is to collect data from proton-proton or heavy-ion collisions that are provided from the LHC (the Large Hadron Collider, see The Accelerator Complex at CERN). In a nutshell, collisions are provided 40 million times per second by the accelerator to the experiment, which uses highly advanced silicon sensors, calorimeters, and gas particle detectors, and records information about the result of the collisions. Finally, physicists from the experiment, using fast custom-made electronics regulate the amount of data to be stored and reconstruct the results of each collision that is collected.

In the following sections, it is a detailed description of the individual detectors and systems that assemble the CMS Detector. In Figure 8 one can find a layout illustrating the transverse section of the apparatus, the central silicon detectors, the calorimeters, the 4 Tesla solenoid, and the muon gas detectors positioned between steel material.

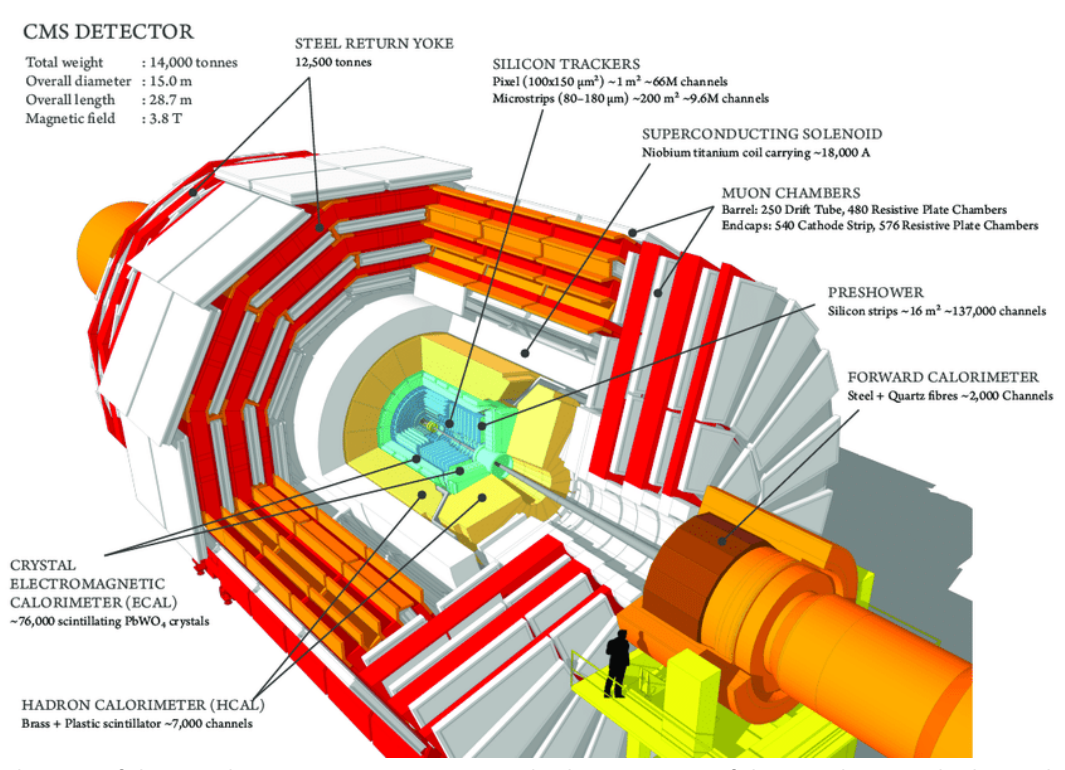


Figure 8: Schematic of the CMS detector at CERN LHC. Longitudinal cross-section of the CMS detector, displaying the various layers surrounding the LHC beam axis, with the collision point at the center.

The CMS apparatus is optimized so that it achieves the optimal performance to fulfill the following requirements [3]:

- ✓ Robust tracking and vertexing for accessing the full range of physics that LHC is providing.
- ✓ Categorization of W and Z events in an extended range of lepton momentum, since their decays are illustrated by many theoretical models, and similarly for W' and Z'.

- ✓ Meet the necessary isolation performance to provide information for identifying efficiently isolated electrons. Isolated leptons play a crucial role suppressing background for two main physics targets of the CMS, the Higgs and SUSY searches. (The effective isolation requires reconstruction of hadronic tracks down to 1 GeV.)
- ✓ The efficient reconstruction of b jets and the identification of the B-mesons play an important role. Both are essential in top physics and CP violation studies. (It requires the tracker to identify tracks from different vertices, reconstruct decay chains, and proper characterize decay lengths by studying displaced vertices.)
- ✓ While searching for new physics, tau-lepton recognition and their reconstruction play a significant role too, since taus are present in some theoretical final states. (The tau reconstruction relies on tracking and the experiment's capabilities on displaced vertices)
- ✓ Most of the questions that are targeted by CMS require high luminosity in order the collected statistics to be enough to allow for meaningful research. The systems of the experiment are designed to be efficient for luminosities up to 10³⁴ cm⁻²s⁻¹. (High luminosities translate to multiple simultaneous and unrelated vertices in each bunch crossing, the "pileup", with the tracker required to cope with reconstructions of up to 65 simultaneous vertices for Run2 and Run3, and a foreseen 2000 vertices per bunch crossing for the Phase-2 projects.)

A specialized coordinate system is used to describe the positions and trajectories of particles produced in the collisions. It is a cylindrical system and centered around the beam axis, which is defined as the z-axis. The transverse plane, perpendicular to the beam axis, is described using the radial distance (r) and the azimuthal angle (φ) . The angle φ (phi) is measured in the transverse plane from a fixed direction, typically the x-axis, and ranges from $-\pi$ to π .

To describe the angle of a particle relative to the beam axis, the CMS experiment uses pseudorapidity (η) instead of the polar angle θ . Pseudorapidity is defined as $\eta = -ln[tan(2\theta)]$,

where θ is the angle between the particle's momentum vector and the beam axis. This transformation is helpful because differences in η are Lorentz invariant under boosts along the beam axis, making it the variable of choice for collider physics. Particles that are produced at small θ (close to the beam direction) have large η values, with the parallel to be infinity (∞), while those produced perpendicular to the beam ($\theta = 90^{\circ}$) have $\eta = 0$.

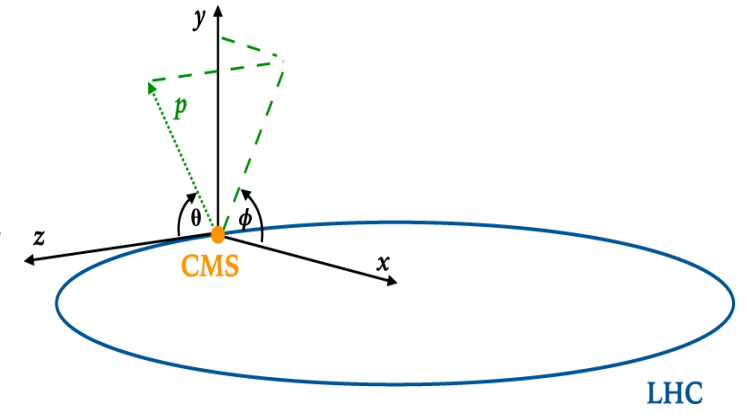


Figure 9: The reference system that is used by the CMS experiment. Two angles describe the position of the momentum vector of the particles, where θ is the angle between the beam axis (axis-z) and the vector, and φ the projection of the vector to the transverse plane x-y.

The CMS detector is structured into two main regions based on η : the barrel and the endcaps. The barrel region surrounds the beam line and covers low pseudorapidity values (typically

 $|\eta| < 1.3$), where particles are emitted nearly perpendicular to the beam. The endcap regions extend coverage to higher pseudorapidity values (up to $|\eta| \approx 2.5$), capturing particles emitted at more forward angles.

7. The Silicon Tracker

The tracking system for the CMS experiment [4] consists of two different systems, the Pixel vertex detector and the Silicon Strips. The design was required to meet strict requirements of extremely fine granularity, since it covers the area with the highest particle density, fast signal readout to cope with 25ns bunch crossings, and radiation hardness for a 10-year lifetime using minimal material to reduce secondary interactions. The solution was a silicon-based detector, with pixel sensors at the innermost region and microstrip sensors for the outer tracker.

The CMS Tracker consists of co-axial cylinders around the collision point and circular endcaps at each end of the barrel. The pixel detector forms the inner core of 16cm radius using 4 layers of active material, and the silicon outer tracker extends out to a radius of about 1.3m using 10 more layers. This layout results in multiple measurements per track, with a typical particle that crosses the tracker leaving hits in 14 layers on average, with 3-4 hits in the pixel and 9–10 hits in the strips.

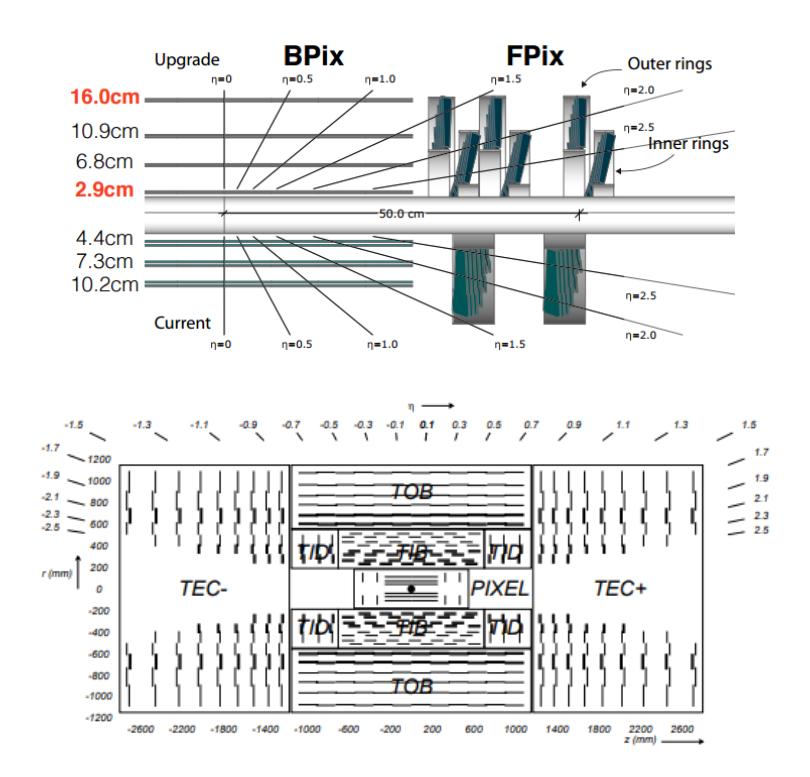


Figure 10: The geometry of the Pixel detector (upper) and the complete Tracker system (bottom). The pixel detector is presented in 2 phases, current was the Pixel detector that was used through Run1 and 2016, and Upgrade is the new Pixel detector that is used from 2017 onwards, when the design changed to 4 layers in the barrel and tilted rings at the endcap. The Tracker system is presented as a schematic, where each line represents a detector module.

7.1. The Pixel Detector

The CMS Pixel Detector is the closest to the interaction point. It is a cylindrical device that consists of tiny silicon pixel sensors arranged in layers. Currently, the CMS uses 4 layers in the barrel

wrapping around the beam and extend to 16cm in radius, 3 endcap disks per side, and uses 124M pixels in total. Due to excessive use of electronics for the readout and high density of particles a CO_2 cooling system is used, which provides cooling with minimal material without significant effects on the tracking performance. The pixel covers pseudorapidity up to $|\eta| < 2.5$. The first pixel layer sits roughly 3 cm from the beam and is exposed to an intense flux of about 600M particles per cm² each second.

Performance

The primary target is precise position measurements near the primary interaction, providing a special resolution of about 10 μ m. With 3 or 4 hits per track in the pixel detector, the CMS achieves an impact parameter resolution of about 10-20 μ m, which is crucial for secondary vertex identification.

The pixel detector itself has a short lever arm and its standalone p_T measurements have low precision; however, pixel inputs improve significantly the combined momentum fit. The timing of the Pixel sensors [5] provides a response time of about 3ns, which is dominated by the drift time of the carriers inside the silicon, making it quick enough to time-stamp hits to the correct bunch crossing (25ns).

7.2. The Silicon-Strip Detector

The Silicon Strip Detector surrounds the pixel detector and is segmented into several substructures. The Tracker Inner Barrel (TIB) and the Tracker Inner Disks (TID) cover a radius from 20 to 55 cm with 4 barrel-layers and 3 endcap-disks respectively, the Tracker Outer Barrel (TOB) extends up to about 130 cm radius (including the strips) with 6 more barrel-layers, and the Tracker Endcaps (TEC) complete the detector enclosing the TOB using two more endcap-disk systems.

In practice, a particle at pseudorapidity $\eta\approx 0$ will cross 10 barrel-layers (4 TIB + 6 TOB), while a particle towards the endcaps will cross barrel-layers and multiple endcap-disks, in practice at least 9 hits (or more) for $|\eta|<2.4$, providing vital information for pattern recognition algorithms. The resolution, per hit, is roughly 20–50 μ m in r- ϕ (azimuthal) direction and a few hundreds of μ m in z (coarse measurement based on strips' dimensions), while the p_T resolution combining both tracker detectors is about 1% at 100 GeV (central). On average, the material through the tracker is about 0.4 X_0 (radiation lengths, energy drop to $1/e\approx36\%$) at $\eta=0$, increases to about 1.8 X_0 at $|\eta|\sim1.4$, where particles cross the most tracker material, and decreases to about 1.0 X_0 at $|\eta|=2.5$.

7.3. Physics Goals, Upgrades, and Cost

A significant target of the CMS Tracker is the isolation performance, which played a central role in the design of the detectors, since the isolation requirements were expected to be crucial to suppress the background for Higgs and SUSY searches. By Run 2, the LHC luminosity exceeded the design $10^{34}\ cm^{-2}s^{-1}$ and the original pixel detector started to show inefficiencies at higher

rates, so CMS scheduled the Phase-1 Pixel Upgrade [7, 9] at the end of 2016. The old pixel detector (2008-2016) was removed and the new pixel detector (with 4 layers and upgraded CO₂ cooling) was inserted in place. Lastly, in LS2 (Long Shutdown 2) the pixel detector went through the "Layer-0 upgrade" [8] that replaced the first layer closer to the beam due to the damage from 2018.

The cost of the Tracker project [4] is significant, with the initial cost of the project at CHF 74.1M for Phase-1, and the total cost for the Phase-2 Upgrade to be estimated to be at least CHF 87.4M. The Phase-2 cost, according to newer resources [6], is estimated to be about CHF 110M and includes the Outer Tracker, Inner Tracker, and Common Systems. The update benefits from existing infrastructure, ensuring lower cost and risks.

8. The Calorimeter Detector

8.1. The Electromagnetic Calorimeter

The CMS Electromagnetic Calorimeter (ECAL) [10] is a homogeneous, hermetic calorimeter designed to measure the energy of electrons and photons. It is placed between the silicon tracker and the hadron calorimeter, inside the coil of the CMS Magnet. The ECAL plays a significant role in analysis, it contributes to isolation sums and was built with fine granularity and fast response characteristics. It is constructed from scintillating lead tungstate crystals (PbWO₄) that produce light proportional to the energy deposits from crossing particles. Photodetectors convert the scintillation to electrical signals during readout. The calorimeter is segmented in three sections as shown in Figure 11, the barrel (EB) for the central region, two endcaps (EE), and a preshower detector (ES) in front of the endcaps separating π^{o}/γ candidates.

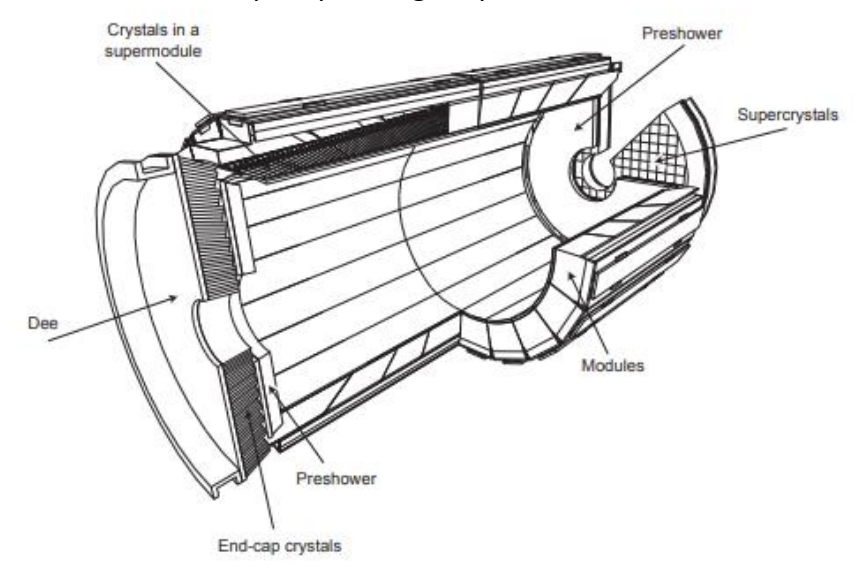


Figure 11: The geometry of the ECAL Project [11]. It is separated to the Barrel (EB), the two Endcaps (EE), and the Preshower (ES).

8.1.1. The Barrel ECAL (EB)

The ECAL EB is a cylindrical array of 61,200 lead tungstate crystals that cover the central pseudorapidity $|\eta| < 1.48$. It is placed about 1.3m away from the beam line, forming a detector about 7.8 m long and 3.5 m in diameter. The barrel crystals have approximately 22mm resolution on the front side facing the collision with a radiation length of about 25.8 X_0 . The barrel is

segmented into a grid of 360 readout sections in φ and 170 in pseudorapidity. The front-end electronics cover a dynamic range in the energy measurement, from a few MeV up to TeV energies without saturation.

Performance

The measurement resolution is parameterized using 3 terms [11], a stochastic term (significant for ECAL), a noise term that contributes about 120 MeV in measurements, and a constant term that becomes significant as the measurement goes to the TeV scale, giving about 30GeV offsets. The characteristics of the detector come as a result of the choice of photodiodes that are used for the readout.

$$\sigma_E/E \approx \sqrt{\left(2\%/\sqrt{E}\right)^2 + (0.12/E)^2 + (0.3\%)^2}$$

The energy resolution of the EB for high-energy photons is about 2% at 100 GeV photons (for example $H \to \gamma \gamma$ decays), with the results becoming even better for measurements at 120 GeV after calibrations. The time resolution of the EB is about 200ps contributing to pileup mitigation techniques.

8.1.2. The Endcap ECAL (EE)

The two ECAL Endcaps (EE) extend the electromagnetic calorimeter to the forward region, with pseudorapidity $1.48 < |\eta| < 3.0$. Together, the two EEs, contain about 14,600 lead tungstate crystals (7300 per endcap) placed in a projective geometry. The crystals of the EE section are slightly shorter than the crystals at the EB section, with a radiation length of about 24.7 X_0 , and have approximately 28.6mm resolution at the front size facing the collision. Each endcap crystal is read out by one Vacuum Phototriode, small vacuum-tube photodetectors with an anode that handles radiation better than the photodiodes.

Performance

The EE section has slightly worse energy resolution (the preshower and the readout are a factor). The stochastic term in the endcap is slightly greater (around $2.5\%/\sqrt{E}$) and results to an energy resolution typically 2–5% at 100 GeV photons; however, calibration keeps the resolution under acceptable levels. The timing resolution of the EE section is around 300ps (25 ns bunch crossing).

8.1.3. The Preshower (ES)

The primary role of the ECAL Preshower (ES) is to identify photons from π^0 decays, which due to their proximity can fake a single high-energy photon in the ECAL. Each ES detector is placed in front of the EE, covering pseudorapidity of $1.65 < |\eta| < 2.6$. It is a disk made of silicon, about 20cm thick, with 63mm of spatial resolution. The preshower is a calorimeter of two layers of lead absorber and silicon sensors, causing electrons/photons that cross the lead to initiate a shower before reaching the EE crystals. The total radiation length is about 3 X_0 , which results to 95% of lower-energy photons to begin showering inside the ES.

Performance

The contribution to the energy resolution from the preshower itself is not as much as from the crystals (relatively short radiation length), however, the stochastic term is large due to the material that is used, with a stochastic term about $5\%/\sqrt{E}$. When combined with the EE crystals for measurements, the preshower contributes a varying 1 to $3\%/\sqrt{E}$ at 20 to 100 GeV, a result of 1999 [12].

8.1.4. Upgrades and Cost

In LS1 and LS2, no major changes were made to the ECAL crystals or photodetectors, but maintenance and repair work was carried out. Specifically, EE electronics and preshower modules went through minor repairs in LS1, while in LS2 few prototypes (for the Phase-2 upgrade) were validated in EB, together with new front-end electronics that provide higher sampling rate and better timing.

The ECAL project is split into different areas of responsibility and the required funding for each one is estimated accordingly. According to estimations back from `97 [10], for the barrel the cost is estimated to about 60M CHF, and for the endcaps to about 23M CHF. The cost for the preshower, that is considered a separate component than the endcaps, is estimated to be about 5.5M CHF, and it is already part of the amount assigned to the endcaps.

8.2.The Hadronic Calorimeter

The CMS Hadronic Calorimeter (HCAL) [13] is a key component of CMS, designed to measure the energy of hadrons and contribute significantly to the measurement of missing energy. It is a calorimeter that is made of layers of dense absorbing material, together with scintillators that produce light pulses when particles cross. The readout electronics collect the signal that comes from the light.

The HCAL is divided into 4 subprojects covering different regions (as shown in Figure 12), the Barrel (HB), the Endcap (HE), the Forward Calorimeter (HF), and the Outer Calorimeter (HO) just outside the barrel. All four together, they ensure nearly full coverage around the collision point, with a total absorber depth equivalent to about 10 interaction lengths¹ (λ_I) for hadrons in most regions.

¹ One interaction length (λ_I) is the average distance that a particle travels in one medium before undergoes some interaction. A detector that delivers $n*\lambda_I$ is more efficient than one other with $\frac{n}{2}*\lambda_I$, meaning that is more likely to contain the complete shower that comes from a particle and so measure its energy in full.

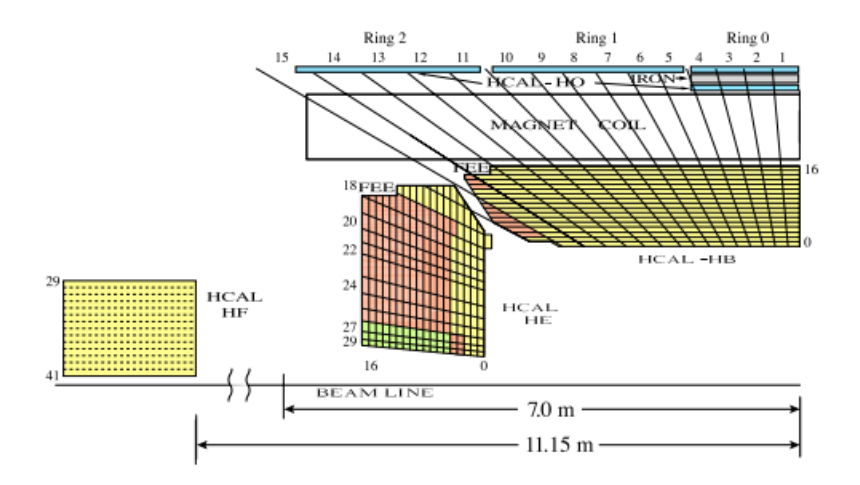


Figure 12: The geometry of the HCAL Project [16]. It is separated to the Barrel (HB + HO), the Endcap (HE), and the Forward (HF). The numbers on the diagram indicate the segmentation of the system into several readout modules (scintillators). With "FEE" are noted the location of the Front-End Electronics for HB and HE.

8.2.1. The Barrel Hadronic Calorimeter (HB and HO)

The HCAL Barrel [15] is a cylindrical structure surrounding the CMS electromagnetic calorimeter, covering the central region ($|\eta| < 1.3$). It fits in the radial gap between the outside of the electromagnetic calorimeter (at radius R \approx 1.77 m) and the inner surface of the superconducting solenoid magnet (R \approx 2.95 m). It is made of a non-magnetic brass (70% Cu / 30% Zn) as absorber and it was chosen due to its high density, and interaction length characteristics that allow to contain entire showers. Notably, recycled World War II artillery material was used to manufacture the absorber plates, reducing the cost significantly.

HB Geometry

The barrel is separated into sectors (each covering about 10° in ϕ). The plates are put together with scintillator layers in a configuration that ensures complete coverage. Within a sector, the active scintillator is segmented into cells corresponding to towers of a size of approximately $5^{\circ} \times 5^{\circ}$, which defines the resolution of the barrel and matches the granularity of the electromagnetic calorimeter. Along the η direction, HB is segmented into 16 sampling scintillator layers. The layers were originally grouped to form 2 longitudinal readout modules (inner and outer HB), but upgrades increased the resolution later. The full barrel calorimeter provides about $5.8 \, \lambda_I$ of absorber centrally (η =0), increasing to about $10.5 \, \lambda_I$ at the edge ($\eta \approx 1.3$) due to the projection from the collision point.

Each sector weighs about 26 tons because of the brass that is contained in the design. The full barrel extents to 9m in z (matching the magnet), with an inner radius of 1.8m and outer of 3m.

HB Performance

The energy resolution [16] of the HB calorimeter was designed to have a stochastic term $\sim 100\%/\sqrt{E}$ and a constant term $\sim 5\%$. The combined measurement from ECAL+HB corresponds to about 10% energy resolution for a 100 GeV hadronic jet in the barrel. The front-end electronics

and photodetectors were designed to allow a dynamic range using LUTs (Look-Up Tables²), typically corresponding to a range of about 0.2 GeV to 1 TeV. The HB also provides timing information for energy deposits, with a typical time resolution of a few nanoseconds per deposit enabling

pileup rejection.

The Outer Hadronic Calorimeter (HO)

The HCAL Outer Calorimeter (HO) [14] is in principle an extension of the barrel, using the yoke of the CMS magnet as an absorber to capture hadronic showers deep in the detector. The HO consists of scintillator layers that is mounted on the inner side of the muon system, at radius around 4m. In total, HO provides outer coverage up to $|\eta| \lesssim 1.25$.

Geometry and Performance

HO scintillator sectors are mapped onto the same $\Delta\eta \times \Delta\phi$ grid as the HB towers, so that each tower corresponds to a tower in HB (5° in ϕ). HO, by itself, is not used to measure the energy of hadrons, but to correct the measurements of the HB, providing more linear response up to multiple hundreds GeV, and improving the missing transverse energy resolution by capturing energy that otherwise would end-up to be missing.

Cost Effect

Since HO reuses existing structures (magnet iron) and involves relatively small-area scintillators, it was a cost-effective addition. In the 90s the estimates for HO were only a small fraction of the HCAL budget (a few million CHF).

8.2.2. The Endcap Hadronic Calorimeter (HE)

The HCAL Endcaps cover the area just beyond the barrel, with pseudorapidities in the range $1.3 < |\eta| < 3.0$. There are two HEs, each forming a large disk that fits inside the endcap muon system. About 34% of all final-state particles in CMS reach HE, measuring a significant portion of the energy of the event. As for the case of the barrel, the endcaps use brass for the absorber and each disk is approximately 2 m in radius, while all layers provide roughly 10 interaction lengths (λ_I) of material, when crossing the material in vertical direction. Each endcap weighs about 150 tons

HE Geometry

The HE scintillator is segmented in towers like HB, but their size progressively changes at higher η . In the range up to $|\eta|=1.6$ the fine granularity of the barrel is maintained, while the tower size is slightly larger at greater pseudorapidities ($|\eta| \geq 1.6$). The HE towers are readout in 2 sections (front and back), with few of them at higher $|\eta|$ region, separated in 3 sections for better shower-

² A Look-Up Table refers to specialized memory on-chip that holds digitized outputs (energy, momentum, ...) corresponding to specific input combinations, easily accessible to reduce the process time of an on-chip implementation of an algorithm.

depth measurements, since this segmentation helps to identify early vs late energy deposition. The size of such an HE sector is about 2m in radius and 4m along the beam.

HE Performance

As in the case of HB, the HE was designed to have a stochastic resolution [16] of about $100\%/\sqrt{E}$ for single hadrons. However, the jet energy resolution in HE is dominated by physics effects, like pileup, and any degradation on the stochastic term is not critical for physical measurements. In real scenarios of combined measurements with ECAL, the measurements achieve a resolution of about 10% for multiple hundreds of GeV. The signal from the HE is also sampled per 25 ns and is timed with about 1 ns precision, like in the HB, contributing also to the pile up handling techniques.

8.2.3. The Forward Hadronic Calorimeter (HF)

At very large pseudorapidities and close to the beam line ($3.0 < |\eta| < 5.2$) a specialized calorimeter is required because the radiation levels are extreme. The Forward Hadronic (HF) calorimeters are two cylindrical detectors located about 11m on each side of the CMS interaction point, behind steel shielding walls, and are the outmost detectors to intercepting particles from the collisions. On average, more than 7 times the energy that is deposited to the CMS from each collision (about 100 GeV) is deposited in the two HFs.

Given this challenge, the HF is a Cherenkov calorimeter and use a different approach from HB/HE. Instead of scintillator, HF's active material is made of radiation-hard quartz fibers (for their radiation resistance), which emit Cherenkov radiation as charged particles cross these fibers faster than the speed of light (in that medium). The absorber is a steel cylinder along the beam, corresponding to about 10 interaction lengths (λ_I), and a little hole of about 13cm radius is left to fit the beam pipe.

HF Geometry

The angular spanning of each HF module is 20° , which is further split into towers of coarser size than HB and HE but is sufficient (given the physics needs at high η), where the jet sizes are larger than the resolution that the segmentation provides. Since at these pseudorapidities the ECAL calorimeter is not extended, a 2-phase readout is implemented with sorter fibers covering only the second half of the detector. This 2-phase readout design is capable of distinguishing electromagnetic showers from the hadronic ones. An electromagnetic shower from a high-energy electron or photon leaves most of its energy in the first part of HF, so the short fibers will capture weaker signals compared to the long fibers.

HF Performance

This detector must be capable of measuring very energetic jets and discriminate them from beam debris, so the design incorporates a large dynamic range up to the TeV scale. For example, a single HF sector may record energies of several TeV because of very high-momentum forward jets. The HF is mostly sensitive to the electromagnetic component of showers since it is based on the Cherenkov light that is emitted by secondary charged particle decays inside the material. As

a result, the stochastic term of its hadron energy resolution is relatively large [16], about $150-200\%/\sqrt{E}$ or worse, for single particles. In practice, when combining information from long and short fibers (in the same fashion as when combining ECAL with HCAL), CMS achieves energy resolutions of about 20% for multiple hundreds of GeV.

8.2.4. Cost and Upgrades

The total cost of CMS HCAL (all sections HB, HE, HF, HO, including electronics) was estimated to 45M CHF in the late 90s (about 10% of total CMS detector) [13]. The barrel was the largest single fraction of the HCAL budget, roughly 20M CHF (with HO included, 1-2M CHF). The endcap accounted for about 15M CHF of the HCAL budget. Also, the forward calorimeters were relatively cheaper, costing roughly 10M CHF for both.

Since Run 1 and its original installation, HCAL was upgraded during the Long Shutdowns. The motivation for these upgrades was not only to mitigate issues and compensate for degradation, but also to ensure good performance at luminosities of $2\times 10^{34}cm^{-2}s^{-1}$ for Run 2 and beyond, with harsher pile-up conditions. More upgrades are scheduled for the High-Luminosity program.

9. The Muon Detectors

The CMS Muon detectors [17] were designed to meet the challenging physics requirements of the LHC. The primary goal was to ensure the accurate measurement of muon momentum, which is crucial for identifying processes such as the Higgs boson decay into four leptons, or the search for new particles like Z' or W' bosons. Additionally, they needed to be sustainable in the harsh environment of intense radiation and responsive while transversed by high particle fluxes because of the provided LHC luminosities.

The geometry of the Muon detectors for Run2 (2016-2018) and Run3 (2022 - 2025), which is shown in Figure 13, was optimized to maximize detection efficiency, and momentum resolution. The CMS Muon system is arranged in a multilayered layout outside the CMS Magnet, with the Drift Tubes (DTs) occupying the barrel region, the Cathode Strip Chambers (CSCs) in the endcaps, and the Resistive Plate Chambers (RPCs) complementing both regions. This arrangement ensures coverage up to a pseudorapidity of $|\eta| < 2.4$, allowing for the detection of muons with a wide range of momenta and angles.

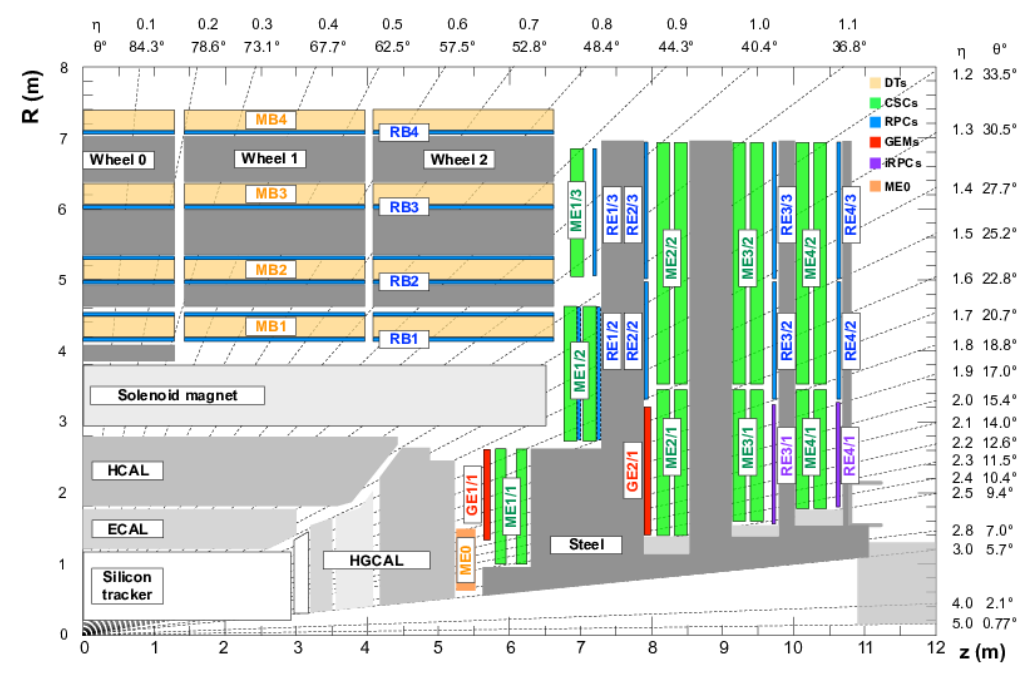


Figure 13: The geometry of the DT, RPC, CSC, and GEM modules arranged at the outermost part of the CMS detector [18]. The schematic represents the geometry after the installation of the GEM modules GE1&2 (in red) and the prototype MEO, during the third era of data collection Run3 (2022-2025). The purple RPC modules RE3/1, RE4/1, and HGCAL (in place of ECAL & HCAL) are foreseen as upgrades for Phase-2.

Between Run2 and Run3, the Muon detectors underwent significant upgrades [19, 20] to enhance their performance. The upgrades addressed issues such as aging detector components and the need for higher granularity to endure the increasing luminosity of the LHC in Run 2 and Run 3. For example, the Gas Electron Multiplier (GEM) detector was introduced to improve the muon trigger and tracking performance in the high-luminosity environment. These detectors added redundancy in the pseudorapidity range $1.6 < |\eta| < 2.2$, where the detection layers were previously coarse.

9.1.Drift Tubes

The Drift Tubes (DTs) are muon detectors that provide precision measurements in the barrel region, designed to measure muon trajectories up to a pseudorapidity of $|\eta| < 1.2$. Each DT chamber contains a grid of wires inside a gas mixture that is ionized when a muon transvers the chamber, allowing the position of the muon to be measured using the drift time of the electrons along the wires.

Each chamber is equipped with custom-designed readout electronics that amplify and read the signals generated by muons while passing through the gas mixture. A sophisticated control system ensures stable operation and monitoring of the DT status of the chambers, providing also the necessary voltage and managing data acquisition. The DT chambers use a specific gas mixture aiming to optimize the signal quality when muons interact with the atoms, it consists of 85% Argon (Ar) and 15% Carbon Dioxide (CO₂).

Performance

During Run2, the DTs maintained a spatial resolution of approximately 200 μ m, contributing significantly to the reconstruction of muon tracks and regulating the High-Level Trigger rates, which was vital for various physics analyses. The timing resolution is limited by the area inside the Drift Tube that the muon has crossed, where in worst cases electrons are required to drift for about 400ns, but the typical drift time is less than a bunch-crossing (25ns). In preparation for Run3, the Drift Tube detector went through maintenance to ensure their continued high performance in the face of increased luminosity and radiation levels.

9.2. Cathode Strip Chambers

The Cathode Strip Chambers (CSCs) are precision detectors that are employed in the endcap regions, covering pseudorapidities of $0.9 < |\eta| < 2.4$. The CSCs are composed of arrays of cathode strips and anode wires, providing high-resolution tracking and triggering capabilities in the high-radiation zones of the endcaps. When muons cross, electrons are released from the gas atoms in the chambers, which are attracted to the anode wires creating an avalanche of electrons. The gas mixture of the CSC chambers is different than that of the DTs, it consists of 40% Argon (Ar), 50% Carbon Dioxide (CO₂), and 10% Tetrafluoroethane (CF₄).

Performance

In Run 2 and Run 3, the CSCs have a spatial resolution of about 100µm on average, playing a crucial role in identifying and measuring high-momentum muons at the endcap regions of the CMS detector. The typical timing resolution of the detector is less than 10ns, while in worst cases it might reach about 60 to 100ns that exceed the bunch-crossing (25ns). The CSCs provide faster responses than the DTs, yet not as quick as the RPCs (see the next section). For Run3, the CSCs received upgrades to their electronics to enhance data acquisition and processing, leading to improved handling of the data-stream during higher rates and even better timing accuracy.

9.3. Resistive Plate Chambers

The Resistive Plate Chambers (RPCs) serve as fast-timing detectors that supplement the DTs and CSCs. They provide additional measurements along the muon trajectory, improving the efficiency and robustness of the muon trigger system. The RPCs cover pseudorapidities up to $|\eta| < 1.6$ in the barrel and $1.6 < |\eta| < 2.4$ in the endcaps. In terms of their design, these chambers consist of two resistive parallel electrode plates and the gap between the plates is filled with gas, 96% Freon (Fr), 3.5% Isobutane (C₄H₁₀), and 0.5% with Hexafluoride (SF₆). Electrons from the gas that is ionized are attracted by the charged plates that subsequently produce a signal with approximately 1ns response time.

Performance

The RPCs don't offer fine segmentation of the electrodes, so the detector doesn't allow for a fine spatial resolution that is typically a few cm, however, they offer fast and reliable muon detection with a timing resolution of about 1 ns. In Run3, the RPCs were updated with new link boards and

control systems to improve their timing resolution and rate capability, ensuring their continued contribution to the trigger system.

9.4. Gas Electron Multiplier (GEM) Detectors

The GEM detectors [18] represent a significant upgrade to the CMS muon system for Run3. These detectors are installed in the first endcap station and are designed to operate in the high radiation environment that is present at pseudorapidities of $1.6 < |\eta| < 2.2$. The GEM detectors provide additional information in places where the amount of detection layers is the lowest and the background rates are the highest.

A GEM chamber is a micro-gas detector that uses thin foils to amplify ionization electrons. The key material is the copper foil, densely pierced with microscopic holes, and high voltage applied between the two sides of the foil. When a muon crosses the chamber, it ionizes the gas and electrons drift to the closest hole creating an avalanche and a signal for the electronics to collect.

Performance

The detector uses a triple-layer structure of foils that is segmented in 100-300µm strips and define the spatial resolution of the detector. The timing of the GEM signals is about 5ns, which is not as fast as the RPCs but also contributes information that is faster than a bunch-crossing (25ns). Also, a custom-designed chip (VFAT3) in the front-end electronics provides fast input for the Level-1 muon trigger. The expected performance of the GEMs includes improved spatial resolution, crucial for the high-luminosity environment.

9.5. Cost and Upgrades

The CMS Muon Project is a significant investment in the pursuit of high-energy physics research. The overall cost of the project, including the Phase-II upgrade with Gas Electron Multiplier (GEM) detectors is estimated about 65M CHF, with also including a small excess with respect to the original TDR proposal back in `97 [17]. The breakdown allocates about 25M CHF to each of the DTs and the CSCs, 7-8M CHF to the RPCs, and 4-5M CHF to the GEMs [21]. This budget covers the design, construction, testing, and integration of the muon detectors into the CMS experiment.

The original installation of the system took place before 2008, while some of the chambers were installed during the long shutdown before Run2. Before Run 3, the Muon system was upgraded with the GEM detectors and further upgrades with newer RPCs and electronics are targeted for Phase-2.

10. The CMS Magnet

The CMS Magnet [22] is a critical component of the CMS Experiment. The magnet generates an axial magnetic field up to 4 Tesla, bending charged particles to allow for precise momentum measurement. It is 6m in diameter, 12.5m in length, and capable to store energy of about 2.6GJ at 4T. The solenoid is supported by a return yoke weighing approximately 12,000 tons, and this structure is providing mount support to subdetectors.

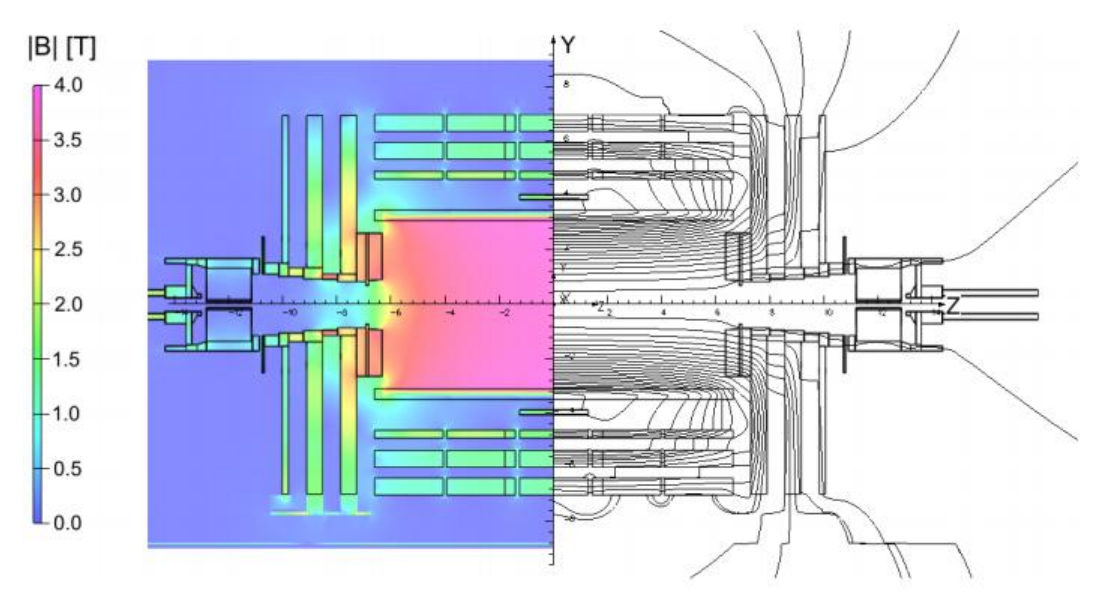


Figure 14: Simulated mapping [23] of the Magnetic field strength of the CMS Magnet and illustration of its field lines. Inside the coil there is a constant amplitude and outside there is reduced magnetic field present at the area of the gaseous muon detectors.

10.1. The Barrel and Endcap Return Yokes

The CMS magnet's return yoke is an enormous structure made of steel, designed to guide the magnetic flux, and provide mechanical support. At the operating field strength of 3.8T, roughly 2/3 of the magnetic flux is captured by the yoke, while 1/3 "leaks" out as weakening field that decays rapidly to about 10^{-3} T at 50m from the detector. The return yoke consists of two main sections, the barrel yoke and the endcap yokes. The barrel yoke consists of five wheels, each with a 12-sided formation and layered plates with gaps, where the muon detectors are installed. The barrel yoke extends approximately 21.6m in length and weighs about 12,000 tons.

The endcap yokes feature three circular steel disks per endcap, 14m in diameter, which are complemented by two extra nose disks that are cone-shaped. The nose disks enclose the barrel sides and guide the magnetic flux more efficiently and in a continuous manner between the barrel and the endcap disks. The addition of a fourth disk was added during LS1 to help reduce muon background and radiation. The entire yoke system not only supports the CMS experiment's structural integrity but also contributes significantly to its ability to measure charged particle momenta with precision.

10.2. The Superconducting Coil and the Vacuum Tank

The vital part of the CMS magnet is the superconducting solenoid that generates the magnetic field. The coil is made from Niobium-Titanium superconducting wires (type-2 superconductor), it is designed for a field of 4T, but CMS operates it at 3.8 T to stay within a safety margin to prolong its life. It is 12.5m long with an inner empty diameter of about 6m for the Tracker and the Calorimeters. The coil is housed in a cryostat (vacuum tank) that brings the total magnet's outer diameter to 7.6 m. The nominal operating current for 3.8T field is about 18.2 kA, and for 4T is about 19.5kA.

The vacuum tank provides the required insulation (high vacuum and thermal isolation) to keep the coil at a cryogenic temperature, which is around 4.5K during operation, and takes about a month to cool the magnet down from room to operating temperature.

10.3. Physics Goals, Performance, and Cost

The 4T Magnet is a significant asset that has a direct impact on the performance of the experiment and its measurements. Furthermore, the structure is supporting all the detectors. The cost, including the design, manufacturing, assembly, and integration of all components, is estimated about 120M CHF. This estimation is reported in technical reports during the design stage of the project at '97 [22].

11. The Trigger System of the CMS

The CMS uses a two-tier Trigger System to reduce the readout rate from 40 MHz down to a manageable rate of the order of 1 kHz. Firstly, is the Level-1 Trigger (L1T) [24, 25], which is a custom-made system that processes the data fast in real-time and selects potentially interesting events. The L1T reduces the rate to about 100 kHz, however recently during Run 3 rates up to 130 kHz have been tested. The next stage is the High-Level Trigger (HLT) [27], a software-based system running on the HLT computing farm, which further reduces the rate by processing the complete event down to about 1-3 kHz. This output is meant for permanent storage. These systems enable CMS to record only the most interesting collisions for physics analysis.

11.1. The Level-1 Trigger (L1T)

The L1 Trigger is entirely implemented using custom electronics (prototype boards with high-end FPGAs) located close enough to the detector and connected to the front-end electronics using optical fiber links. L1T is designed to make a trigger decision within a fixed latency of about 128 bunch crossings (about 3.2 μ s), after which the data from the detectors are no longer available. It receives low-granularity data from the detectors and reconstructs "simplistic" objects in real time, like muons, electrons/photons, τ leptons, jets, and energy sums. The L1T architecture is pipelined, meaning that detector data for these 128 bunch-crossings are processed in a first come first served fashion, and the trigger accept signal (L1A) is produced at the end to indicate whether the event record will be stored or rejected. The L1 trigger must be reliable, because once an event is rejected is lost forever, so the system is designed to avoid accidental losses or deadtime, during which LHC collides protons but CMS doesn't record them.

L1 Subsystems

The L1 Trigger is divided into several sub-systems that handle different detector inputs and run in parallel, before forwarding the reconstructed objects to the Global L1 Trigger, which makes the decision. A block diagram of the design is in Figure 15 (right).

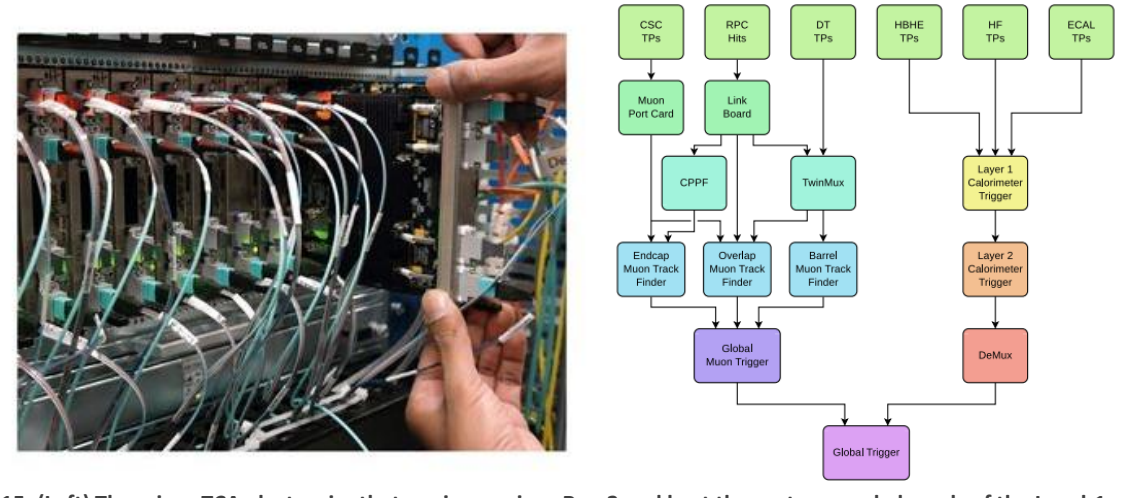


Figure 15: (Left) The micro-TCA electronics that are in use since Run 2 and host the custom-made boards of the Level-1 system at the Service Cavern in the CMS. (Right) A schematic of the Level-1 design and the sub-systems that reconstruct the event at the L1 and make the decision whether an event is kept or discarded. The left half shows the Muon Trigger with inputs from DTs, CSCs, and RPCs, and the right half shows the Calorimeter Trigger with inputs from ECAL and HCAL.

Data from the calorimeters (ECAL and HCAL) are input to the Calo Layer 1, where neighboring calorimeter cells are summed into trigger towers and calibrated. The data are then forwarded to Calo Layer 2, where calorimeter-based objects are formed (electrons/photons, τ leptons, jets, and global sums like "hadronic missing" and "total missing" energies) before being sorted and forwarded to the Global Trigger. Data from the muon detectors (DT+RPC, CSC+RPC, and GEM) are input to the Muon L1 Trigger, where separate track-finders cover the barrel, the endcap, and the overlap between the two. These regional muon triggers use methods like Kalman filter, Pattern Recognition, and refined Neural Networks to form muon objects and assign p_T measurements and quality flags. The Muon Trigger sorts and selects the best-quality objects before forwarding the event to the Global Trigger.

The Global L1 Trigger receives the trigger objects from Calo Layer 2 and the Muon Trigger for each bunch crossing in the pipeline and applies the L1 trigger menu, which is a list of selection conditions (or rules, e.g. Single Muon with 24 GeV momentum, Double Jet with momenta 100 GeV and 80 GeV, or Missing Energy Sum of 120 GeV) that all are evaluated in parallel. If any condition is satisfied, the event is accepted for readout. In Run 2 the Global Trigger introduced the ability to make more complex decisions, like mass or angular cuts on the trigger objects. Such upgrades enabled the use of advanced triggers at L1 which were not possible in the original design. Furthermore, in Run 3 the barrel muon trigger introduced upgrades that took place during 2018 and LS2 (Kalman Filter), which allowed to have displaced muons in the triggering algorithms for the first time in the online trigger of the experiment. Developments like this targeting displaced muons have also been carried out from the other L1 systems targeting Run 3, which provides sensitivity to long-lived particles decaying in the muon system.

11.2. The High-Level Trigger (HLT)

The High-Level Trigger (HLT) is the second stage of event selection, which is software implemented, runs on the HLT computing farm, and has access to the complete detector readout.

The HLT has also access to information from the Tracker that, up to Run 3, is not available to the L1 Trigger.

Upon receiving an L1 accept signal, the event (approximately 1–2 MB) is transferred from the readout buffers to the Event Builder computers. The HLT software then reconstructs the event with algorithms similar with the offline reconstruction but optimized for speed. The HLT decision must be quick enough to keep up with the input rate (about 100 kHz from L1), but it is not as time-limited as for the L1T. On average, processing time is few hundreds of milliseconds per event, while in rare cases it may be up to a few seconds for complex events. In the end, the HLT delivers a yes/no decision, reduces the event rate to a few kHz, and the event is written to permanent storage, where is available for further physics analysis.



Figure 16: A Run 3 HLT node [26], installed with 2 AMD Milan 64-core CPUs and 2 NVIDIA Tesla T4 GPUs.

HLT Infrastructure

The HLT runs on a dedicated farm of commercial computers, which included about 30,000 CPUs (64-bit processors) in Run 2. Events that are accepted by L1 are sent via a high-bandwidth network to the HLT nodes, where each node runs an instance of the CMS reconstruction software (CMSSW) in multi-threaded mode, and processes events in parallel. The HLT farm is designed to be upgradeable, as new servers are added on demand with the latest CPUs. By 2018, the farm size was capable to handle about 100 kHz input within an average of 200ms per event. For Run 3, a significant upgrade was made to the HLT farm, adopting heterogeneous computing architecture with incorporating also GPUs [29, 30]. The Run 3 HLT farm includes nodes with two 64-core AMD CPUs and two NVIDIA Tesla T4 GPUs (Figure 16), for a total of about 25.500 CPUs and 400 GPUs. About 30% of the HLT computing workload was put to run on GPUs in Run 3, while transparently HLT can fall back to CPUs in case of need.

HLT Reconstruction and Algorithms

The HLT software environment is a streamlined version of the CMSSW, ensuring that trigger decisions are based on objects of near-offline quality. The complete detector data are available,

including tracking, which is crucial for running Particle-Flow (PF) algorithms (e.g. muons identification or track-based isolation). The HLT workload is organized to a menu of paths analogous to when someone runs offline analysis steps like MiniAOD and NanoAOD processing. Typically, over 600 distinct paths constitute the HLT Menu, each targeting some final state or a calibration stream. An HLT path is a sequence of modules (code) that filter the event, for example low-level reconstructions, higher-level calculations (e.g. isolation, fits, etc.), and filters checking conditions.

The HLT menu is considerably richer than the L1 menu and reflects the physics program of CMS. For Run 2, the HLT menu covered Single Lepton Triggers, e.g. HLT_IsoMu27 (isolated single muon with $p_T > 27$ GeV), di-lepton or multi-lepton Triggers, e.g. HLT_Ele23_Ele12 (di-electron with $p_{T-1} > 23$ and $p_{T-2} > 12$ GeV), Jets and Missing Energy Triggers, e.g. HLT_Jet450 or HLT_MET120 (single jet with $p_T > 450$ GeV or missing energy with $p_T > 120$ GeV), and other Exotic or Special Triggers, e.g. long-lived particle triggers or calibration triggers using known signals like $j/\psi \to \mu\mu$.

Additionally, an innovation in the menu (during Run 2) [28] was the introduction of Scouting triggers, which simply save high-level reconstructed quantities (for example a list of jets) with a significantly greater output rate (tens of kHz). This allows to study, for example, a scouting di-jet trigger with low p_T threshold at 5-10kHz rate but only store the jets' momenta and event summary (a few kB/event instead of 1 MB). Furthermore, HLT paths for "parked" data streams were also considered to collect data at higher rates that can't be sustained online, store them, and process the dataset offline later. These strategies effectively extend the physics reach of the HLT beyond the nominal output bandwidth. For Run 3, the HLT menu continues to cover all the above categories, with adjustments for the higher expected pile-up and other detector or algorithmic developments.

11.3. Phase 2 upgrade and Cost

The L1 trigger upgrade is a significant project in terms of investment and international contributions. It involves development and production of many custom boards and firmware. As an example, the University of Ioannina, the National and Kapodistrian University in Athens, and the Institute of Accelerated Systems and Applications, in Greece, designed and contributed the Barrel Muon Layer-1 board, featuring the Xilinx VU13P FPGA and 28Gbit/s optical links for the Phase-2 L1 upgrade targeting the HL-LHC.

The total cost of the L1 trigger project, including subsystems, was estimated back in 2000 about 12.5M CHF, allocating about 5.5M CHF to the Calorimeter Trigger, about 5M CHF to the Muon Trigger, and about 2M for the Global Trigger. This amount has been exceeded later due to upgrades and maintenance, while for the Phase-2 upgrade an even larger budget is allocated, with about 40% of it corresponding to off-the-shelf components (FPGA boards, fibers, crates). The electronics for the L1 Trigger are considered a justifiable long-term investment for the CMS Collaboration, since they must reliably operate for many years and not fall back compared to the fast-moving technology when the operation of each era takes place.

The HLT computing infrastructure is a major component of the CMS operational costs, and it scales with the increasing physics demands. Unlike the L1 trigger, whose cost is largely upfront investment capital mainly for hardware development that will last for decades, the HLT farm is an ongoing expense for maintenance and upgrades. The initial cost to build the HLT system was estimated to be about 25M CHF, back in 2000s. For the current system in Run 3 the cost is estimated to be increased by a few million CHF. Lastly, for the Phase-2 upgrade the latest Technical Design Report estimates about 16M CHF for the HLT hardware in the HL-LHC.

The Barrel Muon Track Finder and The Condition DB

The Barrel Muon Track Finder (BMTF) is a custom-made system that reconstructs muon candidates in the barrel section of the muon detectors (DTs and RPCs). It processes data from the region | η | < 0.83, reconstructing L1 candidates, with momentum p_T , pseudorapidity η , and azimuthal angle ϕ . The candidates, sorted in p_T , are forwarded to the Global Trigger (GT), where participate in algorithm checks whether an event will be further processed or discarded. The reconstruction algorithm, in Run 3, is upgraded to use a Kalman Filter approach, which has been introduced and tested in 2018. This upgrade offered about 5% better efficiency than the legacy system, reaching 96%, while also provided momentum measurements without the constraint at the Primary Vertex of the event, leading to the development of displaced muon algorithms, at Level-1, for the first time.

12. The Kalman Filter in BMTF (Run 3 and Phase-2)

The BMTF algorithm [31] is separated into 2 track finders, the *Phi* and *Eta* Track Finders (TF), separating the logic of the algorithm for track segments that come from ϕ -cluster and η -cluster DTs. In the barrel section, ϕ -cluster DTs form five cylindrical wheels, with 4 stations of DT chambers covering the area after the magnet and up to 7m in radius. The DTs in η -cluster are grouped in 3 stations, covering the same area as those in the ϕ -cluster, and each station is separated into 7 chambers. This η - ϕ structure is repeated in 12 pizza-shaped slices (wedges), covering 360^o completing the cylindrical shape of the CMS. The algorithm implementation in the FPGAs follows a pipeline, meaning that each step of the algorithm processes events in a First-In/First-Out fashion, sequentially.

Eta-TF processes track segments in the η -cluster stations. Simple pattern recognition is performed on the η hits using look-up-tables (LUTs) that are stored on chip memory. The patterns are grouped by quality and η -tracks are assigned with a priority value. According to the priority value, the highest ranked track is selected. Finally, tracks are combined with those received from the *Phi-TF*, extracting an η -coordinate measurement with greater resolution because of the match.

Phi-TF processes track segments in the ϕ -cluster stations. A Kalman Filter (KF) scans the detector from the outmost station to the innermost and creates track candidates in the ϕ -coordinate. The Kalman algorithm is a loop that consists of four steps³:

- a. The Estimation Update $\chi_k' = \chi_k + G_k(z_k H\chi_k)$
- b. The Covariance Matrix⁴ Update, $P'_k = (1 G_k H)P_k$
- c. The Projection of χ_k' and P_k' to the next measured input $\chi_{k+1} = \Phi \chi_k$ and $P_{k+1} = \Phi P_k \Phi^\intercal + Q$

³ Derivation of the steps and the equations can be found in Appendix A in [31].

⁴ P_k is expressed as the estimated value of the difference between the updated estimation and the prior prediction, $P_k = E[(\chi_k' - \chi_k)(\chi_k' - \chi_k)^T].$

d. The Kalman Gain Calculation $G_{k+1} = P_k H^{\mathsf{T}} (H P_k H^{\mathsf{T}} + R)^{-1}$

If a prior estimate of the measurement (χ_k) and the related Kalman Gain (G_k) both exist (from a previous iteration or due to initialization), the equations in (a) and (b) are used to update the estimate to χ_k' and the covariant matrix to P_k' , considering also the latest inserted measurement z_k . The measurement z_k is described by a state vector, which is a representation of the quantities in question in the most reasonable parameter space (see following paragraph), and H is a mapping between that space and the estimate space, $z_k = H\chi_k$. The next step (c) is the projection of the estimate to the next measurement with a transformation of the vector χ_k' and the matrix P_k' by using the matrix Φ , which describes the geometry and specific features of each problem. The last step (d) is the recalculation of the Kalman Gain, for estimating the next measurement in the iteration. The quantities Q and R are covariances that are introduced due to signal noise (like white noise, detector noise, background noise, etc.).

For the BMTF the produced signals are DT/RPC measurements of stubs. An input stub-k can be described by its angle and bending angle as a state vector $z_k = (\phi, \phi_b)_k$. The output of BMTF Kalman Filter should be muon quantities like $\chi_k = (p_T, \phi)_k$, the 2D momentum vector related to a trajectory that is measured at some specific surface of the detector geometry. The coordinates of a track segment can be also the coordinates of the measured stub, at that point of the curvature \tilde{k} , and the trajectory is proportional to $1/p_T$, meaning that a better formulation of the estimate space is $\chi_k = \left(\tilde{k}, \phi, \phi_b\right)_k$ and the mapping H between these spaces is trivial.

$$z_k = (\phi, \phi_b)_k$$

$$x_k = (\tilde{k}, \phi, \phi_b)_k$$

$$H = \begin{pmatrix} 0 & 1 & 0 \\ 0 & 0 & 1 \end{pmatrix}$$

A trimmed version of the Kalman algorithm is implemented on the BMTF boards and runs in Run 3, serving also as an illustration for the capability of running a more advanced Kalman Filter, at Level-1 Trigger, using Phase-2 boards that offer more resources. The four steps can be reduced into two if one calculates in advance the required values of the Kalman Gain (G_k) for a specific geometry, magnetic field, and noise level. (If the next gain G_{k+1} is already available to be fetched from some on-chip memory, estimating the covariance matrix P'_k and P_{k+1} can be skipped.)

12.1. The BMTF System and the Kalman Filter at P5

The BMTF subsystem uses 12x MP7, 2x AMC13 boards, and is housed in two crates at the S1D03 rack in the USC room at CMS (LHC P5). Each crate contains one AMC13 for DAQ, while six MP7s manage a 30° azimuthal wedge of the muon detectors. Each AMC13 is assigned with a DAQ FED ID that is used to control the system centrally, the corresponding IDs are 1376 (top crate) and 1377 (bottom crate). Each MP7 board receives, from the TWINMUX system, η and ϕ stubs originated by three successive wedges, via 30 asynchronous Gbit links operating at 9.6 Gb/s, and deliver Muon candidates to the μ GMT system using a similar link. Supporting software that is installed and running at the CMS Control Room machines, is responsible for monitor and control

of the system. The Online Software (slow control) acts as a control panel for the system, providing monitoring and control commands, and the Offline DQM Software (Data-Quality Monitoring Modules) monitors the physical Input (stubs) and Output (muons) during the runtime.

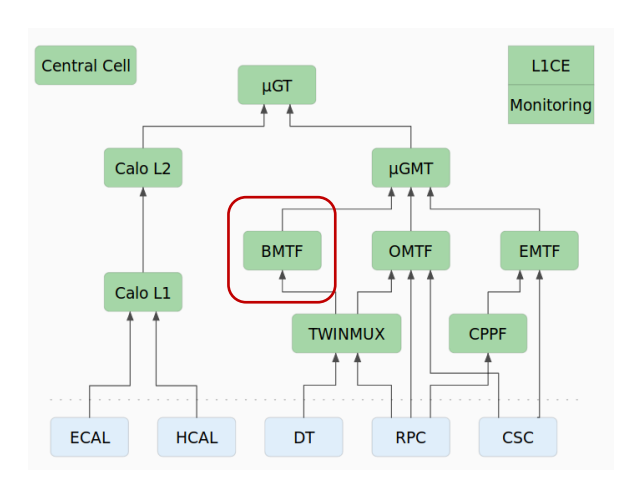




Figure 17: (Left) A simplified schematic of the L1 Trigger System in Run 3, highlighting the connectivity of the BMTF with the TWINMUX and μGMT systems. (Right) Two crates with 12 MP7 and 2 AMC13 DAQ processors, located in the S1D03 rack of the CMS Service Cavern (USC), at LHC P5.

The implementation in the BMTF boards follow the same principles that are described above, with some necessary modifications to facilitate the firmware design on the Virtex FPGA. First, in the Track Propagation step, the state vector χ_k is propagated to the next stub k+1. This propagation is the step described by equation (c) and the required multiplications are implemented using specialized digital processors (DSP cores) on the Virtex-7 FPGA, which are designed to efficiently perform complex mathematical operations such as multiplications and signal processing. Second, in the State Vector Update step, stored Kalman gains are used to update the stub estimation, as shown in (a). The Kalman gain values have been precalculated as a function of the curvature k and a 4-bit hit pattern, which signifies the stations with stubs present. For example, "1011" means stubs at the stations 1-3-4, while "0101" means stubs at the stations 2-4.

Last, the Kalman loop that is approximated by steps (a) and (c) is implemented in each BMTF board 22 times. All possible input stub scenarios (described by the 4-bit pattern) are being processed simultaneously in each BMTF processor. The number of scenarios, 22, comes from counting combinations of possible tracks with at least two stubs in the muon stations (11), which is multiplied by 2 because each station can deliver up to two stubs.

$$\binom{4}{2} + \binom{4}{3} + 1 = 6 + 4 + 1 = 11$$

The KF algorithm is a recursive estimator that updates a state vector and its covariance when a new measurement is available, incorporates effects such as multiple scattering (using the Q and R noise matrices), and produces a statistical χ^2 figure-of-merit as a track-quality measure to distinguish the best reconstruction of the trajectory.

12.2. Run 3 Validation

In this section, we present recent results of the validation of the Kalman Algorithm using Cosmics data from 2024 data-taking period of the CMS, the run 378200. The following graphs compare hardware values for muons reconstructed by the BMTF (fw-ver 3.1.0) and compared to emulated values for the same inputs that TWINMUX was propagating to the BMTF. The validation performed over 6363 output BMTF muons and show perfect agreement within an error of 0.09% for the η variable, which is the worst case.

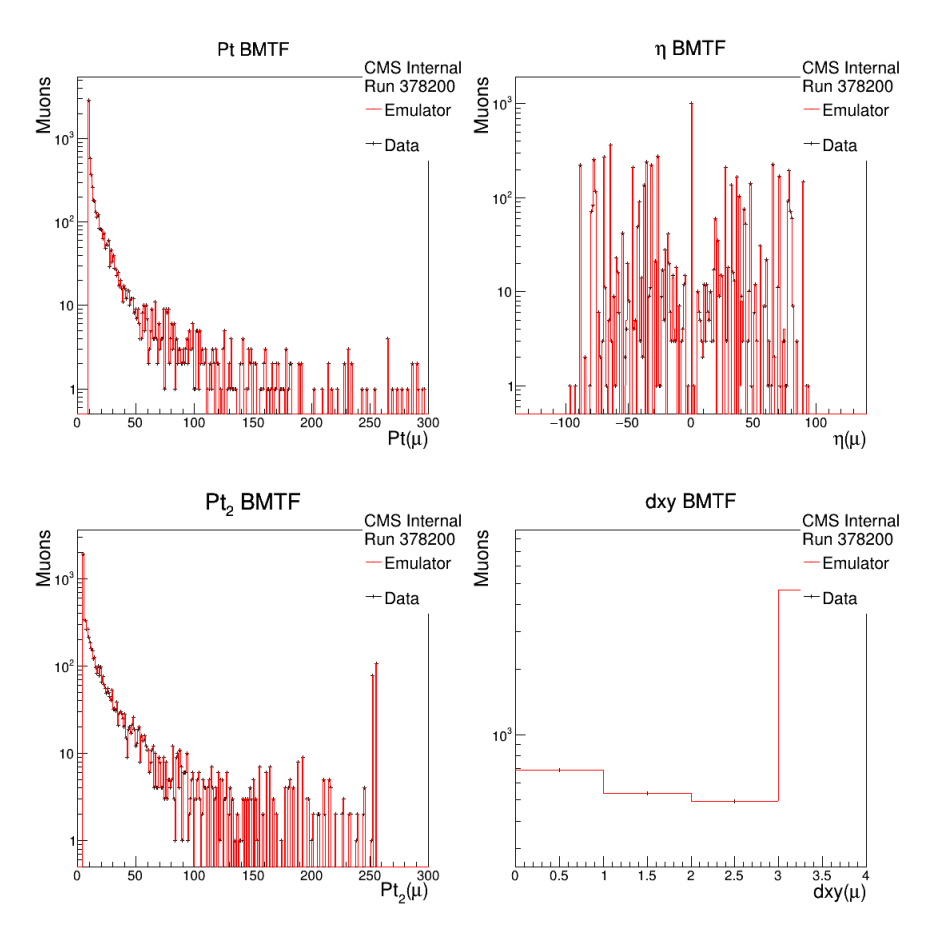


Figure 18: (From Top to Bottom and Left to Right) Plots comparing hardware values for the Run 378200 that were propagated to the L1 Global Trigger and emulated values with the CMSSW of transverse momentum (p_T) at the vertex, η , transverse momentum (p_T 2) at the first muon station, and transverse impact parameter from the vertex (d_{xy}). Calculations associated to these plots show an almost perfect agreement within 0.09% for the η variable, which is the worst case.

13. Online-to-Offline (O2O) Workflows in CMS and L1 Trigger

The Online-to-Offline (O2O) system sits at the interface between the CMS detector's operational environment and its offline reconstruction workflows. At its core lies the CMS Conditions Database (CondDB), which exists in both an online manifestation that is hosted at P5 (ORCON), and an offline replica (ORCON ADG) that is maintained in the central computing infrastructure. The O2O's purpose is to guarantee that the conditions (non-event data such as calibrations, alignment constants, and hardware configuration parameters) in use during data-taking are faithfully reproduced in offline reconstruction, ensuring reproducibility and consistency across all physics analyses and other purposes.

The fundamental design of the database is based on the use of Object-Relational Mapping (ORM). ORM is a software abstraction layer that bridges the gap between the object-oriented programming model used in CMSSW and the relational schema of the underlying Oracle databases. In CMS, each conditions payload is an instance of a C++ class, noted as the Payload type, containing the full set of parameters required for a given record. For example, a tracker alignment geometry or a set of L1 trigger configuration registers. These objects are serialized into a binary Blob and stored in the database tables alongside a SHA-1 hash identifier (Secure Hash Algorithm). ORM tools automatically translate object manipulations, like appending a new Interval of Validity (IOV) to a Tag or querying the state of a Global Tag at a given snapshot time, into the required SQL operations. This allows physicists to work entirely with C++ or Python objects, without composing SQL statements manually, while ensuring type safety, schema versioning, and backend independence between Oracle and SQLite deployments. The mapping logic also enables relationships between entries in the database: payloads are grouped into versioned sequences called *Tags*, which in turn are grouped into complete CMS configurations called Global Tags. In O2O, ORM ensures that online conditions are consistently extracted, converted into CMSSW payload objects, and inserted into the offline database according to the schema of the CondDB.

The execution of the O2O flow mechanism begins at the start of a new run. The system queries OMDS (or other subsystem-specific online stores) to retrieve the exact running configuration and calibration payloads active in the hardware and high-level trigger software. Each raw payload is deserialized into its corresponding CMSSW object and annotated with metadata: the *since* parameter defining the IOV lower bound (typically a run number, a lumisection, or a timestamp), an identifying Tag name, and a provisional synchronisation type. These payload objects are then uploaded via the PopCon (Populator of Conditions) framework into both the online and offline ORCON databases. Once in ORCON, the new Tags are associated with the appropriate open Global Tag queues. A Global Tag in CMS is an *immutable snapshot* mapping record types that are required by a workflow to a specific Tag; queues are a *special mutable* form of Global Tag, with an "infinite" snapshot time, used as staging areas for preparation and validation of new conditions (usually for MC Campaigns and Run preparations).

From this point, the approval process is coordinated by the Alignment and Calibration (AlCa) group. Subsystem contacts review the new Tags within their respective queues, checking the payload content, the correctness of the IOV boundaries, and the proposed synchronisation type. Synchronisation types implement workflow-specific update policies. For example, *hlt*, *express*, and *prompt* enforce that new IOVs can only be appended after a defined *Safe Run ID*, while *offline* and *mc* have their own, stricter rules. Once validated, all Tags are promoted from the queue into a production Global Tag.

Navigation and inspection of conditions data, both during O2O validation and in routine operations, is supported by a set of tools built on the same ORM foundations. Within CMSSW releases, the conddb command-line client allows experts to search for Tags and Global Tags, list

contents, inspect IOVs, verbosely check differences, and dump deserialized payloads to human-readable XML format. Also, a web application, the CMS Conditions Database Browser (cmsDbBrowser), provides similar functionality via a graphical interface, together with features for submitting requests to queues, creating candidate Global Tags for testing, and visualising Tag and Global Tag contents.

13.1. A framework-compliant, immutable backend for the CMS L1 Trigger O2O mechanism

This section presents the redesign and migration of the CMS Level-1 (L1) Trigger Online-to-Offline (O2O) backend to an immutable, framework-compliant architecture aligned with CMSSW 12.4.X requirements. The work centers on replacing the legacy EventSetup access methods with explicit esConsumes/ESGetToken usage, refactoring thus the L1 conditions writer layer, and ensuring deterministic repeatable behavior during concurrent EventSetup prefetching. We describe the design, implementation, and validation of the new backend, using dedicated unit and integration tests, and discuss core framework aspects uncovered during development (notably exception propagation under EventSetup prefetching). The result is a robust O2O mechanism that embeds CI-like practices, preserves reproducibility, and integrates flawlessly with the Conditions DB workflows used by L1 and AlCa.

As CMSSW evolved toward stricter concurrency and immutability in the *EventSetup* system, O2O backends that were relying on implicit or mutable interactions risked undefined behaviors. This work targeted CMSSW 12.4.X release cycle and reimplements the L1 O2O backend to

- adopt explicit EventSetup data dependencies (esConsumes/ESGetToken)
- enforce immutability at the writer/proxy layer
- guarantee *idempotence* (consistent repeatable behavior without duplicate side effects across retries)
- and provide comprehensive tests that execute end-to-end O2O workflows within the release environment

This rework was proposed in the Pull Request (PR) 37602 [32], titled "[L1-O2O] ESGetToken migration L1CondDBPayloadWriter and O2O unit tests", affecting the packages CondTools/L1Trigger and L1TriggerConfig/L1TConfigProducers. The change was reviewed and signed by L1, AlCa, and core CMSSW participants and subsequently integrated for the 12.4.X cycle.

13.1.1. Background and Requirements

EventSetup in CMSSW has progressively moved to explicit dependency declaration and prefetch-driven concurrency. Producers and analyzers must declare their consumption of EventSetup products using esConsumes to receive ESGetToken handles at beginRun or beginJob. This enables the framework to prefetch data deterministically and to detect missing dependencies early. The legacy L1 O2O backend used generic EventSetup access methods and exception-driven control flow (e.g. catching DataAlreadyPresentException). These access

methods do not integrate well with modern prefetching, and when exceptions are rethrown asynchronously, they can make identifying root-cause errors difficult.

Two non-functional requirements were therefore central:

- *Immutability.* All O2O state transitions must be expressed as pure reads of *EventSetup* plus atomic writes to the Conditions DB. No mutable global state may influence results across runs or retries.
- *Idempotence*. Re-executing the same O2O step, with identical inputs, must cause no side effects beyond the first successful write and a deterministic outcome should return to callers (e.g., "already present").

Within these constraints, the backend must continue to produce the same payloads (*Rcd* objects) and tag associations that are used by the L1 online menus and configurations, and to support the O2O orchestration scripts that exercise the full chain in continuous integration.

13.1.2. Design and Implementation

ESGetToken migration and explicit dependencies

We migrated the L1 writer components (e.g., L1CondDBPayloadWriter and the associated WriterProxy) to declare their EventSetup dependencies explicitly via esConsumes, storing ESGetTokens at construction time using an edm::ConsumesCollector passed down to the CMSSW plugins. Each write step acquires data with iSetup.getData(token) method, eliminating implicit Record (Rcd) lookups and exception-based presence checks. This ensures the framework can prefetch and schedule ESProducers consistently with other modules, and it allows static analysis (and the cmsDriver tool) to verify the presence of required ESProducers in the top-level configuration.

Immutable writer/proxy layer

The writer/proxy layer was refactored to obey strict immutability:

- It computes payloads purely from *EventSetup* inputs and configuration parameters, without side effects or hidden caches
- It performs a single atomic write to *CondDB*, handling "already present" cases as a query outcome (idempotence) rather than as control flow with exceptions
- It maps *Record (Rcd)* identifiers to their O2O containers deterministically (e.g., L1TriggerKeyExtRcd@L1TriggerKeyExt), and it never mutates in-memory across events.

The prior method of catching framework-specific exceptions (e.g., *DataAlreadyPresentException*) in the *EventSetup* access path was removed. This proved essential because *EventSetup* prefetching masked exception types in certain failure cases, leading to undefined behaviors. The new code does not rely on exception identity for logic and therefore behaves robustly under prefetching.

ESProducer coverage and configuration

The O2O machinery handles both "offline" and O2O-specific ("online") Records, e.g. L1TGlobalPrescalesVetosOnlineProd and L1TGlobalPrescalesVetosFractO2ORcd. When using explicit esConsumes, the required ESProducers for these Records must be present in the process configuration. We updated the O2O configurations to include the necessary producers unconditionally, without depending on other modules to provide them. When the EventSetup graph needed O2O variants of Records at write time, we ensured they were available by the time the writer requested them, either by esConsumes dependencies or by explicitly placing the ESProducers in the configuration path.

13.1.3. Validation and Testing

We added focused unit tests for the writer/proxy layer to verify token acquisition, deterministic *EventSetup* access, and thorough handling of "already present" conditions. In addition, we implemented scram tests that exercise the end-to-end O2O workflow, including setup of a local *sqlite Conditions DB* populated of baseline content, execution of the writer, and inspecting the IOV contents before and after the run.

A dedicated script (runL1-O2O-scramTests.sh) prepares a per-test workspace, copies a template sqlite file (l1config.db) from CMSSW_SEARCH_PATH into the test directory, inspects the IOV table before the write, executes the O2O writer path, and re-inspects the table afterward to assert the expected transition. This test runs inside IBs (CMSSW Integration Builds on github) and PR testing to catch failures in framework and configuration.

During early testing in *CMSSW 12.3.X IBs*, we observed failures in an online producer (*L1TGlobalPrescalesVetosOnlineProd*) manifesting as *MakeDataException* on O2O *Records*, with no diagnostic information. Investigation with framework developers revealed that *EventSetup* prefetching, in some cases, lost the original exception type thrown from *ESProducer::produce()*, always reporting the *MakeDataException*. This behavior confused legacy O2O code that relied on catching specific exception types. The rewritten backend's logic did not depend on exception identity; however, we validated that the framework would rethrow the exact exception type once the core fix would be shipped. In parallel, we addressed missing *esConsumes* registrations that were preventing O2O-specific *Records* from being produced, ensuring all required *ESProducers* were present and declared consumed. With these changes in place, the O2O tests passed reliably in the master branch.

13.1.4. Results, Discussion, and Lessons learned

The migrated backend compiles cleanly, adds negligible repository footprint (≈16 KB), and integrates with CMSSW master. Reviewers from L1, AlCa, and CMSSW core validated the approach; the PR was signed and merged after confirming *esConsumes* was implemented correctly and that O2O tests were robust. The L1 and *CondDB* packages reflect the explicit dependency model, and the O2O writer now operates deterministically with immutable state and repeatable behavior. The tests demonstrate that the same O2O job, re-run on unchanged inputs, produces no duplicate IOV entries and reports consistent outcomes. The end-to-end

scram test harness establishes a reproducible baseline for maintenance and for catching failures in either future framework or *ESProducer* developments.

The migration surfaced two lessons. First, exception-driven control flow tied to specific framework exception classes are fragile under concurrency and prefetching, they should be avoided in favor of explicit, declarative *ESProduces* dependency models and real-time *idempotence*. Second, complex O2O operations that combine "online" and "offline" *Records* require explicit *ESProducer* coverage in configurations; implicit availability of *ESProducers* via third-party modules is fragile and hides failure messages. The combination of *esConsumes*, immutable writer logic, and end-to-end unit tests provides a sustainable path forward as *CMSSW* continues to evolve.

This work delivered robust unit and integration tests and resolved issues uncovered by *EventSetup* prefetching in the 12.4.X cycle. The result is a maintainable O2O pipeline aligned with *CMSSW* concurrency and reproducibility principles, ready to support L1 and AlCa operations in Run 3 and Phase-2.

The Soft Multilepton Analysis

This is a search for electroweakinos in scenarios beyond the Standard Model (BSM) in compressed mass spectra [36]. Compressed theoretical signatures of new physics illustrate particles in (nearly) degenerate states of mass. In these scenarios, when a BSM particle is created, the cascade of its decay appears as though most of its energy and momentum is carried away by one or more lighter and stable BSM particles. The remnants of the decay are observable particles with low momentum that are referred to as "soft". The soft multilepton analysis focuses on final states with at least two soft leptons and missing transverse energy (more about this in section 15.1). In simple terms, by requiring more than one soft lepton in the final state the background can be suppressed to comparable levels of cross-section with the signal.

The analysis is targeting the production of electroweak bosons ("electroweakinos") in final states with low energy leptons of opposite charge. In SUSY scenarios, where the lightest neutralino $\widetilde{\chi}_1^0$ is the Lightest Supersymmetric Particle (LSP), the soft leptons may be produced in decays of heavier neutralinos via off-shell Zs. The Feynman diagrams in Figure 19 present the processes under consideration.

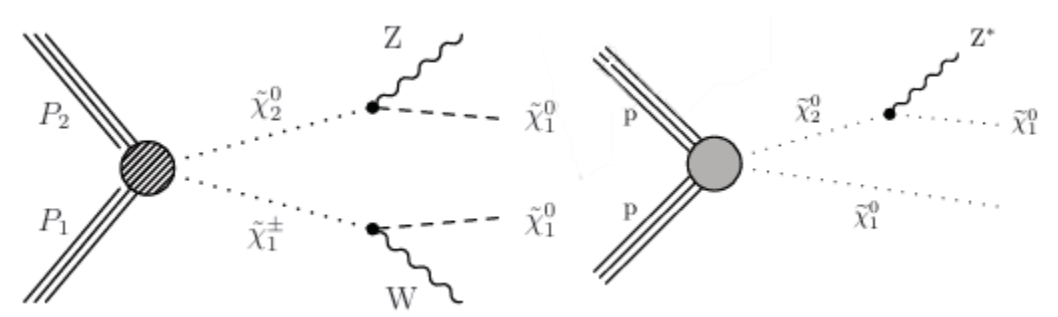


Figure 19: Electroweak processes leading to a pair of soft leptons from an off-shell Z decay, also a possible third soft lepton from the off-shell W decay. The diagrams feature the decays $\widetilde{\chi}^0_2 \to Z^*(\ell\ell) + \widetilde{\chi}^0_1$ and $\widetilde{\chi}^\pm_1 \to Z^*(\ell\ell) + \widetilde{\chi}^0_1$, which are included in the "Wino-Bino" and "Higgsino" scenarios.

The "Wino-Bino" scenario suggests that the gaugino masses are comparable and much smaller than the Higgsino (M_1 , $M_2 \ll \mu$), which leads into two closely degenerate neutral states with one charged fermion-antifermion pair. Theoretically, the scenario is motivated by the presence of relic dark matter density and R-parity conservation in the minimal SUSY model (MSSM).

In a similar manner, the "Higgsino" scenario suggests that the gaugino masses (Wino-Bino) are massively larger than the Higgsino triplet, with 2 neutral and 1 charged states nearly degenerate. According to MSSM, the Higgsino mass parameter (μ) contributes to the SM Higgs mass, while it is also restricted by the principle of naturalness to be relatively low (at some hundreds of GeVs).

The analysis considers simplified simulated models which capture the basic features of these theoretical scenarios while also allowing a broader interpretability of the results.

Finally, some BSM theories predict decays with long-lived electroweakino states. Specifically, the Wino-Bino coannihilation in the "spread" and the "mini-split" SUSY models can lead to long-lived

neutral Wino states, and the decay is mediated by a much heavier Higgsino state. For this reason, proper lifetime of $\widetilde{\chi}^0_2$, along with the degenerate masses of $\widetilde{\chi}^0_1$ and $\widetilde{\chi}^0_2$, are taken as free parameters to be scanned. For the proper lifetime, theory calculations motivate the following range of values that is presented in Figure 20. The analysis here is restricted to decays of up to 10cm, in order not to crossing boundaries with other analyses in the CMS experiment.

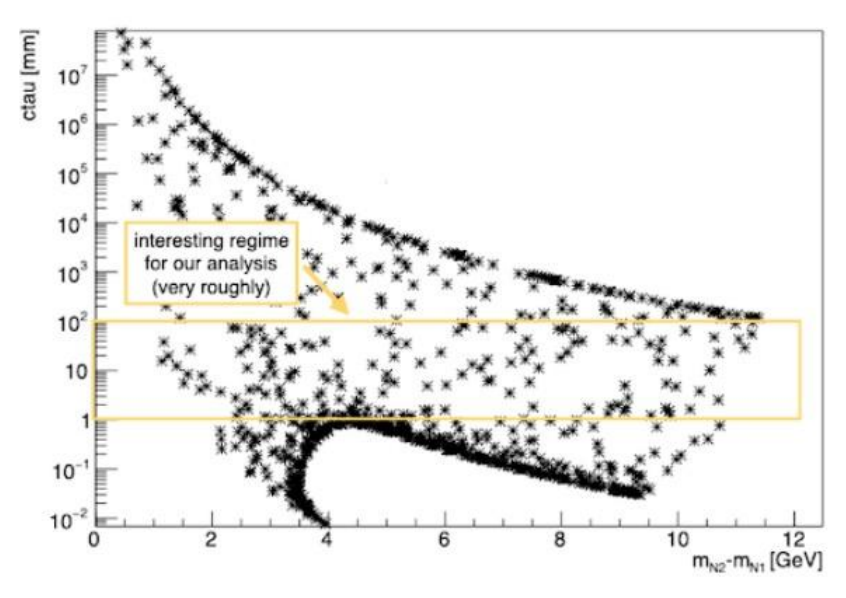


Figure 20: Mass vs decay length phase-space for Wino-Bino coannihilation in the mini-split SUSY model, calculated with SoftSusy 4.1.8 [35]. The parameters for the simulation scan are set to M_1 =100 GeV, M_2 in (90,100) GeV, μ in (500 GeV, 25 TeV), and $\tan(\theta)$ =30. The phase-space at low (high) $c\tau$ is saturated at μ =500 GeV (5 TeV).

14. Supersymmetry & Compress Mass Scenarios

The Supersymmetry (SUSY) Framework is based on the Standard Model of Particle Physics and introduces a new symmetry between bosons and fermions, proposing that for every fermion exists a bosonic "superpartner" and vice versa. The analysis that is discussed in this chapter concerns a search that is interpreted in the contexts of two supersymmetric extensions of the Standard Model, the Minimal Supersymmetric Standard Model (MSSM) and the Split SUSY Model. Both are discussed later in this section, after a brief discussion of the Standard Model⁵.

The Standard Model of Particle Physics

The Lagrangian of the Standard Model (SM) can be broken down into three main components: the leptons, the quarks, and the Higgs sector. The overall Lagrangian is described as

$$\mathcal{L}_{SM} = \mathcal{L}_{gauge} + \mathcal{L}_{leptons} + \mathcal{L}_{quarks} + \mathcal{L}_{higgs}$$

and each sector with their expression as follows.

$$\mathcal{L}_{gauge} = -\frac{1}{4} G^{a}_{\mu\nu} G^{a\mu\nu} - \frac{1}{4} W^{i}_{\mu\nu} W^{i\mu\nu} - \frac{1}{4} B_{\mu\nu} B^{\mu\nu}$$

⁵ This section is a summary of the Standard Model of Particle Physics, as presented in [31] and follows that formulation.

$$\begin{split} \mathcal{L}_{leptons} &= i \overline{L}_{l} \gamma_{\mu} D^{\mu} L_{l} + i \overline{R}_{l} \gamma^{\mu} D_{\mu} R_{l} - y_{L}^{i} \Phi R_{l} + h. \, c. \\ \mathcal{L}_{quarks} &= i \overline{L}_{l} \gamma^{\mu} D_{\mu} L_{l} + i \overline{R}_{l} \gamma^{\mu} D_{\mu} R_{l} - y_{qq'} \overline{Q}_{l} \Phi R_{l} + h. \, c. \\ \mathcal{L}_{higgs} &= - \left(D_{\mu} \Phi \right)^{\dagger} (D^{\mu} \Phi) - V(\Phi) \end{split}$$

The interaction terms for the gauge fields (G_{μ}^{a} , W_{μ}^{a} , and B_{μ}) with leptons and quarks, each corresponding to a strength anti-symmetric tensor in \mathcal{L}_{gauge} and to the strong (gluons), weak (W and Z bosons), and electromagnetic (photon) interactions, are introduced via the covariant derivatives (D_{μ}). The covariant derivatives are terms that combine the gauge fields of each interaction with its appropriate generator, so writing all of them identically is only a formulation serves clarity and readability.

In the **Leptonic and Quark Sectors**, the interactions of leptons and quarks with the gauge fields are formulated with a sum of terms over the generations (i), and each combine the appropriate covariant derivative with left-handed and right-handed fermionic doublets (L_g) and singlets (R_g) . These lead to Dirac equations that describe the dynamics of particle physics as is known for the fermions. In the same sectors, the last terms are fermionic interactions with a scalar Higgs field (Φ) , which lead to the Yukawa terms (and their coupling constants y_L^g and $y_{qq'}$) that give rise to the masses of the fermions.

The **Higgs Sector** describes the dynamics of the scalar Higgs field, responsible for the spontaneous breaking of electroweak symmetry, and gives masses to the gauge bosons. The potential $V(\Phi)$ that enters this sector is of the form $\lambda(\Phi^{\dagger}\Phi-v^2)^2$, which leads to the spontaneous breaking of the electroweak symmetry and the Yukawa terms that are included in the leptonic and quark sectors.

Supersymmetry (SUSY) Framework

Supersymmetry is a framework that facilitates many theoretical models and shares the following concepts: firstly, a supersymmetric model is formulated in the "superspace", an expanded spacetime that holds 2 more degrees of freedom, a left-handed spinor θ , and its right-handed complex conjugate θ^* . In superspace, a field is also a function of these spinors and is called "superfield", $\Phi(\chi^\mu, \theta, \theta^*)$. A Lagrangian in SUSY consists of terms with integral $\int d^4x$ invariant under supersymmetry transformations. These terms can be named **D-terms** ($[\Phi^\dagger\Phi]_D$) and **F-terms** ($[W(\Phi)]_F$), which consist of vector and left-handed chiral superfields respectively.

⁶ For example, left-handed lepton spinors interact within $SU(2)\times U(1)$, so $D_{\mu}=\partial_{\mu}-\frac{ig'}{2}\sigma^{a}W_{\mu}^{a}-igYB_{\mu}$. Right-handed spinors and scalars don't interact with the weak mediators W_{μ}^{a} , so $D_{\mu}=\partial_{\mu}-igYB_{\mu}$. Left-handed quark spinors interact within $SU(3)\times SU(2)\times U(1)$, so $D_{\mu}=\partial_{\mu}-\frac{ig''}{2}\lambda^{a}G_{\mu}^{a}-\frac{ig'}{2}\sigma^{a}W_{\mu}^{a}-igYB_{\mu}$. The generators $\frac{\sigma^{a}}{2}$ and $\frac{\lambda^{a}}{2}$ are the fundamental representation of the group generators for SU(2) and SU(3), with the Pauli and Gell-Mann matrices respectively.

$$\mathcal{L}_{SUSY} = [\Phi^{\dagger}\Phi]_{\text{D-Terms}} + ([W(\Phi)]_{\text{F-Terms}} + \mathcal{L}_{\text{Soft SUSY Breaking}} + h.c.)$$

In the abstract form above, the **D-terms** involve interactions between vector superfields like bosons and gauginos, while the **F-terms** (or the Superpotential) involve interactions between chiral superfields, like quarks, leptons, Higgs bosons, and their superpartners⁷.

The Minimal Supersymmetric Standard Model (MSSM)

MSSM is the baseline model⁸, within the Supersymmetry framework, which features a solution for the hierarchy problem and delivers dark matter candidates to be "observed" by experiments. These points are achieved by the conservation that is imposed by **R-parity symmetry**.

$$R = (-1)^{3B+L+2S}$$

Table 1: Baryon, Lepton, Spin, and total exponent that defines the result of the R-Parity rotation.

| | В | L | S | 3B+L+2S |
|----------|-----|---|-----|---------|
| quark | 1/3 | 0 | 1/2 | 2 |
| s-quark | 1/3 | 0 | 0 | 1 |
| lepton | 0 | 1 | 1/2 | 2 |
| s-lepton | 0 | 1 | 0 | 1 |

R-parity forbids terms that predict decays of SUSY particles directly to Standard Model particles, limiting consequently the interactions that can contribute to the Higgs mass in a divergent way. Additionally, the logic behind this conservation law dictates that the **lightest supersymmetric particle (LSP)** should be stable, since the restriction that is described above is manifested with the requirement that SUSY particles should be created and annihilated in pairs. The transformation is a continuous rotation with the following result, depending on whether the particle is a superpartner or not.

The SUSY Lagrangian of the MSSM, accommodates the minimal number of superfields and couplings necessary to generate mass for the quarks, leptons, their superpartners, and the gauginos. It can be separated in three parts, a part with chiral superfields, the "superpotential" terms that contain Yukawa-like terms, including a cross-term for the Higgs doublets, and symmetry breaking terms that are put by hand to accommodate the observation that SUSY particles don't have the same mass as their SM counterparts. All these terms respect the R-parity symmetry, preserving the quantum numbers as shown in Table 1.

The necessary superfields (f) are 2 doublets $Q = \binom{U}{D}$ and $L = \binom{N}{E}$ for left-handed quarks, leptons, and superpartners, 3 singlets $U^c = \overline{U}$, $D^c = \overline{D}$, and $E^c = \overline{E}$ for right-handed, and 2

⁷ Each Standard Model particle gains a superpartner: Fermions, like quarks and leptons, have the scalar counterparts squarks and sleptons, while Gauge bosons, like photon, W, Z, and gluons, have the fermionic partners gauginos. The Higgs is paired with a fermionic Higgsino.

⁸ Among other resources that are listed in the References, the formulation and explanation is based on the Chapters 3 and 5 of [33].

Higgs doublets $H_1=H_d=\begin{pmatrix} H_1^0\\H_1^-\end{pmatrix}$ and $H_2=H_u=\begin{pmatrix} H_2^+\\H_2^0\end{pmatrix}$. (For more specific definition of the formulation one can refer to Chapter 5 of [67].) These superfields can be combined with the following expressions for the superpotential W(f) and the Soft SUSY Breaking section of the Lagrangian. These expressions are sums over different generations (i), while the indices d, u, e on the coupling constants are used only for distinguishing the coupling of each interaction term.

$$\begin{split} W(f) &= \lambda_d^i Q^i \cdot H_d \; \overline{D} + \lambda_u^i Q^i \cdot H_u \; \overline{U} \; + \lambda_e^i L^i \cdot H_u \; \overline{E} - \mu H_u \cdot H_d \\ \\ \mathcal{L}_{SUSY \, SB} &= \frac{m}{2} |\Phi_{\rm i}|^2 + \frac{m'}{2} \left(\Phi_{\rm i}^2 + \Phi_{\rm i}^{*2}\right) - A \left(\Phi_{\rm i}^3 + \Phi_{\rm i}^{*3}\right) - \frac{M_i}{2} \, \overline{\widetilde{\Psi}}_{L \, i} \, \widetilde{\Psi}_{L \, i} \end{split}$$

These two expressions, together with formulating the **D-Terms** and **F-Terms**, can lead to the following Lagrangian that describe the MSSM. Simple partial derivatives have been substituted by covariant derivatives to incorporate gauge bosons and gauginos.

$$\begin{split} \mathcal{L}_{MSSM} &= \sum_{\substack{i = \{Q,L,U^c,D^c,E^c,H_u,H_d\}\\ p_{g,i} = 1 \text{ of } Q_{g,i} = 1$$

Focusing on the scalar potential of the Higgs sector, including the doublets H_d and H_u and all its components $(V_F + V_D + V_{SB}, \text{F-term}, \text{D-term}, \text{and SUSY breaking of the scalar potential}), one can identify free parameters that determine the masses of several physical particles (via Gauge Symmetry Breaking <math display="inline">^{10}$ for $SU(2) \times U(1)$). These are the mass of the Z-boson $M_Z = (g_{SU2}^2 + g_{U1}^2)(v_d^2 + v_u^2)$, the mass m_{h^0} of the lightest scalar component of H_d and H_u , which after loop (radiative) corrections becomes the SM Higgs at 125 GeV, the mass of the pseudoscalar Higgs $m_{A^0}^2 = m_d^2 + m_u^2$, which remains after the Goldstone process that makes Z boson massive, and the mixing angle β that is defined by selecting real vacuum expectation values for the Higgs doublets $tan\beta = v_u/v_d$.

Mass-splitting and long-lived particles

Using free parameters like m_{h^0} , m_{A^0} , $tan\beta$ and M_Z , and setting higgs and Z masses to the measured values, one can build SUSY models (MC simulations) that illustrate several relations between the free parameters. Interesting assumptions, which are also related to the analysis

⁹ It's remarkable to note that studying different sectors in the Lagrangian, as described for the Higgs sector, the total free parameters that MSSM generally supports are 124, including masses, mixing angles, and CP-violating phases. (To be compared with 19 for the SM)

 $^{^{10}}$ With 2 Higgs doublets, initially, the model is dependent on eight scalar degrees of freedom (Goldstone bosons), where three of them are eliminated to make Z and W^{\pm} massive, and five Higgs states, two even on Charge conjugation and Parity (CP-even) transformations h^0 , H^0 , one CP-odd A^0 , and two charged H^{\pm} .

below, are cases with almost degenerate masses, where $\Delta M = m_1 - m_2 \sim O(1 GeV)$ or lower. A small mass difference for two states, e.g. Next-to-LSP (m_2) and LSP (m_1) , means that decays have little kinetic energy available, which often suppresses the decay rate, extending the lifetime of the heavier particle.

A known case is a **Wino-like LSP**, where charged wino and neutral bino can be heavier than the wino LSP at only O(1~GeV). Similarly, a **Higgsino-like LSP** yields a chargino-neutralino splitting of order 0.1-1~GeV (see the Compressed SUSY Summary section), depending on mixing angles. These small mass-splittings, as one reaches below 1 GeV scale, arise predominantly from one-loop radiative corrections. When Δm is very small, the decay is kinematically constrained, resulting to off-shell decays and small decay width Γ . Since $\tau=1/\Gamma$, the proper decay length $c\tau$ becomes significant. According to the work of Sakurai and Rolbiecki [34] about the wino and bino NLSPs, the proper decay length is proportional to the mass-splitting inverted, leading to small widths and large displacements in the experiment. The following expressions illustrate published theoretical predictions of proper decay lengths for 2-body and 3-body decays.

$$c\tau_{2\text{-body}} \sim O(1cm) \times \left(\frac{500 \text{ GeV}}{\Delta m}\right)$$

$$c\tau_{\text{3-body}} \sim O(1cm) \times \left(\frac{30 \text{ GeV}}{\Delta m}\right)^3$$

These results show that even a few hundred MeV splitting can yield to centimeters of proper decay length $c\tau$.

15. General Description of the Analysis Methodology

15.1. Categories & Regions

This analysis is separated to five categories, incorporating 4 different final states, and different Regions that are used for extracting information about the background estimation for each physical process in the Signal Region and calculating the final limits. This section describes the structure of the analysis.

There are **five distinct categories** in this analysis, and each one corresponds to a different final state of the decays of interest. Firstly, we have a "2 prompt leptons" category that is subsequently divided into two more, "2 prompt muons" and "2 prompt electrons". Following that, we also have "2 displaced muons" and "2 displaced electrons" categories. And finally, we have the "3 prompt leptons" category, which for the selections is subcategorized into "2 muons with extra lepton" and "2 electrons with extra lepton", but in the distributions the 3-lepton category is considered inclusively. Each one of these categories is associated with its Signal Region that is designed so that these selections capture the main characteristics of the underlying final state and optimize the acceptance of these processes.

Table 2: The selection requirements that define the 4 prompt Signal Regions, ee, $\mu\mu$, $ee\ell$, $\mu\mu\ell$

| Cuitonia a(u) | 2-leptons | | 3-16 | 3-leptons | |
|-------------------------------|------------|-------------------------|----------------------|-------------|--|
| Criteria - <i>e(μ)</i> | Low- p_T | Med/High/Ultra- p_{T} | $Low-p_T$ | $High-p_T$ | |
| # leptons | | 2 | | 3 | |
| $p_T(\ell 1)$ [GeV] | 5 - 30 | 1(3.5) - 30 | 5 - 30 | 1(3.5) - 30 | |
| $p_T(\ell 2)$ [GeV] | 5 - 30 | 1(3.5) - 30 | 5 - 30 | 1(3.5) - 30 | |
| $p_T(\ell 3)$ [GeV] | | - | 5 - 30 | 1(3.5) - 30 | |
| Same-Flavor | | ✓ | | | |
| Opposite-Sign | | | | | |
| $\Delta R_{\ell\ell}$ | - | > 0.05 | - | > 0.05 | |
| $M_{SFOS}^{min}[GeV]$ | 4 - 50 | 0.1 - 50 | 4 - 50 | 0.1 - 50 | |
| veto $M_{SFOS}^{min}[GeV]$ | | J/Ψ (3 - 3.2) and | Υ (9 - 10.5) | | |
| $M_{SFOS}^{max}[GeV]$ | | - | < 60 | - | |
| $p_T(\ell 1, \ell 2)$ [GeV] | | > 3 | | - | |
| veto tight lepton | | ✓ | | _ | |
| (for leading jet) | | V | | | |
| $m_T(\ell,p_T^{miss})$ [GeV] | | < 70 | | - | |
| H₁ [GeV] | | > 100 |) | | |
| p_T^{miss}/H_T | | 2/3 - 1.4 | | - | |
| veto b-Jet | | ✓ | | | |
| veto $M(au	au)$ | | 0 - 160 | | - | |
| $p_T(\ell)/M(\ell\ell)$ | | $p_T(\ell_2) > 0.6 +$ | $0.25M_{SFOS}^{min}$ | | |
| $\Delta\Phi(\ell,p_T^{miss})$ | | < 1.5 | | - | |

The Signal Regions (SRs) for the prompt decays are designed so that they are optimized for events where the observed 2 or 3 lepton tracks are compatible with the Primary Vertex. The "3 lepton" category is used, since studies from past published versions of this analysis have illustrated additional sensitivity by a category with 3 leptons, especially at mass-splittings around 40 GeV. These prompt SRs are separated in p_T^{miss} bins with boundaries at 125-200 GeV (Low), 200-240 GeV (Medium), 240-290 GeV (High), and 290+ GeV (Ultra). Table 2 presents the selection of the events for these Signal Regions.

Table 3: The selection requirements that define the non-prompt Signal Regions, ee and $\mu\mu$.

| Sie 3. The selection requirem | Displac | Displaced <i>ee</i> | | | | |
|-------------------------------|--------------------------------|----------------------------|----------------------------|--|--|--|
| Criteria | $\textit{Low-}p_T$ | High- p_T | High- p_T | | | |
| | Low/High $\sigma_{L_{xy}}$ | Low/High $\sigma_{L_{xy}}$ | Low/High $\sigma_{L_{xy}}$ | | | |
| # pairs | | 1 | | | | |
| $p_T(\ell 1)$ [GeV] | 5 - 30 | 3 - 30 | 1 - 30 | | | |
| $p_T(\ell 2)$ [GeV] | 5 - 30 | 3 - 30 | 1 - 30 | | | |
| Same-Flavor | | ✓ | | | | |
| Opposite-Sign | | | | | | |
| $\Delta R_{\ell\ell}$ | - | > 0.05 | > 0.05 | | | |
| $M_{SFOS}^{min}[GeV]$ | 4 - 50 | 0.1 - 50 | 0.1 - 50 | | | |
| veto $M_{SFOS}^{min}[GeV]$ | J/Ψ (3 - 3.2) and Υ (9 - 10.5) | | | | | |
| veto b-Jet | | ✓ | | | | |
| H_T [GeV] | > 100 | | | | | |
| p_T^{miss}/H_T | 2/3 - 1.4 | | | | | |
| veto $p_T(\ell) > 30$ [GeV] | | ✓ | | | | |
| $p_T(jet1)$ [GeV] | - | | > 130 | | | |
| Collinearity | >- | 0.5 | > 0.5 | | | |
| $log(\Delta xy/\Delta z)$ | > -1 | 5 | > -1.25 | | | |
| $\Delta\Phi(\ell1,\ell2)$ | - | | < 1.5 | | | |
| | | | | | | |

On the contrary to the Signal Regions for prompt decays, regions that are designed for displaced decays are optimized for lepton tracks that are compatible with vertices separated from the Primary Vertex. Displaced decays are much more related to the states that are very tightly degenerate and subsequently within small mass splitting scenarios. The additions of displaced SRs, especially the soft-electron displaced category, enhance the sensitivity and the reach of the analysis down to sub-GeV level. Special treatment is necessary for the displaced categories, firstly due to the provenance of the leptons as they originate from decays away from the Primary Vertex (vertices that may refer to as "Secondary" in following sections), and secondly because of the different composition of the background. For the displaced SRs there are 4 bins in total, separation in p_T^{miss} of 125-200 GeV (Low) and 200+ GeV (High), and in the significance of the transverse displacement $\sigma_{L_{xy}}$ of 0-25 (Low) and 25+ (High). Combining these binnings we define 4 displaced Signal Regions, Low p_T^{miss} -Low $\sigma_{L_{xy}}$, Low p_T^{miss} -High $\sigma_{L_{xy}}$, High p_T^{miss} -Low $\sigma_{L_{xy}}$, and High p_T^{miss} -High $\sigma_{L_{xy}}$. The displaced selections of the events are presented in Table 3.

The optimization of the objects that define the categories is presented in detail in section 16.2. Here, with help of the schematic in Figure 21, we present the flow of the information that is extracted from different regions and how this information is used, this is the strategy of the analysis.

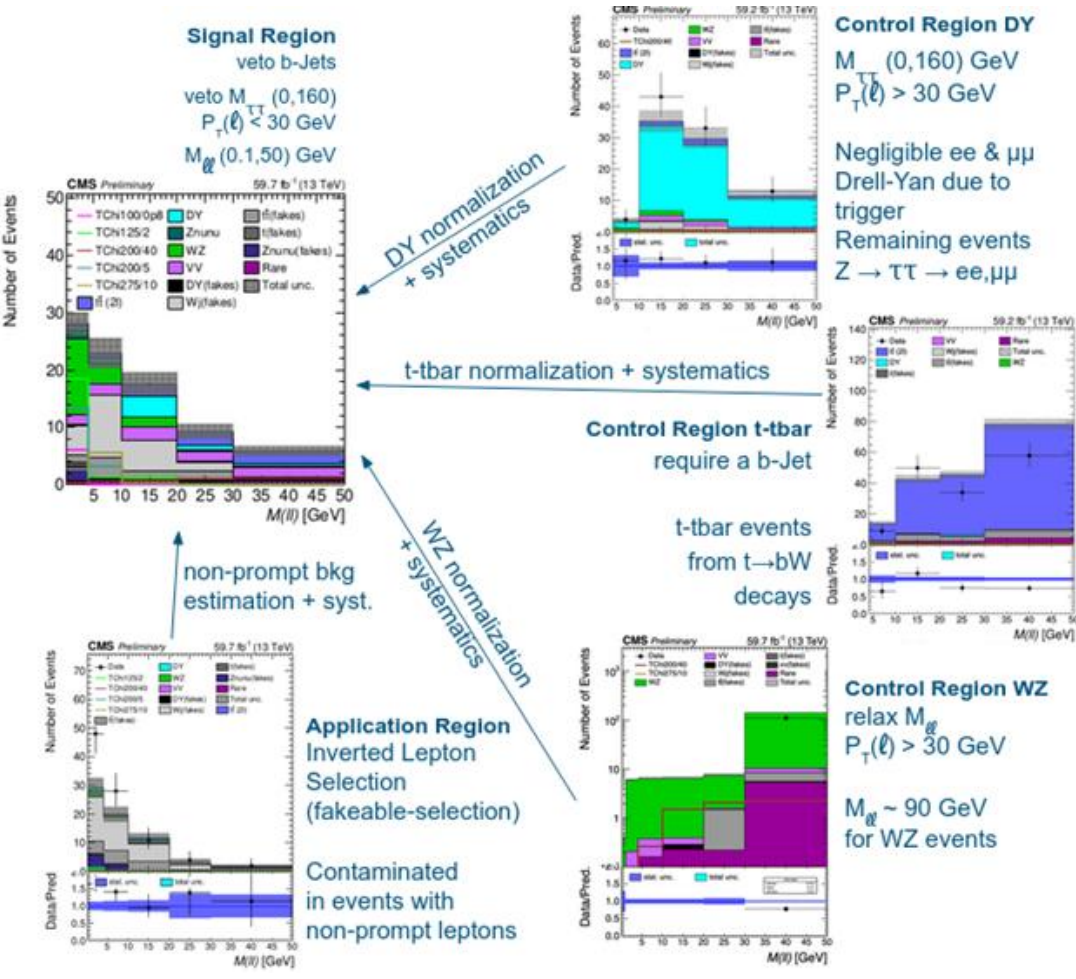


Figure 21: Schematic describing the different regions of the Soft-Multilepton analysis and the flow of information between regions.

On top of separating the analysis into categories, the datasets are furtherly separated into different Regions. The analysis uses "Search Regions" that are dedicated to the final states of the search and "Control Regions" that are dedicated to each important background that is present in the Search Regions and is estimated using MC simulation. The Control Regions have a similar selection of events to that of the Signal Region, but with few key selection requirements inverted so that the region is mostly populated by background events and data-to-simulation corrections and systematic nuisance parameters to be derived. Special Regions also exist and are named after their usage in the strategy of the analysis. These special Regions are called "Application Regions" and "Validation Regions" and are used in the estimation of the non-prompt background processes that exist in the Signal Regions. The Application Regions are enriched in non-prompt events and are used for applying the data-driven (or MC enhanced data-driven, named "semidata-driven") methods for obtaining the estimation of the background in the Signal Regions. The Validation Regions are also non-prompt regions that are used for validating the derived estimation of non-prompt background events after using the data-driven methods. More information on the background estimation methods is given in section 15.2.

The most important backgrounds that are found in the Signal Regions are events from Drell-Yan processes, $t\bar{t}$ production processes, leptons from W and Z decays, and the non-prompt decays (usually inside jets) that conclude into multiple leptons and fake the final states. For these cases, there are related Control Regions designed and presented in the schematic (Figure 21), where the selection criteria of the Signal Regions are adjusted so that the Control Regions are enriched with background events. These background events can be placed into 4 major categories, as described below.

Firstly, the 2 prompt lepton backgrounds that come from Drell-Yan (DY) and $t\bar{t}$ quark production, which can lead to 2 prompt leptons at the final state with real p_T^{miss} at different proportions. For $t\bar{t}$ processes, prompt leptons are produced due to W decays that arise from the process $t\to bW$, resulting also to an undetectable neutrino that contributes real p_T^{miss} in the event. For the DY processes, the direct 2-lepton production (ee, $\mu\mu$) does not add to the background due to the requirement of real p_T^{miss} (125 GeV). However, in case of a tau decay of the Z^0/γ , the taus are capable of decaying to lighter leptons and neutrinos ($Z^0/\gamma \to \tau\tau \to ee/\mu + 2\nu$), which may also contribute to the real p_T^{miss} populating the 2-lepton Signal Region.

Secondly, the 2 prompt boson backgrounds in both 2- and 3-lepton Search Regions, with events from pairs of Ws contributing to the 2-lepton region, and events from WZ and ZZ pairs to the 3-lepton region. Also, there are less significant SM processes that can add to the background in Search Regions and collectively are named "Rares". These consider the production of W bosons together with t-quarks in the event concluding to pairs of leptons. Examples can be ttV, ttH, tZq, tWZ, VVV, and the conversion of photons.

Finaly, even though the lepton selection is optimized to reject non-prompt or fake leptons, there are some residual processes that can still fake the selection of the Signal Regions, due to the complexity of such events. Such events for the 2-lepton SR are the W+Jets and t+Jets, while for the 3-lepton SR the tt+Jets and DY+Jets. The jets in these events can be identified as leptons, or even contain a displaced lepton, leading to a significant background that populates the Signal Regions in case the criteria of the selections are met.

15.2. Background Estimation

For 2-lepton prompt processes, Drell-Yan and $t\bar{t}$, the background estimation in the Signal Region is based on simulation. Two Control Regions, specific for these processes, are used to normalize the simulated predictions in the Signal Regions and to extract systematic uncertainties.

For 2-boson Standard Model processes there are 2 more Control Regions that are used, one to validate the simulated prediction in 2-lepton final states and one to normalize WZ background events that exist in the 3-lepton final state. Even though WZ events is a significant background for the 3-lepton final state, both WZ and WW contribute to the 2-lepton final states too, in which case are estimated using MC simulation and the 2-lepton predictions are validated using the VV Validation Region that is enriched in 2-boson events.

15.2.1. Drell-Yan Control Region

The Drell-Yan (DY) process leads to an opposite-sign lepton pair and low missing transverse energy in the event, but it could still populate the Signal Region because of the intermediate process Z $\to \tau\tau$ when the tau lepton decays to an electron or a muon with an accompanying neutrino. The DY contribution can be suppressed by using the mass of the τ -pair and requiring $m_{\tau\tau} \geq 160$ GeV. (It is possible that $m_{\tau\tau} < 0$, momenta of leptons that are decay components of the τ are used to estimate $m_{\tau\tau}$, and negative values are assigned if τ travels oppositely than the leptons).

The remaining contribution is estimated with simulated events, extracting a normalization factor using a dedicated Control Region (CR) that is designed orthogonal to the SR and rich in "hard" DY events from τ -pairs. The DY Control Region follows a similar Low/High binning scheme (125-200-inf) to facilitate the corrections in all the SR p_T^{miss} bins by using also the same triggers. Prefit dilepton mass distributions for the DY-CR are shown in Figure 22. Normalization floats freely by a factor of 2 and is left to be determined, with its uncertainty, by the final Combine fit (see section 15.4).

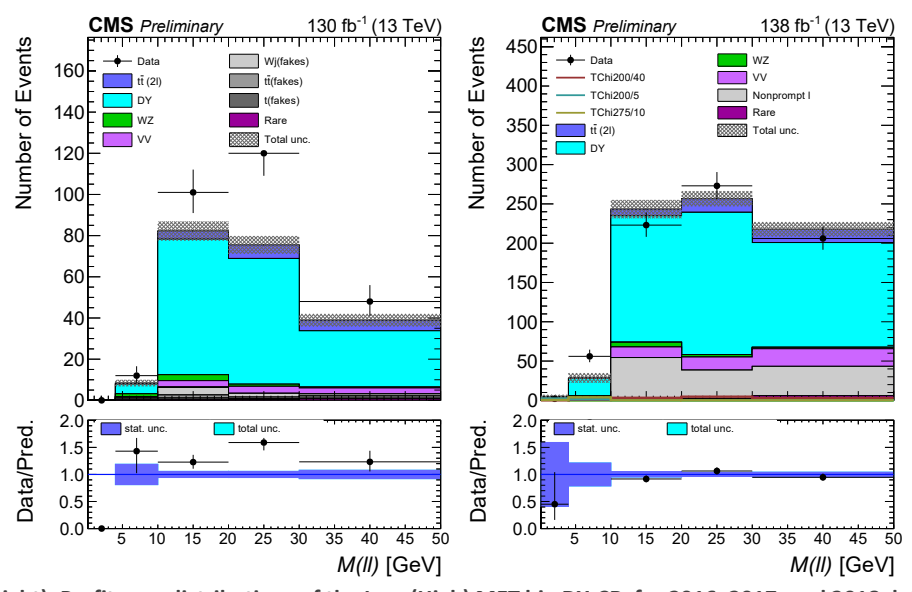


Figure 22: Left (Right): Prefit $m_{\ell\ell}$ distributions of the Low (High) MET bin DY-CR, for 2016, 2017, and 2018 datasets. The purity of the region (measured in 2018 dataset) is estimated at 71% (60%) with MC simulation. Only the statistical uncertainty is included.

15.2.2. TT Control Region

The $t\bar{t}$ process (TT) includes, among many others, 2- and 3-lepton final states due to intermediate W boson decays. A significant part of the process contains leptons in jets that come from B-decays, so a b-jet veto is applied in the event selection for the Signal Region to reduce this contribution.

The remaining contribution is estimated with simulated events, which are normalized to data in a dedicated Control Region defined to be orthogonal that is rich in events from this process. Orthogonality is ensured by inversing the b-tag jet requirement. The TT-CR follows a similar

Low/High binning scheme, like DY-CR, to facilitate the corrections that are propagated to the SR in all p_T^{miss} bins, and it uses the same triggers in these bins. Prefit dilepton mass distributions for the TT-CR are shown in Figure 23. Again, the normalization and its uncertainty are floating parameters to be determined by the final Combine fit (see section 15.4).

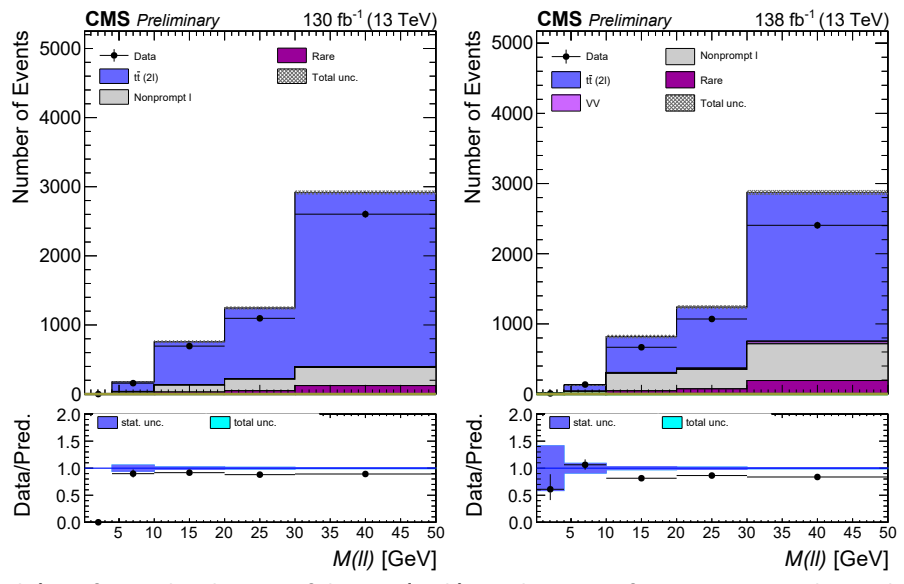


Figure 23: Left (Right): Prefit mee distributions of the Low (High) MET bin TT-CR, for 2016, 2017, and 2018 datasets. The purity of the region (measured in 2018 dataset) is estimated at 78% (64%) with MC simulation. Only the statistical uncertainty is included.

15.2.3. The 2-boson (VV) Validation Region

The 2-boson production (VV) accounts for the mixture of WW, WZ, and ZZ events, where each contribution is given in descending order. The selection is based on the 2-lepton Signal Region by inverting the M_T requirement and asking the leading lepton to have p_T >30 GeV, ensuring orthogonality. Again, the VV-Region follows a similar scheme of Low/High binning, as for the other Control Regions, to facilitate the uncertainties that are derived using information from this region. It also uses the same triggers like in the SR. Prefit dilepton mass distributions for the VV Validation Region are shown in Figure 24. A systematic uncertainty is assigned to the 2-boson MC prediction in the 2-lepton final state and is derived from the final Combine fit (see section 15.4).

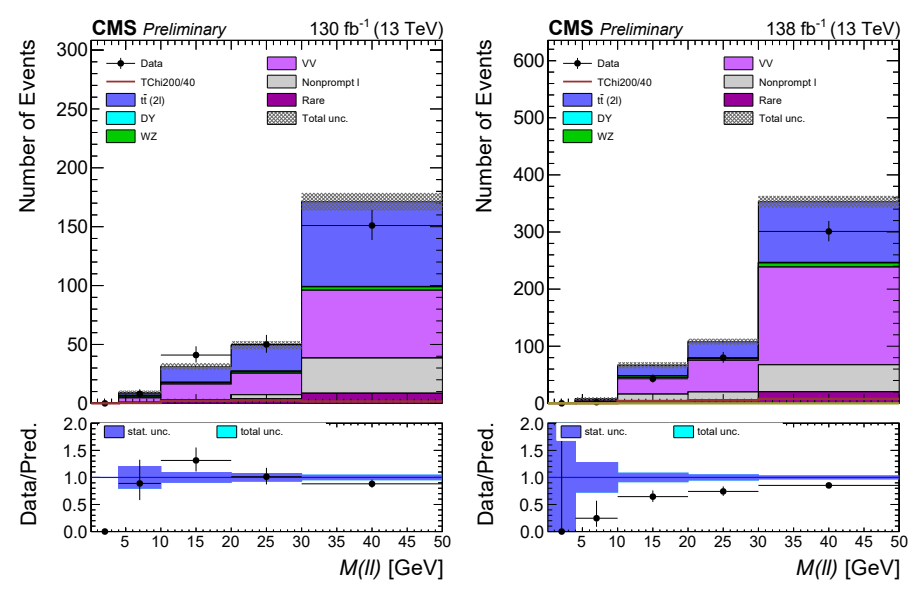


Figure 24: Left (Right): Prefit mee distributions of the Low (High) MET bin VV Validation Region, for 2016, 2017, and 2018 datasets. The purity of the region (measured in 2018 dataset) is estimated at 40% (60%) with MC simulation. Only the statistical uncertainty is included.

15.2.4. The WZ Control Region

Because of relaxing the lepton requirement to $p_T < 3(5)$ GeV for muons(electrons), an important contribution of events from the WZ process exists at low $m_{\ell\ell}$, when the Z can be "off-shell" by tens of GeV. To estimate this background in the analysis and normalize the prediction using data events, an enriched WZ Control Region is designed and is separated into two p_T^{miss} bins, as in the other CRs.

For the reason of including WZ* events with low $m_{\ell\ell}$, which typically populates the Signal Region (SR), two modifications have been introduced with respect to the older iteration of the analysis [45]. Firstly, the 2-muon trigger for the LowMET bin is replaced by 2 single-lepton triggers (see Table 6), and the selection for the leptons in the WZ-CR is modified to select a leading lepton with p_T >30(37) GeV, and the subleading and trailing leptons with p_T >3.5(1) GeV for muons(electrons) respectively. This selection is also used in both Low/High MET bins. The leading lepton ensures orthogonality with the SR, while the next two low p_T leptons result in many opposite-sign pairs from the Z* decay. These modifications allow for reliable normalization and proper assessment of the uncertainty of this type of background with floating parameters that are determined from the final Combine fit (see section 15.4).

Because of significant contamination from some signal mass-points (with ΔM in the range 30-40 GeV), the selection of events is separated in the WZ-like Signal Region for $m_{\ell\ell} < 30$ GeV, and in the WZ-CR for $m_{\ell\ell} > 30$ GeV. Prefit dilepton mass distributions for the WZ-like SR and WZ-CR are shown in Figure 25.

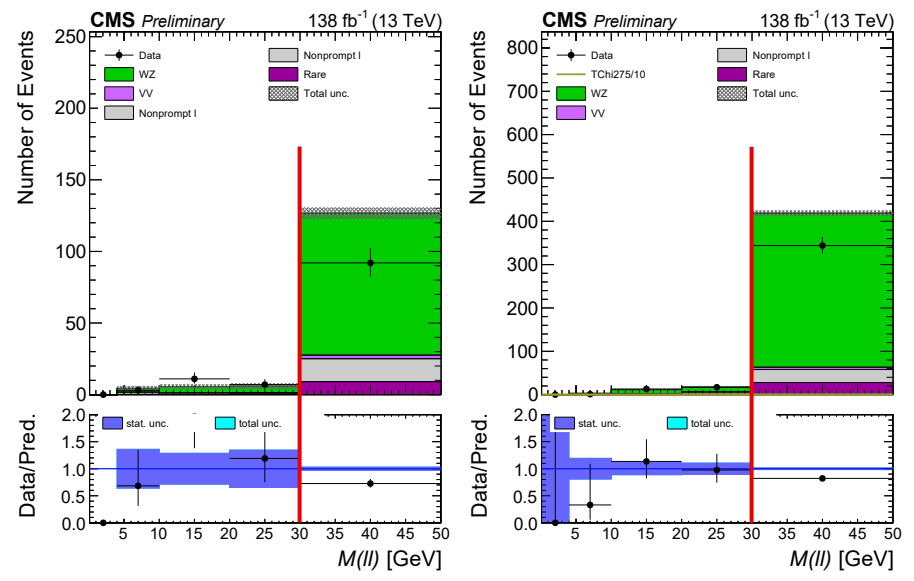


Figure 25: Left (Right): Prefit $m_{\ell\ell}$ distributions of the Low (High) MET bin WZ-CR, for 2016, 2017, and 2018 datasets. The vertical red lines separate the WZ-CR (on the right of the line) from the WZ-like SR (on the left of the line).

15.2.5. Non-Prompt Background Estimation

A "non-prompt" or "fake" lepton is a reconstructed object that doesn't correspond to a real lepton from the primary vertex. For electrons, the main sources of fakes are semi-leptonic heavy flavor decays, misidentified charged hadrons, or photon conversions. For muons, the non-prompt background is related to in-flight meson decays (e.g. charged kaons or pions) and semi-leptonic heavy flavor decays. For simplicity, hereafter, this type of background will be referred to as "non-prompt lepton background" or simply "fakes".

The Fake-Rate Method

The background from non-prompt leptons is estimated by using 3 independent regions as presented in Figure 26. Firstly, the Search Region (SR) is where the number of events with non-prompt leptons needs to be estimated. Secondly, the Application Region (AR) is an enriched region with fake leptons, which is orthogonal to the SR by requiring at least one lepton to fail the lepton selection of the Signal Region. The estimation is based on data events from the AR by weighing them with a transfer factor that depends on the probability of a fake lepton to pass the Tight ID criteria of the SR. This misidentification probability is called Fake-Rate and is measured using data in a QCD enriched region, the Measurement Region (MR). The leptons that are included in the Application Region define a **Loose Selection** in the same manner like the leptons that enter the Signal Region define a **Tight Selection**, which both are optimized by looking at the MR and the AR to make the Fake-Rate measurements compatible with the composition of the fake-events in the AR.

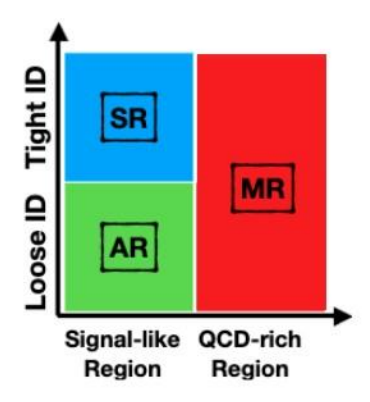


Figure 26: The 3 orthogonal regions that are used for the non-prompt background estimation.

This approach is widely known as the "Tight-to-Loose" method in the CMS experiment. In this analysis, the transfer factor formulas depend also on the separation, ΔR , of the leptons because they are treated differently. Leptons that are **not** separated ($\Delta R < 0.3$) require a treatment where the Fake-Rate probabilities describe both leptons as one object due to isolation peculiarities, as described further below.

The Application Region

This region is defined by using the same kinematic selection as in the SR, but with the extra requirement that at least one lepton fails the selection of the Signal Region (Tight ID and isolation), leading to a region that is enriched in fake lepton events. These regions follow the binning scheme of the SR, in the prompt analysis, with four p_T^{miss} bins (Low, Medium, High and Ultra) in the 2-lepton final state and two bins (Low/High) in the 3-lepton final state, while in the displaced analysis, with two p_T^{miss} bins (Low/High) and two in significance $\sigma_{L_{xy}}$ (Low/High). The $M_{\ell\ell}$ distributions for the 2- and 3-lepton Application Regions for 2018 dataset are presented in Figure 27 and Figure 28. Also, the displaced Application Regions for both final states are presented in Figure 29.

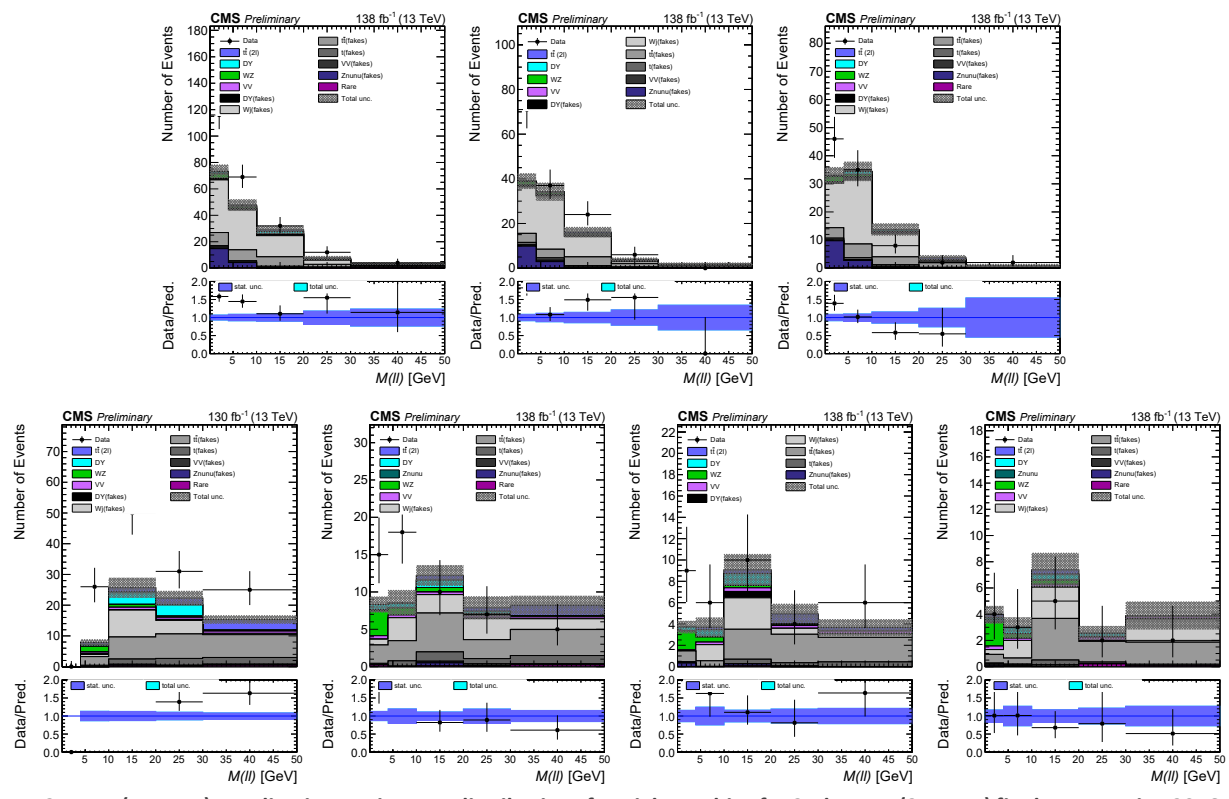


Figure 27: Top (Bottom): Application Region Mee distributions for HighMET bins for 2-electron (2-muon) final states, using 2016, 2017, and 2018 datasets. Left to right: (Low), Medium, High and Ultra p_T^{miss} bins. All distributions, except the Low p_T^{miss} bin, are scaled with the "Semi Data Driven" Scale Factors and the Rate Factors.

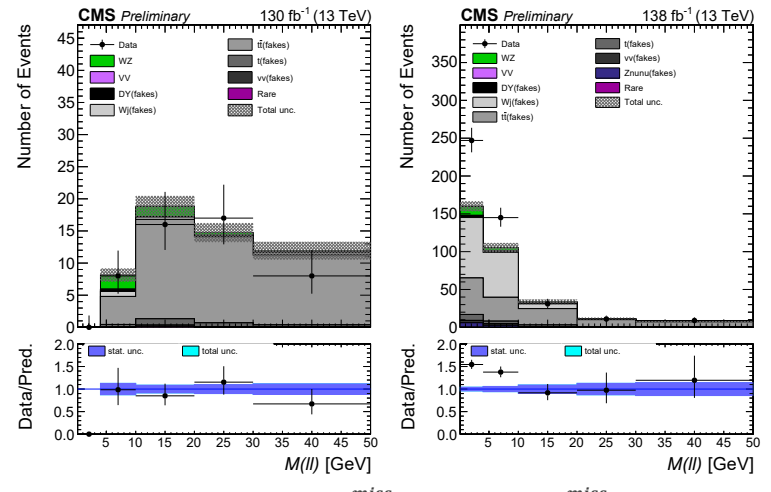


Figure 28: Application Region $M_{\ell\ell}$ distributions for Low p_T^{miss} (left) and High p_T^{miss} (right) bins for the 3-lepton final state, including the "Semi Data Driven" Scale Factors, and using 2016, 2017, and 2018 datasets.

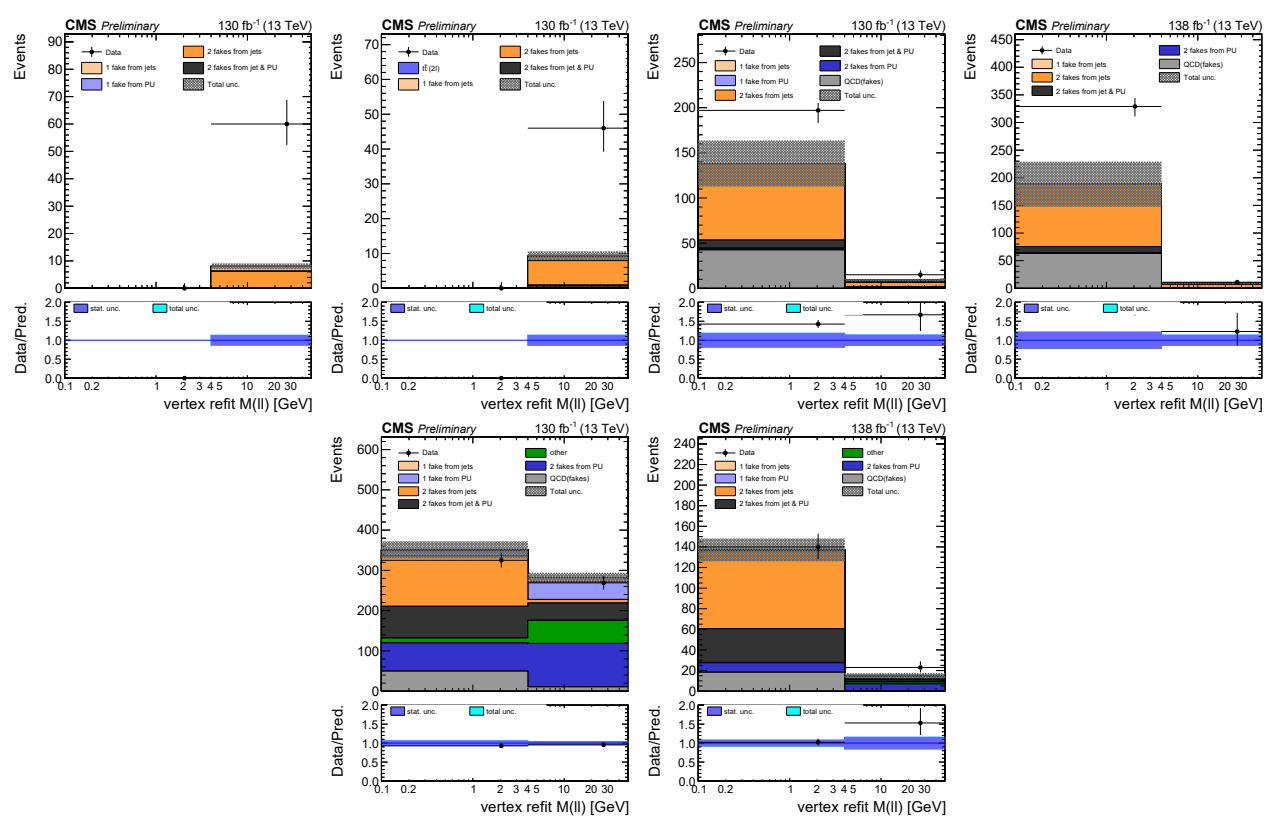


Figure 29: Top & Left-to-Right: Application Region Mee distributions of Low p_T - Low $\sigma_{L_{xy}}$, Low p_T - High $\sigma_{L_{xy}}$, High p_T - Low $\sigma_{L_{xy}}$, and High p_T - High $\sigma_{L_{xy}}$ bins for 2 displaced muons, using 2016, 2017, and 2018 datasets. Bottom & Left-to-Right: High p_T - Low $\sigma_{L_{xy}}$ and High p_T - High $\sigma_{L_{xy}}$ bins for displaced electrons, using 2016, 2017, and 2018 datasets.

Data-Driven and Semi Data-Driven Methods

To estimate the fake background in the Signal Region, a transfer factor is applied on *data* events of the AR. This is the Data-Driven (DD) approach and is preferred because it avoids any mismodeling at the simulation. However, in ARs with low-statistics¹¹ data, it is possible that the DD approach leads to predictions that are negative, with poorly defined uncertainties. To properly predict the fake lepton contribution in the Signal Region for these cases, the transfer factors are applied on the "non-prompt" MC events of the AR that are scaled to data. With this approach the yields of the AR, which are used for background estimation, are given by the following expression, and we profit from better statistics in the simulation.

$$\left(MC_{non-prompt} \times \frac{data - MC_{prompt}}{MC_{non-prompt}}\right)_{AR}$$

This approach is named Semi Data-Driven (SemiDD) and the ratio term is the SemiDD Scale Factor (SemiDD SF).

Using AR simulated events introduces a source of uncertainty, but due to good agreement of the kinematical variables between prediction and observed data in the AR, this source of uncertainty

¹¹ See Appendix 25 for unscaled Application Region plots

is negligible and is omitted. Also, comparing the resulting $closure^{12}$ of the two methods with an inclusive region with high statistics suggests dropping this extra uncertainty. When following the SemiDD approach, the most significant source of statistical uncertainty is still the Poisson error on the number of data events in each $M\ell\ell$ bin of the AR, and it is propagated to the SR by scaling the statistical uncertainty of the prediction in SR, with the ratio of statistical uncertainties in AR, between data and scaled non-prompt simulation (SemiDD).

For all three higher p_T^{miss} bins in the prompt 2-lepton Application Regions, the SemiDD SFs are calculated separately in bins of $M_{\ell\ell}$, using inclusively all statistics available for $p_T^{miss,corr}>200$ GeV, avoiding in this way statistical fluctuations. The normalization of the non-prompt predictions in the individual p_T^{miss} bins (Medium/High/Ultra) is thus dependent on a "Rate

Factor" that is applied along with the SemiDD SFs, as
$$\left(\frac{MC_{non-prompt}(METbin)}{MC_{non-prompt}(p_T^{miss,corr}>200GeV)}\right)$$
. This

factor makes sense since the $M_{\ell\ell}$ distributions between the 3 higher p_T^{miss} bins are similar, which is confirmed by comparing the distributions and using a linear fit on the ratio points between different p_T^{miss} bins to establish that the dependance is similar across all $M_{\ell\ell}$ bins too. This validation is presented in Figure 30 and the errors that come from this procedure define a systematic uncertainty for the estimation of the non-prompt $M_{\ell\ell}$ shape in the final Combine fit (section 15.4).

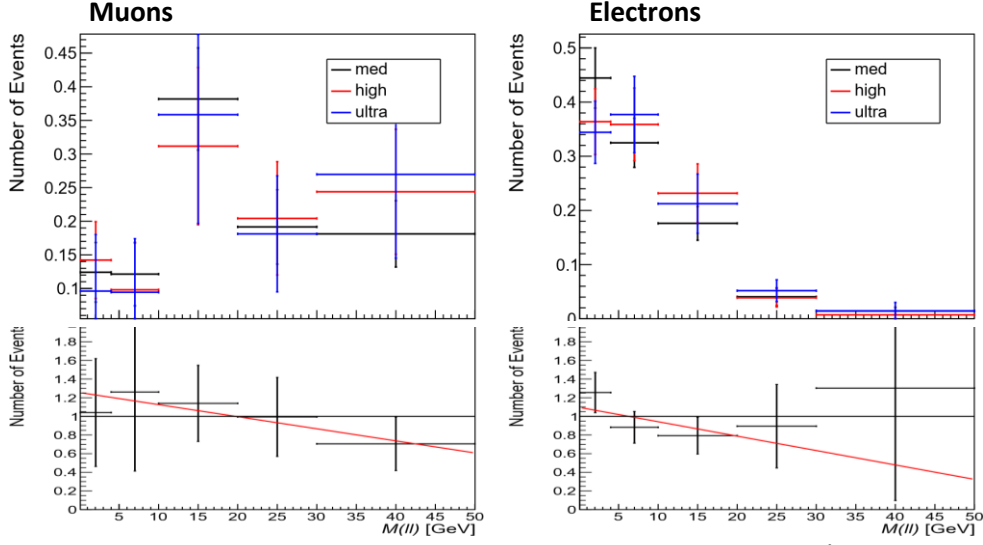


Figure 30: Top: Normalized non-prompt MC Mee distributions for Medium, High, and Ultra p_T^{miss} bins for 2-muon (left) and 2-electron (right) final states in the AR for 2018 dataset. Bottom: Ratios of Medium to the average of High and Ultra for muons and electrons. A linear fit $(f(x)=c_0+c_1x)$ to the ratio points results in slopes compatible with zero (within some error that defines a systematic uncertainty). The slope is -0.013 ± 0.014 for muons and -0.015 ± 0.016 for electrons.

¹² Closure: Comparison of kinematic distributions between the simulated events in the Signal Region and the Fake-Rate prediction in the SR, resulting from weighting Application Region simulated events with the Fake-Rates that are calculated with QCD simulation in the Measurement Region.

For the 3-lepton final states, the simulation describes effectively the data, while the SemiDD SF is measured inclusively in $M_{\ell\ell}$ for both low and high bins of the AR. However, to prevent negative predictions in the Signal Region, the SF is measured separately in different sidebands with 1, 2 or 3 leptons failing the SR selection.

The Application Region distributions for HighMET bins of 2-lepton final states are presented after applying Scale Factors and Rate Factors in Figure 27, while for 3-lepton final states are shown in Figure 28 including Scale Factors. An overview of the methods that are used for estimating the non-prompt background in all regions is presented in Table 4.

| | | | pp | ong. cama per m |
|------|------------|---------------|-------------|-----------------|
| | Low- p_T | Medium- p_T | High- p_T | Ultra- p_T |
| ee | - | SemiDD | SemiDD | SemiDD |
| | | bin-by-bin | bin-by- | bin-by-bin |
| | | | bin | |
| ee | - | | DD | |
| disp | | | | |
| μμ | DD | SemiDD | SemiDD | SemiDD |
| | | bin-by-bin | bin-by- | bin-by-bin |
| | | | bin | |
| μμ | DD | | DD | |
| disp | | | | |
| 3€ | SemiDD | | SemiDD | |
| | inclusive | | inclusive | |

Table 4: Summary of the methods that are used for estimating the non-prompt background per final state and p_T^{miss} bin.

Transfer Factors for independent leptons (prompt $\Delta R > 0.3$)

In this case, the Fake-Rate is the probability of a single fake lepton entering the Signal Region selection. Subsequently, the probability of a fake lepton to not entering the SR is (1-FR). Also, the probability of a prompt (real signal) lepton entering the SR is called Prompt Rate and is measured in W or Z simulated events¹³, while the probability of a prompt lepton not entering the SR is (1-PR). Using these probabilities, one can formulate the component of the yields that include leptons that are Tight-Tight (N_{TT}), Tight-Loose (N_{TL}), Loose-Tight (N_{LT}), and Loose-Loose (N_{LL}) to the true yields including leptons that are Prompt-Prompt (N_{PP}), Prompt-Fake (N_{PF}), Fake-Prompt (N_{PP}), and Fake-Fake (N_{FF}).

$$N_{non-prompt} = f_1(PR, FR)N_{TT} + f_2(PR, FR)N_{TL} + f_3(PR, FR)N_{LT} + f_4(PR, FR)N_{LL}$$

The resulting formulas for the transfer factors, after solving the appropriate 4x4 matrix equation, which express the relation of these 2 spaces (Tight/Loose space and Prompt/Fake space), are the following and express the Data-Driven approach.

¹³ The results for the Prompt Rates are included in the Appendix 27

$$W_{TT} = \frac{-PR_1FR_2(1-FR_1)(1-PR_2) - FR_1PR_2(1-PR_1)(1-FR_2) + (1-PR_1)(1-PR_2)FR_1FR_2}{(PR_1-FR_1)(PR_2-FR_2)}$$

$$W_{TL} = \frac{PR_1FR_2PR_2(1 - FR_1)}{(PR_1 - FR_1)(PR_2 - FR_2)}, \qquad W_{LT} = \frac{PR_1FR_1PR_2(1 - FR_2)}{(PR_1 - FR_1)(PR_2 - FR_2)}$$

$$W_{LL} = \frac{-PR_1PR_2FR_1FR_2}{(PR_1 - FR_1)(PR_2 - FR_2)}$$

These transfer factors in the Semi Data-Driven approach are simplified significantly under the assumption that PR>>FR. Again, solving the matrix equation results in the following transfer factors.

$$W_{TT} = 0$$
, $W_{TL} = \frac{FR_2}{1 - FR_2}$, $W_{LT} = \frac{FR_1}{1 - FR_1}$, $W_{LL} = \frac{-FR_1FR_2}{(1 - FR_1)(1 - FR_2)}$

Transfer Factors for correlated leptons (prompt $\Delta R < 0.3$ & all displaced)

In this case, the leptons are treated as one object and the Fake-Rate is the probability that both fake leptons of the pair enter the Signal Region. Similarly, the Prompt Rate is the probability that a pair of 2 prompt leptons entering the SR, and the failing probabilities are also defined in a corresponding way, (1-FR) and (1-PR). Using these probabilities, one can formulate the component of the yields that include lepton pairs that are both Tight (N_T) and both Loose (N_L) , to the true yields including lepton pairs that are both Prompt (N_P) and both Fake (N_F) .

$$N_{non-nromnt} = f_1(PR, FR)N_T + f_2(PR, FR)N_L$$

The resulting formulas for the transfer factors, after solving the appropriate 2x2 matrix equation, are following and illustrate the Data-Driven approach.

$$W_T = \frac{-(1 - PR)FR}{PR - FR}$$

$$W_L = \frac{PR \ FR}{PR - FR}$$

These transfer factors in the Semi Data-Driven approach are simplified under the same assumption that PR >> FR. Again, solving the matrix equation results in the following transfer factors.

$$W_T = 0$$
, $W_L = \frac{FR}{1 - FR}$

15.2.6. Non-Prompt Leptons from Pile-Up (Displaced Regions Only)

This component of the background concerns only the displaced analysis. It is about coincidences of di-leptons that are formed by displaced leptons from Pile-Up (PU), which succeed to enter the Signal Region selection due to isolation calculations that are not compatible with the PU vertices. Displaced leptons from PU appear to be isolated and fake the signal because of the wrong point

of reference of the isolation cone, as in the Particle-Flow algorithms the point of reference for the momenta vectors is at the main PV of the event, and this leads to an isolated picture of this component of the background with inconsistent Fake-Rates with the "tight-to-loose" method.

Considering the facts above, the data-driven prediction does not include this component, and therefore it is estimated using the simulation. For this purpose, an orthogonal displaced Same-Sign Control Region is used to validate the trustworthiness of the simulation before used to estimate PU events in the displaced Signal Regions. Inverting the charge requirement makes the region orthogonal to the Signal Region, also more statistics are achieved by relaxing the requirements $\log_{10}\frac{\Delta_{xy}}{\Delta_z}$ that are designed to eliminate PU events from the Signal Region. Since the double-muon trigger that is used to collect events for $p_T^{miss} < 200$ GeV includes an implicit requirement of an opposite-sign pair of muons, the displaced Same Sign CR is defined only for $p_T^{miss} > 200$ GeV.

In Figure 31, the Same-Sign Control Region is presented for both displaced muons and electrons. Since the agreement between data and simulation is acceptable, the simulation is used in Signal Region directly to predict the contribution of events with dileptons from Pile-Up.

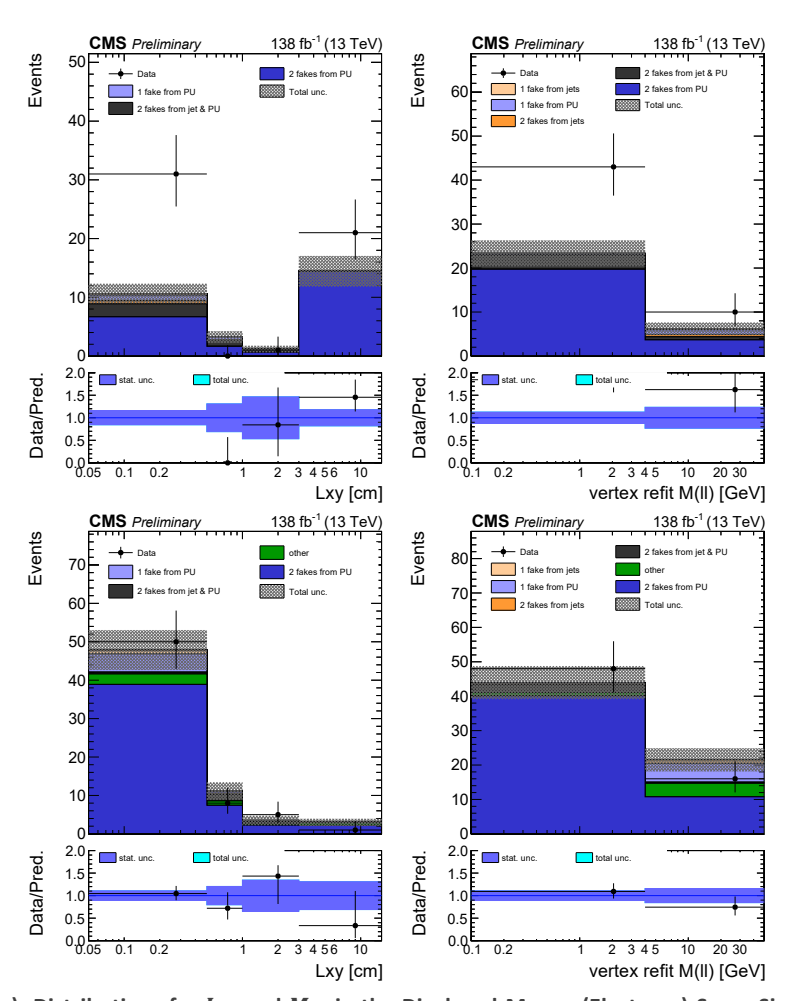


Figure 31: Top (Bottom): Distributions for L_{xy} and $M_{\ell\ell}$ in the Displaced Muons (Electrons) Same-Sign Control Region, using 2016, 2017, and 2018 datasets. The agreement between data and simulation is within acceptable levels, therefore the simulation can be directly used in the Signal Region to predict the Pile-Up background.

15.3. Uncertainties

All systematic and statistical uncertainties that are considered in this analysis are incorporated in the likelihood as nuisance parameters, which eventually are constrained by the data due to the use of the Control Regions.

Trigger Efficiency

To account for any mismodeling of the online event selection and in simulated events, data-to-simulation corrections are applied to all simulated events, in all regions. Up to 5% on the predicted yield is assigned due to the trigger efficiency. Different years are treated separately, with a new nuisance parameter, since the HLT muon reconstruction and the MET definitions differs over the years.

Lepton Selection Efficiency

Corrections are derived by comparing data and simulation to account for differences in lepton reconstruction and selection criteria for the leptons to enter the Signal and Control Regions. These adjustments help equalize the performance between data and simulation, while any residual systematic uncertainty (due to the extraction methods for these corrections) is also propagated to the likelihood fit with extra nuisances.

B-Tagging Efficiency

The performance of the b-tagging algorithm [47] is equalized between data and simulation through dedicated corrections.

- Contamination from light-flavor jets (u/d/s/g + c) in heavy-flavor regions
- Contamination of b + c jets in light-flavor regions
- Linear and quadratic statistical fluctuations for b jets and light jets
- Additional uncertainty for c jets to accommodate differences on their modeling

These corrections are treated as shape nuisance parameters, allowing for decorrelated treatment along the bins of the invariant mass $(M_{\ell\ell})$ during the final fit. Certain components of these uncertainties are also decorrelated across years too, due to different detector performance throughout the years.

Jet Energy Corrections (JECs)

Small variations in the jet energy scale, as determined by the recommended corrections centrally from CMS [48], have a sizable impact on the shape of the $M_{\ell\ell}$ fitting templates. The recommended jet energy scale (JES) uncertainties are implemented as shape uncertainties, correlated across years.

Pileup Modeling

A reweighting is applied to correct the simulated Pile-Up per bunch crossing. The expected number of interactions is estimated based on the inelastic cross section (69.2 mb, 4.6% uncertainty) and is propagated to the pileup weights [49]. The resulting shape uncertainty is included to the fit.

Luminosity Measurement

This uncertainty on the luminosity measurement directly impacts both the expected signal and the background yields. For Run2, the uncertainties are 1.2% for 2016, 2.3% for 2017, and 2.5% for 2018 [50]. These are implemented as log-normal restrictions to the likelihood profile.

ISR Modeling and Pre-fire Corrections

For initial-state radiation (ISR), a conservative flat uncertainty of 5% is assigned. This choice is motivated by studies from the SUSY Group (SUS PAG), where several tunings on the parton-simulator were benchmarked and may have an effect from triggers to selections (due to variations in jet p_T). Additionally, pre-fire corrections that account for issues to the electromagnetic calorimeter in 2016 and 2017, are provided from CMS along with the appropriate uncertainties, and are included as nuisances too.

Normalization Uncertainties

The estimation of important background processes is subject to normalization uncertainties that are constrained via dedicated control regions and dedicated nuisance parameters. These are processes of Drell-Yan, $t\bar{t}$, and WZ, for the 2-lepton final states.

Systematic Uncertainties to the Simulation

Backgrounds, other than those with a corresponding Control Region, are estimated directly from simulation and an uncertainty of 50% on this estimation is assigned. These are processes of di-Bosons (ZZ and $Z\gamma$, except WZ that comes with a CR) and other rare processes as one extra component/nuisance.

Fake (or Non-Prompt) Leptons

The normalization uncertainties for these backgrounds depend on the lepton type, 40% for prompt leptons and 50% for displaced ones (this comes from the closure studies in Section 17). Additionally, specific shape uncertainties arise due to (a) how the data statistics in the Application Region (AR) influence the simulation scaling to data, and (b) averaging the $M_{\ell\ell}$ templates in the AR for $p_T^{miss} >$ 200 GeV. In (a), the fake-lepton estimation is influenced since the shape of the simulation is limited to that of data in the AR before applying the Semi-DD method to get the $M_{\ell\ell}$ templates. In (b), the approach could potentially lead to loss of modelling information due to averaging the templates, leading to an extra uncertainty.

Theoretical Uncertainties on the Signal

Signal modeling includes theoretical uncertainties by doubling and halving the factorization scale, while renormalization scale variations were studied and determined negligible for this analysis.

15.4. Statistical Analysis

A short description is presented of how the analysis uses a likelihood-based statistical test and the Combine framework [44] to calculate the expected and observed limits. A simplistic example of the method is illustrated using two Signal Region bins (SR1 and SR2), a background estimation

within these regions, and a Control Region (CR) that is used to constrain a background process with a nuisance parameter.

The Combine framework is a flexible statistical tool originally developed by CMS, for the Higgs analyses back in 2012. Today, it is widely adopted across multiple analyses, including those from CMS and ATLAS, for performing maximum likelihood fits and other limit-setting procedures (p-values, significances, Asimov toys, etc.). At its core, Combine leverages a detailed likelihood model that captures signal and background predictions, while incorporating systematic uncertainties as nuisance parameters. This approach is particularly effective and flexible [41] when dealing with multiple regions, for example several bins from a SR distribution, where one hopes to observe a signal, or several bins from a CR that is constraining the background estimation. Eventually, the likelihood is fit to the data or to the Asimov dataset [41], for observed or expected results respectively.

15.4.1. Likelihood Construction and Model Building

In our example, the overall likelihood is built as the product of Poisson probabilities corresponding to the individual regions and their respective bins. For example, for an $M_{\ell\ell}$ distribution that is separated in 5 bins, the likelihood is a product of 5 Poisson terms.

Signal Regions (SR1 and SR2)

These regions are designed to maximize sensitivity to a potential signal using a sequence of selection cuts that focuses on the phase-space in question. For example, in the multilepton analysis a selection cut of $p_T^{miss} > 200$ GeV focuses to a SR, whose main background comes from the tails of QCD distributions, making easier measurements on EWK processes. The number of expected events, for each bin of the SR, is modeled as a combination of the expected signal events $(S_{bin\,i})$, the background contributions $(B_{bin\,i})$, and the signal strength (μ) that is considered floating and non-zero.

$$\langle x^{exp}(bin i) \rangle = \mu S_{bin i} + B_{bin i}$$

However, since signal and background predictions suffer from uncertainties (see the formulation below), these estimates are adjustable with floating normalizations, which act as nuisance parameters that can adjust the yields during the fit. The functions f_1 and f_2 are separate Poisson distributions that regulate the expected events in each bin, with respect to some theoretical mean value.

$$S_{bin i} = C_S \int_{bin i} dx f_1(x; \theta_S)$$

$$B_{bin i} = C_B \int_{bin i} dx \, f_2(x; \theta_B)$$

For the signal, the constant C_S can be incorporated within the signal strength. For the background, this constant acts as an extra nuisance parameter, the floating normalization parameter that is constrained by the CR.

Control Region (CR)

The control region is chosen such that it is enriched by background events (of some specific source, if the point of enlarging the model with a CR is fine-tuning) and largely free of the potential signal. Data in this region help constrain the nuisance parameters, especially the floating normalization parameter C_B for the background. By doing so, the analysis reduces the uncertainty in the background prediction in the signal regions. The CR is added to the likelihood as an independent Poisson term, with the background expectation modified by the same floating factors that influence the SR predictions. The number of expected events in the CR is modeled similarly with the term $B_{bin\ i}$ and is subject to all the nuisances θ_S , θ_B , and to C_B itself.

The complete likelihood function, which describes expected yields in all regions simultaneously, is a product of Poisson terms that depend bin-by-bin on the signal contributions, background, and systematic uncertainties (the nuisance parameters). In mathematical terms, if μ is the signal strength modifier, and θ collectively denotes the nuisance parameters, then one formulates the likelihood as:

$$\mathcal{L}(\mu,\theta) = \prod_{bin: SR1,SR2} \frac{(\mu S_{bin} + B_{bin})^{N_{bin}}}{N_{bin}!} e^{-(\mu S_{bin} + B_{bin})} \times \prod_{bin: CR} \frac{B_{bin}^{M_{bin}}}{M_{bin}!} e^{-M_{bin}} \times \prod_{syst} \pi(\theta_i)$$

Here, $\pi(\theta_j)$ represents the probability density functions (usually Gaussian or log-normal) that constrain the nuisance parameters. Each floating normalization parameter (for the background components) is also treated as one such nuisance parameter, which is constrained by data in the control region during the fit.

15.4.2. Maximum Likelihood Minimization and Limits

The Combine framework performs a simultaneous fit to the data in SR1, SR2, and CR by maximizing the likelihood (or equivalently, minimizing the negative log-likelihood). During this minimization, it adjusts the nuisance parameters (and the normalization factors) to best match the observed data across all regions, thus the floating normalization ultimately results in a constrained background model that is enhanced by the control region data.

Because the normalization factors are shared between the Control and the Signal Regions, any issue on the modeling that is observed in the CR directly impacts the background estimate in the SRs. However, it also works in reverse as this "simultaneous fit" allows the analysis to profit from the modelling in the CR, which is usually better populated, reducing the overall impact of systematic uncertainties on the results.

When searching for a discovery, one formulates two hypotheses: the null hypothesis H_0 that represents the "background-only" scenario that is signal-free, and the alternative hypothesis H_1

that represents the presence of both background and the signal in question. A "test statistic" is afterwards constructed as the profile likelihood ratio of H_1 -to- H_0 and quantifies the level of agreement (or disagreement) between the observed data and H_0 . A **significance greater than** 5σ , equivalent to p-value **less than** 2.9×10^{-7} , is required to **accept** the new hypothesis H_1 .

When setting limits for excluding a theoretical hypothesis, one formulates the hypotheses in reverse: the null hypothesis H_0 represents the presence of both background and signal, and the alternative hypothesis H_1 represents the signal-free scenario that is meant to be tested for acceptance. Usually, limits are set along some parametrized phase-space and the acceptance of H_1 can be proven (with the collected data) in a subspace of the tested phase-space. The "test statistic" is again constructed as the profile likelihood ratio of H_1 -to- H_0 and any significance lower than 1.65σ , equivalent to p-value greater than 0.05 (CL 95%), is considered enough to reject the new hypothesis H_0 .

The profile likelihood ratio is defined as follows: the numerator is the "conditional" maximized likelihood (ML) for some specific value $\mu=\mu'$, and the denominator is the "unconditional" maximized likelihood. To simplify the situation, in the asymptotic limit with enough statistics, where the "test statistic" is proven that follows χ^2 -distribution (Wilks' theorem), and the signal strength estimator from the ML fit $\hat{\mu}$ follows with enough accuracy a Gaussian distribution (Wald's theorem), the numerator and the denominator can be approached with the conditional maximized likelihoods using $\mu=1$ (nominal signal) and $\mu=0$ (signal-free) respectively.

$$\lambda(\mu) = \frac{\mathcal{L}\left(\mu = \mu', \widehat{\hat{\theta}}\right)}{\mathcal{L}(\widehat{\mu}, \widehat{\theta})} \approx \frac{\mathcal{L}_{S+B}}{\mathcal{L}_{B}}$$

The corresponding "test statistic" then is $q_{\mu}=-2\ln\lambda(\mu)$ and is also implemented using these approximations in the Combine framework, since it greatly simplifies the computations of p-value and significance without requiring extensive Monte Carlo simulations.

Observed Limit

The observed limit is obtained by fitting the likelihood function to the actual observed data. This fit yields the best-fit values for both the signal strength μ and the nuisance parameters θ (ML estimators $\hat{\mu}$ and $\hat{\theta}$). The profile likelihood ratio is then computed. The observed limit is defined as the point where the p-value crosses the reference confidence level (95% for rejections or 5σ for discovery).

Expected Limit

To estimate the expected limit, the analysis uses the Asimov dataset, which represents the median expectation yields in the absence of the signal. In practice, one constructs the Asimov dataset using the background-only hypothesis ($\mu=0$), incorporating the same systematic uncertainties. The likelihood is then maximized using this pseudo-dataset, and the same test

statistic is computed, as used for the observed limit. The expected limit is usually quoted as the median limit along with $\pm 1\sigma$ bands that represent deviations because of fluctuations in the background and the systematic uncertainties. This usually serves as a benchmark test for the analysis before inspecting the actual data.

The Combine framework calculates both expected and observed limits by constructing and maximizing appropriately the likelihood that may incorporate contributions from multiple regions.

16. Event Reconstruction

16.1. Datasets & Triggers

The analysis is based on proton-proton collision datasets recorded by the CMS experiment during the LHC Run-2 period. These data correspond to an integrated luminosity of about $137\ fb^{-1}$ ($36.3\ fb^{-1}$, $41.5\ fb^{-1}$, and $59.8\ fb^{-1}$ for 2016, 2017, and 2018 periods respectively) and were collected with several triggers implemented by the HLT group of the experiment. The trigger algorithms that are used in this analysis are mostly based on Missing Transverse Energy (MET) and Double Muon and the primary datasets are named after these algorithms.

The reconstruction of the collected and simulated events is centrally operated by the CMS experiment. This round of reconstruction is named "Ultra Legacy" (UL) and is a re-reconstruction campaign for the entire Run-2 dataset that targeted issues that were discovered during the first round of analysis on Run-2 datasets, while also incorporates new algorithms that are expected to boost data purity and physics efficiency. One of these new algorithms is the reconstruction of "LowPt-Electrons", used in this analysis extensively, and is built with different requirements compared to the Particle-Flow reconstruction (see section 16.2.2).

Simulated physics samples are used to estimate yields from Standard Model background processes with the leading components to be events from $t\bar{t}$, DY and W leptonic decays that also contain hadronic activity (jets). These samples are produced at leading order (LO) using the Madgraph framework. Other backgrounds like di-boson, single top quark, and rare processes are produced at next to leading order (NLO) with the aMCatNLO or the Powheg software. The standard NNPDF3.1 framework for LO and NLO PDF sets is used for the production, Pythia 8 framework handles the showering and hadronization steps, GEANT4 framework handles the detector simulation, and finally all the simulated samples are reconstructed centrally by CMS according to the UL campaign using the CMSSW framework.

From here on, the output quantities that come after the hadronization step (after Pythia 8) are referred to as "generated", and the output quantities that come after the CMS reconstruction (after CMSSW) are referred to as "reconstructed".

The complete list of the MC samples that are used by this analysis is shown in Table 5, together with cross-sections, and is categorized in different background groups, as presented in the plots of the analysis.

Table 5: List of simulated samples together with cross-sections. They follow a categorization specifying in which processes of the analysis they are used.

| Process | Datasets | Cross-section[pb] |
|--------------|---|-------------------|
| Signal | SMS-TChiWZ_ZToLL_mZMin-0p1_TuneCP5_13TeV-madgraphMLM-pythia8 | SUSYCrossSections |
| | SMS-TChiWZ_ZToLL_mZMin-0p1_LLN2_TuneCP5_13TeV-madgraphMLM-pythia8 | [43] |
| | SMS-HiggsinoN2N1_ZToLL_LLN2_TuneCP5_13TeV-madgraphMLM-pythia8 | |
| | SMS-HiggsinoN2C1_ZToLL_LLN2_TuneCP5_13TeV-madgraphMLM-pythia8 | |
| Fakes | WJetsToLNu_TuneCP5_13TeV-madgraphMLM-pythia8 | 1935.68 |
| | ST_t-channel_4f_InclusiveDecays_TuneCP5_13TeV-powheg-madspin-pythia8 | 216.97 |
| | ST_s-channel_4f_leptonDecays_TuneCP5_13TeV-amcatnlo-pythia8 | 3.68 |
| | WWTo1L1Nu2Q_4f_TuneCP5_13TeV-amcatnloFXFX-pythia8 | 43.53 |
| | WZTo1L1Nu2Q_4f_TuneCP5_13TeV-amcatnloFXFX-pythia8 | 10.71 |
| DY, Fakes | DYJetsToLL_TuneCP5_13TeV-madgraphMLM-pythia8 | 1279925 |
| | ZJetsToNuNu_TuneCP5_13TeV-madgraphMLM-pythia8 | 352.25 |
| Rares, Fakes | ST_tW_top_antitop_5f_NoFullyHadronicDecays_TuneCP5_13TeV-powheg-pythia8 | 39.1 |
| | TTJets_SingleLepton_TuneCP5_13TeV-madgraphMLM-pythia8 | 364.35 |
| | TTWJetsToLNu_TuneCP5_13TeV-amcatnloFXFX-madspin-pythia8 | 0.2043 |
| | TTZToLL_M-10_TuneCP5_13TeV-amcatnlo-pythia8 | 0.306 |
| | tZq_II_4f_ckm_NLO_TuneCP5_13TeV-amcatnlo-pythia8 | 0.07358 |
| | ST_tWll_5f_TuneCP5_13TeV-madgraph-pythia8 | 0.01123 |
| tt, Fakes | TTJets_DiLept_TuneCP5_13TeV-madgraphMLM-pythia8 | 87.31484 |
| Rares | TGJets_leptonDecays_TuneCP5_13TeV-amcatnlo-pythia8 | 1.018 |
| | TTGJets_TuneCP5_13TeV-amcatnloFXFX-madspin-pythia8 | 4.09 |
| | WGToLNuG_TuneCP5_13TeV-madgraphMLM-pythia8 | 466.1 |
| | ZGToLLG_01J_5f_lowMLL_lowGPt_TuneCP5_13TeV-amcatnloFXFX-pythia8 | 172.4 |
| | Tri-Boson_(WWW/WWZ_4F,_WZZ/ZZZ)_TuneCP5_13TeV-amcatnlo-pythia8 | 0.24193 |
| VV, Rares | WWTo2L2Nu_TuneCP5_DoubleScattering_13TeV-pythia8 | 0.20870 |
| | WpWpJJ_EWKnotop_TuneCP5_13TeV-madgraph-pythia8 | 0.02687 |
| VV, Fakes | WZTo2Q2L_mllmin4p0_TuneCP5_13TeV-amcatnloFXFX-pythia8 | 6.43 |
| | VVTo2L2Nu_MLL-1toInf_TuneCP5_13TeV-amcatnloFXFX-pythia8 | 14.75 |
| | ZZTo2Q2L_mllmin4p0_TuneCP5_13TeV-amcatnloFXFX-pythia8 | 3.698 |
| VV | WZTo3LNu_mllmin0p1_TuneCP5_13TeV-powheg-pythia8 | 40.4105 |
| | ZZTo4L_M-1toInf_TuneCP5_13TeV_powheg_pythia8 | 13.74 |

Finally, for the Signal processes, the corresponding SUSY samples that are based on the simplified models are processed with the CMS UL campaign and the simulation of the dynamics, the hadronization, and the detector response of the SUSY particles is modeled at LO, using the same frameworks as for the background samples. The generated mass-hypotheses, for both Wino-Bino and Higgsino signals, include gaugino (fully degenerate) masses from 100 to 600 GeV, in steps of 25 GeV, and mass-splitting values of 0.6, 0.8, 1.0, 1.5, 2, 3, 5, 7.5, 10, 15, 20, 30, 40 and 50 GeV. The cross-section values that are used are Wino-like and Higgsino-like calculations at 13 TeV and NLO, with chargino-neutralino and neutralino-neutralino topologies. The cross-sections are provided as function of mass, by the CMS SUS PAG group in the Twiki (see Table 5). [43]

The data selection for the analysis is achieved with several HLT Paths, presented in Table 6. It categorizes different paths by year, by MET bin, and by region that are used to populate. Using HLT paths that trigger exclusively on $p_T^{miss,corr}$, a p_T^{miss} calculation without muons, makes it possible to study regions without complex requirements on the muon momenta due to the p_T^{miss} , which correlates the muon p_T . For these regions (HighMET regions), the lowest threshold of "unprescaled" HLT triggers that is based on $p_T^{miss,corr}$ is used to filter events, while is seeded by pure $p_T^{miss,corr}$ paths at the L1 too. Choosing only $p_T^{miss,corr}$ triggers made it simpler to benefit from the full recorded luminosity, for all 3 years.

DoubleMuon and Electron Triggers

Because of lower efficiency at the turn-on of HighMET trigger, a dedicated DoubleMuon trigger with p_T^{miss} is used as well. This trigger was developed by a previous iteration of this analysis, covering specifically the loss of efficiency below 200 GeV of p_T^{miss} , and was designed to be at the plateau at $p_T^{miss} > 125~GeV$ (LowMET region, only muons SR). It is seeded by DoubleMuon and $p_T^{miss,corr}$ paths at the L1 trigger and includes DoubleMuon and p_T^{miss} requirements at HLT. Furthermore, extra requirements that vary between years are also added, such as "the distance of the muons on the z-axis", $\Delta z(\mu\mu)$, "the distance of Closest Approach or minimum distance of tracks", DCA, and the Invariant Mass. These extra requirements regulate the rate. Additionally, a soft¹⁴ Single Electron trigger is also used for the "3L LowMET" WZ region, allowing the subleading and trailing (third) lepton to be even softer.

¹⁴ Trigger that requires low thresholds on p_T

Table 6: A complete list of the triggers (HLT paths) that are used to select data and simulated events in all the regions/years of the analysis. In this table, the three higher p_T^{miss} bins, Medium, High, and Ultra, are noted as High p_T^{miss} .

| Year | Region | Trigger (Lumi) | Requirements |
|------|--|--|---|
| 2016 | Low p _T ^{miss} SR & CR | HLT_DoubleMu3_PFMET50 (33.5fb⁻¹) | $p_T^{miss} > 50 	ext{ GeV}$ $M(\ell\ell) < 60 	ext{ GeV}$ $p_T > 3 	ext{ GeV}$ $DCA < 0.5 	ext{ cm}$ |
| | Low p _T ^{miss} WZ CR | HLT_IsoMu24 <i>(36.3fb⁻¹)</i> HLT_Ele27_WPTight_Gsf <i>(36.3fb⁻¹)</i> | $p_T > 24 \text{ GeV} + \text{Iso03}$ $p_T > 26 \text{ GeV} + \text{WP}$ |
| | High p _T ^{miss} SR & CR | HLT_PFMETNoMu120_PFMHTNoMu120_IDTight (36.3fb ⁻¹) | $p_T^{miss,corr} > 120 \text{ GeV}$ |
| 2017 | Low p _T ^{miss} SR & CR | HLT_DoubleMu3_DZ_PFMET50_PFMHT60 <i>(36.7fb</i> -1) | $p_T^{miss} > 50 \text{ GeV}$ $3.8 < M(\ell\ell) < 60 \text{ GeV}$ $p_T > 3 \text{ GeV}$ dz < 0.2 cm |
| | Low p _T ^{miss} WZ CR | HLT_lsoMu27 (41.5fb⁻¹) HLT_Ele35_WPTight_Gsf (41.5fb⁻¹) | $p_T > 27 \text{ GeV} + \text{Iso03}$ $p_T > 35 \text{ GeV} + \text{WP}$ |
| | High p _T ^{miss} SR & CR | HLT_PFMETNoMu120_PFMHTNoMu120_IDTight (41.5fb ⁻¹) HLT_PFMETNoMu120_PFMHTNoMu120_IDTight_PFHT60 (41.5fb ⁻¹) | $p_T^{miss,corr} > 120 \text{ GeV}$ |
| 2018 | Low p _T ^{miss} SR & CR | HLT_DoubleMu3_DCA_PFMET50_PFMHT60 <i>(59.3fb⁻¹)</i> | $p_T^{miss} > 50 \mathrm{GeV}$ $3.8 < M(\ell\ell) < 60 \mathrm{GeV}$ $p_T > 3 \mathrm{GeV}$ $DCA < 0.5 \mathrm{cm}$ |
| | Low p _T ^{miss} WZ CR | HLT_lsoMu24 (59.8fb⁻¹) HLT_Ele32_WPTight_Gsf (59.8fb⁻¹) | $p_T > 27 \text{ GeV} + \text{Iso03}$ $p_T > 32 \text{ GeV} + \text{WP}$ |
| | High p _T ^{miss} SR & CR | HLT_PFMETNoMu120_PFMHTNoMu120_IDTight (59.8fb ⁻¹) HLT_PFMETNoMu120_PFMHTNoMu120_IDTight_PFHT60 (59.8fb ⁻¹) | $p_T^{miss,corr} > 120 \text{ GeV}$ |

The efficiency of selecting an event with these trigger paths is different between simulated and real data, so corrections (data/simulation Scale-Factors) need to be calculated and applied to the simulation. The efficiency is measured in both data and simulated background events for a mixture of DY, $t\bar{t}$, and DiBoson processes, and are parametrized differently depending on the peculiarities of each trigger path. The trigger corrections are defined by the following ratio.

$$SF_{trigger} = \frac{\varepsilon_{data}}{\varepsilon_{simulation}}$$

In HighMET regions the corrections are parametrized using an error function, an integration of a gaussian around the mean value (μ) of the missing energy of the events in the dataset of the measurement. The same parametrization is used across all years. An example of these efficiency measurements is presented for 2018 in Figure 32, together with the parametrization of the corrections. A similar approach holds for the "METNoMu" triggers.

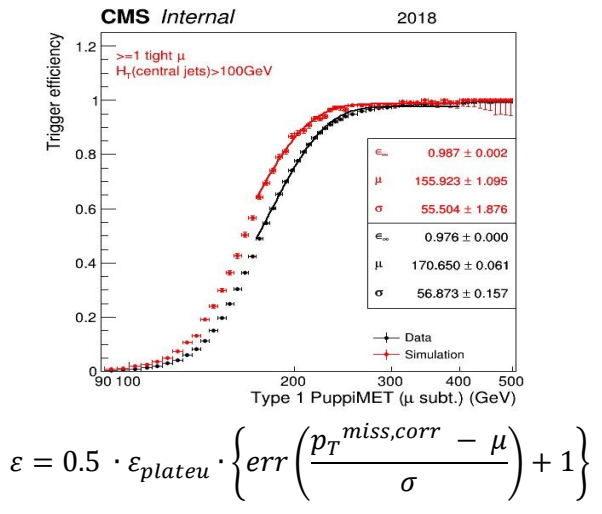


Figure 32: Efficiencies measured in simulation and real data for the "HLT_PFMETNoMu120" trigger for 2018 dataset (59.3 fb⁻¹). They are parametrized and fitted with the expression above using an error function.

The dedicated DoubleMuon plus p_T^{miss} triggers are used in the LowMET Signal Regions and in all the Control Regions except WZ. The efficiency measurements are factorized using 3 terms, the leptonic ($\mu\mu$), the missing p_T^{miss} , and the extra requirements like DCA (or Dz). These triggers also include an invariant mass requirement on the muons ($M_{\ell\ell} < 60~GeV$), but its inefficiency was negligible below 56 GeV. As an example, measurements for 2018 and the DCA variant of this trigger are presented below.

$$\varepsilon = \varepsilon_{\mu 1} \varepsilon_{\mu 2} \times \varepsilon_{distance} \times \varepsilon_{p_T^{miss}}$$

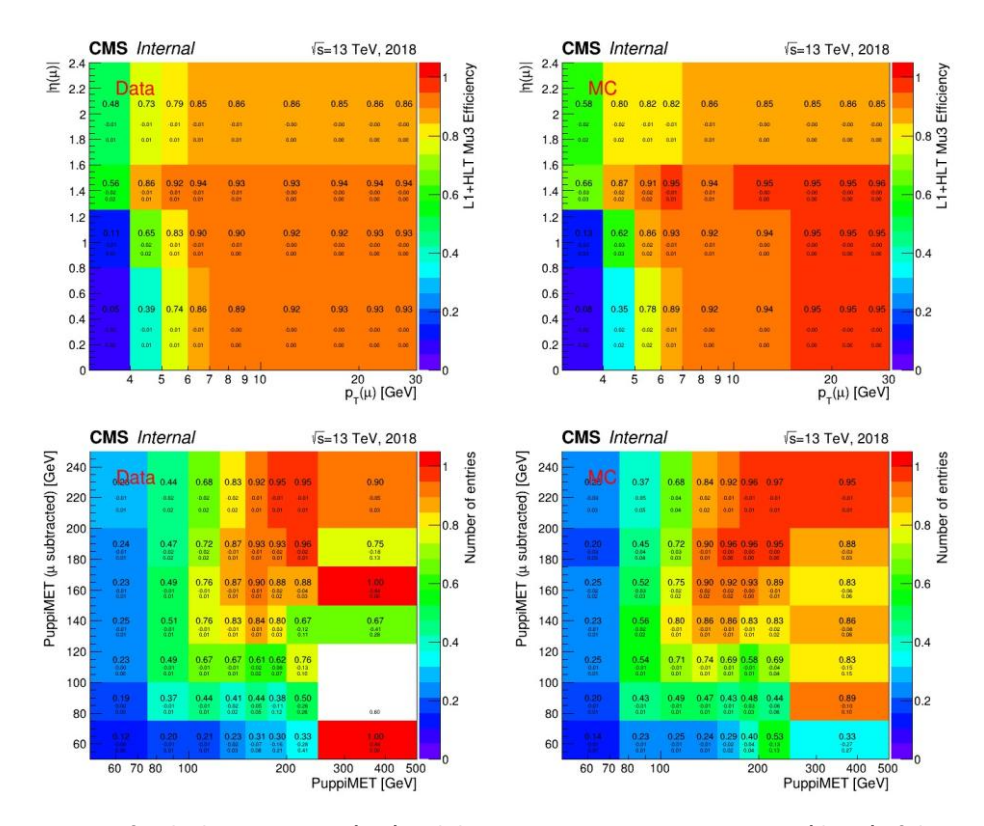


Figure 33: Measurements for the leptonic terms (top) and the transverse missing energy term (down) of the trigger efficiency for data on the left and for MC simulation on the right. The leptonic efficiencies are parametrized as a function of muon p_T and p_T^{miss} and p_T^{miss} , and both are measured with the tag & probe method on DY, ttbar, and DiBoson events for 2018 (59.3fb-1). The DCA contribution is measured separately and is estimated to be 96.2% for real data and 96.5% for simulation.

On the displaced regions, the plan is to use the same triggers to select events with displaced leptons, but this is not applicable in all cases. In HighMET regions, the triggers that are used (METNoMu) do not depend on the Primary Vertex, making them useful for displaced regions too. On the contrary, in LowMET using the same triggers to populate regions with displaced events is not always possible, so both LowMET regions have been dropped for 2016 and 2017, since a compatible trigger with the displaced regions wasn't an option. In 2018, the DCA trigger was active, with verified efficiency for long-lived particles.

In terms of Scale-Factors, the calculation was separated to two steps. The terms that depend on p_T^{miss} do not present dependency on the displacement, while the leptonic terms, in general, is expected to depend on the reconstruction efficiency of the muon track. Due to this, the LowMET trigger for 2018 is also parameterized in displacement too. SFs are derived as a function of displacement and measured on displaced J/ψ events that have been collected with orthogonal triggers based in p_T^{miss} , hadronic activity, and electrons, probing always the displaced muons inside jets. Other dependencies on the distance of closest approach (DCA) and/or the mass requirements are consistent with a SF=1. Figure 34 shows the difference in data and simulation efficiencies for the displacement part of the LowMET trigger.

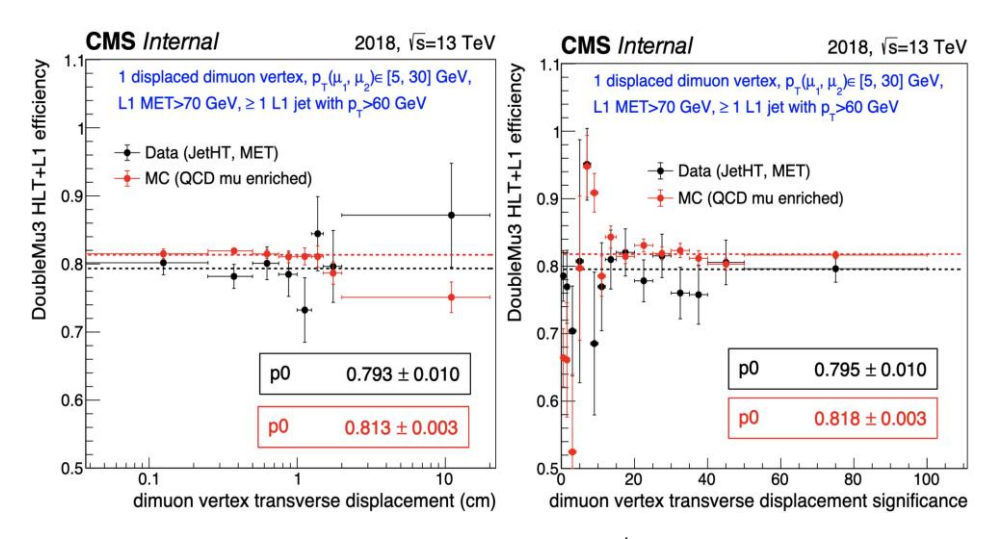


Figure 34: The efficiency for the leptonic part of the Double Muon plus p_T^{miss} trigger that is used for the "LowMET" region in 2018 parametrized in displacement of the muon vertex (left) and in the significance of the displacement (right)

16.2. Object Reconstruction

16.2.1. Primary and Secondary Vertices

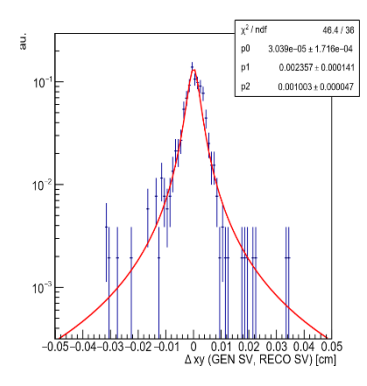
The analysis depends on identifying correctly the points within the detector where the decays have taken place. In the prompt regions, the identification of the lepton tracks from the signal relies only on the "Primary Vertex" (PV), which is the intersection of the tracks that are (usually) included in the most energetic jets of the event, and this vertex is located almost at the center of the x-y plane of the detector. This vertex is commonly thought as the position of the hard interaction of the event, however other softer interactions (Pile-Up) result to more than one "PV-like" vertices to be reconstructed in the event, making it non-trivial to correctly identify the original position of the hard process.

In CMS, the PV is reconstructed from tracks with the "deterministic annealing algorithm" that clusters tracks together, which originate from the same point, by minimizing a distortion function to conclude to the final number of clusters (final PVs). Finally, the vertices are fitted and updated by their associated tracks and are classified using the quadratic sum of the tracks' momenta. The PV is selected to be the most energetic vertex that lies within ± 24 cm in z-direction and up to 2 cm away from the beam collision point in the x-y plane.

Identifying the correct "Secondary Vertex" (SV) of an event, which is considered as the decay position of the signal neutralino to off-shell Z* and leptons, is crucial for displaced regions. The reconstruction of the extra vertices, which are related to the decay of the neutralino, follows a custom approach that depends on lepton tracks that are not consistent to the selected PV of the event.

The reconstruction of the candidate SVs relies on fitting a pair of lepton tracks to a common vertex without considering the PV for the fit. The selection includes Particle-Flow tracks of electrons and muons that are not consistent with the PV (large impact parameter). Pairs of such tracks are processed by a Kalman Vertex Fitter (the "Refitter Module") that updates the vertex

location as the tracks are appended to the fit in a "Kalman Filter" fashion¹⁵. Finally, the track parameters are refitted to the SV and a probability related to the fit is assigned. The result is then validated by requiring the output location of the SV to be within the Tracker of the CMS detector.



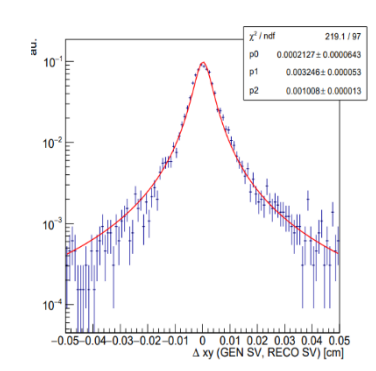


Figure 35: Left (Right) Secondary Vertex resolutions for Muons (Electrons), the x-axis is the distance between the simulated decay vertex and the reconstructed Secondary Vertex, for the signal dataset.

16.2.2. Prompt Electrons

This section presents the reconstruction and the selections of the analysis for electron candidates from the primary vertex (PV), also highlighting customizations to enhance the sensitivity at very low ΔM (mass splitting) points. This is succeeded by optimizing the selection of low-pT electrons and is crucial for probing compressed mass spectrum scenarios. This approach aims to maximize the efficiency and the signal acceptance while minimizing background events. Two distinct electron reconstruction algorithms, *GED* (*Global Event Description*) and *LowPt Electrons*, are merged to supply a wide range of transverse momentum (pT), targeting soft electron signals that are characteristic of low ΔM regions.

GED electrons are optimized for transverse momentum above 3 GeV and are tailored for scenarios where bremsstrahlung-induced energy losses significantly affect the track reconstruction. The reconstruction process uses the *Gaussian Sum Filter (GSF)* algorithm, which considers non-Gaussian effects caused by bremsstrahlung and provides accurate track fitting and energy measurement for electrons. Two seeding techniques are employed for GED electrons. Firstly, the ECAL-driven seeding, which is initiated by superclusters that are identified in the electromagnetic calorimeter (ECAL), is effective for high-pT tracks and isolated electrons typically arising from prompt processes. Secondly, the tracker-driven seeding, which is initiated using general Kalman Filter tracks and propagates towards the calorimeter, is designed for low-pT and non-isolated electrons that are more challenging to reconstruct. GED electrons can be upgraded to Particle Flow (PF) electrons when they meet additional selection requirements for matching calorimetric and tracking information, contributing to a comprehensive event reconstruction.

¹⁵ The Kalman Filter method relies to appending a new input to a collection of previously analyzed inputs, calculating gains, and updating the fitted quantities with each new iteration. Examples of inputs can be hits in a trajectory, or in this case, multiple tracks defining an intersection (the SV), with the parameters of the trajectory or the coordinates of the intersection to be the fit results respectively. An extensive example of a Kalman Filter and theory can be found in [31].

LowPt electrons address the reconstruction inefficiency for very low transverse momenta, critical for reconstructing the signal down to 1 GeV, and boosting the acceptance at very compressed scenarios. This reconstruction uses exclusively tracker-driven seeding that is more suitable for low-momentum tracks. It utilizes boosted decision tree (BDT) classifiers, a kinematic-agnostic classifier, which operates using general track properties independent of kinematic assumptions, and a kinematic-aware classifier, which leverages track momentum and positional correlations to enhance reconstruction accuracy. The identification of *LowPt electrons* employs the MVA ID (trained at 28-Nov-2020 by CMS), integrating a comprehensive set of features including tracking, calorimetric, and geometric information to distinguish electrons from background.

To prevent double counting of electrons reconstructed by both GED and LowPt algorithms, an overlap removal algorithm is implemented. Overlap is determined based on the spatial resolution threshold ($\Delta R < 0.05$). Above 3 GeV GED electrons are prioritized over LowPt electrons due to their superior accuracy in high-p_T regimes and the threshold is selected in such a way that the background rejection of the 2 collections is as smooth as possible transitioning from one to the next region.

One of the most important criteria that is applied on the selections is the threshold on the PF Isolation to reduce background from hadronic decays. Setting the ΔR threshold to 0.05 results in occurrences of leptons very close-by in the Signal Region and the Isolation sums are compromised with energy that comes from the close-by electron. In cases where the second electron does not pass the PF-ID, these sums need to be recalculated after removing its p_T component from the isolation sum, because the track and the CALO cluster primitives are included to the original isolation sum as PF hadrons and photons¹⁶.

Loose and Tight Selections

Electrons are categorized into 2 selections depending on further analysis requirements and how they will be used downstream to define the regions. Selection criteria involve factors such as geometry and momentum, where thresholds are at 1 GeV for LowPt and at 3 GeV for GED electrons, with $|\eta| < 2.5$. Impact parameter thresholds, transverse (dxy) and longitudinal (dz), are used to reduce contributions from non-prompt sources such as B-hadron decays. Corrected isolation sums are computed within a cone ($\Delta R < 0.3$), excluding electrons from nearby leptons as described above to reduce the hadronic background, and the thresholds are adapted to balance signal efficiency and background rejection. CMS Standard ID definitions, which follow CMS recommendations, are used for $p_T > 10$ GeV, while custom "Tight 90%" and "Loose 98%" MVA IDs are used below 10 GeV, optimizing the performance to maintain the efficiency relatively constant as merging the 2 collections of electrons.

 $^{^{16}\,}PF\,Abs\,Iso_{03} = \sum_{cone} p_T(h^{\pm/0}) + \sum_{cone} p_T(\gamma^0)$

| Criteria | | | | | Tight | |
|-----------------------|--------|---------------------|----------|--------------|---------------------|--------|
| Inl | | | < | < 2.5 | | |
| p⊤[GeV] | 1-5 | 5-10 | > 10 | 1-5 | 5-10 | > 10 |
| MVA ID | Cu | stom Loose 98% | WPL | Cu | stom Tight 90% | WP90 |
| no missing | | | | √ | | |
| pixel hits | | | | • | | |
| conversion veto | | | | \checkmark | | |
| PF Isocorr [GeV] | | < 10 | | | < 5 | |
| IP _{3D} [cm] | < 0.05 | < 0.05-0.0065(pt-5) | < 0.0175 | < 0.025 | < 0.025-0.003(pt-5) | < 0.01 |
| SIP _{3D} | < 5 | < 5-0.5(pt-5) | < 2.5 | < 2.5 | < 2.5-0.1(pt-5) | < 2 |
| d _{xy} [cm] | < 0.05 | | | | | |
| d_z [cm] | | | < | < 0.1 | | |
| DeepJet veto | | - | | | < 0.45 | |

Table 7: Loose and Tight requirements definitions for electrons.

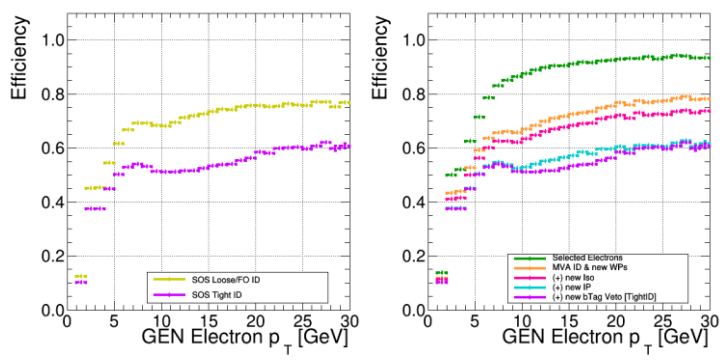


Figure 36: Left: Comparison of the reconstruction efficiency of the signal for Loose (in Yellow) and Tight (in Purple) selections for 2018 dataset. Right: Breakdown of the efficiency drops for the Tight selection starting from the merged collection (in Green), the MVA-ID (in Orange), the Isolation (in Pink), the Impact Parameter cuts (in Blue), and the DeepJet bTag-veto (in Purple). All other years, 2016 and 2017, have been tested and illustrate the same performance as for 2018.

Background includes electrons from photon conversions, jets misidentified as electrons, and electrons from heavy-flavor decays. Mitigation strategies involve using advanced isolation definitions, tailored to suppress fake electrons, and applying the DeepJet b-tagger to identify and reject electrons originating from B-hadron decays.

16.2.3. Displaced Electron Pairs

The pairs of Low-Pt electrons that result from the Refitter Module selected keeping only those that illustrate good compatibility of the electron pair to the formed SV. The selection is made by imposing cuts to the Kalman fit probability and the minimum distance of the 2 tracks in each pair (DCA, distance of closest approach). In the displaced electron regions, it is decided to include only the Low-Pt reconstruction, since studies have shown that its efficiency is beneficial compared to Particle-Flow electrons. Additionally, any SV with transverse distance from PV (L_{xy}) less than 0.05 cm or including an electron track with impact parameter to the PV (IP_{3D}) less than 0.0175 cm, it is removed from the selection. This is necessary to maintain the orthogonality between the prompt and displaced regions, making it possible to combine the results in a trivial manner.

Table 8: Loose and Tight definitions for displaced pair of electrons.

| | _ | | |
|--------------------------------|--------|-------------------------------------|--------------|
| Criteria | | | Tight |
| Inl | | < 2.5 | |
| p _T [GeV] | 1-5 | 5-10 | 10-30 |
| IP _{3D} [cm] | > 0.05 | > 0.05 – 0.0065 (p _T -5) | > 0.0175 |
| $\sigma_{IP_{3D}}$ | > 5 | $> 5 - 0.5 (p_T - 5)$ | > 2.5 |
| Displaced ID | - | Custo | om 95% WP |
| CHG | | | |
| PF Iso ^{abs} [GeV] | < 50 | | < 3 |
| L_{xy} [cm] | | > 0.05 | |
| · · | | > 0.03 | |
| Charge OS | | ✓ | |
| DCA _{3D} [cm] | | < 0.2 | |
| Fit prob. | | > 0.1 | |
| B-vertex veto | - | | \checkmark |

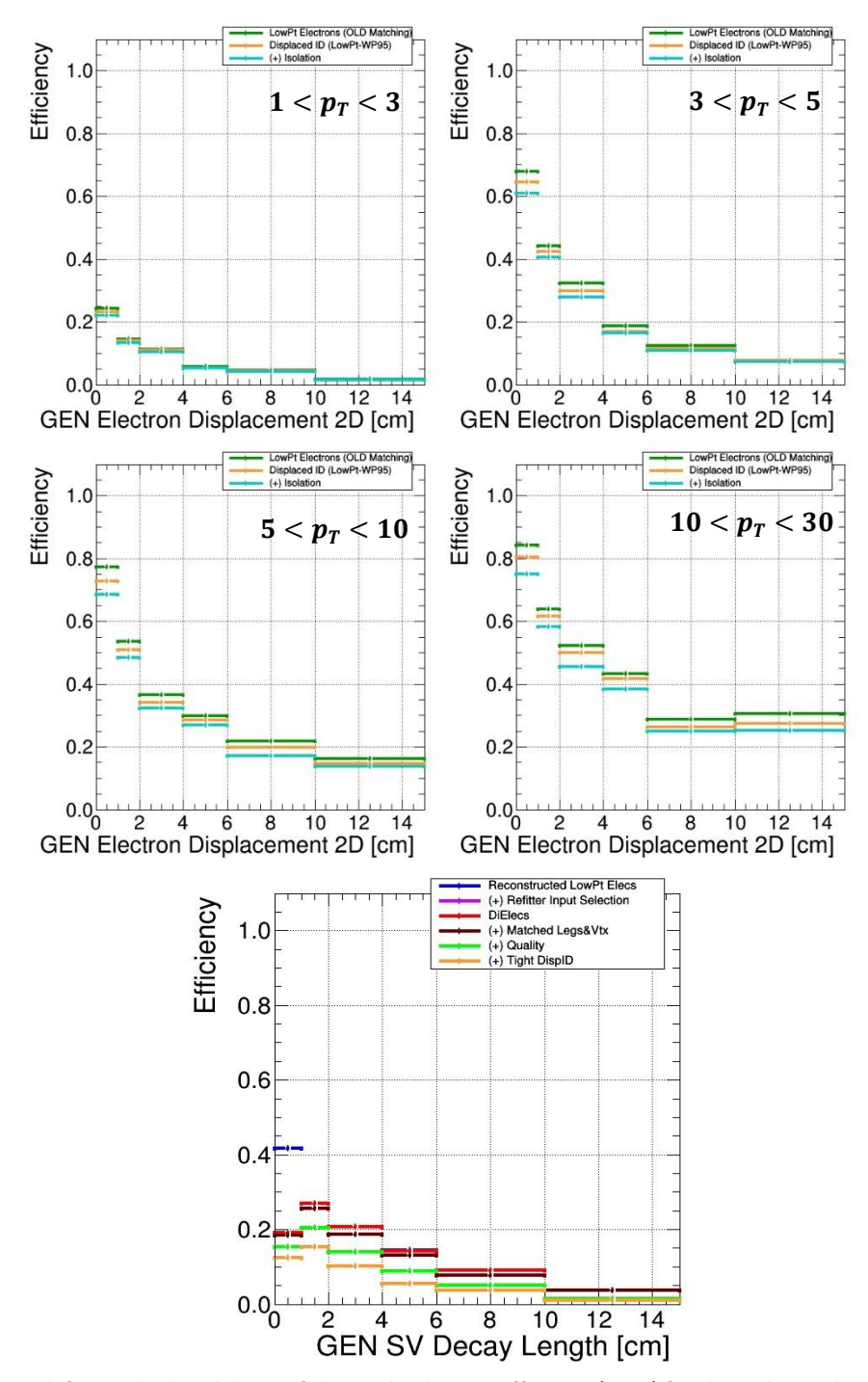


Figure 37: Top: From left to right, breakdown of the single electron efficiency (2018) for the Tight Displaced selection in the ranges 1 < p_T < 3 GeV, 3 < p_T < 5 GeV, 5 < p_T < 10 GeV, and 10 < p_T < 30 GeV, starting from the selected LowPt electron tracks (in Green), the Displaced-ID (in Orange), and the Isolation cuts (in Light Blue). Bottom: A p_T inclusive breakdown of the Displaced Dielectron efficiency starting from the selected Electrons (in Dark Blue), the Input to the Refitter (in Pink), the Output of the Refitter (in Red), the effect of the Δ R-Matching to identify the signal (in Dark Red), the Quality selection (in Light Green), and the impact of applying the Displaced ID on both electron tracks (in Orange).

Table 8 shows the list of selection criteria applied on reconstructed candidates to be identified as Tight Dielectrons. The selections include the Displaced ID, which is a modified 95% Working-Point (WP) version based on the same Low-Pt BDT that was provided by CMS for Run2 and was used in the regions with prompt electrons. The isolation requirement uses a different calculation

of the Particle-Flow sum, using only charged components, since it was found that the nominal PF Isolation performs worse for $p_T > 10$ GeV. The reconstruction of the displaced electrons from signal for these p_T is already weak as can been seen in the efficiency plots in Figure 37.

Isolation and Displaced ID for the displaced regions are tuned to maintain signal efficiency across the p_T range as constant as possible, with a uniform cumulative impact of around 10% on top of the LowPt reconstruction.

16.2.4. Prompt Muons

The Muon candidates of the analysis rely on the standard CMS reconstruction techniques and some predefined identification criteria that are provided by CMS.

The candidates in the analysis originate from two categories, tracker-only and tracker-plusmuon-system, but they are not treated differently. Candidates that are not associated with any tracker track are dropped in this analysis, because compared to the other categories they have relatively poor momentum resolution at low p_T . On the contrary, Tracker tracks that are reconstructed, using an inside-out approach, result in selections with better low p_T resolution. Since only a single matched muon station is required to qualify as a tracker muon, the tracker reconstruction introduces a challenge to separate muon tracks from other charged tracks, like pions, that hardly reach the muon system.

Muon candidates should satisfy the Particle-Flow ID in three ways; tracker-plus-muon-system candidates that have a relative isolation less than 0.1, track-only candidates with a minimum number of track segments and a good compatibility between the muon segment and calorimeter deposit regardless of the isolation, or candidates with momentum significantly larger than the associated energy deposit in the calorimeter.

Loose and Tight Selections

As for electrons, for Muons we define 2 selections that are used in the analysis in a different manner, the Tight selection that is used to define the Signal Regions of the analysis, and the Loose selection that is used for the background estimation in the Application Regions. The loose and soft CMS IDs are applied on all muons, while muons are also required to be PF candidates implicitly by the CMS loose ID too. The soft ID imposes requirements on the number of Tracker and Pixel layers with hits, track purity, and on the impact parameters of the tracks (d_{xy} and d_z).

Additionally, to these Muon Group requirements, customized selection criteria based on isolation, impact parameters, and a jet association veto are applied, which further optimize the selections for their use in the Signal and Application Regions respectively. The key target of this customization is to reject analysis specific background like muons that may be included in jets from B-hadrons. Also, by optimizing the cut on the DeepJet score [47] for the b-tagger eliminates (as much as possible) the flavor dependency of the fake rate measurements that are used in the background estimation on data events in the Application Region.

< 2.4 p_T [GeV] > 3.5 **POG Loose ID** \checkmark POG Soft ID √ PF Iso_{cone03} [GeV] < 5 < 1.0 < 0.5 $PF Iso^{rel}_{cone03}$ IP_{3D} [cm] < 0.0175 < 0.01 SIP_{3D} < 2.5 < 2.0 d_{xy} [cm] < 0.05 < 0.1 d_z [cm] DeepJet veto < 0.15

Table 9: Loose and Tight requirements definitions for muons.

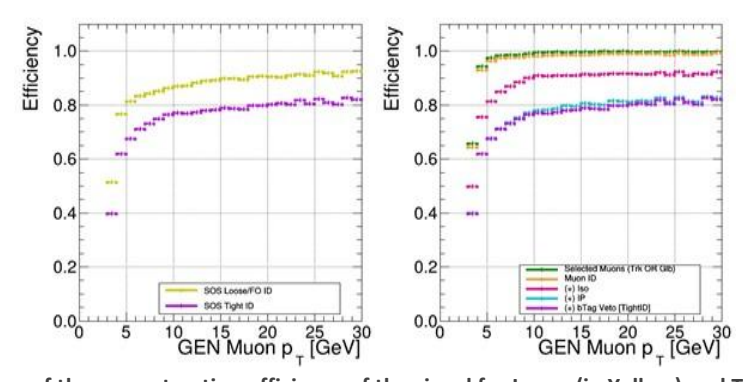


Figure 38: Left: Comparison of the reconstruction efficiency of the signal for Loose (in Yellow) and Tight (in Purple) selections for 2018 dataset. Right: Breakdown of the efficiency drops for the Tight selection starting from the merged collection (in Green), the CMS Loose Muon-ID (in Orange), the Isolation (in Pink), the Impact Parameter cuts (in Blue), and the DeepJet bTagveto (in Purple). All other years, 2016 and 2017, have been tested and illustrate the same performance as for 2018.

Backgrounds include muons from B-hadron decays and misidentified jets, like in the electron case. Similar strategies are used to mitigate these backgrounds, involving isolation to suppress fake muons, and the DeepJet b-tagger to reject muons originating from B-hadron decays.

16.2.5. Displaced Muon Pairs

The resulting pairs of muons that result from the Refitter Module are cleaned and a subset of these is selected keeping only the pairs that show good compatibility of the refitted muon tracks to the formed SV. This selection is made by imposing cuts to the Kalman fit probability and the minimum distance of the 2 tracks in each pair (DCA, distance of closest approach). Additionally, any SV with transverse distance from PV (L_{xy}) less than 0.05 cm or including a muon track with impact parameter to the PV (IP_{3D}) less than 0.0175 cm, is removed from the selection. This is necessary to maintain the orthogonality between the prompt and the displaced regions, making it possible to combine the results in a trivial manner.

Table 10: Loose and Tight definitions for displaced pair of muons.

| Criteria | Loose | Tight |
|--------------------------------|---|---|
| Inl | | < 2.4 |
| p⊤ [GeV] | | > 3.0 |
| IP₃D [cm] | > | 0.0175 |
| Displaced ID | PF-ID and (Global or Tracker) | PF-ID and (Global or Tracker) highPurity and TMOneStation |
| PF Iso ^{abs} [GeV] | < 50 | < 10 |
| PF Iso _{cone03} | - | < 1 |
| L _{xy} [cm] | | > 0.05 |
| Charge OS | | ✓ |
| DCA _{3D} [cm] | | < 0.2 |
| Fit prob. | | > 0.1 |
| B-vertex veto | - | ✓ |

To select the signal events and to separate some of the background processes in different categories (from PU and from Jets), this analysis relies on matching simulated leptons (muons/electrons) with reconstructed leptons using a ΔR cone of 0.3. In this calculation, the reference point of the cone is the PV, but in decays of long-lived particles like the Neutralino, the appropriate reference for the cone should be the SV, because for simulated events the momentum vector is calculated with respect to the decay position. This fact is not causing any problem to the displaced muons, but in the case of displaced electrons it leads to inefficiency reconstructing the signal and a subsequent worsening in the limits. So, a relaxed version of ΔR -Matching is used.

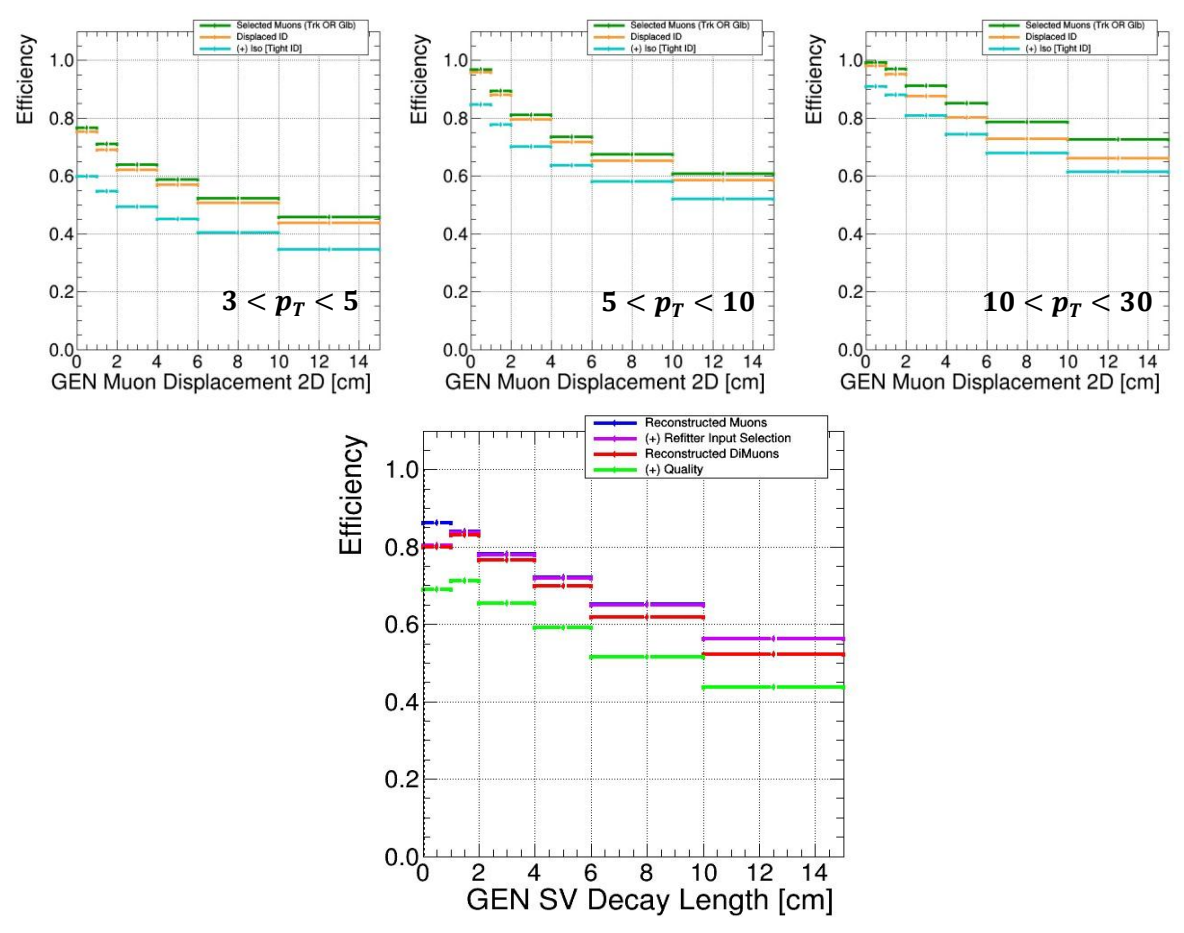


Figure 39: Top: From left to right, breakdown of the single muon efficiency (2018) for the Tight Displaced selection in the ranges $3 < p_T < 5$ GeV, $5 < p_T < 10$ GeV, and $10 < p_T < 30$ GeV, starting from the selected muon tracks (in Green), the Displaced-ID (in Orange), and the Isolation cuts (in Light Blue). Bottom: A p_T inclusive breakdown of the Displaced Dimuon efficiency starting from the selected Muons (in Dark Blue), the Input to the Refitter (in Pink), the Output of the Refitter (in Red), and the Quality selection (in Light Green).

Table 10 shows the list of selection criteria applied on reconstructed dimuon candidates to be identified as Tight Dimuons. The selections include the Displaced ID, which is an adjusted version of the CMS Soft-ID [46] that is used in the prompt muon analysis. This version of ID does not apply impact parameter cuts or requirements on the number of pixel and tracker hits, preserving efficiency for larger displacements.

The isolation criteria use standard PF variables, still effective on rejecting background candidates from B-decays even at large displacements. The thresholds are slightly relaxed compared to tight prompt selection.

16.2.6. Scale Factors

Selection Efficiencies may differ between the simulation and real data because of several components and algorithms that are involved in the tables that have been shown previously about the requirements. For each object that is used in the analysis, the selection efficiency is split into terms, which are calculated separately. Eventually, the Scale Factors that were applied to the simulated events are defined as ratios of data-to-simulation efficiencies.

The Scale Factors are measured in specially designed regions with the Tag & Probe method, an approach that identifies the lepton that is triggering the event ("tags it"), and it measures the efficiency ("probing") using other high-quality leptons. Once the appropriate collection of leptons (or Dileptons) is selected, the sample is divided in 2 sets for the denominator and the numerator by applying the appropriate selection cuts that define the efficiency term that to be measured. These sets of probe objects are named "Passing" and "Failing".

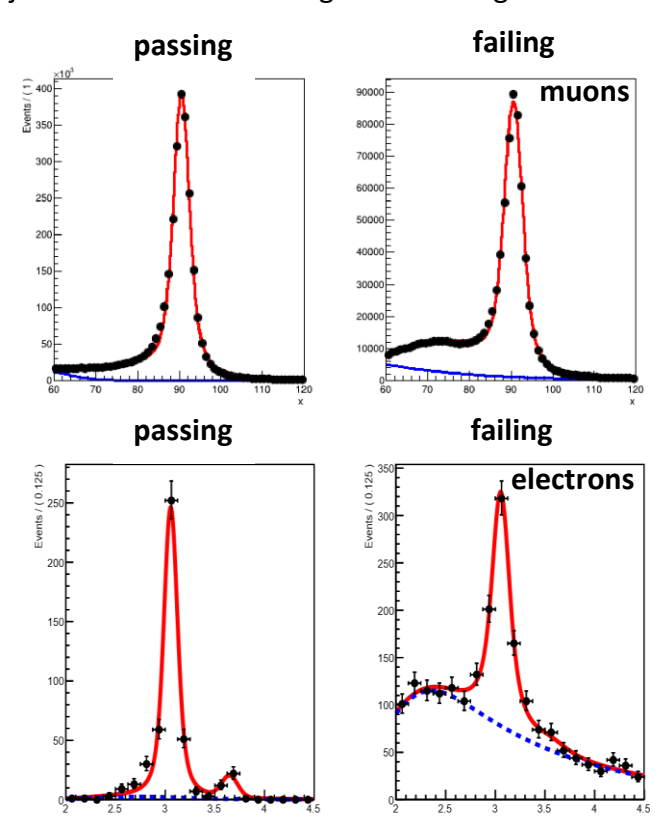


Figure 40: Passing and Failing sets used to measuring data efficiencies for muons and electrons. Such selections are described in next sections, corresponding to the terms $\varepsilon(\mu; TightID|LooseID)$ and $\varepsilon(e; RECO)$ for the prompt analysis in the ranges $20 < p_T < 30$ and $1.2 < |\eta| < 2.4$ for the muons and in the range $2 < p_T < 5$ for GED electrons. The selections of tag&probe leptons peak around the mass of the Z boson (91.2 GeV) and J/ Ψ resonant (3.1 GeV), while by fitting the invariant mass in regions of p_T - $|\eta|$ ranges, the signal is extracted and is parametrized to perform the measurement.

The invariant mass distribution calculated using the triggering lepton and one probe lepton, for Passing and Failing sets of probes, is fitted to the resonance mass that has been chosen for the measurements (e.g. Z or J/ Ψ), and the signal for the measurement is extracted. The background is subtracted by including in the fit a "CMS Shape", which involves a convolution of an error function with a falling exponential, or alternatively using simply falling exponentials (helping to evaluate systematic uncertainties for the method). Eventually, efficiencies are calculated by the following ratio for "passing" and "failing" signal yields.

$$\varepsilon = \frac{passing}{passing + failing}$$

Prompt Muons

 $\varepsilon(\mu) = \varepsilon(\mu; TrackRECO) \times \varepsilon(\mu; Muon|TrackRECO) \times \varepsilon(\mu; LooseID|Muon) \times \varepsilon(\mu; TightID|LooseID)$

The efficiency for Muons can be broken down into four terms, which are evaluated separately either exclusively measured or using prior CMS results. The first three terms, efficiencies and Scale-Factors, are centrally provided by CMS (from track reconstruction to the Loose ID). The last term, specific to the analysis, is exclusively measured using events from Z decays to muons. This measurement is performed on events selected with the HLT trigger *IsoMu24* and subsequently employing the Tag & Probe method within the region as described in Table 11, targeting events from Z decays to muons.

The fitting procedure uses a signal shape composed of two Voigtian functions and a custom function called "CMS Shape" as background. For the final yield, the fitted background is subtracted. This procedure is repeated over the entire selected parameter space for the muons, resulting in a 2D parametrization (p_T - η) of the efficiency. Finally, the information regarding the bump on the left of the Z mass peak, whether this originates from signal or background muons, is obtained by examining the DY MC and fitting it solely with the signal pdf while setting the background to zero.

Table 11: Tag and Probe selection of muons for measuring the term $\varepsilon(\mu; TightID|LooseID)$.

*Matched SIM refers to ΔR -matching between simulated muons, reconstructed or generated.

| Criteria | Tag | Probe |
|--------------|-------------|----------------------|
| Matched TRG | ✓ | - |
| Matched SIM* | | \checkmark |
| η | < | 2.4 |
| p_T [GeV] | > 29 | > 3 |
| ID | POG TightID | POG LooseID |
| os | | \checkmark |
| Z mass [GeV] | 60 < m | $t_{\ell\ell} < 120$ |

Alternative fits are performed using Gaussian and falling Exponential functions, as signal and background respectively, to evaluate the systematic uncertainty that is introduced due to the choice of specific functions. Systematic and statistical errors are incorporated in the results that are presented below, and both uncertainties are propagated to the analysis when this correction is applied to the simulation.

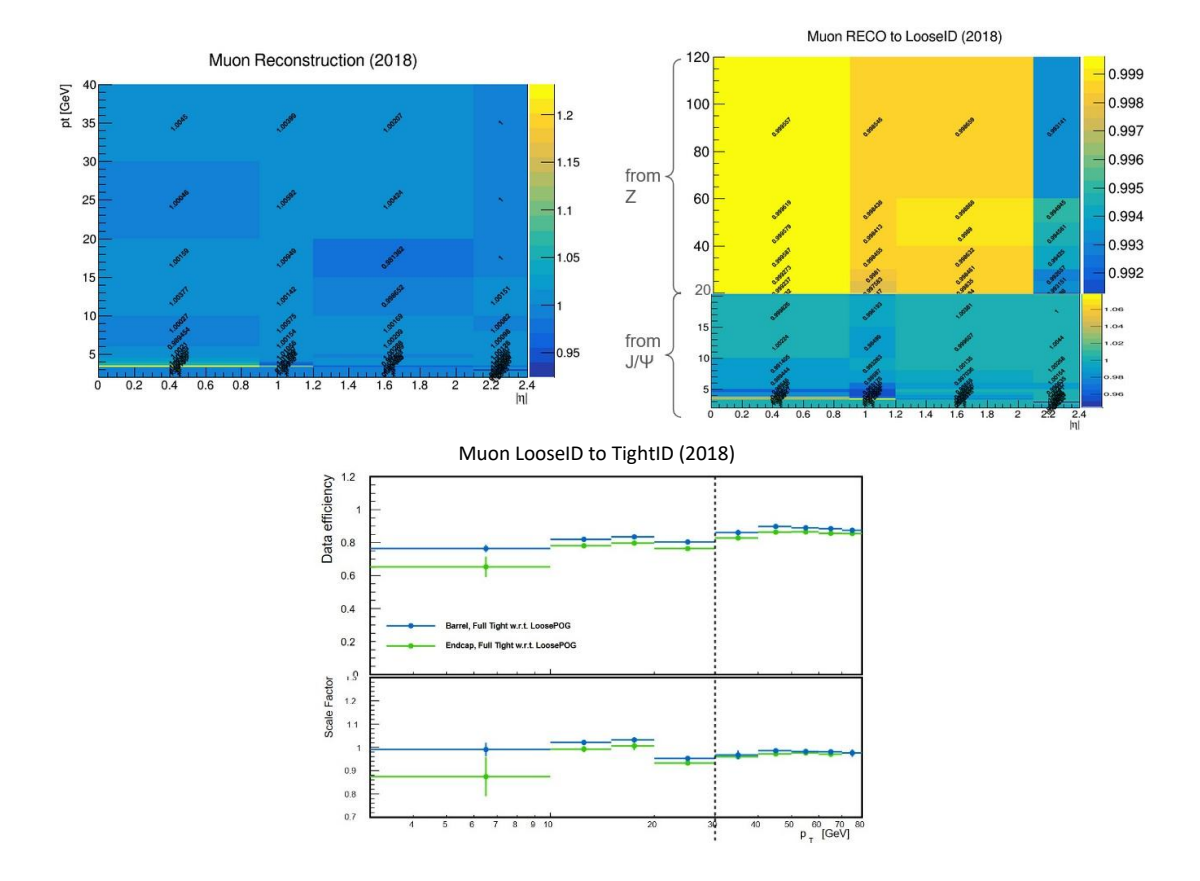


Figure 41: Muon corrections (2018 dataset) that are applied on the simulated predictions. They correspond to the last 3 efficiency terms and are based on Z and J/Ψ measurement selections. The first term is recommended by CMS to be taken as 1, as there is a minor difference between simulation and data efficiency.

Prompt Electrons

$$\varepsilon(e) = \varepsilon_1(e; RECO) \times \varepsilon_2(e; TightWP \& Iso|RECO) \times \varepsilon_3(e; TightID|TightWP \& Iso)$$

The efficiency for Electrons can be split into three terms, the reconstruction efficiency for the track, the efficiency of a reconstructed track to pass the selected Tight WP requirements (MVA id, conversion veto, and missing pixel hits) together with Isolation, and the efficiency to also satisfy impact parameter and B veto cuts.

Table 12: Tag and Probe selection of tracks for measuring the term $\varepsilon(e;RECO)$ with $B\to K^\pm J/\Psi$ events, for GED and LowPt electrons with $p_T<10$ GeV.

| Criteria | Tag | Probe | Kaon |
|-----------------|----------------------|-------|-------|
| ΔR all 3 | > 0.0 |)3 | |
| ΔR probe | - | | > 0.1 |
| p_T [GeV] | > 3 | - | > 5 |
| GED electron ID | mvaFall17V2nolsoWP80 | - | - |
| os | ✓ | | - |

Reconstruction efficiencies are measured with events from Z decays and scale factors (SF) are provided for p_T down to 10 GeV. Therefore, another technique based on events from $B \to K^\pm J/\psi$ decays is designed to measure SF for p_T below 10 GeV and the LowPt electron

reconstruction. For this purpose, events are used from the SingleLepton triggered data streams, together with private simulation samples that have been produced based on a configuration for $R_{K(*)}$ measurements. Because LowPt electrons are track-seeded, the general track collection is used for Probe candidates, and GED electrons that pass the Tight MVA ID are used as Tag to make the selection as pure as possible. Also, a third track, which makes the invariant mass consistent with the B, results to even better purity of the measurement sample and helps reducing the background. The requirements for the $B \to K^\pm J/\psi$ selection are presented in Table 12 and the results are presented in Figure 42. Scale factors are parametrized in p_T and measured using background subtraction with fits to the J/ψ mass, using for the signal a combination of Voigtian profile (J/ψ) , a Gaussian peak $(\psi(2S))$, and a CMS Shape background. Alternative fits are performed using double-Gaussian signals and exponential or polynomial background shapes to estimate the systematics that are introduced by the choice of the fitting functions.

The remaining terms, $\varepsilon_2(e; TightWP \& Iso|RECO)$ and $\varepsilon_3(e; TightID|TightWP \& Iso)$, are measured using a combination of Z decays and J/ψ within Pile-up (PU) decays. For Drell-Yan events, $Z \to ee$, the dataset for the measurements is collected with SingleElectron trigger (e.g., HLT trigger Ele32_WPTight_Gsf for 2018). On the other hand, for $J/\psi \to ee$ events, the requirement for measuring SFs down to 1 GeV demands soft J/ψ candidates, but electrons from such soft decays cannot fire efficiently SingleElectron triggers. As a result, the measurement is performed with soft J/ψ candidates found within PU interactions (away from the PV), in events that are triggered from a third energetic lepton (e.g., HLT triggers Ele32_WPTight_Gsf or IsoMu24 for 2018). The measurement of these terms is further split in three p_T ranges of 1-5 GeV, 5-10 GeV, and 10-30 GeV, since these ranges require different treatment.

Table 13: Tag and Probe selection of GED and LowPt electrons for measuring the term $\varepsilon_2(e; TightWP + Iso|RECO)$ for $p_T > 10$ GeV and the term $\varepsilon_3(e; TightID|RECO + TightWP + Iso)$ for $5 < p_T < 10$ and $p_T > 10$ GeV, using $Z \rightarrow ee$ events.

| Criteria | Tag | Probe |
|--------------|-----------------|-----------------|
| Matched TRG | ✓ | - |
| ΔR | > 0. | 3 |
| η | > 2 | .5 |
| p_T [GeV] | > 34 | - |
| ID | Cut based Tight | Denominator |
| os | , | / |
| Z mass [GeV] | $60 < m_{\ell}$ | $_{\ell} < 140$ |

Measurements in the $Z \to ee$ region are used to extract Scale Factors mainly for $p_T > 10$ GeV, where the off-shell Z is still reachable to exploit. The background subtraction is achieved by fitting the di-electron (Tag & Probe) mass with a double Voigtian, while the background is still handled with the "CMS Shape". On the other hand, $j/\psi \to ee$ decays from PU events are used in cases where the Drell-Yan off-shell decay products are not efficiently reachable with the available datasets from the experiment. There, the background subtraction is achieved by fitting the Tag & Probe mass distribution with a Gaussian signal and modeling the background simply using an

exponential. Finally, alternative fits are again performed in these cases too, using simple polynomials instead of exponential background, to estimate the uncertainties that the modeling functions are introducing to the measurements. The selections, which are applied on the datasets for performing these $Z \to ee$ and $j/\psi \to ee$ measurements, are presented in Table 13 and Table 14 respectively.

Table 14: Tag and Probe selection of GED (LowPt) electrons for measuring the term $\varepsilon_2(e; TightWP + Iso|RECO)$ for $p_T > 10$ GeV, for $5 < p_T < 10$, and $2(1) < p_T < 5$ GeV, using $j/\psi \rightarrow ee$ events within PU.

| Criteria | high- $p_T e(\mu)$ | Tag | Probe |
|---------------------|--------------------|----------------------|------------|
| Matched TRG | ✓ | - | - |
| ΔR | - | > 0.3 | |
| η | < 2.5 (2.4) | > 2.5 | |
| p_T [GeV] | > 34 (25) | > 3 | - |
| ID | Tight | Analysis Tight D | enominator |
| os | - | ✓ | |
| j/ψ mass [GeV] | - | $2.4 < m_{\ell\ell}$ | < 3.8 |
| $\Delta dz $ [cm] | - | < 0.1 | |
| $ dz_{PV} $ [cm] | - | > 0.1 | |

Measuring the remaining efficiency terms is divided as follows, by applying the above-mentioned methodologies. Firstly, for both terms ε_2 and ε_3 for $p_T > 10$ GeV, the measurements are based on $Z \to ee$ events. For ε_2 and p_T (1,5) or p_T (5,10) GeV, the efficiency is calculated using $J/\psi \to ee$ events from PU because the background at low- p_T is substantial and the off-shell Drell-Yan signal is weak. For the efficiency ε_3 and $p_T < 10$ GeV, $Z \to ee$ events are used again, because when focusing on the region where we require prompt impact-parameter cuts, $\varepsilon_3(e; TightID|TightWP \& Iso)$, the population of soft J/ψ is limited since some of them are produced in displaced B decays ($c\tau \approx 0.5mm$). This, however, is the case only for the range (5,10) GeV of the measurement of ε_3 , while below 5 and down to 1 GeV neither population of these measurement regions is sufficient for a robust calculation, and a SF=1 with 20% systematic uncertainty is imposed. The decision is based on a good agreement between data and simulation for the impact-parameter variables of J/ψ events from PU, according to a study that was performed in that region [36].

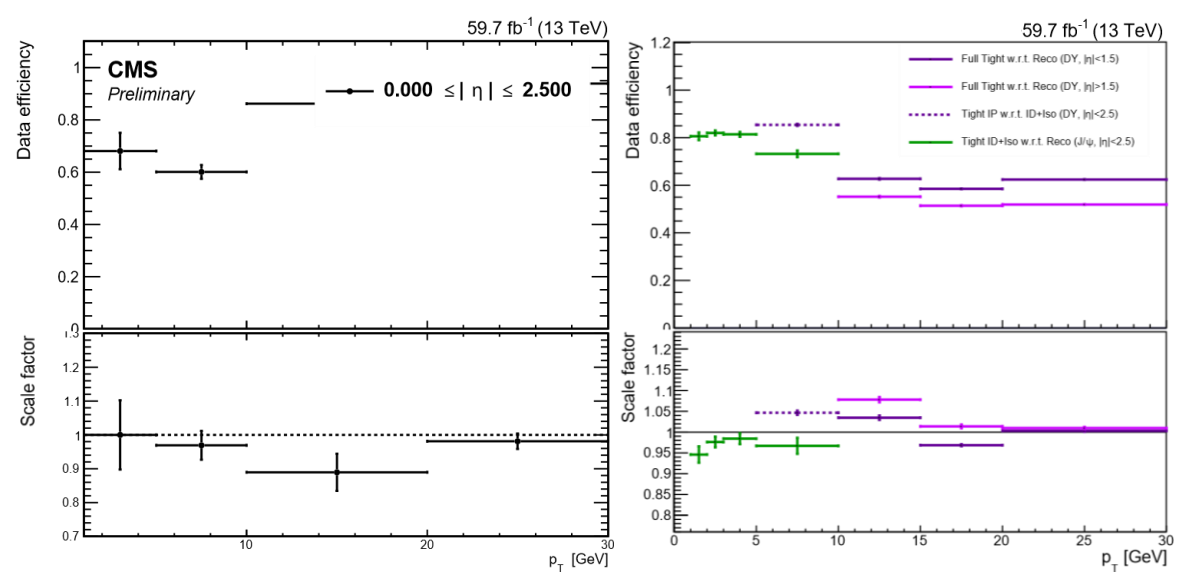


Figure 42: Results of custom measurements for the electron corrections (2018) that are applied on the simulated predictions. (Left) Data efficiency and Scale Factors for the LowPt reconstruction for the term $\varepsilon_1(e;RECO)$ using $B\to K^\pm J/\psi$ events. (Right) Data efficiency and Scale Factors for the LowPt reconstruction for the terms $\varepsilon_2(e;TighWP+Iso|RECO)$ and $\varepsilon_3(e;TightID|RECO+TightWP+Iso)$ using Z and J/Ψ events.

Displaced Di-Muons

$$\varepsilon(\mu\mu) = \varepsilon_1(SV, \mu \text{ track}; RECO) \times \varepsilon(\mu_1; Tight DispID|RECO) \times \varepsilon(\mu_2; Tight DispID|RECO)$$

The efficiency of displaced dimuon objects to pass the tight displaced ID selection is corrected (in simulation) to better match what is observed in data. To facilitate the measurement the total efficiency is split into three subcomponents, one term about reconstructing displaced tracks together with fitting them into a secondary vertex, and two more identical terms, one for each track to be selected as a Tight Displaced Muon by the Displaced ID as described in Table 10.

The first term (ε_1) is obtained by measuring displaced $K^0_S \to \pi^+\pi^-$ decays in Z+Jets events, which is similar to the signal topology of our displaced signal (a neutral particle that decays into 2 oppositely charged tracks within a few cm). The measurement is carried out at events selected with 2 muons and without b-Jets, using as a vertex fitter algorithm a custom replica of the V⁰-vertex fitter algorithm that is used for the reconstruction. Finally, data and simulation yields are compared per displacement bin (as can be seen in the results in Figure 43) after the background has been subtracted using fits with double gaussian for the signal and modeling the background with a simple linear polynomial.

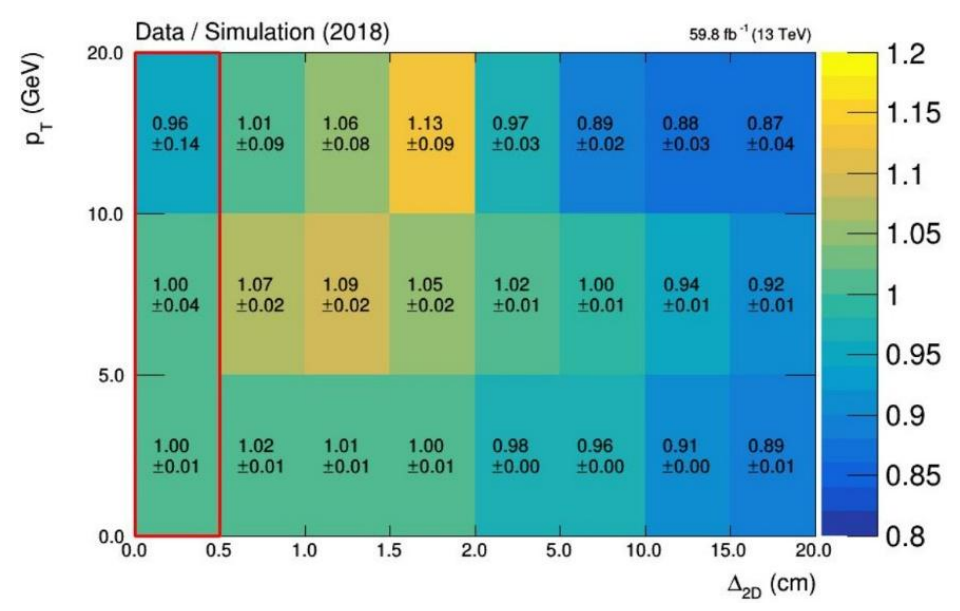


Figure 43: Results for the reconstruction of a displaced SV from tracks that correspond to the $K^0_S \to \pi^+\pi^-$ decays (2018 dataset). These corrections are applied on the simulated events to account for inefficiencies that are introduced in the analysis because of the Refitter. They correspond to the term $\varepsilon_1(SV,\mu\,TRACK;RECO)$. The background subtraction is based on fits to the K^0_S mass, 497.6 MeV, per Δ_{2D} bin. The yields of the first bin (enclosed in red) are inclusively normalized to account for effects in the measurement that are not related to the systematic difference in the vertexing efficiency due to the V⁰-fitter, but rather due to inconsistency of the modeling between K^0_S and Λ^0 in the simulation.

Two more terms are required to complete the measurement for the displaced selection of muons; each one compensates for one muon associated with the tracks that formed the SV in the first term. These terms are split in the same way, as was the case in the prompt muon selection. The first 2 terms correspond to forming muons from tracks and passing the Loose ID of CMS, like before, since they are not dependent on impact parameter cuts and are identical with the prompt results.

$$\varepsilon(\mu) = \varepsilon(\mu; Muon|TrackRECO) \times \varepsilon(\mu; LooseID|Muon) \times \varepsilon(\mu; Tight DispID|LooseID)$$

The Displaced Muon ID is mostly related to the quality requirements of the reconstructed tracks and the isolation, but not to the displacement. As a result, $Z \to \mu\mu$ events are used for the term $\varepsilon(\mu; Tight\ DisplD|LooselD)$ as in the prompt measurement, even though these events do not offer a handle to displaced muons.

All quality requirements that are related to the reconstruction are already accounted in the first term of the efficiency ε_1 , while for the last term we consider muons with their track already included in the Refitter to create the SV, so the displacement is accounted and parametrized rigorously. Additionally, to evaluate the systematic uncertainty that is introduced by this approach, a study on the remaining dependence of the Tight Displaced selection on the displacement has been carried out, which suggested an additional 5% (10%) flat uncertainty for $p_T < 10$ GeV ($p_T > 10$ GeV).

The corrections and the efficiency of the Displaced Muon ID, including the isolation, is measured following the same approach as for the prompt muon measurement, with the same tag & probe

selections (Table 11) and the same choice of modeling for extracting the signal (2 Voigtian functions) and the background (CMS Shape) using a simultaneous fit of tag-and-probe sets of muons. In a similar manner, to estimate the systematic bias because of the choice of functions, we also performed the measurement with alternative signal and background modeling to conclude to the appropriate systematic uncertainty. Results are presented in Figure 44.

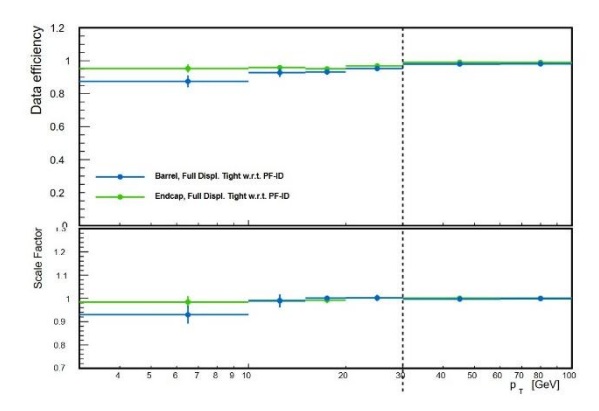


Figure 44: Muon corrections (2018 dataset) that are applied on the simulated predictions for the displaced selection. These correspond to the last term in the single muon efficiencies, are based on $Z \to \mu\mu$ events, and are applied per muon.

Displaced Di-Electrons

Since no convenient Standard Model decay to a displaced electron pair exists, this calibration uses radiative $\gamma \to ee$ conversions in the beampipe and tracker material, in events from $Z \to \ell\ell + \gamma$. The signal for the measurement is events from "external conversions" (a final state photon that travels a macroscopic distance before converting to electrons in the detector material), while the Measurement Region (MR) also includes "internal conversions" (electron pairs in the primary interaction originating from a virtual photon $\gamma^* \to ee$ that leads to a prompt 4ℓ final state) that needs to be subtracted.

The method to extract the corrections for the displaced electrons follows a different approach. Dedicated Control Regions are used to estimate the corrections to the simulation prediction in the MR with a transfer factor ($f_{\text{int/ext conv}}$), one for Internal and one for external conversions.

$$correction = \frac{data^{\text{MR}} - f_{\text{internal conv}} * sim_{\text{internal conv}}^{\text{MR}}}{f_{\text{external conv}} * sim_{\text{external conv}}^{\text{MR}}}$$

The 4-lepton mass peaks sharply at that of Z, providing an excellent handle to reject potential background. With a pure selection in the MR, the ratio of data to simulation yields results to the required correction, which can be parametrized using various properties of the electron pair. (e.g. p_T , displacement, ...) Two important factors must be tackled: background processes and shortcomings of the simulation unrelated to the di-electron reconstruction efficiency (e.g. the quality of the simulation of the detector material). Internal conversion events is background that can be mitigated using mass cuts and by requiring significant displacement of the conversion candidate pair.

The selection of events is based on Single Lepton Triggers (HLT triggers IsoMu27 and Ele35 for 2018) with well separated leptons for prompt and displaced pairs, which is ensured using a ΔR cut in the case of the 4-electron final state. The Control Regions are defined to be orthogonal with the MR by inverting the selection on the significance of the transverse displacement (σL_{xy}), while for the Internal Conversions the CR selection modifies the requirements of the mass too. The selections for the MR and the CRs are summarized in Table 15 and results for the 2018 dataset are presented in Figure 45. The results, which are calculated according to the equation above, are parametrized in displacement only due to limited data statistics in the MR.

Table 15: Selections for Measurement and Control Regions that are used to calculate the corrections to be applied on the displaced di-electrons and the transfer factors that are necessary for subtracting the background, using $Z \to \ell\ell + \gamma$ events and displaced electrons from γ conversions.

| • | | | |
|---------------------------------|--|-----------------|-------------|
| Criteria | $Z \rightarrow \mu\mu \ (ee) + \gamma$ | Internal CR | External CR |
| TRG | | IsoMu27 (Ele35) | |
| Prompt $\ell\ell$ | | Tight ID | |
| $ \eta $ | | < 2.4 (2.5) | |
| $p_T(\ell 1)$ [GeV] | | > 28 (38) | |
| $p_T(\ell 2)$ [GeV] | | > 15 | |
| $\Delta R(prompt, disp)$ | - (> 0.05) | | - |
| Prompt OS | | ✓ | |
| $M(2\ell)$ [GeV] | (30, 80) | > 80 | (30, 80) |
| $M(4\ell)$ [GeV] | (80, 100) | > 100 | (80, 100) |
| Disp $\ell\ell$ σL_{xy} | > 3 \sigma | < | 3σ |
| $p_T(\gamma	o ee)$ [GeV] | | < 60 | |
| Disp OS | | ✓ | |
| Disp e $\log(d_{xy}/d_z)$ | | > -1.25 | |

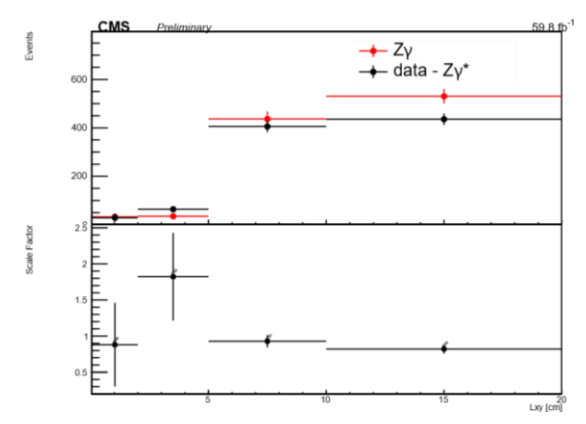


Figure 45: Electron corrections (2018) that are applied on the simulated predictions for the displaced selection of electrons. They correspond inclusively to the complete efficiency, from reconstruction to the Tight Displaced ID, and are based on $Z \to \ell\ell + \gamma$ events.

17. Data-Driven Background Estimation

17.1. For Prompt Categories

The prompt categories have 2 or 3 leptons in the final states that, in general, the Fake-Rates (FR) are independent probabilities. However, this is not always the case after relaxing the $\Delta R_{\ell\ell}$

requirement from 0.3 to 0.05, because the leptons are decay products of the same mother particle (e.g. a light-meson or a B-meson) and the FR probabilities of each lepton are correlated due to their isolation. For the case of correlated leptons, the fake-rate for the analysis is calculated considering the pair of leptons as a single composite object.

The Fake Rate is measured in a QCD-enriched measurement region (MR) and is defined as the probability of a non-prompt object to enter the Signal Region section. The Measurement Region that is used to measure the FR for independent leptons includes one loose lepton to be measured (selection that defines the Application Region, look Figure 26) and a jet with $p_T \ge 50$ GeV, which jet is well separated from the lepton ($\Delta R_{lepton-jet} \ge 0.7$) and does not interfere with the lepton. The triggers that are used for muons and electrons collect events with prescaled settings, different between Single Muon triggers and Single Jet triggers for electrons. The jet that is away from the lepton is required to ensure that both Muon triggers are in fully efficient regions and compatible, as the final measurement comes in the form of a combination of these 2 measurements with different triggers separated at 10 GeV. The definition of the MRs are presented in Table 16.

Table 16: Definition of the Measurement Regions that are used for measuring Fake Rates for independent leptons in MC and data.

| Criteria | Muons | | Electrons |
|-------------------------|-------------|-----|--------------------------------------|
| Trigger | Mu3_PFJet40 | Mu8 | PFJet(25 40 60 80 140 200 260) |
| $ ho_{	au}(\ell)$ [GeV] | > 3 | > 8 | > 1 |
| Loose leptons | = 1 | | = 1 |
| Jets (50 GeV) | ≥ 1 | | ≥ 1 |
| $\Delta R_{lepton-jet}$ | ≥ 0.7 | | ≥ 0.7 |

Fake-rate measurements with simulation

The FR measurements in the Measurement Region, using QCD events, are applied on events in the Application Region that is populated by W+Jets and tt-bar and potentially are of different jet composition and their origin (b-quark, c-quark, and light-quark jets). For this reason, before proceeding to measuring with data, QCD simulation is used to optimize the Signal and Application Regions selections (**Tight** and **Loose** IDs) so that the jet contributions in these regions to be as similar as possible with respect to the Measurement Region, resulting this way to Fake Rates that illustrate minimal dependency on the flavor of the jets in the event. This optimization led to fixing the b-tag veto, which rejects leptons associated to b-jets, in Tight IDs to the values 0.45 and 0.15 for electrons and muons respectively, without significant reduction of signal efficiency.

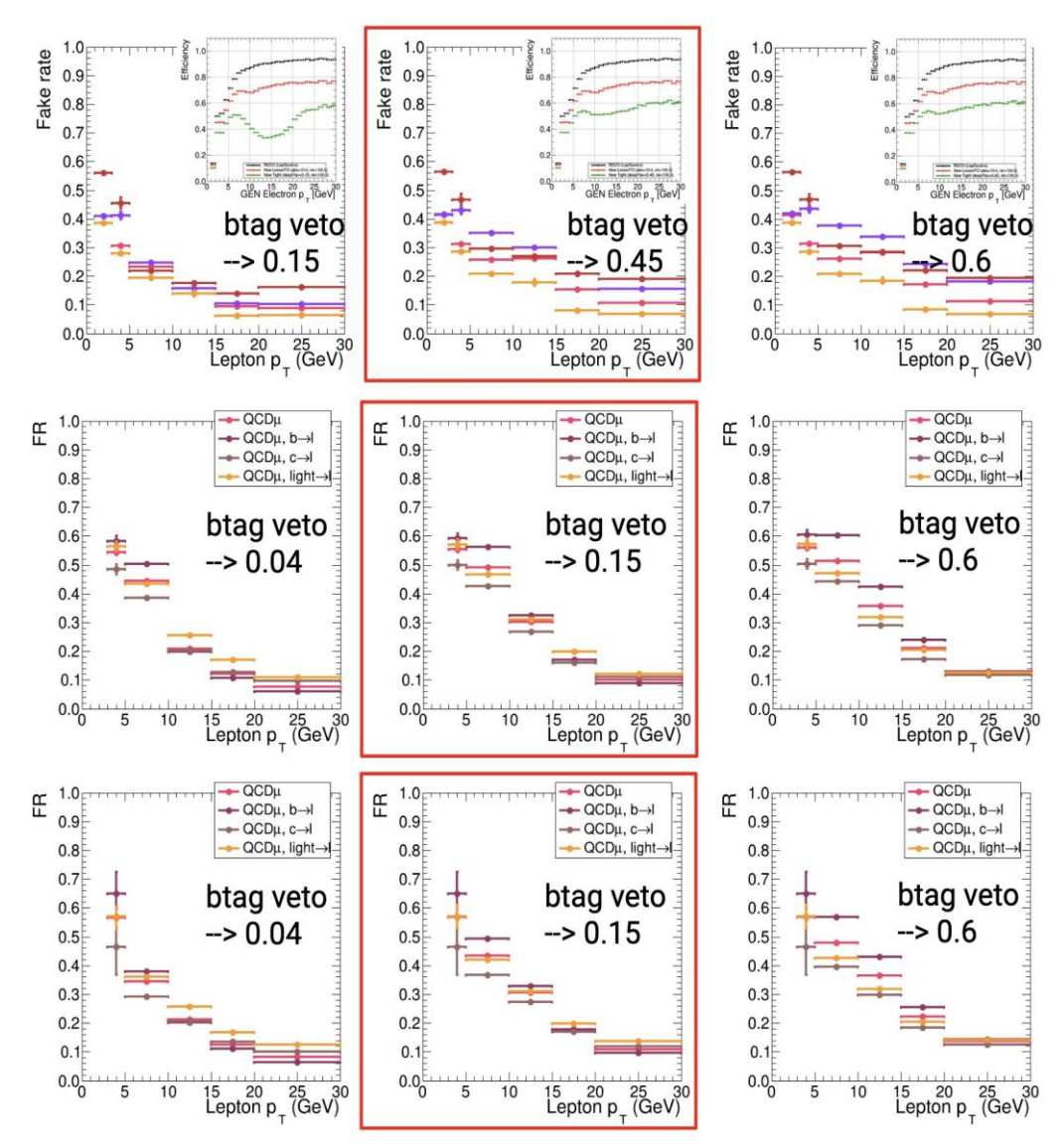


Figure 46: Optimization of the b-tag veto requirement that is included in the Signal Region selection for the muons and the electrons. The optimization is based on the flavor dependency of the Fake-Rate measurements in the MR with QCD simulation. Top to bottom: electron FR, muon FR (with trigger Mu3_PFJet40), and muon FR (with trigger Mu8). The results in the middle column exhibit minimal flavor dependency and thus are chosen for the SR selections. A significant target of the optimization is also maintaining signal efficiency after applying the b-tag veto.

This optimization was performed on 2018 QCD simulation dataset (refer to Figure 46) and the results were confirmed for the rest of the years that retain the same flavor dependency, see Figure 47.

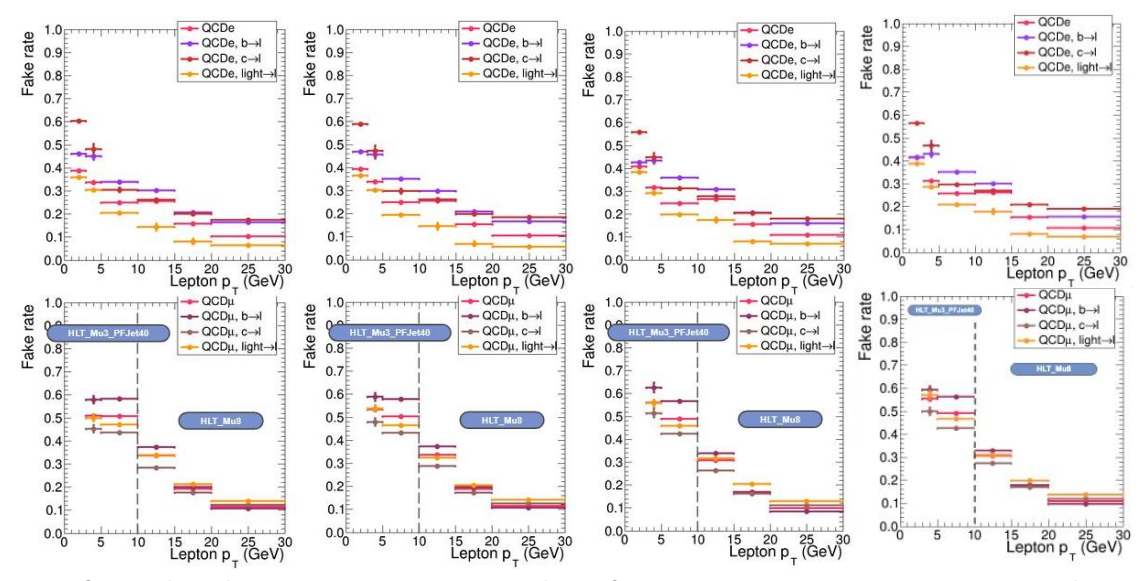


Figure 47: Left to Right: Fake Rate measurements in simulation for 2016-preVFP, 2016-postVFP, 2017, 2018 electrons and muons (top and bottom respectively). The measurement for electrons uses PFJet triggers for the entire pT range (1-30 GeV), while for the muons the measurement is separated at 10 GeV, using the highly prescaled trigger Mu3_PFJet40 for $p_T < 10$ GeV and a simple but also prescaled Mu8 trigger for $p_T > 10$ GeV.

Fake-Rate measurements with data

Based on the same Measurement Region (see Table 6) and incorporating additional pile-up weight corrections due to varying prescale profiles of the data collection triggers, the measurements use two different prompt subtraction techniques to eliminate the electroweak (EWK) component from the data. This allows the use of FR measurements with the QCD component of the MR to be used for the tight-to-loose method. The result is the average of these measurements with both techniques for EWK subtraction.

The discrimination variable, to separate QCD from EWK in events with jets in association with leptons from Z and W, is the transverse mass (m_T) and illustrates different shapes for these two processes. We use a modified definition in which the lepton p_T is substituted with a fixed value (35 GeV) to reduce the correlation between m_T and lepton p_T , because the result of the measurement is parametrized on the lepton p_T .

$$m_T^{fixed}(l, p_T^{miss}) = \sqrt{2 \cdot 35[GeV] \cdot p_T^{miss} \cdot (1 - cos\Delta\Phi)}$$

For the subtraction of the prompt EWK component two different methods are used, unfolding the QCD FR from 2 distinct regions and simultaneously fitting yields from different p_T bins to estimate the EWK background. Their average is used as the result of the measurement with data. Figure 48 presents the Measurement Region (MR) with data and MC simulation, which is separated into the QCD contribution (signal) and the EWK contribution (background that needs to be subtracted). In the MR, the simulation is corrected to the data that was collected with the prescaled triggers by taking also into account that these triggers have a biased PU profile because of the conditions under which they used to avoid extreme recording rates. The prescaled triggers that are used for these measurements are enabled only at the end of the fill of the LHC where the PU is low. This PU correction can be seen in the vertex plot (upper right Figure 48), which

shows a bin-per-bin ratio between real data and simulation that is set to 1 by the normalization of the events to the data.

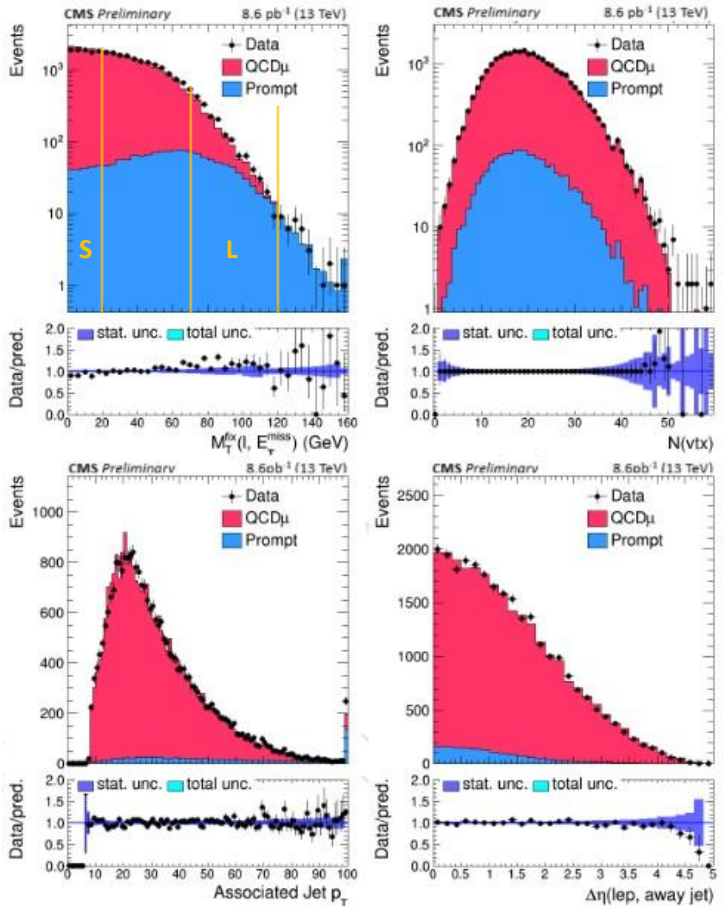


Figure 48: The Measurement Region (MR) for muons that is used in p_T range 10-30 GeV. Left-to-Right and Top-to-Bottom: The fixed transverse mass M_T^{fix} of the lepton and the missing energy in the event, the number of reconstructed vertices in the event (that is used for the PU correction as described above), the p_T of the associated Jet corresponding to the lepton of the measurement, and the distance (in η) between the highest- p_T jet in the event and the lepton of the measurement. The M_T^{fix} distribution is separated in 2 M_T^{fix} regions, S and L with 0-20 and 70-120 GeV respectively, and illustrates the QCD (S) and EWK (L) regions that are used for the unfolding method.

The first measurement (using data) unfolds the QCD fake-rate using information from 2 distinct measurement regions on the M_T^{fix} spectrum, a QCD-like region (S, 0-20 GeV) and an EWK-like region (L, 70-120 GeV). The QCD fake-rate (FR) is calculated using the formula written below, where the result is dependent on a correction term $f_L \cdot r_{\mathrm{Vjets}}^{\mathrm{SL}}$ that is a fake-rate measured in the EWK-like region, and is transferred to the QCD-like region using the ratio of expected events of the background $r_{\mathrm{Vjets}}^{\mathrm{SL}}$. In the denominator, the term $\left(1-r_{\mathrm{Vjets}}^{\mathrm{SL}}\right)$ acts as a normalization and is the relative variation of the EWK yield between the two regions with respect to the EWK-like region where the measurement f_L was performed (see the following expressions).

$$FR = \frac{f_S - f_L \cdot r_{\text{Vjets}}^{\text{SL}}}{1 - r_{\text{Vjets}}^{\text{SL}}}$$

$$r_{Vjets}^{SL} = \frac{\frac{EWK_{MC}(0-20)}{data(0-20)}}{\frac{EWK_{MC}(70-120)}{data(70-120)}} = \frac{r_{0-20}}{r_{70-120}} \quad and \quad (1-r_{Vjets}^{SL}) = \frac{r_{70-120}-r_{0-20}}{r_{70-120}}$$

Secondly, the other method for subtracting the prompt contamination and measuring the Fake-Rate with data relies on simultaneous fits. The Measurement Region is separated into passing and failing probes, that form the numerator and the denominator ($\frac{passing}{passing+failing}$), and we estimate the background to be subtracted while fitting QCD and V+jets simulated templates of M_T^{fix} . These fits are performed simultaneously in p_T - η bins and some examples can be seen in Figure 49.

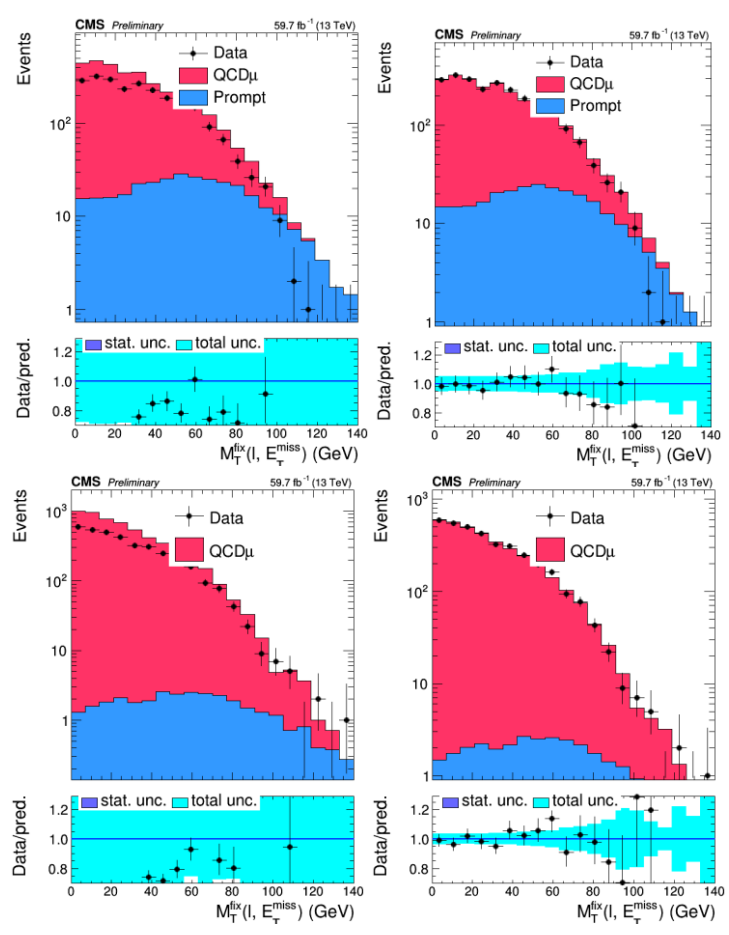


Figure 49: Pre-fit (left) and post-fit (right) distributions for calculating the Fake-Rates for electrons in the central part of the detector, $|\eta|$ <0.4. Top: passing probes for selecting the electrons (Signal Region selection) that selects electrons from prompt processes. Bottom: failing probes. In the failing distributions one can see that the bump on the right side, which is attributed to EWK processes, is not as strong as in the passing distributions.

The result of the measurements is a combination of the two results with data, taking as central value the weighted average, as uncertainty band the envelope of the two uncertainty bands, and is parameterized in p_T and η like in the MC measurements. The results of both data

measurements in 2018 are presented in Figure 50, for muons and electrons, and are compared to the measurements that were performed on simulated QCD samples.

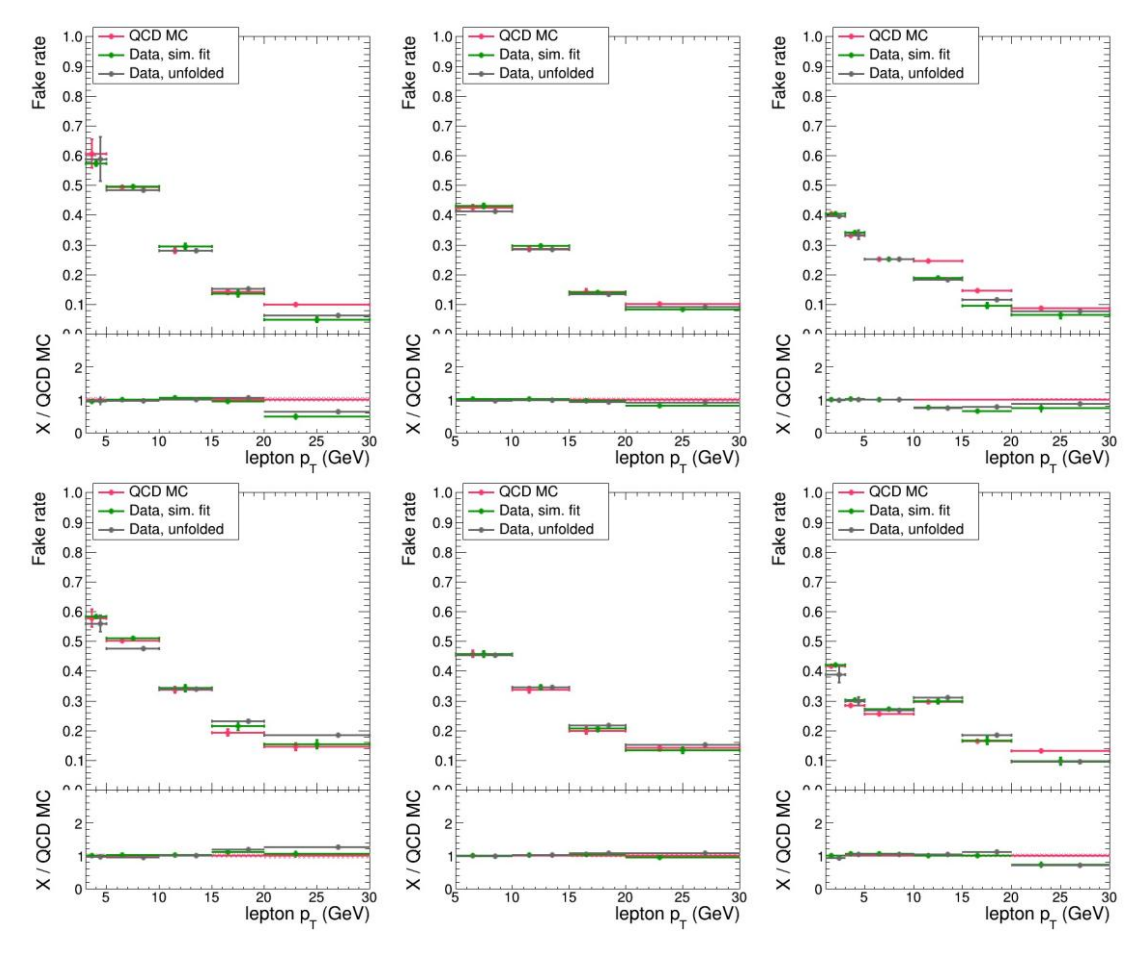


Figure 50: Superimposed fake-rate results for 2018 dataset. Comparison between the 2 data methods (black) unfolding the QCD fake-rate, (green) simultaneous fits, and (red) with QCD MC simulation. Top (Bottom): Measurements for barrel (endcap) that are performed separately. Left to Right: Fake-rate results using different triggers, the two leftmost results are for muons with Mu3 PFJet40 and Mu8 triggers, and the rightmost are results for electrons using a combination of PFJet triggers.

The Closure Test

A closure study is essential to evaluate the *maximum expected disagreement* that is caused by any residual flavor dependency of the measured Fake-Rates, which originates from other kinematic variables than those that the FRs are parametrized (p_T and η in prompt, or M_{LL} , $p_{T_{LL}}$, and L_{xy} in displaced). This test compares the distributions and yields of the non-prompt predictions in Signal Region calculated with two methods, firstly directly from the simulation, and secondly estimated by applying the Semi Data-Driven transfer factors on the appropriate simulation events of the Application Region. The level of disagreement between the distributions defines a systematic uncertainty that is propagated to the prediction of the non-prompt background in the SR as a uniform uncertainty (not a shape).

Closure distributions for muons and electrons are presented in Figure 51 and the systematic uncertainty that is assigned, due to closure, is 50% of the prediction.

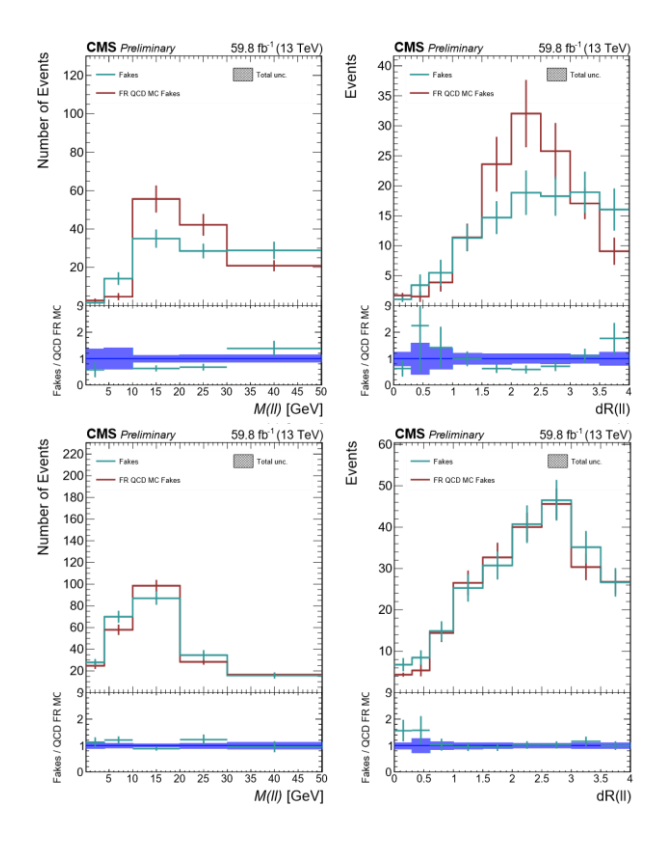


Figure 51: Top (Bottom): Distributions for prompt Muons (Electrons) from the Closure test that compares non-prompt prediction in Signal Region between simulation and "tight-to-loose" method, in 2018 dataset. For both predictions, the test suggests an uncertainty of 50%, driven by a few bins in the $\Delta R(\ell\ell)$ distribution for the muons. The chosen uncertainty for the electrons is common to muons, simplifying the statistical analysis.

Prompt Non-Prompt Control Region

The purpose of this Control Region is to validate the background prediction using a selection of data events and not the simulation as in the closure test. The required orthogonality is ensured by inverting the Opposite-Sign requirement of the Signal Region, making it a region more probable to be filled with fake leptons and ideal to validate the estimation. Because of an opposite sign requirement on the trigger that is selected for Low- p_T bins, the Control Region is defined only for $p_T^{miss} > 200 \text{ GeV}$.

The Application Region that is used for applying the "Tight-to-Loose" method to the Signal Region is still useful for the "Same-Sign" Control Region, since by inverting the charge of the leptons doesn't change the phase-space that is defined with the rest of the Signal Region selection and all calculations for the leptons still hold in the case where they are positive or negative. In Figure 52, the Same-Sign Non-prompt Control Regions are presented for both channels, muons and electrons, in 2018. These regions are included also in the final Combine fit to constrain the normalization of the non-prompt background for the independent leptons ($\Delta R > 0.3$).

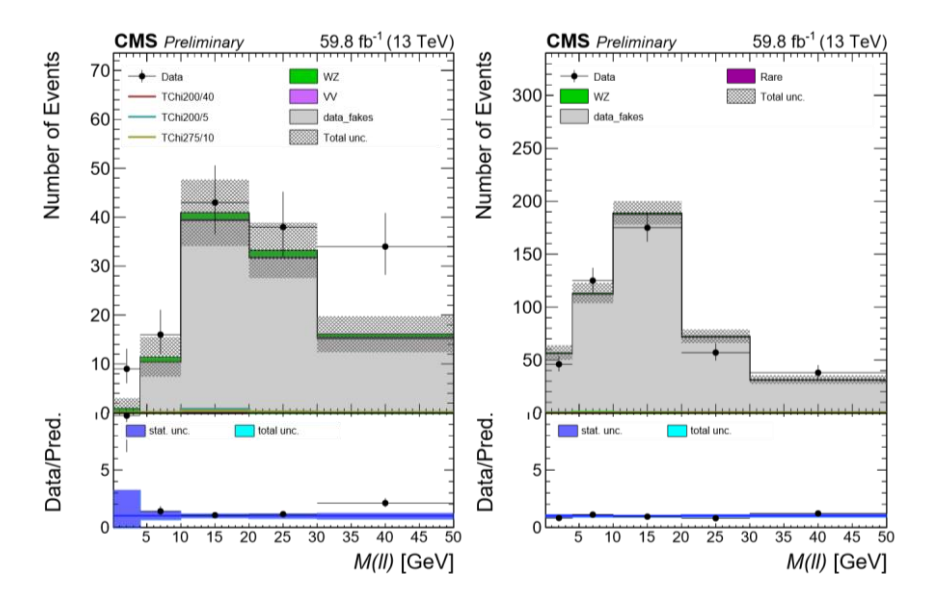


Figure 52: Left (Right): Prompt Same-Sign Control Region for muons (electrons) to validate non-prompt backgrounds, in 2018 dataset. The plots present the distribution of the mass of the system of 2 same-sign leptons.

17.2. For Displaced Categories

For displaced categories the reconstruction procedure makes it easier to treat the displaced pair of leptons in the same manner as for correlated leptons in the prompt Fake-Rate calculations. Refitting the lepton pairs results in objects that can be treated as if they were without internal structure, simplifying the fake-rate analysis by considering the pair as a single composite object, as in the case for $\Delta R < 0.3$.

There are two main background sources in the displaced categories: displaced leptons that are associated with jets in the event and usually belong to B-hadron decays, or displaced leptons that coincidentally form an acceptable pair and are not associated with the PV, to jets, or to each other. For the first source, estimating the expected yield in the Signal Region makes use of the fake-rate method as in the prompt categories, while for the second source the estimation uses information from the simulation.

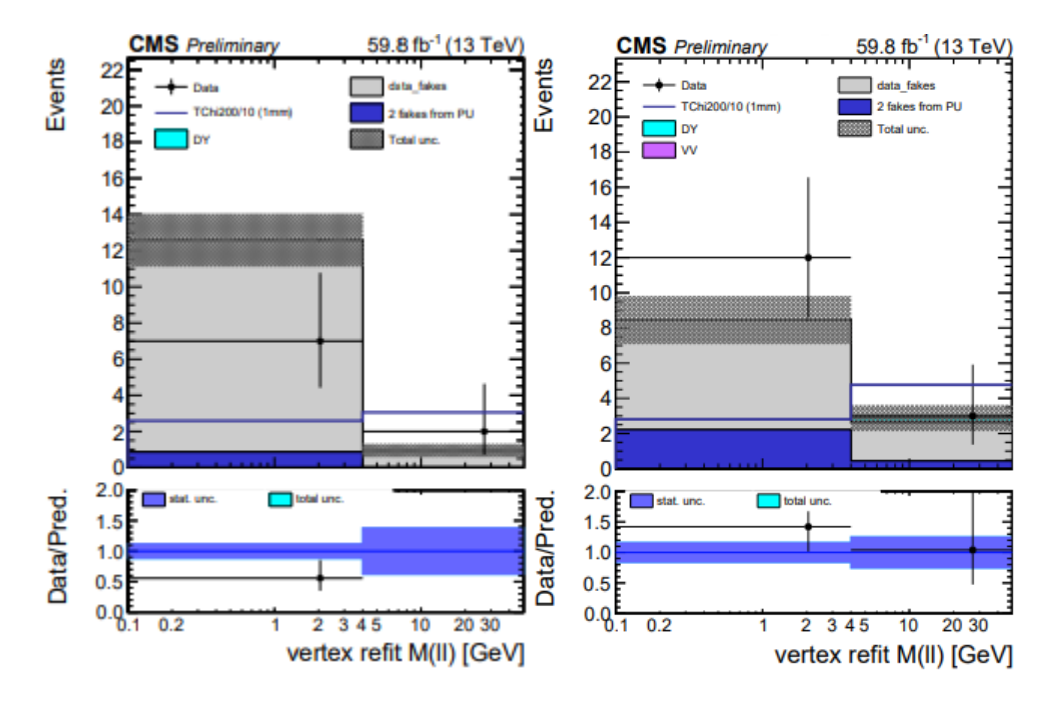


Figure 53: Signal Regions for displaced Muons (left) and Electrons (right) for the bin $High-p_T^{miss}$ and $Low \sigma_{L_{xy}}$, to illustrate the background composition in the analysis.

Measurement Regions for non-prompt leptons from jets

This is the most significant background contribution of the displaced Signal Regions, the method for its estimation is mainly the same Tight-to-Loose approach as predicting the background for the correlated leptons of the prompt analysis. The reconstruction of the di-lepton objects enables the possibility to treat the leptons of these pairs as having correlated FR probabilities to pass the Tight Selection. Three measurement regions for FR calculation are presented in Table 17, one for each Signal Region: LowMET ($125 < p_T^{miss} < 200$ GeV) for muons and HighMET ($p_T^{miss} > 200$ GeV) for both lepton channels. The event selection is like in the Signal Region but looser, notice the missing "hard lepton veto" and "collinearity" requirements, and with the b-jet veto inverted so that MRs and displaced SRs are orthogonal.

Table 17: Definition of the Displaced Measurement Regions that are used for Fake Rates calculation in the displaced analysis with data.

| Cuitouio | Mu | ions | Electrons | | | | |
|--|-------------------------------|---------------|-------------|--|--|--|--|
| Criteria | LowMET | HighMET | HighMET | | | | |
| Triggers | | Same with Sig | nal Regions | | | | |
| Loose pair | = 1 | | | | | | |
| $p_{\scriptscriptstyle T}\!(\ell_{1/2})$ [GeV] | 5-30 | 3-30 | 1-30 | | | | |
| $\Delta R(\ell_1,\ell_2)$ | - | > 0.05 | > 0.05 | | | | |
| $M_{\ell\ell}[GeV]$ | 4-50 | 0.1-50 | 0.1-50 | | | | |
| <i>Wi</i> ₹₹ [GeV] | veto J/Ψ(3,3.2) and Y(9,10.5) | | | | | | |
| HT [GeV] | 1 | 00 | - | | | | |
| p_T^{miss}/HT | 0.2 | -1.4 | - | | | | |
| $log_{10}(\Delta xy$ | | _ | > -1.25 | | | | |
| $/\Delta z)$ | | | 7 1.25 | | | | |
| N _b jets (25 GeV) | | ≥ : | 1 | | | | |

Using the Measurement Regions, as described above, the following results are achieved for Fake-Rates for different contributions. In Figure 54, the contribution in orange is fake leptons that originate from jets, for example displaced B-mesons that have typical decay length of around 5cm, in grey is contribution from other QCD decays, in blue is contribution from non-prompt leptons from pile-up (PU) that do not originate from the PV (but a pair is still formed), and in black are contributions with pair of leptons originating from PU and from jets.

The Fake-Rate (FR) measurements have a few differences between displaced muons and electrons. For muons, the measurement takes into consideration both p_T^{miss} regions inclusively, while for the electrons there is not a LowMET trigger, and the measurement takes into consideration only $p_T^{miss} > 200$ GeV. Also, the results are parametrized in different variables and bins for each channel, for muons in $p_T(\ell\ell)$ and L_{xy} (transverse momentum of the dimuon pair and transverse length from PV), while for electrons in $M_{\ell\ell}$ and L_{xy} (dielectron mass and transverse length from PV). Differences in the binning of the parametrization exist also per year, where 2016 (pre- and post-VFP¹⁷) are treated differently due to the less statistics in the MR and better closure that defines the uncertainty of the Tight-to-Loose method.

Both FR measurements follow the same PU-subtraction procedure, from data, before calculating Tight and Loose selection ratios for the results. This subtraction is performed since non-prompt leptons from PU appear very isolated after studying their isolation profile, so that they have higher FR probabilities than the rest of the non-prompt leptons, leading to closure problems, higher uncertainties, and inconsistent FR results that cannot be used inclusively with the Application Regions. The reason behind the more than expected isolated picture for leptons from PU is attributed to the Particle-Flow Isolation algorithms of the reconstruction, which are not

¹⁷ The 2016 dataset is split in two eras, pre-VFP and post-VFP. The eras are treated separately, since in the pre-VFP era the strips had saturation effects in the readout under high-luminosity conditions. This was mitigated in the post-VFP era by changing the feedback preamplifier bias voltage (VFP) [42]

ideal for leptons that do not come from the PV of the event. The reference point of PU leptons should ideally be PU vertices, other than the PV, a fact leading to complications with energy sums that define the isolation variables. The remaining PU background is estimated separately using simulation.

The rightmost plots in Figure 54 present the 2D maps of the results of the Fake-Rate measurements, applied on Application Region events to predict the Signal Region and Control Region contributions of the non-prompt background.

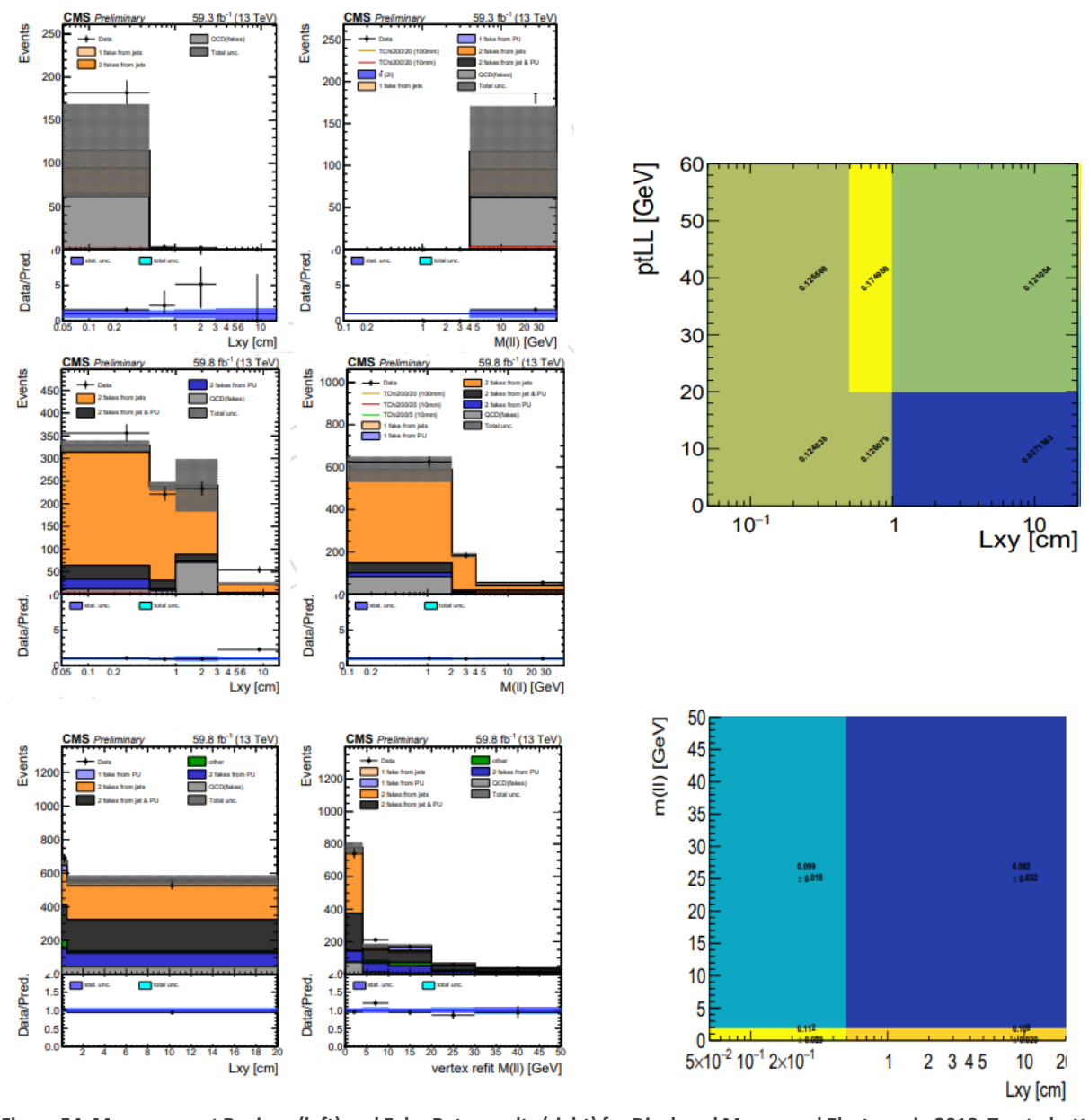


Figure 54: Measurement Regions (left) and Fake-Rate results (right) for Displaced Muons and Electrons in 2018. Top to bottom: LowMET and HighMET for muons, and HighMET for electrons. Right-hand side: 2D maps of FR results using 2018 dataset, inclusively for Low and HighMET regions with muons (top), and for HighMET region with electrons (bottom).

The Closure Test

A closure study, like the one that is performed for the prompt non-prompt estimation, is also performed for the displaced region. This test is important to estimate the expected disagreement due to residual flavor dependency of the Fake-Rates that is not captured by the parametrization (L_{xy} , $p_{T_{LL}}$, or M_{LL} for electrons). The disagreement between the distributions, of about 50%, defines a systematic uncertainty that is propagated to the prediction of the non-prompt background in the SR as a uniform uncertainty (not a shape). Important closure distributions for displaced electrons and muons are presented in Figure 55.

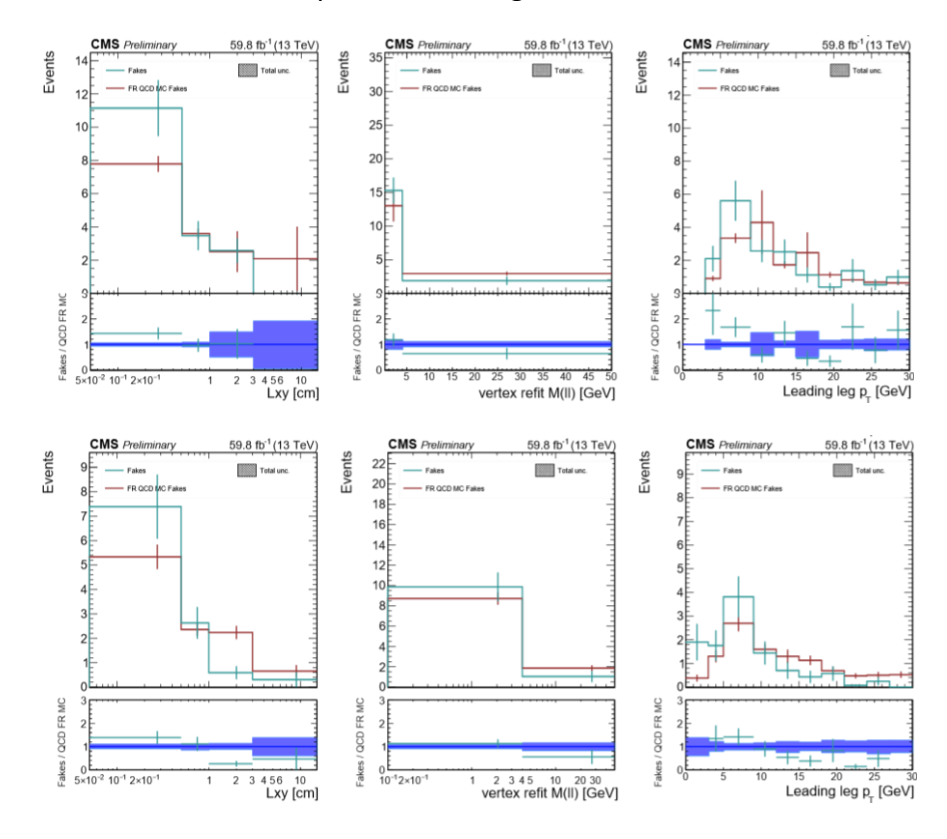


Figure 55: Top (Bottom): Distributions for displaced Muons (Electrons) from the Closure test that compares non-prompt prediction in Signal Region between simulation and "tight-to-loose" method, in 2018 dataset. For both background predictions, the test suggests an uncertainty of 50%, driven by some bins in the leading p_T distributions.

Displaced Non-Prompt Control Region

The purpose of this Control Region (CR) is to validate the background prediction using a selection of data events instead of the simulation that is used by the closure test. Following the same approach for constructing this CR as in the prompt case it is not effective, since a "Same-Sign" selection would be significantly contaminated in coincidences of di-leptons from Pile-Up, and for this reason a different approach is followed by defining an "Opposite-Sign" CR. The required orthogonality is ensured by selecting events with inverting any of the p_T^{miss}/H_T , hard lepton veto, or collinearity criteria of the Signal Region. Inverting the first cut, significantly contaminates the CR with QCD events, making it a good selection of events for validating the background estimation that comes from jets. Because of significant signal contamination at

$M_{\ell\ell}$ > 4 GeV and a dilepton mass requirement of the trigger that is selected for Low- p_T bins, the Control Region is defined only below 4 GeV and p_T^{miss} > 200 GeV.

The Application Region definition is the next step before applying the "Tight-to-Loose" method to estimate the non-prompt contribution in the Control-Region. The same procedure is followed, as with the Application Region for the Signal Region, where the Tight Selection for the dilepton is inverted to "Loose-not-Tight" (Figure 56). In Figure 57, the Opposite-Sign Non-prompt Control Regions are presented for both channels, muons and electrons, in 2018.

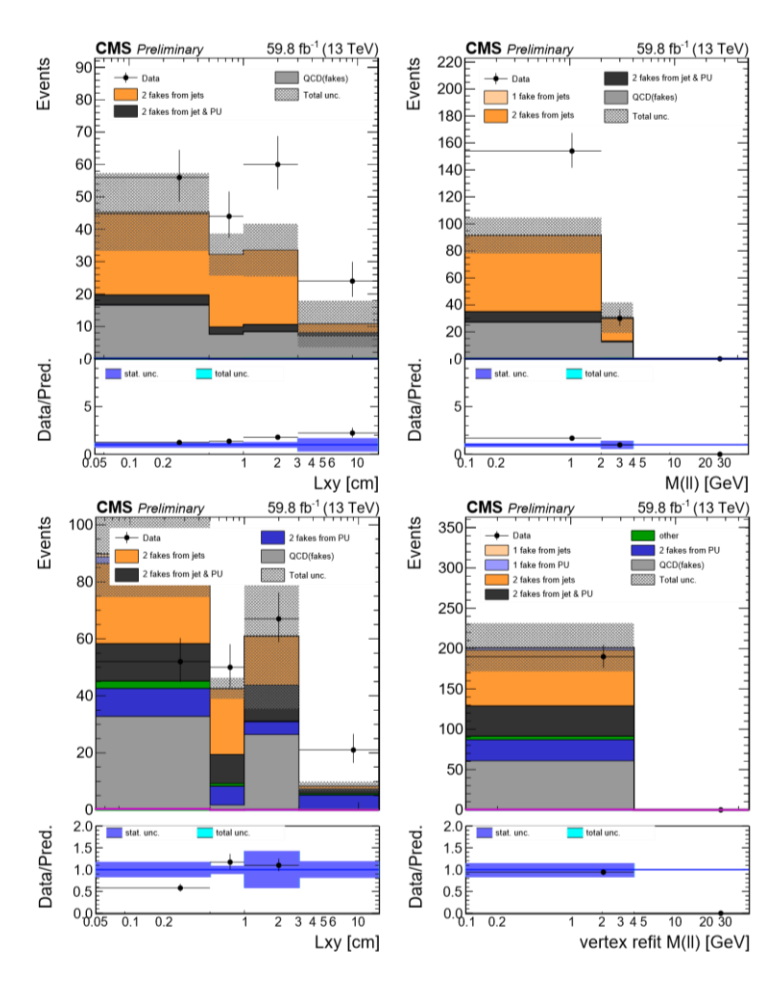


Figure 56: Top (Bottom): Displaced Application Region for the Opposite-Sign Control Region for muons (electrons), in 2018 dataset. Left: transverse displacement of the pair from the PV. Right: mass distributions of the dilepton system $M_{\ell\ell}$ (after refitting the tracks to the SV).

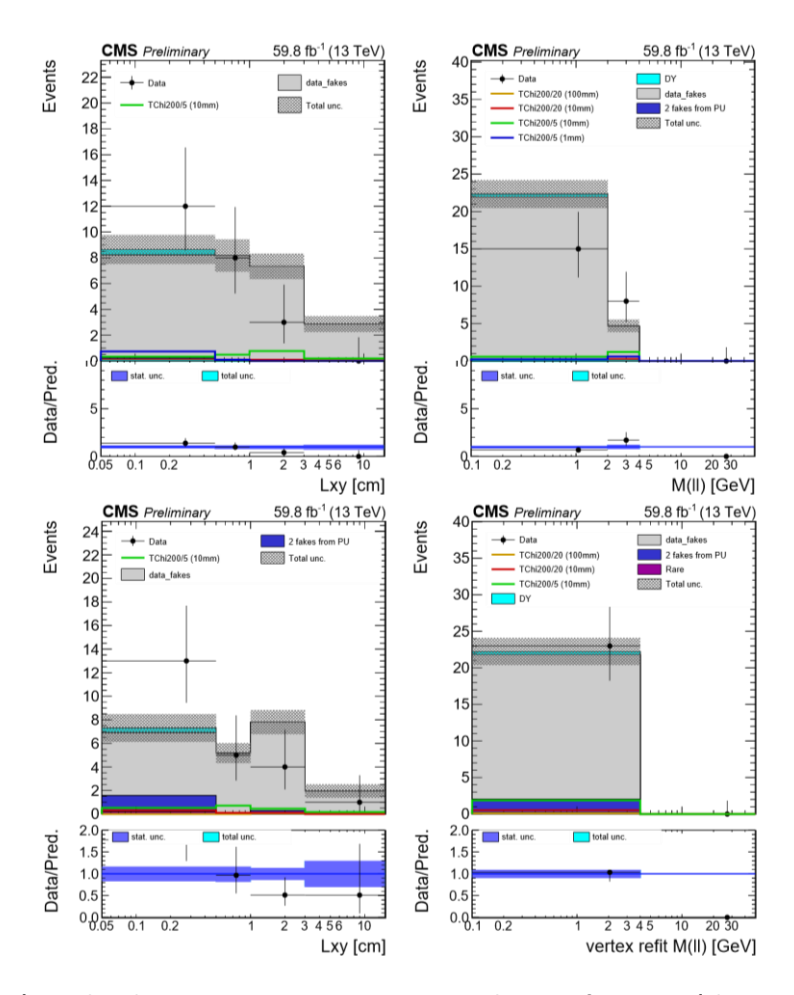


Figure 57: Top (Bottom): Displaced Non-Prompt Opposite-Sign Control Region for muons (electrons), in 2018 dataset. Left: transverse displacement of the pair from the PV. Right: mass distributions of the dilepton system $M_{\ell\ell}$ (after refitting the tracks to the SV).

18. Results & Interpretations

The results of the analysis are presented in Figure 58, in Figure 59, and in Tables Table 18 to Table 20, summarizing the sensitivity across five distinct $c\tau$ scenarios: 0, 0.1, 1, 10, and 100 mm. Each table corresponds to a specific sensitivity mode and presents only the relevant signal regions where sensitivity is observed. For $c\tau$ = 0, sensitivity is exclusively contributed by the prompt Signal Regions. In contrast, for $c\tau$ values of 1, 10, and 100 mm, sensitivity is contributed by the displaced SRs, and Table 20 summarizes all three significantly displaced $c\tau$ scenarios. The scenario $c\tau$ = 0.1 mm illustrates a unique case where both prompt and displaced SRs contribute to its sensitivity. In the tables, post-fit signal and background results are presented, upper limits on signal strengths at 95% confidence level (CL) and 68% CL are given using asymptotic profiling of the likelihoods and non-asymptotic profiling respectively (for comparison). The non-asymptotic profiling (68% CL) is used to extract the presented yields around the exclusion limit line and also for producing the bkg-only post-fit distributions in Figures Figure 58 and Figure 59. This is done by selecting appropriate signal mass-points near the limit's reach. Each table is accompanied by a figure of the expected and observed exclusion limits for each interpretation,

the Wino/Bino scenario with a Bino LSP (TChiWZ), and the Higgsino scenario with the triplet of Higgsinos at hundreds of GeV.

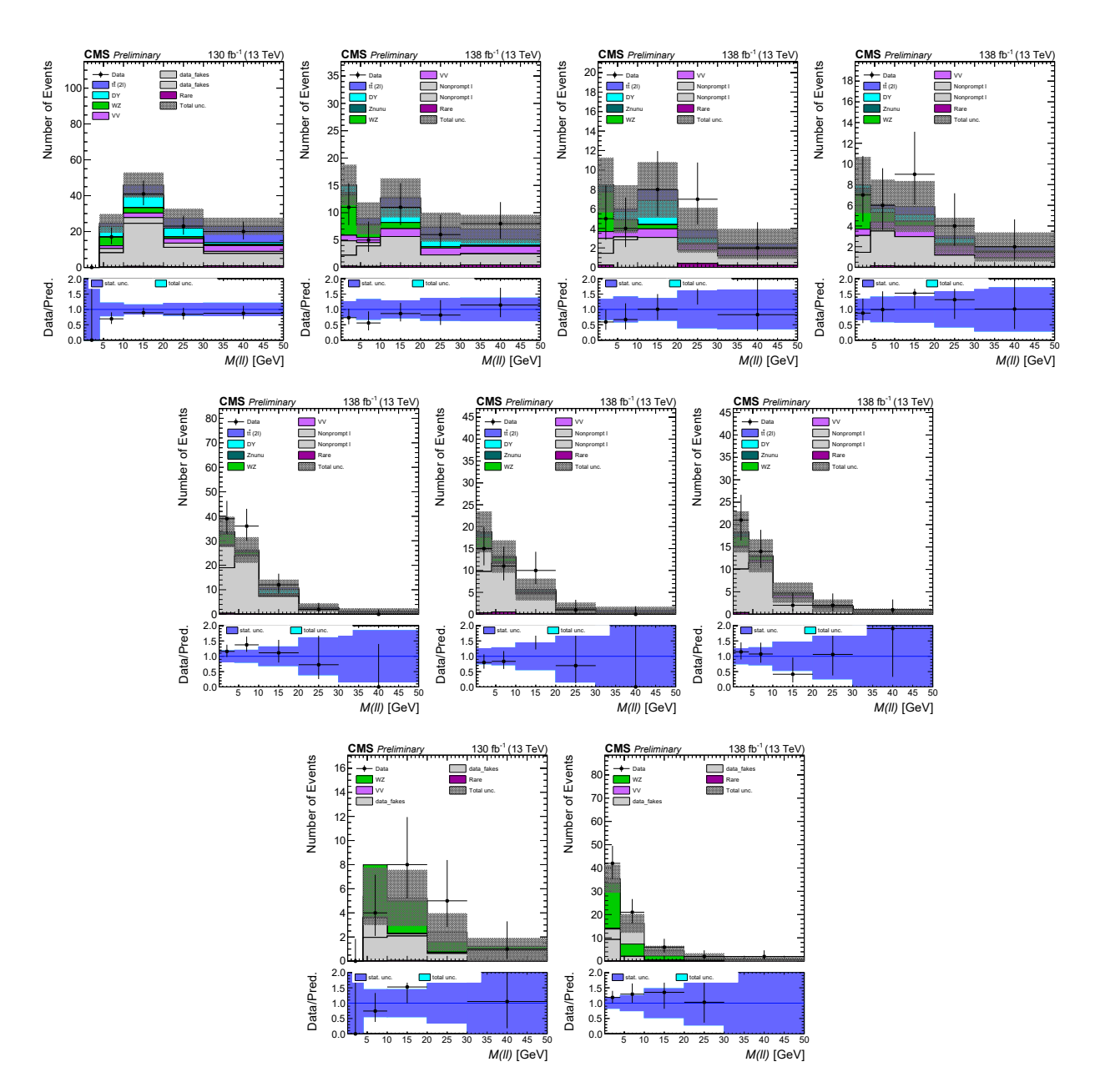


Figure 58: From top to bottom: Post-fit (b-only) $M_{\ell\ell}$ distributions of the SR for the prompt muons ($2\ell OS-\mu\mu$), prompt electrons ($2\ell OS-ee$), and three-lepton (3ℓ) categories using 2016, 2017, and 2018 datasets inclusively. From left to right: $2\ell OS-\mu\mu$: Low p_T^{miss} , Medium p_T^{miss} , High p_T^{miss} , and Ultra p_T^{miss} bins. $2\ell OS-ee$: Medium p_T^{miss} , High p_T^{miss} , and Ultra p_T^{miss} bins. 3ℓ : Low p_T^{miss} and High p_T^{miss} bins.

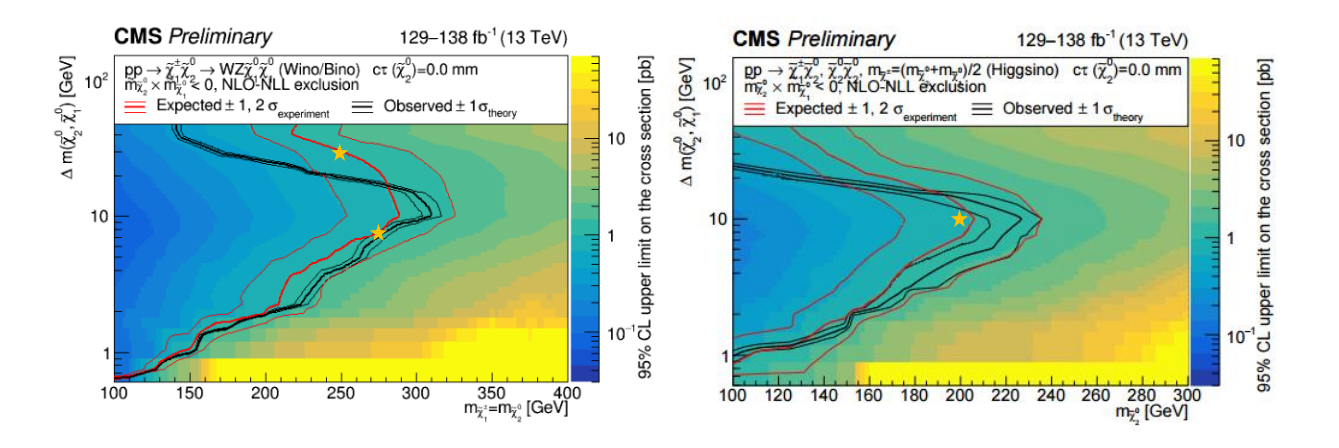
The post-fit distributions for the 2-lepton categories (Figure 58) look as expected, without remarkable excess of data. These categories contribute mostly to lower ΔM phase-space of the prompt limits, where a good agreement of observed and expected bands is shown.

The 3-lepton categories (Figure 58) contribute mostly to the higher ΔM in the prompt limits. In those, under-exclusion of 4σ significance is observed around 30-40 GeV. Recent studies have

attributed this to the way the WZ Control Region for $M_{\ell\ell} > 30$ GeV is included in the combine fit. By using only one bin for all events above 30 GeV, the fit cannot capture correctly the modelling of the WZ component for the 3 bins below 30 GeV in the Signal Region. By removing

Table 18: Post-fit results for the Signal Regions that contribute to the sensitivity of the interpretation with $c\tau$ = 0. Yields of data and background for selected signal mass-points near the expected limit line. The corresponding expected and observed signal strengths (@ 95% CL) are also presented together with the limit. The signal strength at 68% CL from the "sig+bkg" fit, which results the yields presented in the table, is also given for a comparison between expected and observed upper limits.

| c	au=0 | data | <u>TChiWZ-250/30</u> | | <u>TChi\</u> | NZ-275/7.5 | <u> Higgsino-200/10</u> | | |
|--|------|----------------------|------------------------|--------------|------------------------|-------------------------|--|--|
| ct = 0 | uata | signal | background | signal | background | signal | background | |
| Low p _T ^{miss} μμ | 101 | 3.57 | 109.54 | 0.10 | 113.18 | $6.07e^{-14}$ | 113.56 | |
| Med p _T ^{miss} μμ | 41 | 2.46 | 47.10 | 0.36 | 50.17 | $1.15e^{-13}$ | 50.43 | |
| High p _T ^{miss} μμ | 26 | 1.71 | 26.37 | 0.38 | 28.92 | $8.71e^{-14}$ | 28.27 | |
| Ultra p _T ^{miss} μμ | 28 | 3.12 | 23.19 | 0.89 | 24.49 | $2.85e^{-13}$ | 23.33 | |
| Med p _T ^{miss} ee | 89 | 0.88 | 73.00 | 0.38 | 70.73 | $7.96e^{-14}$ | 72.27 | |
| High p _T ^{miss} ee | 37 | 0.66 | 38.79 | 0.31 | 39.86 | $7.88e^{-14}$ | 40.15 | |
| Ultra p _T ^{miss} ee | 40 | 1.47 | 37.38 | 0.81 | 37.63 | $1.22e^{-13}$ | 38.26 | |
| $Low\ p_T^{miss}$ 3ℓ | 18 | 3.33 | 12.87 | 0.03 | 13.67 | $2.13e^{-15}$ | 13.55 | |
| $Med\ p_T^{miss} \ 3\ell$ | 73 | 6.42 | 55.72 | 0.64 | 59.39 | $1.00e^{-13}$ | 60.31 | |
| Signal Strength (μ) Observed 68% CL (non-asymptotic profile) Exp. Sig. Strength (μ) 95% CL upper limit | | 0. | $0.98^{+0.65}_{-0.56}$ | | $0.18^{+0.45}_{-0.37}$ | | $(3.61e^{-14})^{+0.16}_{-3.61e^{-14}}$ | |
| | | < | < 0.83 | | < 0.98 | | < 0.85 | |
| Obs. Sig. Strength (μ) 95% CL upper limit | | < 2.10 | | < | 1.12 | < 0.61 | | |



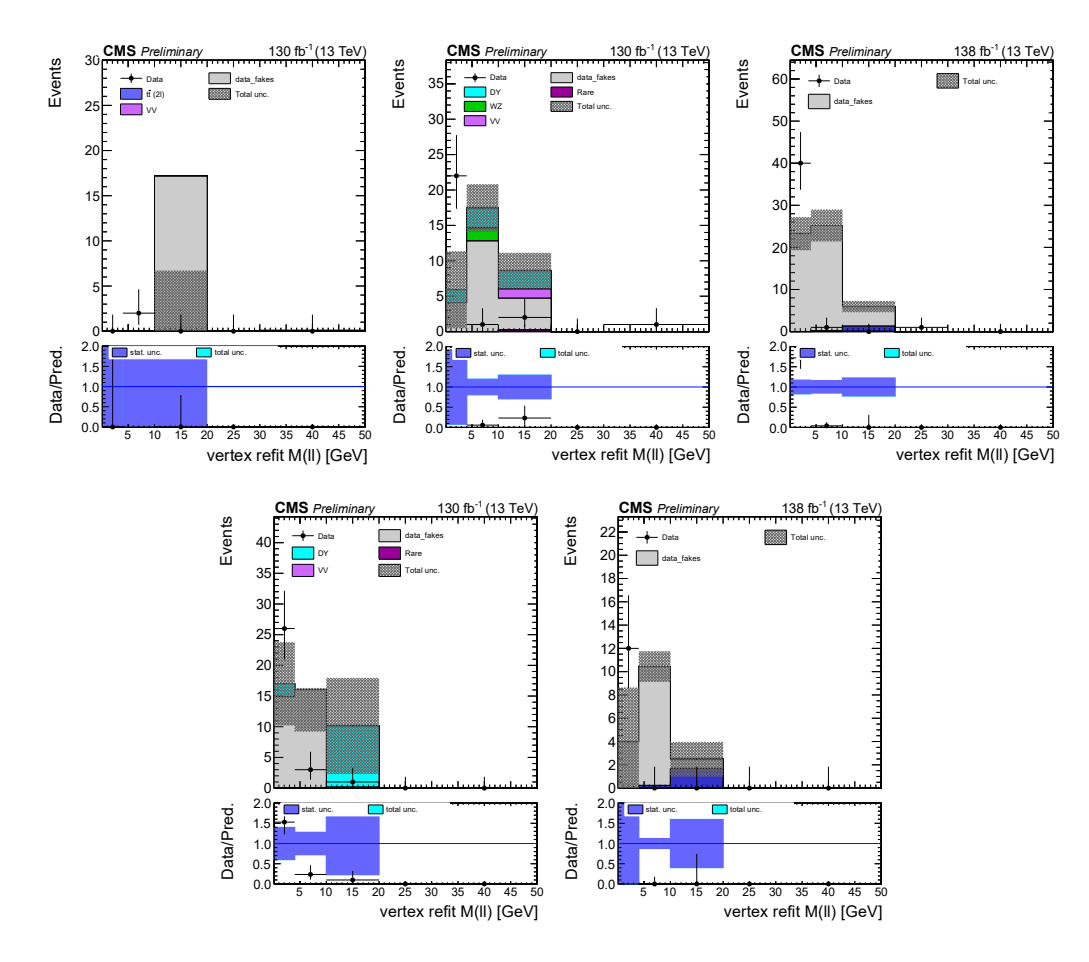


Figure 59: From top to bottom: Post-fit (b-only) $M_{\ell\ell}$ distributions of the SR for the displaced muons (disp- $\mu\mu$) and displaced electrons (disp-ee) categories using 2016, 2017, and 2018 datasets inclusively. From left to right: disp- $\mu\mu$: Low p_T^{miss} – Inclusive σ_{IP2D} , High p_T^{miss} - Low σ_{IP2D} , and High p_T^{miss} – High σ_{IP2D} bins. disp-ee: High p_T^{miss} - Low σ_{IP2D} , and High σ_{IP2D} bins.

this Control Region from the combine fit, the excess is reduced to 2.5σ , which is not considered evidence but rather systematic¹⁸.

The post-fit distributions for the displaced categories (Figure 59) show significant excess, localized to the bin below 5 GeV, especially for the muon channel. The under-exclusion that is presented in the limits for $c\tau$ = 1 and 10 mm, around ΔM = 10 GeV, seems to be related to this excess in the displaced muon channel. Currently, the excess, due to its high significance, is examined for evaluating whether the "Look-Elsewhere Effect" plays a role in these results, but the studies at the time of writing this thesis are not yet concluded by the CMS.

¹⁸ Similar excess is also observed in the previous iteration of this analysis [45] and is attributed to its original structure.

Table 19: Post-fit results for the Signal Regions that contribute to the sensitivity of the interpretation with $c\tau$ = 0.1 mm. Yields of data and background for selected signal mass-points near the expected limit line. The corresponding expected and observed signal strengths (@ 95% CL) are also presented together with the limit. The signal strength at 68% CL from the "sig+bkg" fit, which results the yields presented in the table, is also given for a comparison between expected and observed upper limits.

| ст | | TChiWZ-225/20 | | TChiWZ-225/7.5 | | <u> Higgsino-175/10</u> | |
|---|------|---------------|-------------------------|----------------|----------------------|-------------------------|----------------------|
| 0.1 mm | data | signal | background | signal | background | signal | background |
| Low p_T^{miss} $\mu\mu$ | 101 | 0.13 | 113.04 | 0.15 | 112.95 | 0.90 | 112.93 |
| $Med\ p_T^{miss}\ \mu\mu$ | 41 | 0.08 | 50.86 | 0.33 | 49.59 | 0.83 | 50.03 |
| $High p_T^{miss} \ \mu \mu$ | 26 | 0.10 | 28.04 | 0.32 | 28.70 | 0.88 | 27.97 |
| Ultra p _T ^{miss} μμ | 28 | 0.12 | 23.84 | 0.92 | 24.31 | 1.46 | 22.89 |
| $egin{array}{c} \dots & \dots $ | 89 | 0.04 | 72.46 | 0.53 | 70.62 | 0.56 | 71.72 |
| High p _T ^{miss} ee | 37 | 0.03 | 39.93 | 0.49 | 39.79 | 0.44 | 39.88 |
| Ultra p _T ^{miss} ee | 40 | 0.04 | 38.14 | 0.71 | 37.59 | 1.30 | 37.80 |
| $\begin{array}{c} Low~p_T^{miss} \\ 3\ell \end{array}$ | 18 | 0.07 | 13.68 | 0.02 | 13.38 | 0.02 | 13.44 |
| $egin{aligned} \mathit{Med} \ p_T^{miss} \ 3\ell \end{aligned}$ | 73 | 0.21 | 58.10 | 0.67 | 58.53 | 0.56 | 59.69 |
| $Low~p_T^{miss}-Low~\sigma_{Lxy} \ \mu\mu$ | 0 | - | - | - | - | - | - |
| Low p_T^{miss} — High σ_{Lxy} $\mu\mu$ | 0 | - | - | - | - | - | - |
| High p_T^{miss} — Low σ_{Lxy} $\mu\mu$ | 25 | 0.06 | 12.10 | 0.25 | 12.06 | 1.65 | 11.76 |
| $High p_T^{miss} - High \sigma_{Lxy} \ \mu\mu$ | 43 | 0 | 51.13 | 0 | 50.74 | 0 | 49.15 |
| $High \ p_T^{miss} - Low \ \sigma_{Lxy}$ ee | 29 | 0.03 | 21.91 | 0.27 | 21.93 | 0.70 | 21.99 |
| $High p_T^{miss} - High \sigma_{Lxy}$ ee | 13 | 0 | 19.21 | 0 | 19.07 | 0 | 18.82 |
| Signal Strength (μ) Observed 68% CL (non-asymptotic profile | e) | 0.0 | $038^{+0.835}_{-0.538}$ | 0. | $20^{+0.50}_{-0.44}$ | 0. | $32^{+0.38}_{-0.37}$ |
| Exp. Sig. Strength (μ) 95% CL upper limit | | < 1.04 | | < 0.96 | | < 0.76 | |
| Obs. Sig. Strength (μ) 95% CL upper limit | | < 1.62 | | < 1.16 | | < 1.03 | |

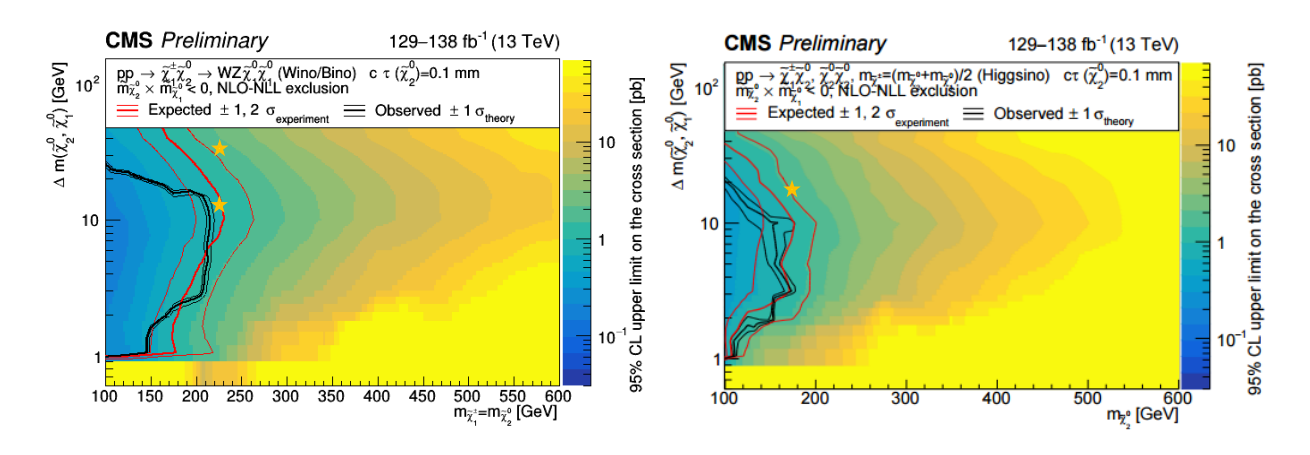
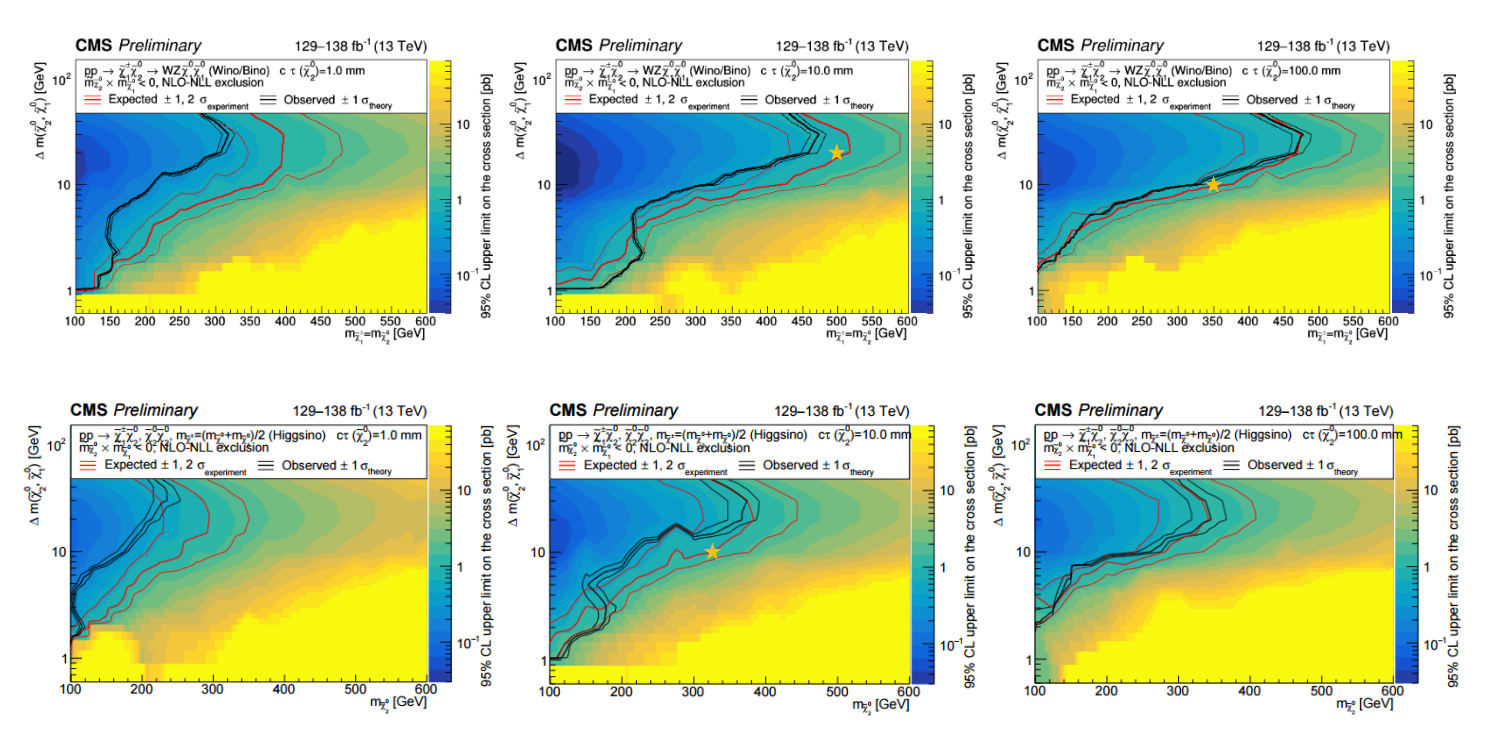


Table 20: Post-fit results for the Signal Regions that contribute to the sensitivity of the interpretation with $c\tau$ = 1/10/100 mm. Yields of data and background for selected signal mass-points near the expected limit line. The corresponding expected and observed signal strengths (@ 95% CL) are also presented together with the limit. The signal strength at 68% CL from the "sig+bkg" fit, which results the yields presented in the table, is also given for a comparison between expected and observed upper limits.

| ст | data | $rac{	extsf{TchiWZ-500/20}}{c	au=10\ mm}$ | | $TChiWZ-350/10 \ c	au = 100 \ mm$ | | Higgsino-325/10 $c	au=10~mm$ | |
|--|------|--|------------|-----------------------------------|------------|------------------------------|------------|
| 1/10/100 mm | | signal | background | signal | background | signal | background |
| $Low~p_T^{miss}-Low~\sigma_{Lxy} \ \mu\mu$ | 0 | - | - | - | - | - | - |
| Low p_T^{miss} — High σ_{Lxy} $\mu\mu$ | 0 | - | - | - | - | - | - |
| High p_T^{miss} — Low σ_{Lxy} $\mu\mu$ | 25 | 0.03 | 12.09 | 0.08 | 11.96 | 0.50 | 11.73 |
| High p_T^{miss} — High σ_{Lxy} $\mu\mu$ | 43 | 0.06 | 51.08 | 1.00 | 50.52 | 1.74 | 49.84 |
| $High \ p_T^{miss} - Low \ \sigma_{Lxy}$ ee | 29 | 0.014 | 21.87 | 0.05 | 21.80 | 0.55 | 21.42 |
| $High p_T^{miss} - High \sigma_{Lxy} \ ee$ | 13 | 0.009 | 19.288 | 0.21 | 19.24 | 0.51 | 18.96 |
| Signal Strength (μ) Observed 68% CL (non-asymptotic profile) | | $0.013^{+0.558}_{-0.283}$ | | $0.12^{+0.46}_{-0.30}$ | | $0.29^{+0.71}_{-0.47}$ | |
| Exp. Sig. Strength (μ) 95% CL upper limit | | < 0.82 | | < 0.67 | | < 0.83 | |
| Obs. Sig. Strength (μ) 95% CL upper limit | | < 1.20 | | < 1.06 | | < 1.72 | |



Compressed SUSY Summary

This chapter presents a summary of the low mass splitting results for the Higgsino pMSSM¹⁹ interpretation, where the large $tan(\beta)$ limit is assumed, exploiting the expected reach of three CMS analyses:

- Search for new physics with compressed mass spectra in final states with soft leptons and missing transverse energy in proton-proton collisions at $\sqrt{s}=13~TeV$ [36]
- Search for compressed electroweakinos with low-momentum isolated track [37]
- Search for supersymmetry in final states with disappearing tracks in protonproton collisions at $\sqrt{s} = 13 \, TeV$ [38]

Additionally, projections of the expected results are studied for 400, 3000, and 6000 fb⁻¹ that correspond to the Run2+Run3 luminosity recorded by CMS, the High-Luminosity LHC (HL-LHC) recorded luminosity that is expected to be collected by the CMS, and HL-LHC total luminosity that is expected to be recorded by both CMS and ATLAS together.

This summary is based on interpretations with the *Sandwich* configuration of the Higgsino model, where 3 nearly degenerate Higgsino states (2 Neutralinos, χ_2^0 and χ_1^0 LSP, and 1 Chargino χ_1^\pm) are at the reachable scale of hundreds of GeV, and all other SUSY particles are significantly heavier and decoupled, with $\Delta m^0 = 2\Delta m^\pm$. The cross sections are taken from the LHC SUSY Working Group Twiki [43] and

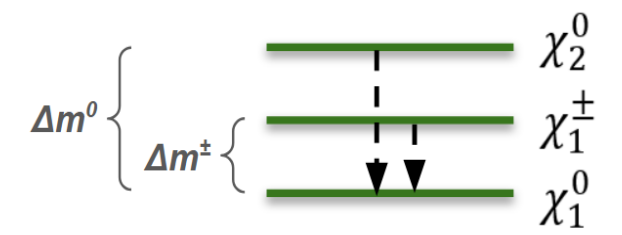


Figure 60: Schematic of the Sandwich Higgsino configuration that is used to interpret results by these 3 analyses, EXO-23-017, SUS-24-012, and arxiv:2309.16823 (SUS-21-006).

assume fully degenerate Higgsino states computed at NLO plus next-to-leading-log (NLL) precision, with all s-particles other than the Higgsino triplet to be heavy and decoupled.

19. THE ANALYSIS WITH SOFT MULTILEPTONS CMS-EXO-23-017 [36]

This analysis exploits prompt $\chi_2^0 \to Z^*(\ell\ell) + \chi_1^0$ decays (and prompt $\chi_1^\pm \to W^*(\ell\nu) + \chi_1^0$ for the 3-lepton channel), leveraging LowP_t Electrons down to 1 GeV for the first time in CMS, while remains efficient to probe the signal down to Δm^\pm of 0.5 GeV.

 $^{^{19}}$ The pMSSM (Phenomenological MSSM) is a CP- and flavour-conserving, subset of the MSSM at the weak-scale, requires only 19 SUSY-soft breaking parameters (MSSM \sim 100). This variant captures many important collider signatures of an R-parity MSSM.

Search for compressed SUSY featuring categories with opposite sign muon (electron) pairs, muon (electron) pT 3(1)-30 GeV and 80(50)% RECO+ID efficiency at 10 GeV, and new LowPT Electrons with acceptance down to p_T of 1 GeV. Triggers include MET120 and DoubleMu + MET50.

The signal regions categorize events in both 2-lepton and 3-lepton channels with opposite-sign pairs, where $\Delta R_{\ell\ell}$ must be greater than 0.05. For jets, the number of jets with p_T greater than 25 GeV should be more than one, and there should be no b-tagged jets. The p_T^{miss} should be greater than 125 GeV and H_T should be above 100 GeV. Additionally, the azimuthal angle between MET and the closest jet, $\Delta \Phi(MET, Jet)$, should be greater than 0.5. Better gains from the 2-lepton channels are observed when Δm^0 is less than 10 GeV and around 15 GeV from 3-lepton channels.

The prompt lepton background includes DY from $Z \to \tau \tau$ events that produce significant MET due to tau neutrinos, $t\bar{t}$ remnants after a b-jet veto, and DiBoson modes (either WZ or VV events) where reconstruction occasionally is challenging. These backgrounds are estimated using transfer-factors from control regions and floating nuisances. Non-prompt lepton background (fakes) arises from either collimated or independent leptons from QCD jets. This is estimated with a data-driven 'Tight-to-Loose' method.

20. The analysis with Soft Isolated Tracks CMS-SUS-24-012 [37]

This analysis exploits prompt and displaced $\chi_1^\pm \to \pi^\pm + \chi_1^0$ decays, identifies the isolated prompt or displaced pion tracks, and it reaches down to Δm^\pm of 0.3 GeV. It is a search for Higgsino Dark Matter that involves soft isolated π^\pm tracks and missing transverse energy (p_T^{miss}). The categories of the analysis include isolated tracks below 20 GeV, use of a MultiClass Neural Network (NN) classifier to differentiate between background and signal tracks, which is parametrized to the signal- Δm^\pm , while another NN refines background predictions that apply regression using a cleaned Drell-Yan Control Region (DY-CR) sample. The triggers employed in this study are MET300 + IsoTrack.

The Signal Regions contain tracks with $p_T < 20$ GeV and $\Delta \Phi(trk, Jets) > 0.4$. Jets for the signal regions are selected depending on the multiplicity in the events $N(p_T > 100) \ge 1$, $N(p_T > 30) < 5$, and rejecting b-jets. Additionally, p_T^{miss} and missing H_T (MH_T) should be greater than 300 GeV, with $\Delta \Phi(MET, Jets) > 0.5$. There should be no isolated photons ($N_{Iso\ \gamma} = 0$), electrons ($N_{Iso\ e} = 0$), or muons ($N_{Iso\ \mu} = 0$) in the events.

The Background is split in 3 main categories. There are two classes of PV-associated background, prompt and displaced, which correspond to contributions from $W \to \ell \nu$ and $Z \to \nu \nu$ events due to their significant p_T^{miss} contribution. Furthermore, spurious backgrounds include tracks categorized as unmatched reconstructions (e.g., PU, fakes). And finally, W(tau)-Jets events, where tracks are classified as WJets with displaced $W \to \tau \nu$ decays.

21. The analysis with Disappearing Tracks CMS-SUS-21-006, arXiv:2309.16823 [38]

This analysis exploits the displaced $\chi_1^\pm \to \pi^\pm + \chi_1^0$ decays, identifies short χ_1^\pm tracks, and reaches below Δm^\pm of 0.3 GeV, down to the pion mass (0.14 GeV). It is a search for charged long-lived SUSY particles that involves several channels with one or more disappearing tracks (DTk), not reconstructed by Particle Flow (PF). These tracks are categorized as either "short" or "long" considering tracks with Pixel-only hits or Pixel+Strips respectively. A Boosted-Decision-Tree (BDT) machine learning technique is used for SR/CR track separation, while DTks are also classified by dE/dx in the Pixel Detector, conceptually the stopping power of the detector. The triggers include MET100 to MET120 HLT paths for hadronic channels and Ele27 & Mu24 for leptonic channels.

Signal regions are defined with the requirement of having at least one DTk, one or more jets, and p_T^{miss} greater than 30 GeV. The transverse mass between DTk and p_T^{miss} should be more than 20 GeV. Additionally, in the leptonic regions, an invariant mass calculation between the disappearing track and the leptons is carried out, while requirements for the mass and the transverse mass are imposed to be substantial in the event (both to be more than 100 GeV), to help with suppressing Drell-Yan (DY) and WJets contributions.

There are two types of backgrounds to consider: genuine-particle and spurious-particle background. The genuine-particle background arises from PF failures when a particle exists, which can occur due to CALO crystal defects or tracker/DT track misalignments. The spurious-particle background results from random patterns in the tracker without PF matching. The method to estimate the background is the SR facilitates scaling factors (k-factors) transferring predictions from dedicated Control Regions. The k-factors are measured in DY Control Regions, specific to each Signal Region.

22. Summary and Projections to Run3 and HL-LHC

We present the phase space with mass splitting below 5 GeV, which is difficult to probe with previous searches. These results benefit from the LowPt Electron reconstruction in the analysis [36] and new ML techniques from [37] and [38], efficiently probing this low region. In Figure 61, results for Run2 and projections are presented for the three analyses. The projected expected limits are derived by scaling the yields to the target luminosity and the statistical uncertainties are set to $1/\sqrt{L_{target}}$, while keeping the systematic uncertainties based on the Run 2 analyses. Furthermore, after reducing the systematic uncertainties according to the YR2018 instructions [39], the improvement in the reach of the limits was marginal. Considering factors like changing pile-up conditions, detector complexity and performance, and minor changes to the cross section associated with the slightly higher \sqrt{s} , it has been concluded that the current version, which is based on Run-2 systematics, provides a reliable projection.

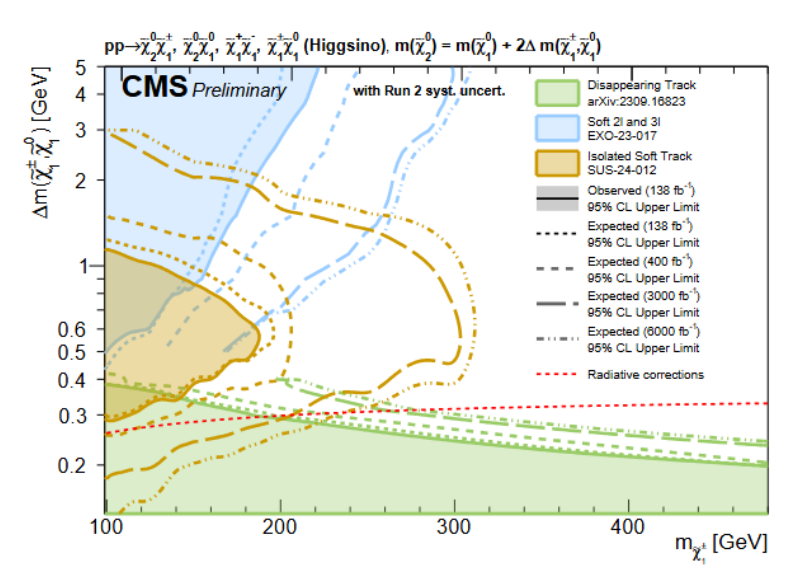


Figure 61: Summary plot of Higgsino exclusion limits with Run 3 and HL-LHC projections [36], focused on the phase space below 5 GeV of mass-splitting between the chargino and the LSP neutralino. With analyses that exploit only Run-2 datasets the observed exclusion limit stands around 140 GeV for the Higgsino mass and 0.4 GeV of mass-splitting, while the projections suggest an expanded reach up to 260 GeV for the HL-LHC. The projections for [36] and [38] are cut at Δm^{\pm} =500 and 400 MeV respectively, since below that point [36] loses acceptance to the signal because of the displacement of the Higgsino, and in [39] the analysis runs out of statistics needed for a smooth curve.

For mass splitting $\Delta m^\pm < 0.5$ GeV, the prompt analysis of [36] is losing acceptance to reconstruct the signal because it becomes significantly displaced, but above 0.5 GeV, the analysis is efficient for the Higgsino signal. This is presented in [40], using SUSYHIT simulations of the decays of the neutralino and the chargino states. The isolated and disappearing track searches ([37] and [38]) account for the realistic chargino and neutrino lifetime across the rest of the Δm^\pm range. (For [36], the acceptance is $\sim 100\%$ at 0.5 GeV for $\chi_1^\pm \sim \chi_1^0$ mass splitting and becomes $\sim 64\%$ at ~ 0.4 GeV, due to impact parameter cuts, while drops rapidly to 0 below 0.4 GeV.)

Furthermore, for [36] in Run-2, we applied a smoothing procedure. In the projections, we identified and removed certain results from the final plot, as they caused the trend of the expected signal strength to exhibit very discontinuous behavior of the limit line, which is nonphysical²⁰. Such results refer to inconsistent signal strength from the Combine fit ("spikes" comparing to their surrounding mass-points) that is the main reason why kinks may appear on the limit line.

²⁰ One should also keep in mind that this treatment has equal impact to the smoothing procedure and applying a smoothing kernel on top of that (like in Run-2 results) has had a negligible impact.

Appendix

23. Signal Regions for the Soft Multilepton Analysis

In this section, the Signal Regions (SR) of the analysis are presented. There are 5 separate regions featuring two prompt muons, two prompt electrons, three prompt leptons inclusively, two displaced muons, and two prompt electrons. Apart from this categorization, SR are further separated into p_T^{miss} bins, where LowMET is 125-200 GeV, MediumMET is 200-240 GeV, HighMET is 240-290 GeV, and UltraMET is 290+ GeV. Special definitions of these bins are still considered in some of the final states, because they are more effective for those cases. Despite the static binning that is presented in these plots, the "Parametric Binning" method is used to extract the results of the analysis.

The displaced Regions are categorized also with binning in the significance of the transverse displacement ($\sigma_{L_{xy}}$ or SIP), together with p_T^{miss} , and separate the SR in 4 categories that are treated separately in the Combine fit. To be exact, LowMET-LowSIP is 125-200 GeV and $\sigma_{L_{xy}} < 25$, LowMET-HighSIP is 125-200 GeV and $\sigma_{L_{xy}} > 25$, HighMET-LowSIP is 200+ GeV and $\sigma_{L_{xy}} < 25$, and HighMET-HighSIP is 200+ GeV and $\sigma_{L_{xy}} > 25$.

In the following Regions, the datasets that have been used are DiMuon for $p_t^{miss} < 200$ GeV and MET for $p_t^{miss} > 200$ GeV, with their respective triggers as mentioned in the analysis section. For reference, data that are presented in the Regions of below sections are based on statistics collected in 2016 (DiMuon dataset: 33.5 fb^{-1} , MET dataset: 36.3 fb^{-1}), in 2017 (DiMuon dataset: 36.7 fb^{-1} , MET dataset: 41.5 fb^{-1}), and in 2018 (DiMuon dataset: 59.3 fb^{-1} , MET dataset: 59.8 fb^{-1}).

23.1. Prompt Signal Muons

Signal Region that features 2 muons that pass the Tight Muon ID of the analysis and originate from the Primary Vertex, with p_T^{miss} binning as explained above.

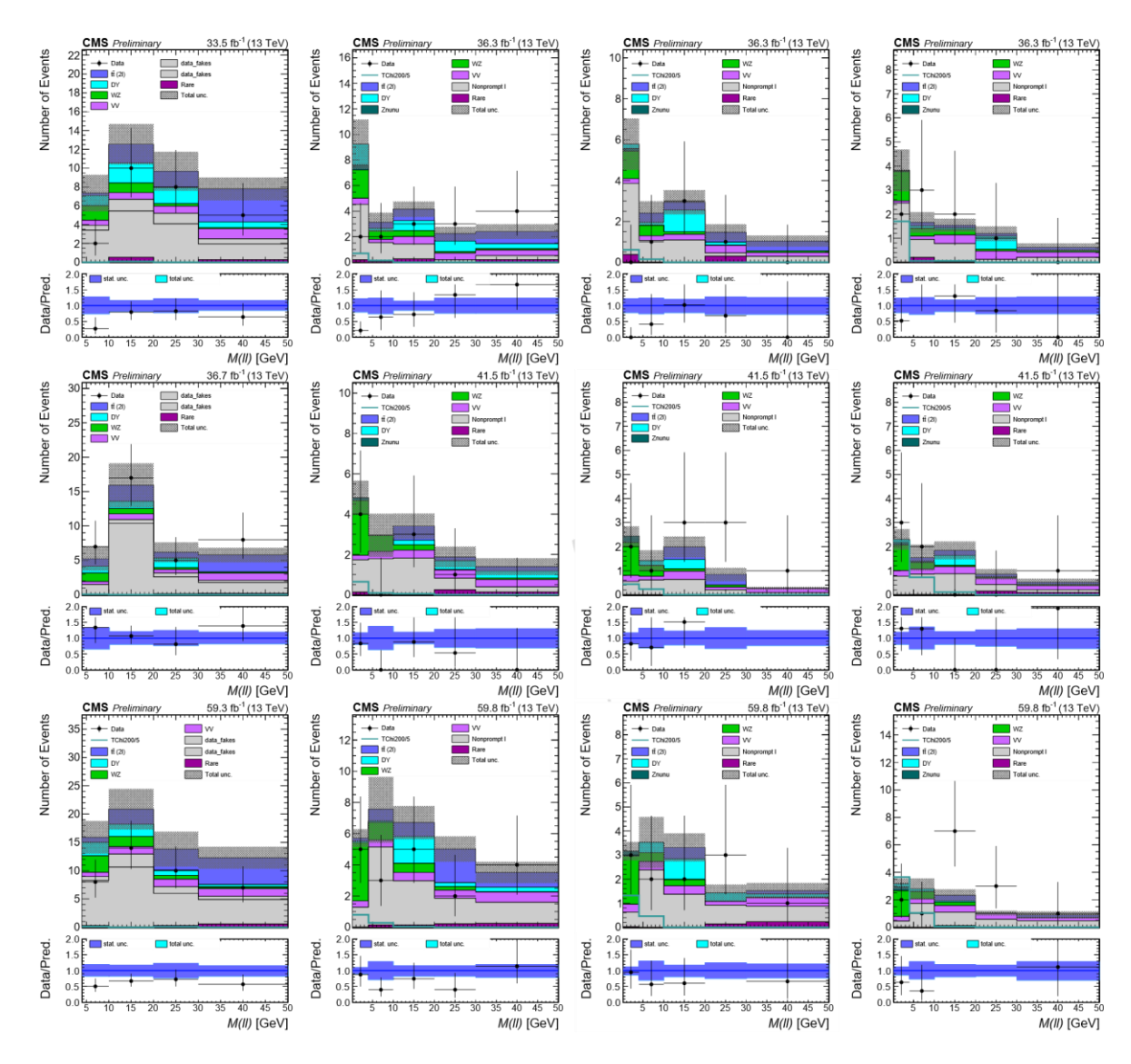


Figure 62: From top to bottom: $\textit{M}_{\ell\ell}$ distributions of the SR for the prompt muons using 2016, 2017, and 2018 datasets. From left to right: Low p_T^{miss} , Medium p_T^{miss} , High p_T^{miss} , and Ultra p_T^{miss} bins.

23.2. Prompt Signal Electrons

Signal Region that features 2 electrons that pass the Tight Electrons ID of the analysis and originate from the Primary Vertex, with p_T^{miss} binning as explained above.

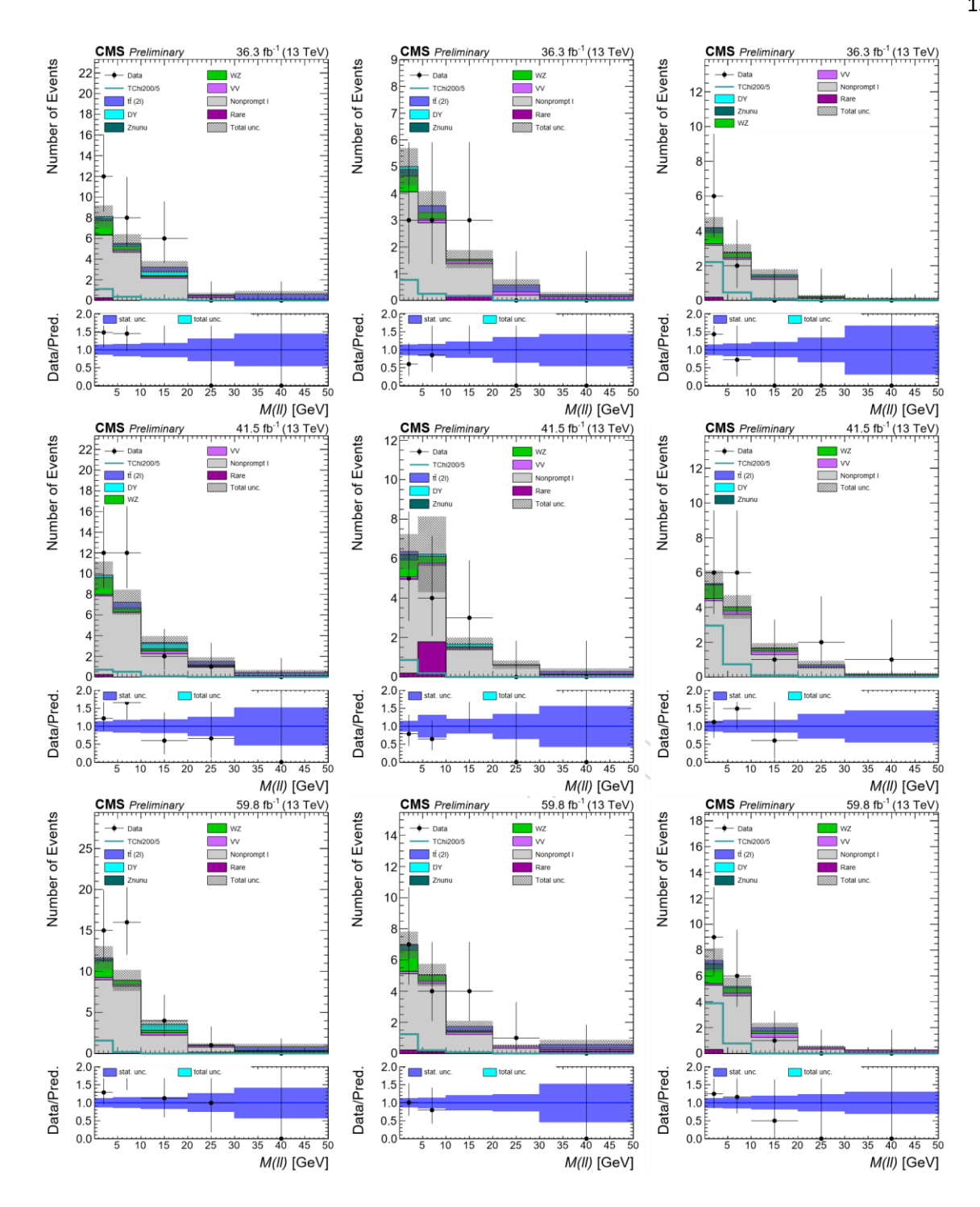


Figure 63: From top to bottom: $M\ell\ell$ distributions of the SR for the prompt electrons using 2016, 2017, and 2018 datasets. From left to right: Medium p_T^{miss} , High p_T^{miss} , and Ultra p_T^{miss} bins.

23.3. Prompt Signal 3-Leptons (μμℓ & eeℓ)

Signal Region that features 3 leptons at the final state that pass the Tight Selections of the analysis and originate from the Primary Vertex, the pair of leptons is considered inclusively either to be 2 muons or electrons, while the third lepton is ambiguously either one more muon or one electron. The p_T^{miss} binning is defined differently for the HighMET bin as it is inclusive for $p_T^{miss} > 200$ GeV, while the MediumMET bin is omitted.

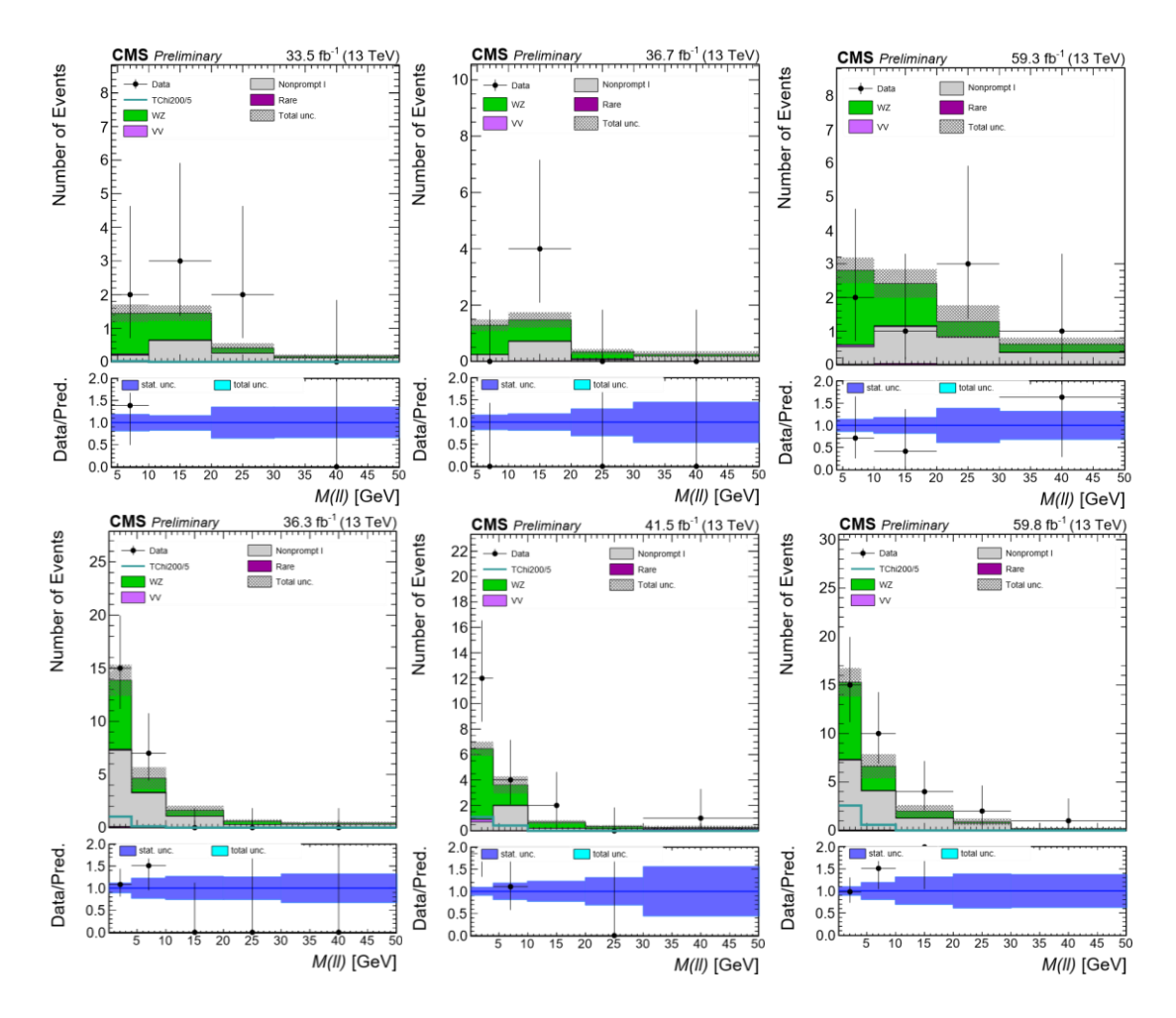


Figure 64: From left to right: $M\ell\ell$ distributions of the SR for the 3-lepton final state using 2016, 2017, and 2018 datasets. Top: Low p_T^{miss} . Bottom: High p_T^{miss} .

23.4. Displaced Signal Muons

Signal Region that features 2 muons that pass the Tight Displaced Muon ID of the analysis and **originate from the refitted Secondary Vertex** that is the intersection of their tracks, with p_T^{miss} binning as explained above for the displaced Regions.

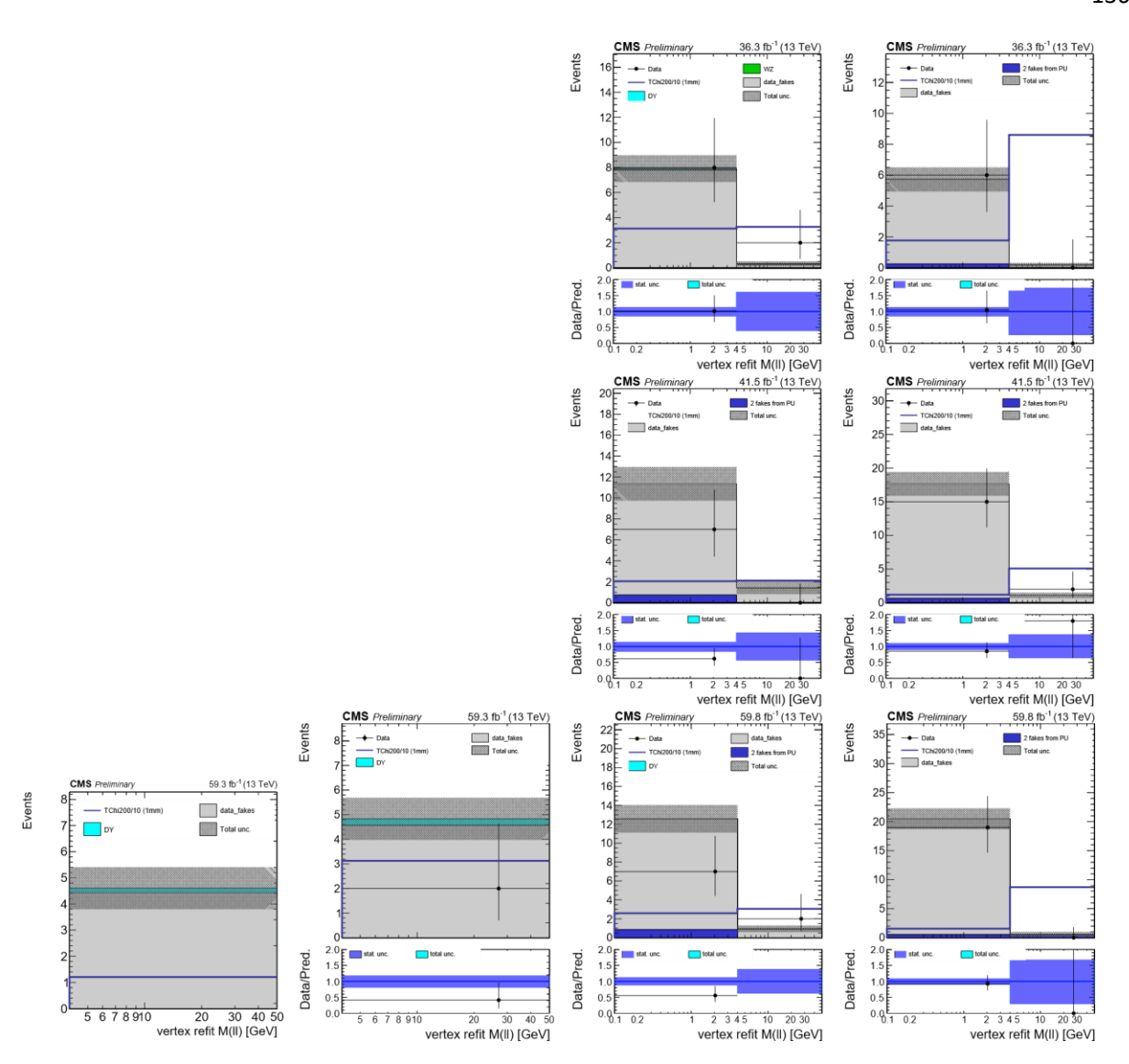


Figure 65: From top to bottom: $M\ell\ell$ distributions of the SR for displaced muons using 2016, 2017, and 2018 datasets. From left to right: Low p_T^{miss} - Low $\sigma_{L_{xy}}$, Low p_T^{miss} - High $\sigma_{L_{xy}}$, High p_T^{miss} - Low $\sigma_{L_{xy}}$, and High p_T^{miss} - High $\sigma_{L_{xy}}$ bins. In 2016 and 2017 the DiMuon trigger that is used to collect data includes a requirement for the tracks to be compatible with the Primary Vertex, making it inefficient for the displaced final states of the analysis.

23.5. Displaced Signal Electrons

Signal Region that features 2 electrons that pass the Tight Displaced Electron ID of the analysis and **originate from the refitted Secondary Vertex** that is the intersection of their GSF tracks, with p_T^{miss} binning as explained above for the displaced Regions.

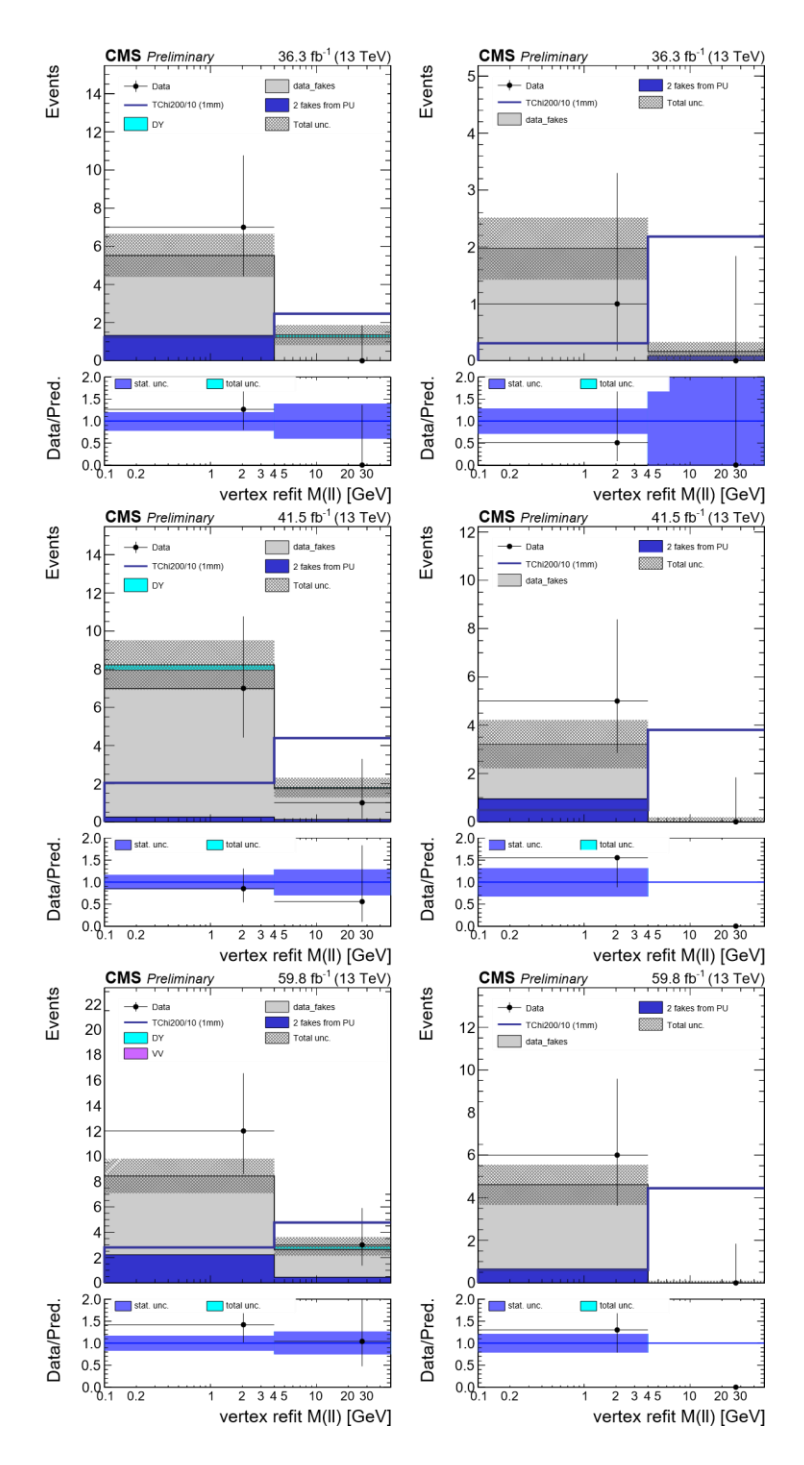


Figure 66: From top to bottom: $M\ell\ell$ distributions of the SR for displaced electrons using 2016, 2017, and 2018 datasets. From left to right: High p_T^{miss} – Low $\sigma_{L_{xy}}$ and High p_T^{miss} – High $\sigma_{L_{xy}}$ bins.

24. Control Regions for the Soft Multilepton Analysis

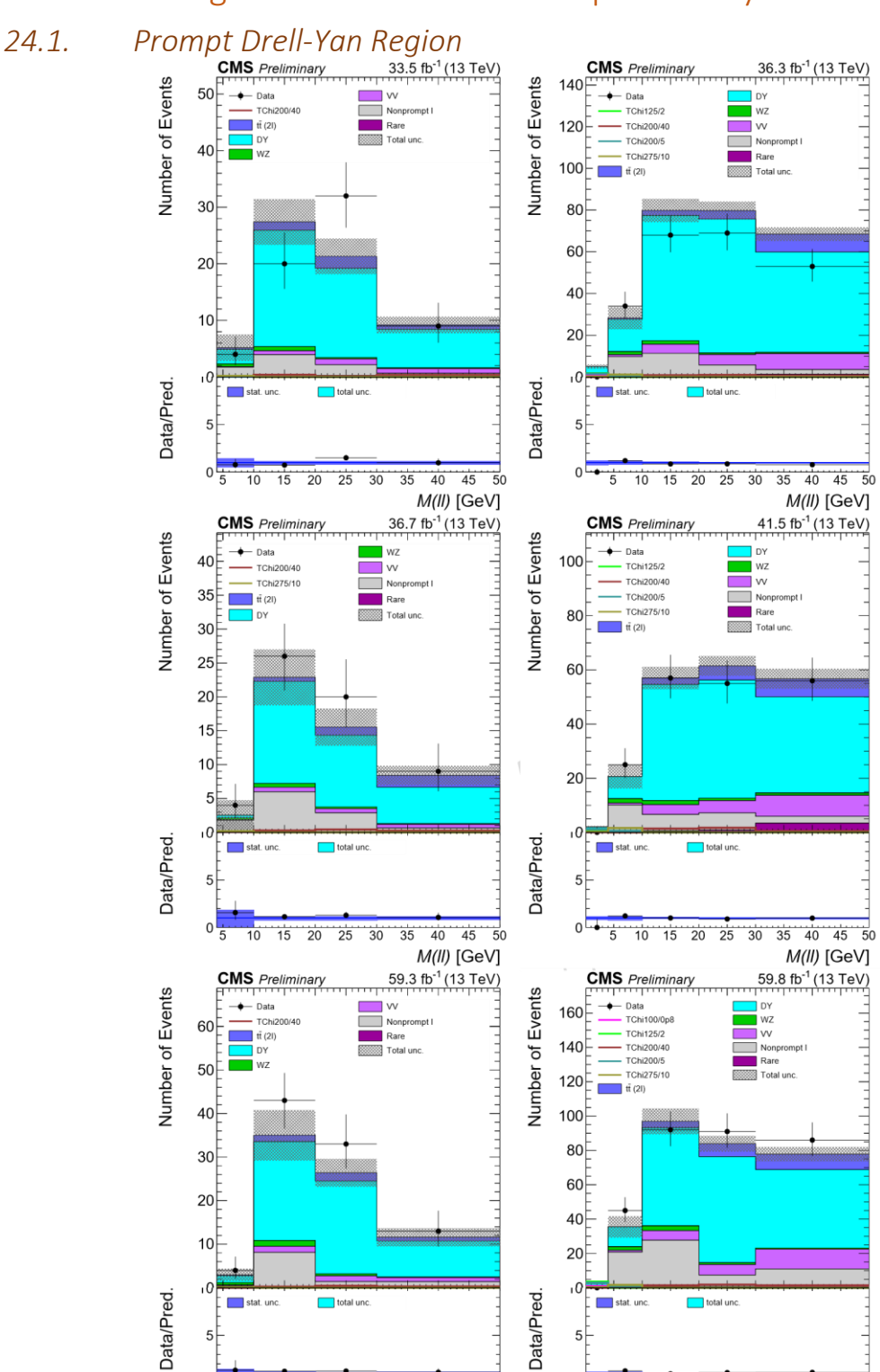


Figure 67: From top to bottom: $M\ell\ell$ distributions of the DY CR, inclusively for muons and electrons, using 2016, 2017, and 2018 datasets. Left: Low p_T^{miss} bin. Right: High p_T^{miss} bin.

10

20

25 30 35

15

40 45 50

M(II) [GeV]

45

M(II) [GeV]

35 40

15 20 25 30

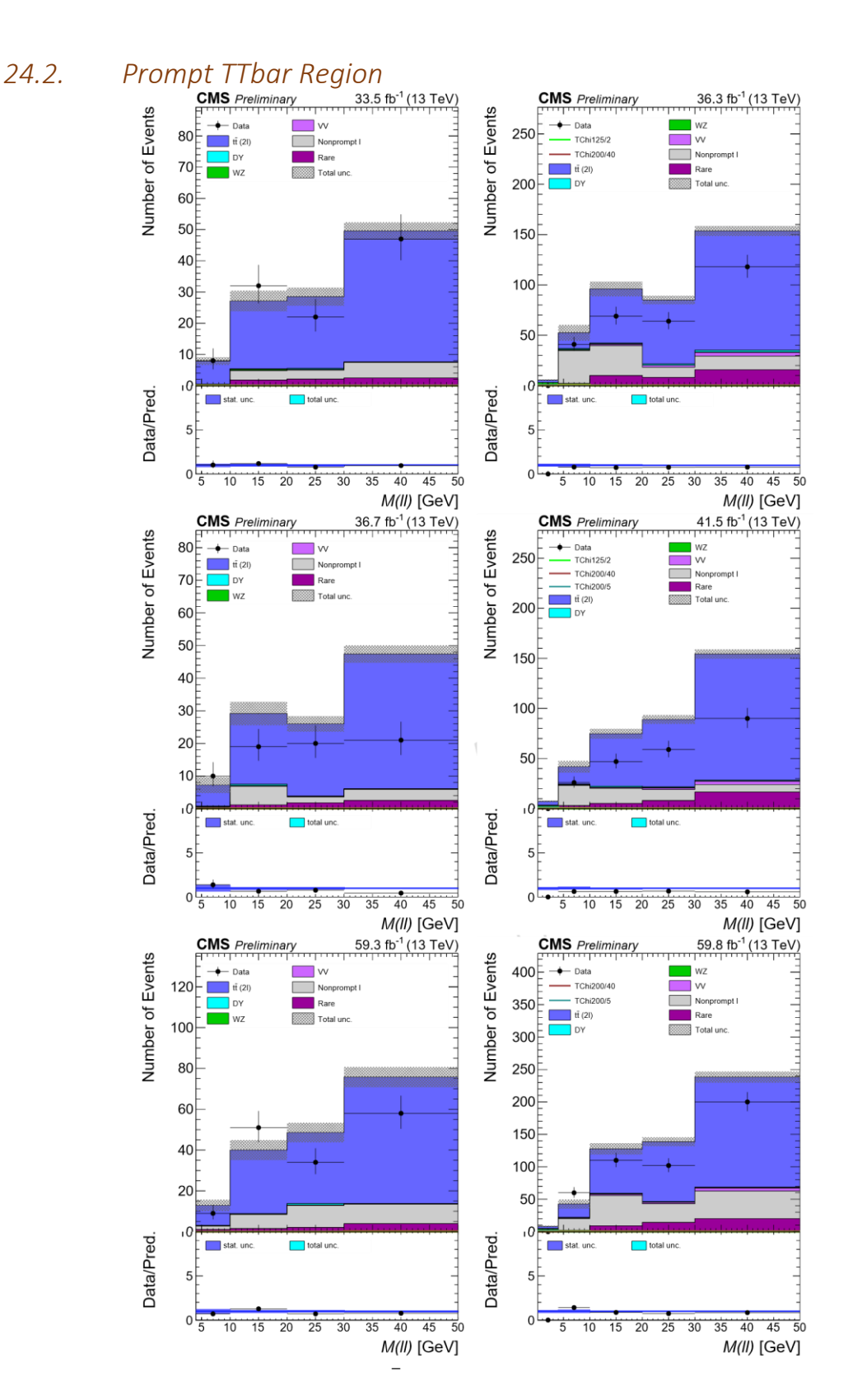


Figure 68: From top to bottom: $M\ell\ell$ distributions of the TT CR, inclusively for muons and electrons, using 2016, 2017, and 2018 datasets. Left: Low p_T^{miss} bin. Right: High p_T^{miss} bin.

24.3. Prompt WZ Region

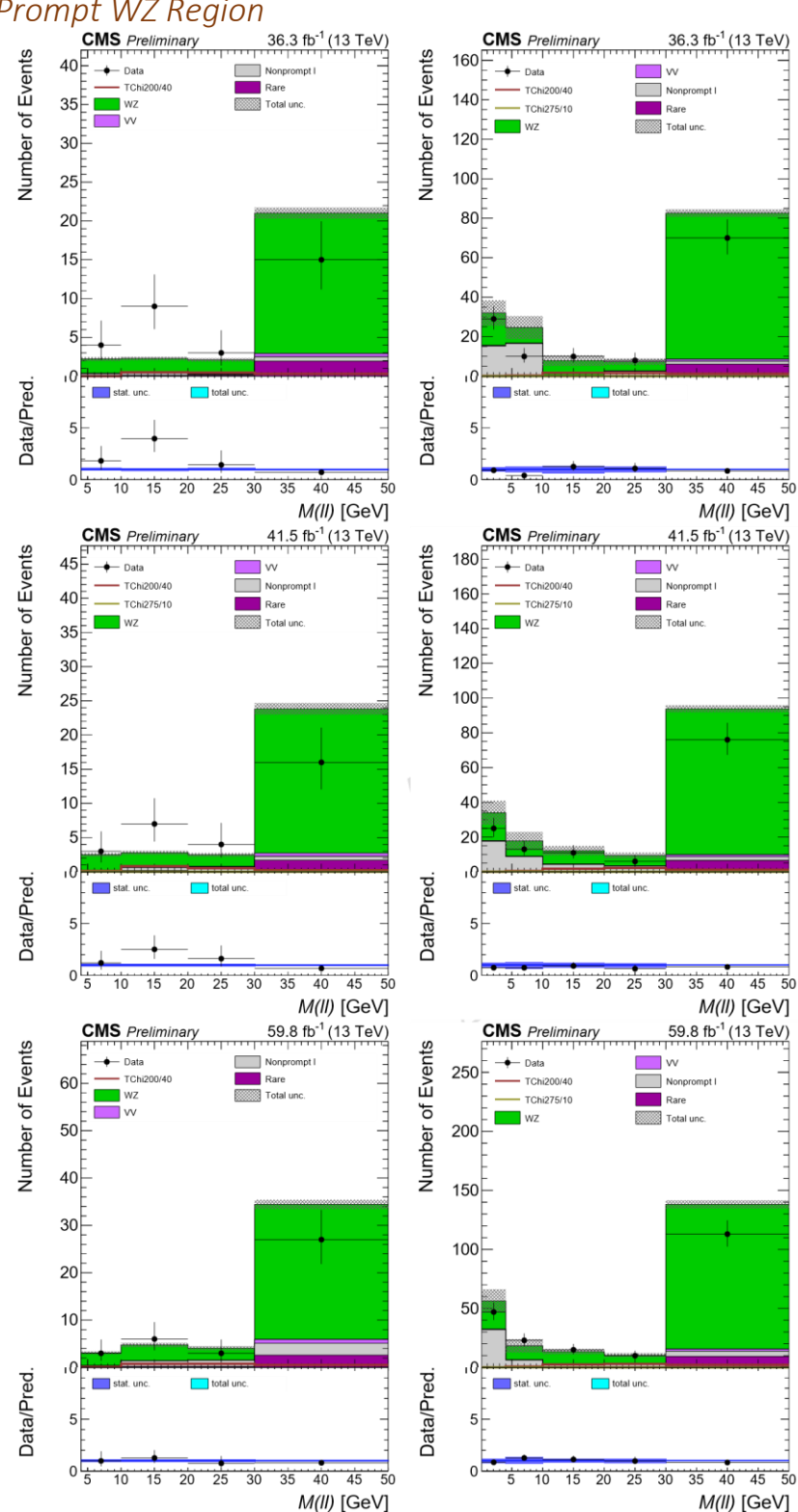


Figure 69: From top to bottom: $M\ell\ell$ distributions of the WZ CR, inclusively for muons and electrons, using 2016, 2017, and 2018 datasets. Left: Low p_T^{miss} bin. Right: High p_T^{miss} bin.

Prompt Muon Same-Sign Region for Non-Prompt 36.3 fb⁻¹ (13 TeV) CMS Preliminary CMS Preliminary 36.3 fb⁻¹ (13 TeV) Number of Events TChi125/2 60 TChi200/5 data_fakes 25 50 20 40 15 30 20 Data/Pred. Data/Pred total unc 10 40 45 50 15 20 25 30 35 M(II) [GeV] dR(II) 41.5 fb⁻¹ (13 TeV) 41.5 fb⁻¹ (13 TeV) CMS Preliminary CMS Preliminary Events Number of Events 50 W data_fakes - TChi200/5 data_fakes - TChi275/10 18 40 16 14 30 12 20 10 Data/Pred. Data/Pred. 35 40 45 50 10 20 25 30 15 *M(II)* [GeV] 59.8 fb⁻¹ (13 TeV) 50 CMS Preliminary CMS Preliminary 59.8 fb⁻¹ (13 TeV) Events Number of Events → Data 60 TChi200/5 40 TChi275/10 50 30 40F 30 20 20 10 10 Data/Pred. Data/Pred. 0

24.4.

Figure 70: From top to bottom: $M_{\ell\ell}$ (left) and $\Delta R_{\ell\ell}$ (right) distributions of the SS CR, for muons, using 2016, 2017, and 2018 datasets. Due to opposite-sign requirement on the trigger for the Low p_{T}^{miss} bin, only High p_{T}^{miss} bin is defined for this CR, inclusively for $p_T^{miss} > 200$ GeV.

dR(II)

40 45

M(II) [GeV]

35

15 20 25

Prompt Electron Same-Sign Region for Non-Prompt CMS Preliminary 36.3 fb.1 (13 TeV) CMS Preliminary 36.3 fb.1 (13 TeV) (13 TeV) (14 CMS Preliminary 36.3 fb.1 (15 TeV) (15 CMS Preliminary 36.3 fb.1 (15 CMS Preliminary 36 36.3 fb⁻¹ (13 TeV) Number of Events 240 Events 220 200 80 180 160 140 60 120 100 40 80 60 20 40 20 Data/Pred. Data/Pred total unc 10 20 25 35 40 45 15 M(II) [GeV] dR(II) 41.5 fb⁻¹ (13 TeV) 41.5 fb⁻¹ (13 TeV) CMS Preliminary CMS Preliminary Events Number of Events ____ data_fakes 160 Total unc TChi125/2 Rare 60 140 120 50 100 40 80 30 60F 20 40 10 20 Data/Pred. Data/Pred. 10 15 30 35 40 45 50 20 25 *M(II)* [GeV] 59.8 fb⁻¹ (13 TeV) dR(II) CMS Preliminary CMS Preliminary 59.8 fb⁻¹ (13 TeV) Events Number of Events 300 120 250 100 200 80 150 60 100 40 50 20 ι0 Data/Pred. Data/Pred. 0 [ᇮ 35 40 45 50 10 20 25 15 M(II) [GeV] dR(II)

24.5.

Figure 71: From top to bottom: $M_{\ell\ell}$ (left) and $\Delta R_{\ell\ell}$ (right) distributions of the SS CR, for electrons, using 2016, 2017, and 2018 datasets. Only High $p_{_{\rm T}}^{\rm miss}$ bin is defined for the Same-Sign electrons, inclusively for $p_{_{\rm T}}^{\rm miss} > 200$ GeV.

25. Application Region for the Soft Multilepton Analysis

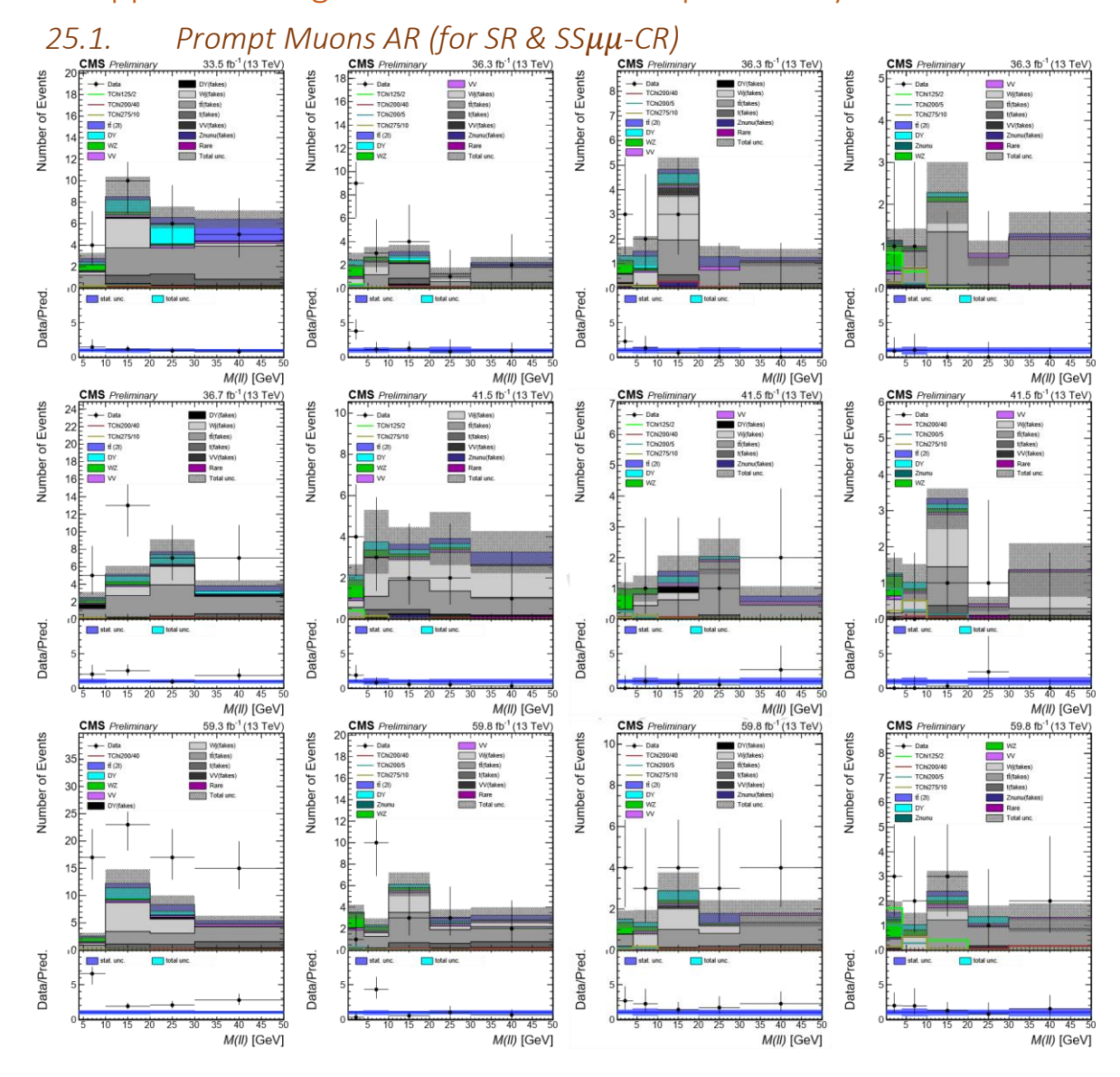


Figure 72: From top to bottom: $M_{\ell\ell}$ distributions of the AR for the prompt muons using 2016, 2017, and 2018 datasets. From left to right: Low p_T^{miss} , Medium p_T^{miss} , High p_T^{miss} , and Ultra p_T^{miss} bins.

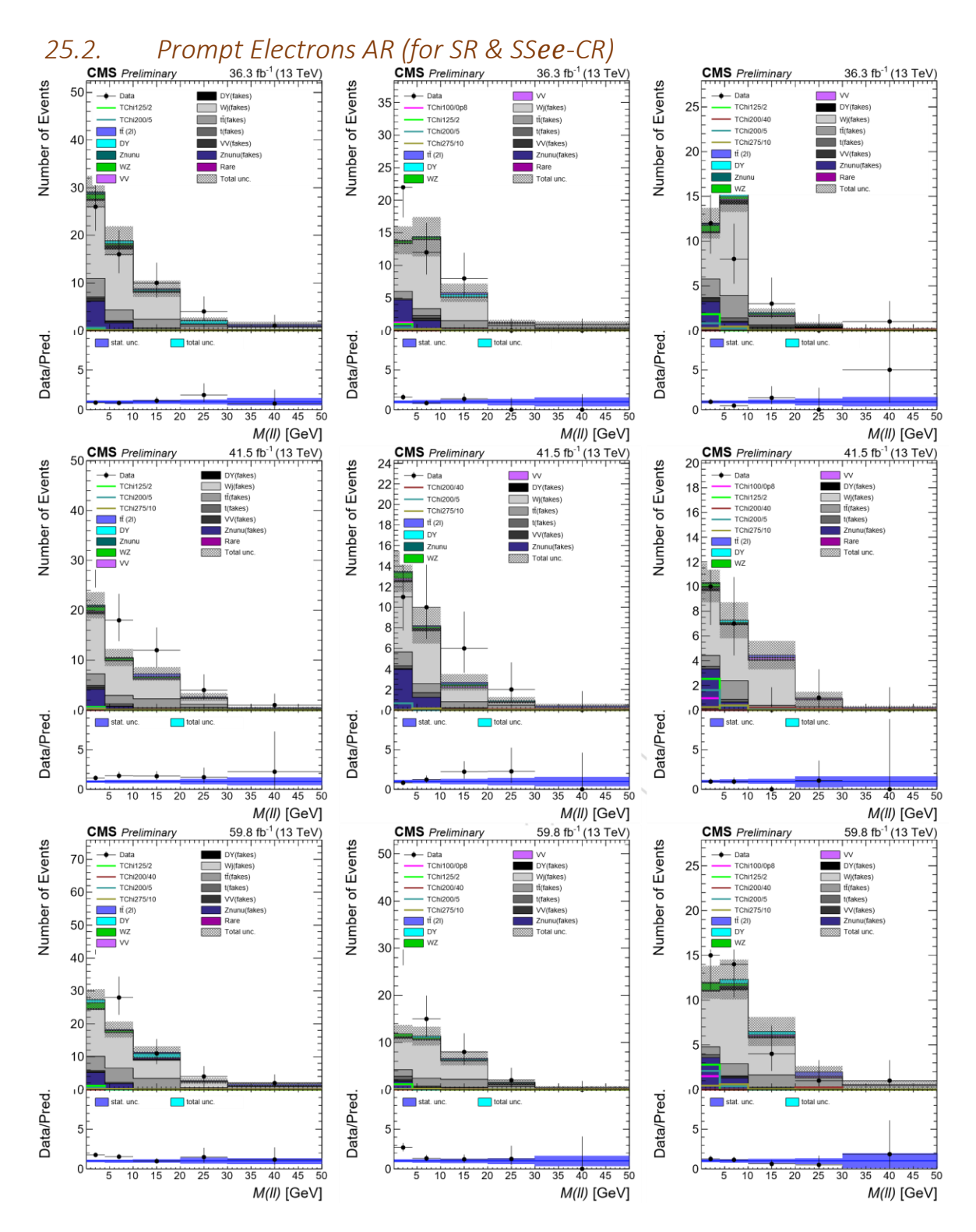


Figure 73: From top to bottom: $M_{\ell\ell}$ distributions of the AR, for prompt electrons, using 2016, 2017, and 2018 datasets. From left to right: Medium p_T^{miss} , High p_T^{miss} , and Ultra p_T^{miss} bins.

25.3. Prompt 3-Leptons AR

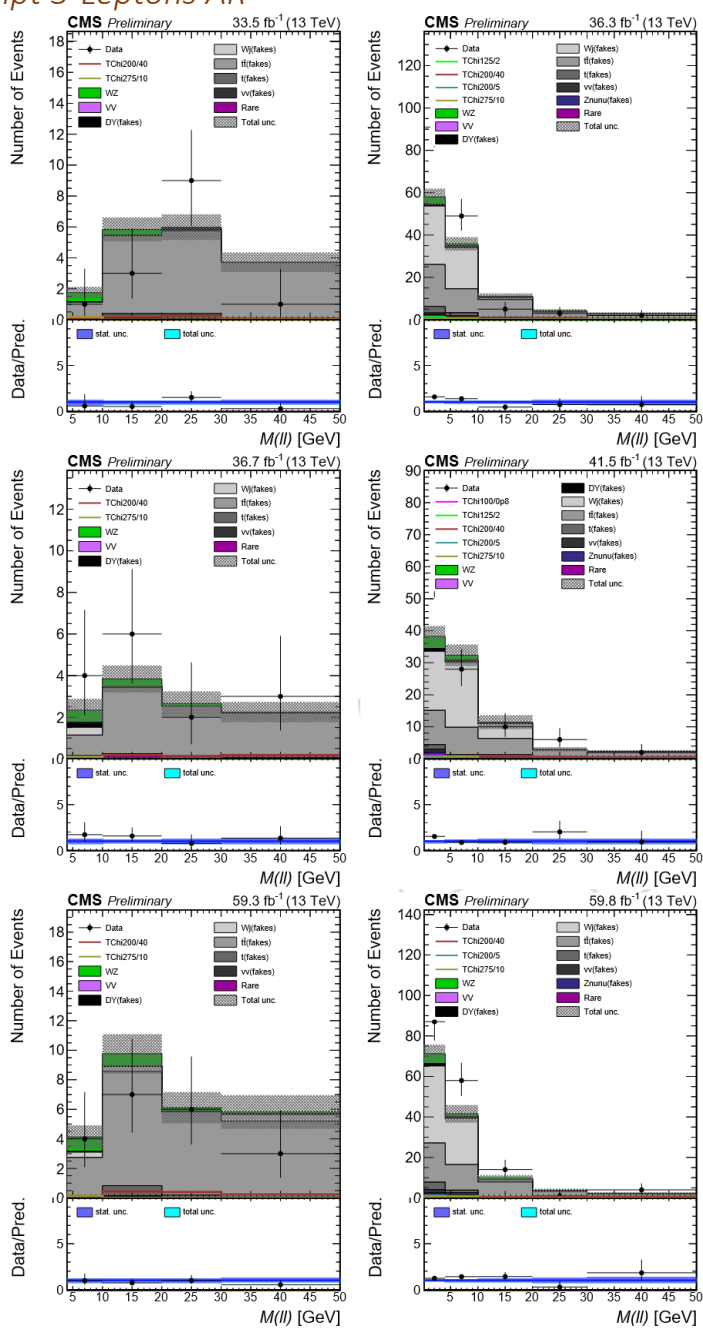


Figure 74: From top to bottom: $M_{\ell\ell}$ distributions of the AR, for 3-lepton final state, using 2016, 2017, and 2018 datasets. Left: Low p_T^{miss} . Right: High p_T^{miss} .

25.4. Muons and Electrons AR with SFs

This Region is used in the background estimation for the "non-prompt" background events as is described in Section 15.2.5. The selection that defines the Application Region can be seen in the tables of that section, while the plots that follow are the Low, Med, High, and Ultra p_T^{miss} bins.

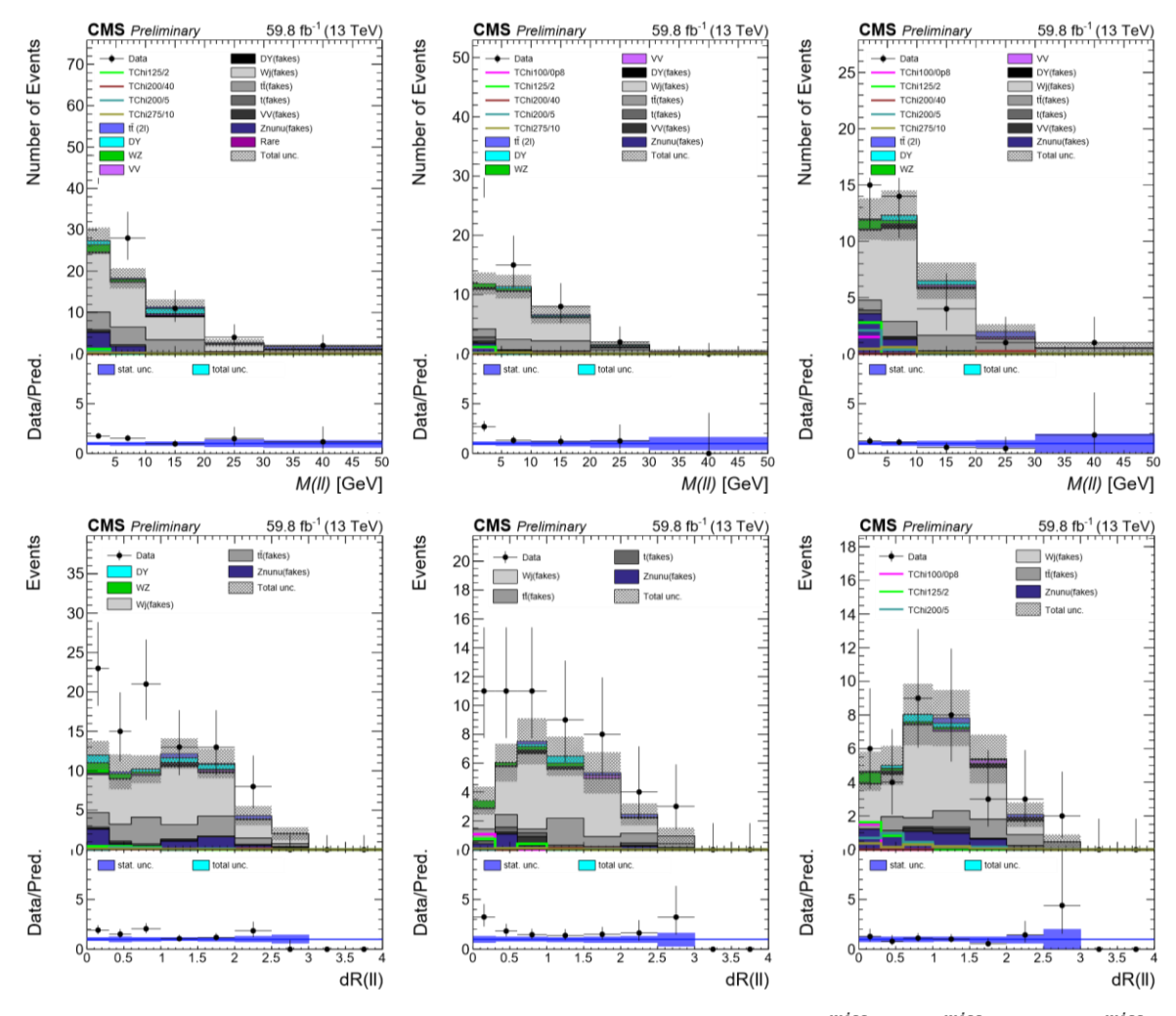


Figure 75: $M_{\ell\ell}$ and ΔR distributions of the electron AR. From left to right: Medium p_T^{miss} , High p_T^{miss} , and Ultra p_T^{miss} bins for 2018 dataset. The plots are inclusive in the number of leptons failing the tight selection criteria.

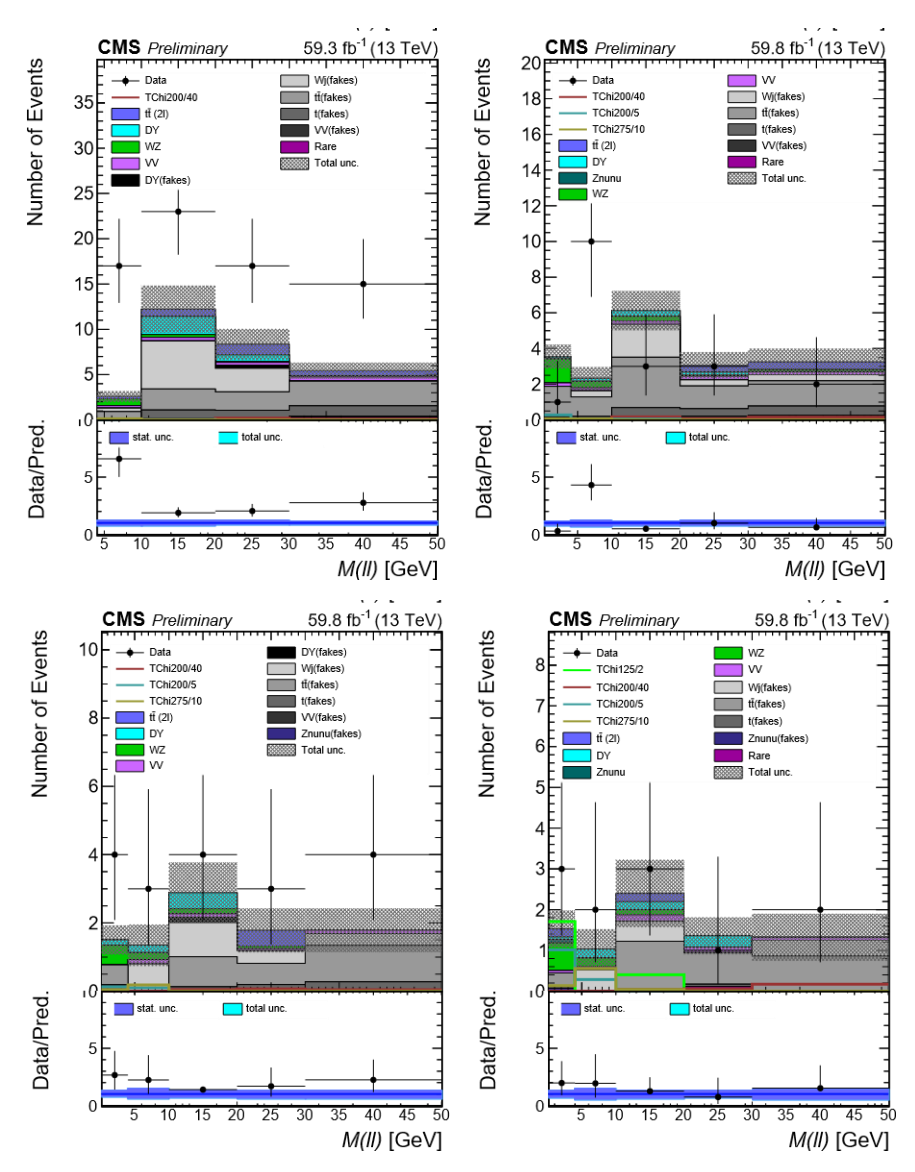


Figure 76: $M_{\ell\ell}$ distributions of the muon AR. From left to right and top to bottom: Low p_T^{miss} , Medium p_T^{miss} , High p_T^{miss} , and Ultra p_T^{miss} bins for 2018 dataset. The plots are inclusive in the number of leptons failing the tight selection criteria.

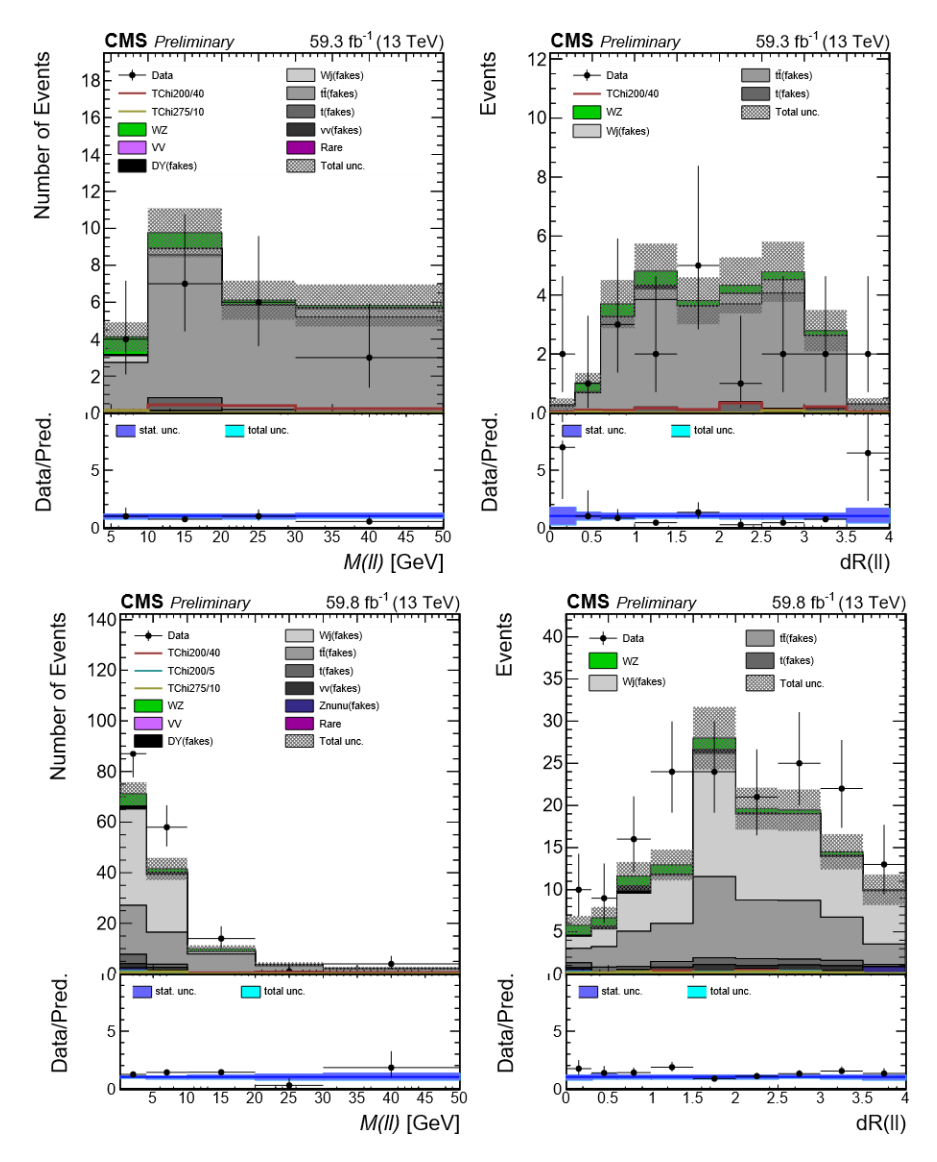


Figure 77: $M_{\ell\ell}$ and ΔR distributions of the 3-lepton AR. The two top (bottom) plots correspond to Low (High) p_T^{miss} bins for the 2018 dataset. Plots are inclusive in the number of leptons failing the tight selection criteria

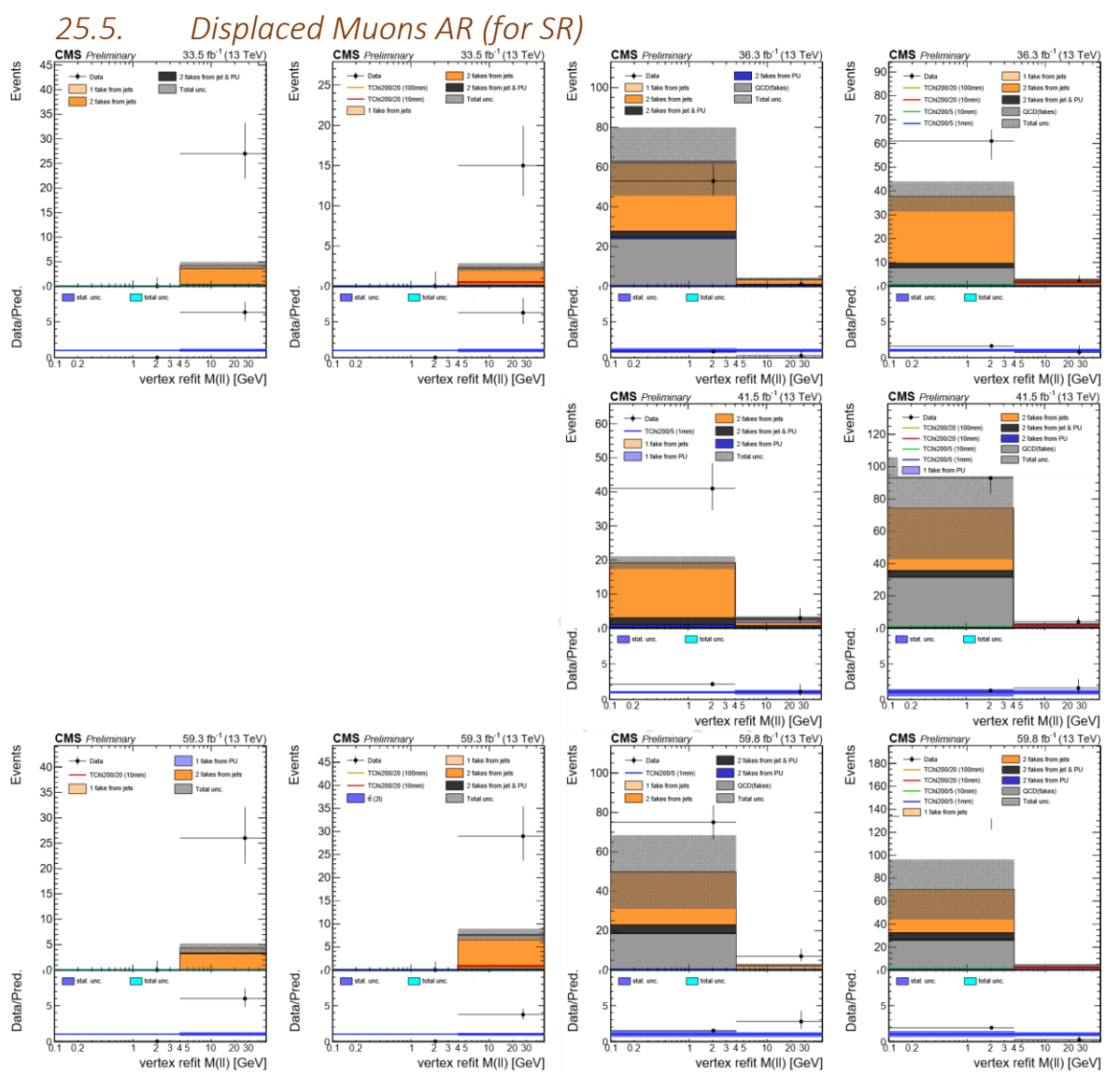
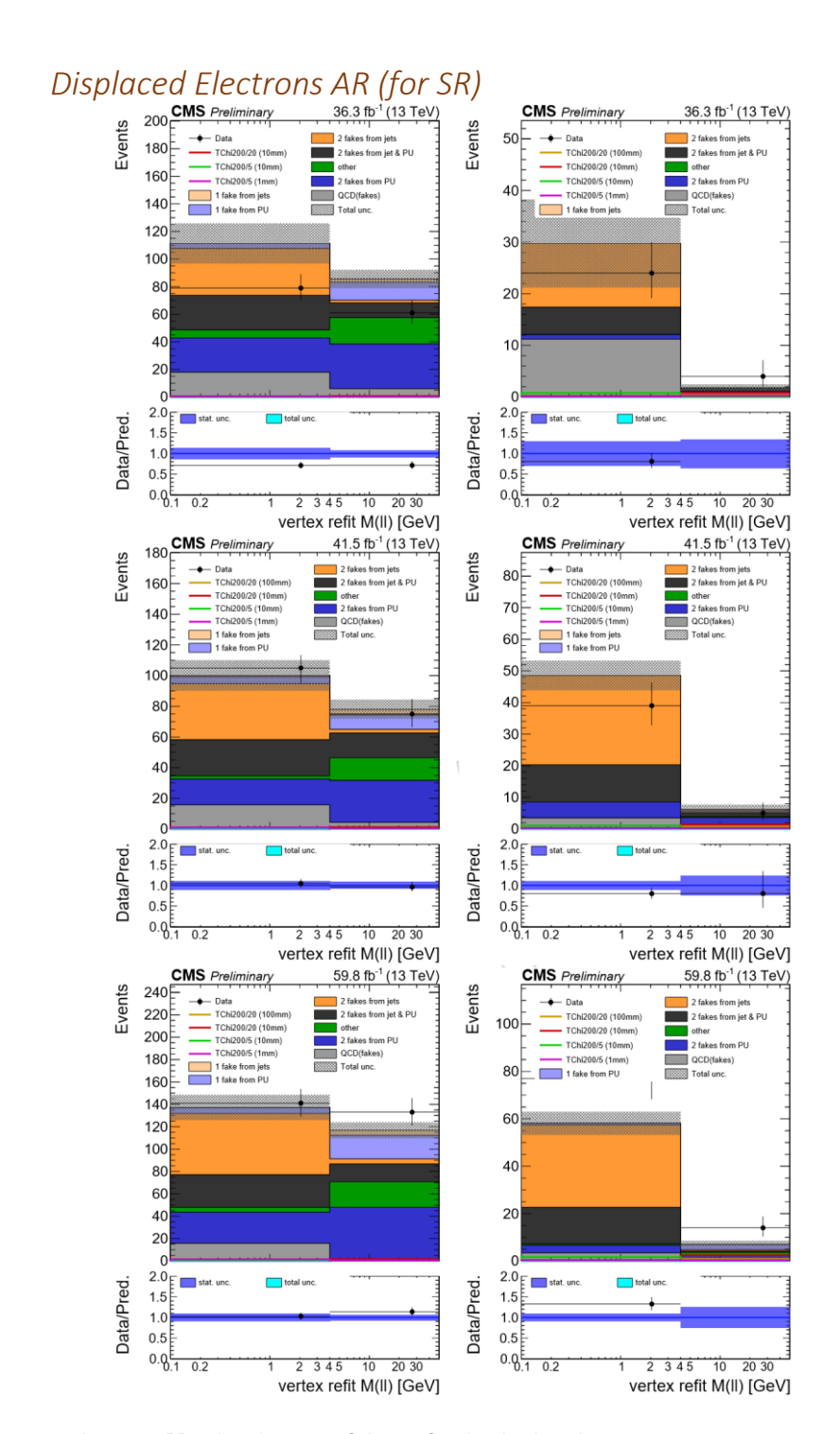


Figure 78: From top to bottom: $M_{\ell\ell}$ distributions of the AR for the displaced muons using 2016, 2017, and 2018 datasets. From left to right: Low $p_{\rm T}^{\rm miss}$ - Low σ_{IP2D} , Low $p_{\rm T}^{\rm miss}$ - High σ_{IP2D} , High $p_{\rm T}^{\rm miss}$ - Low σ_{IP2D} , and High $p_{\rm T}^{\rm miss}$ - High σ_{IP2D} bins.



25.6.

Figure 79: From top to bottom: $M_{\ell\ell}$ distributions of the AR for the displaced muons using 2016, 2017, and 2018 datasets. Left: High $p_{\rm T}^{\rm miss}$ - Low σ_{IP2D} bin. Right: High $p_{\rm T}^{\rm miss}$ - High σ_{IP2D} bin.

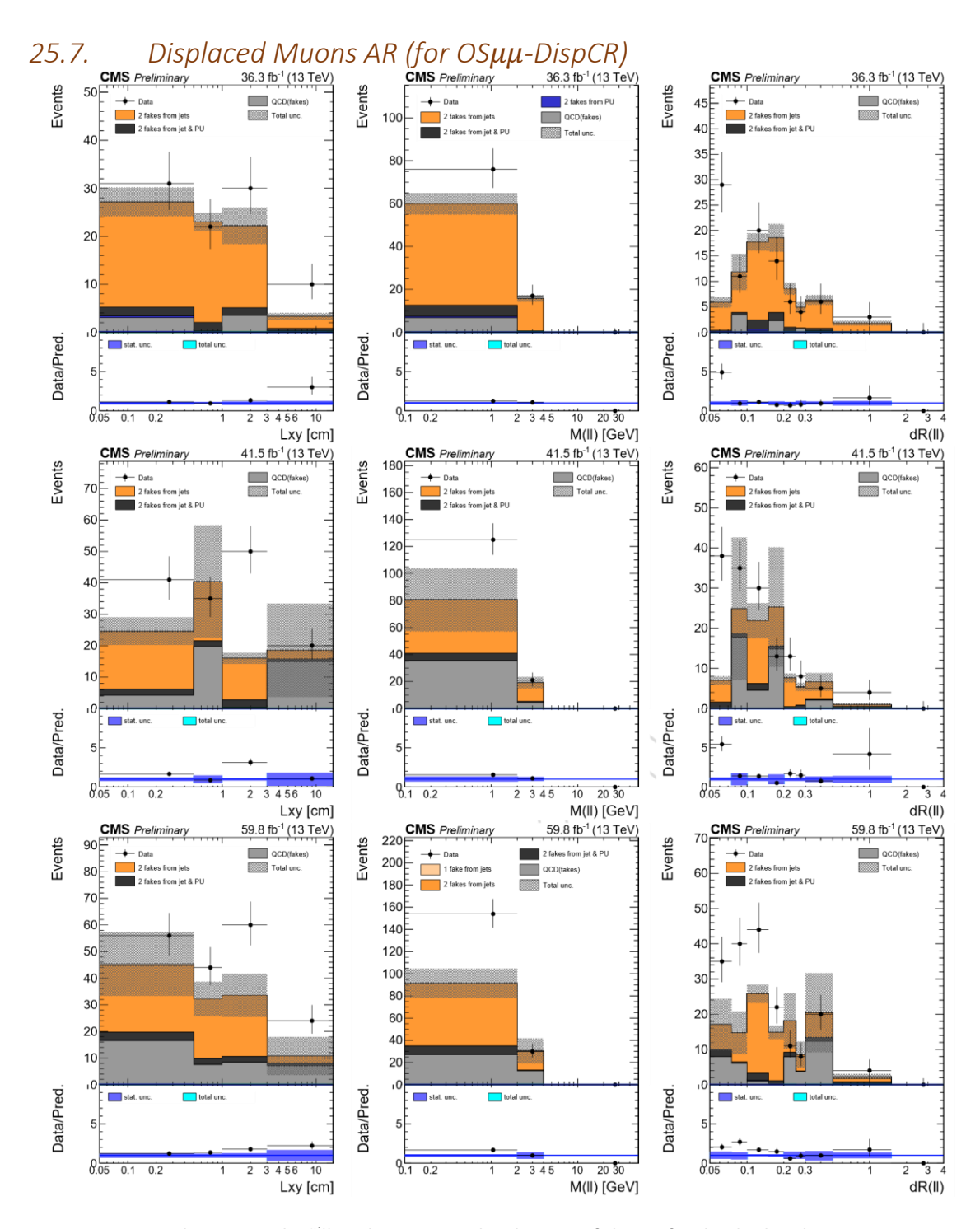


Figure 80: From top to bottom: High p_T^{miss} - Inclusive σ_{IP2D} distributions of the AR for the displaced muons Opposite-Sign CR using 2016, 2017, and 2018 datasets. From left to right: Transverse displacement between PV and SV (L_{xy}), Dilepton invariant mass at SV ($M_{\ell\ell}$), and angle between the 2 leptons ($\Delta R_{\ell\ell}$).

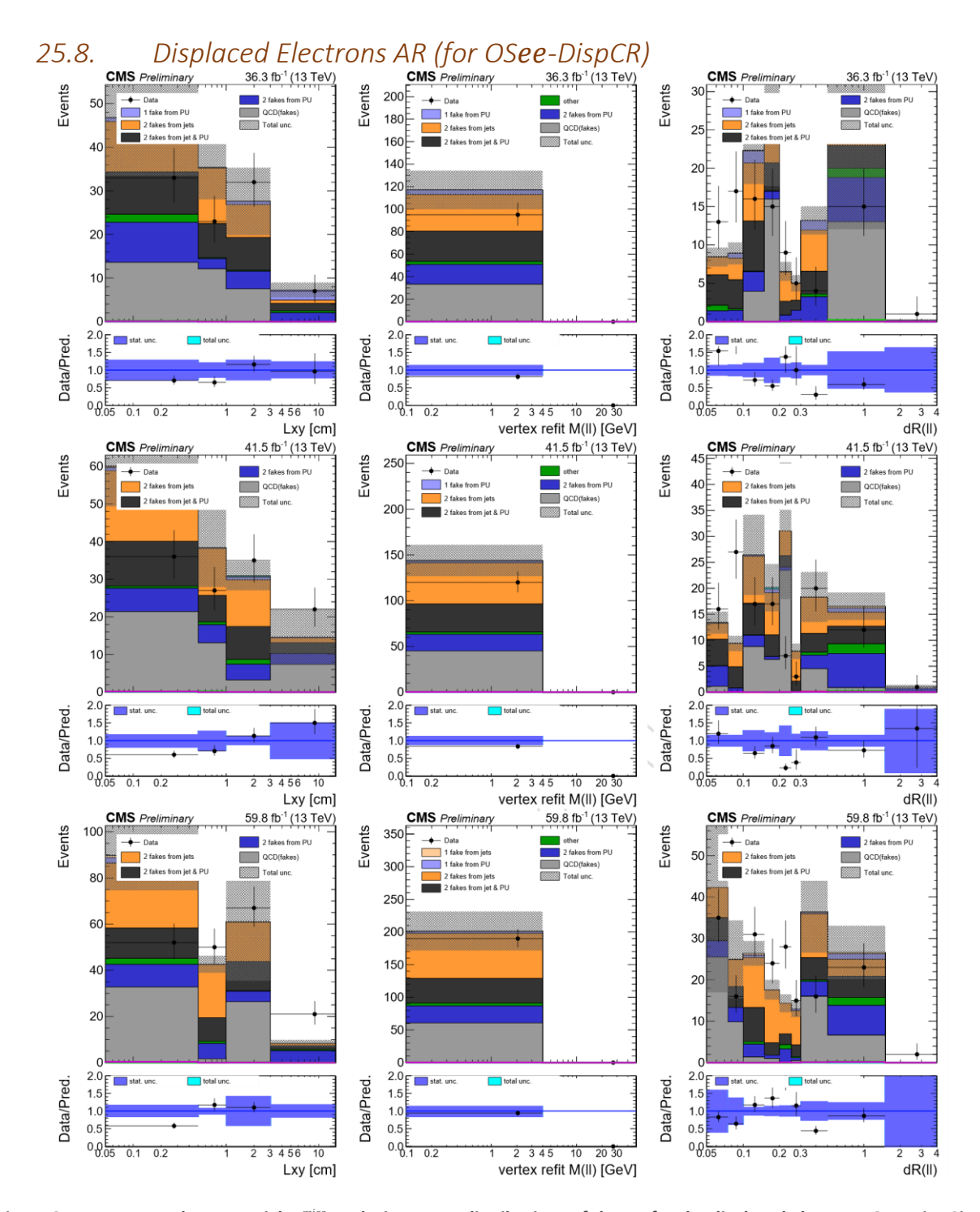


Figure 81: From top to bottom: High p_T^{miss} - Inclusive σ_{IP2D} distributions of the AR for the displaced electrons Opposite-Sign CR using 2016, 2017, and 2018 datasets. From left to right: Transverse displacement between PV and SV (L_{xy}), Dilepton invariant mass at SV ($M_{\ell\ell}$), and angle between the 2 leptons ($\Delta R_{\ell\ell}$).

26. Validation Regions for the Soft Multilepton Analysis

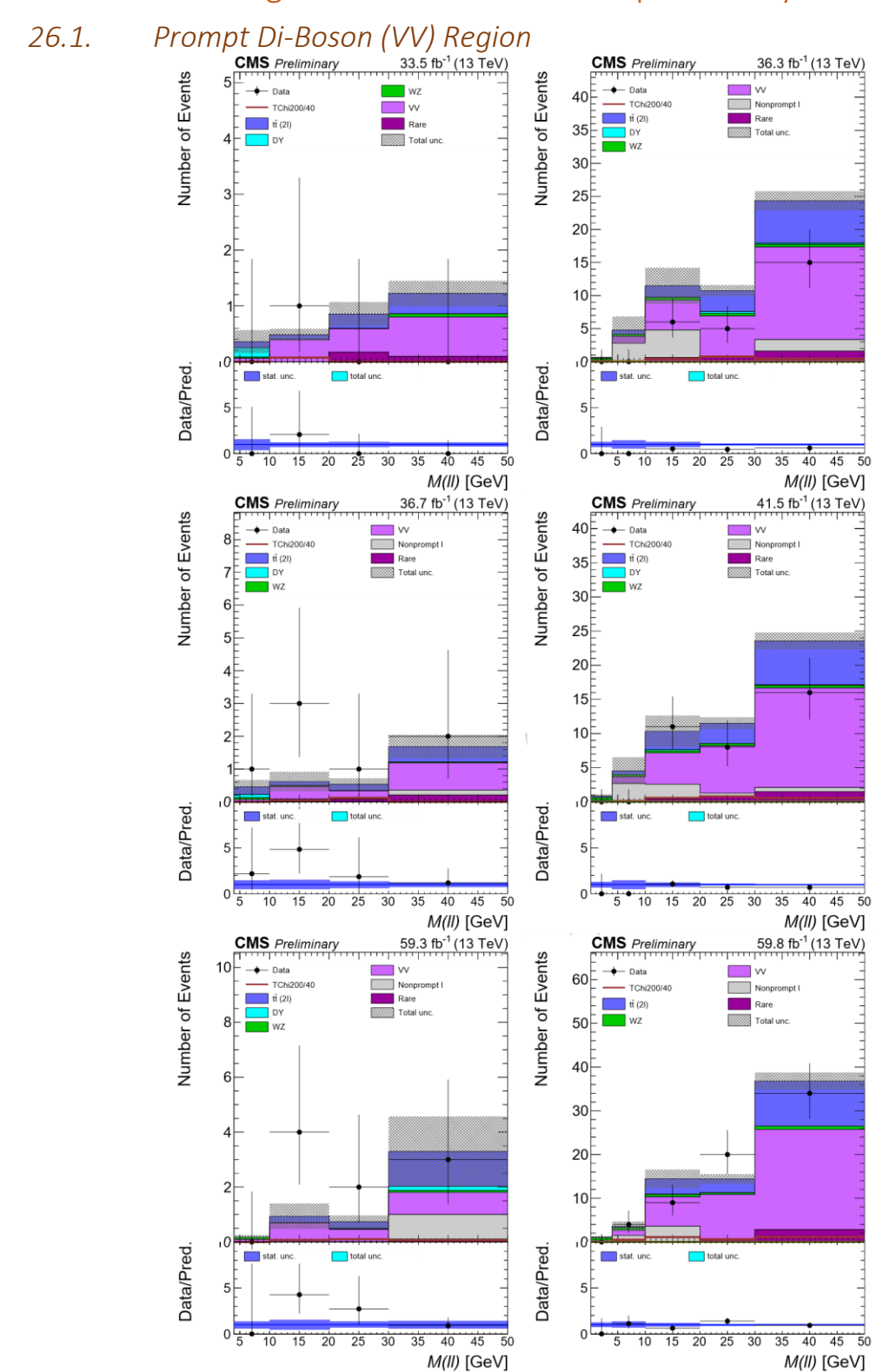


Figure 82: From top to bottom: $M_{\ell\ell}$ distributions of the Di-boson VR for the prompt leptons inclusively using 2016, 2017, and 2018 datasets. From left to right: Low- P_T and High- P_T bins.

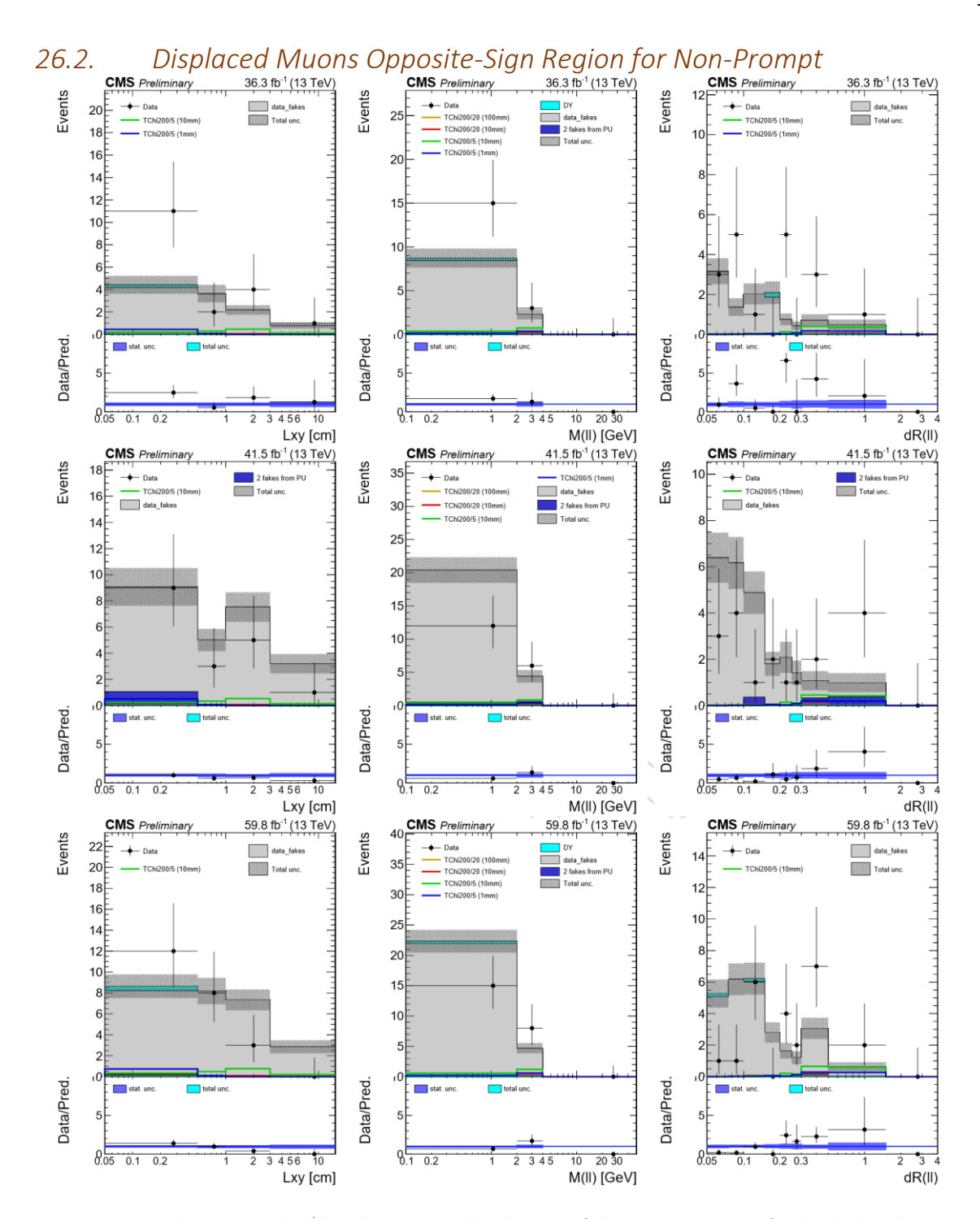


Figure 83: From top to bottom: High p_T^{miss} - Inclusive σ_{IP2D} distributions of the Opposite-Sign CR for the displaced muons using 2016, 2017, and 2018 datasets (not used in the fits). From left to right: Transverse displacement between PV and SV (L_{xy}), Dilepton invariant mass at SV ($M_{\ell\ell}$), and angle between the 2 leptons ($\Delta R_{\ell\ell}$).

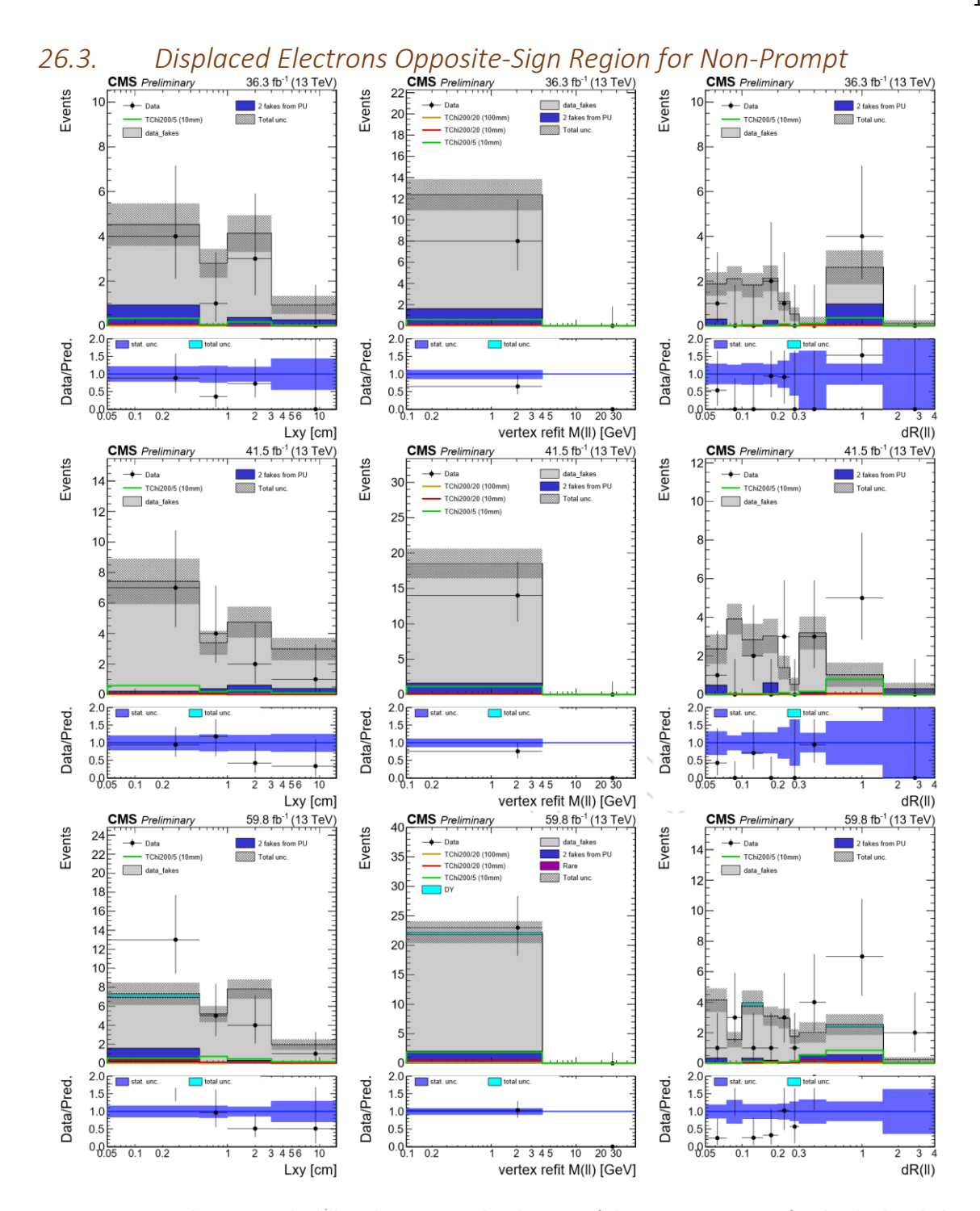


Figure 84: From top to bottom: High $p_{\rm T}^{\rm miss}$ - Inclusive σ_{IP2D} distributions of the Opposite-Sign CR for the displaced electrons using 2016, 2017, and 2018 datasets (not used in the fits). From left to right: Transverse displacement between PV and SV (L_{xy}) , Dilepton invariant mass at SV $(M_{\ell\ell})$, and angle between the 2 leptons $(\Delta R_{\ell\ell})$.

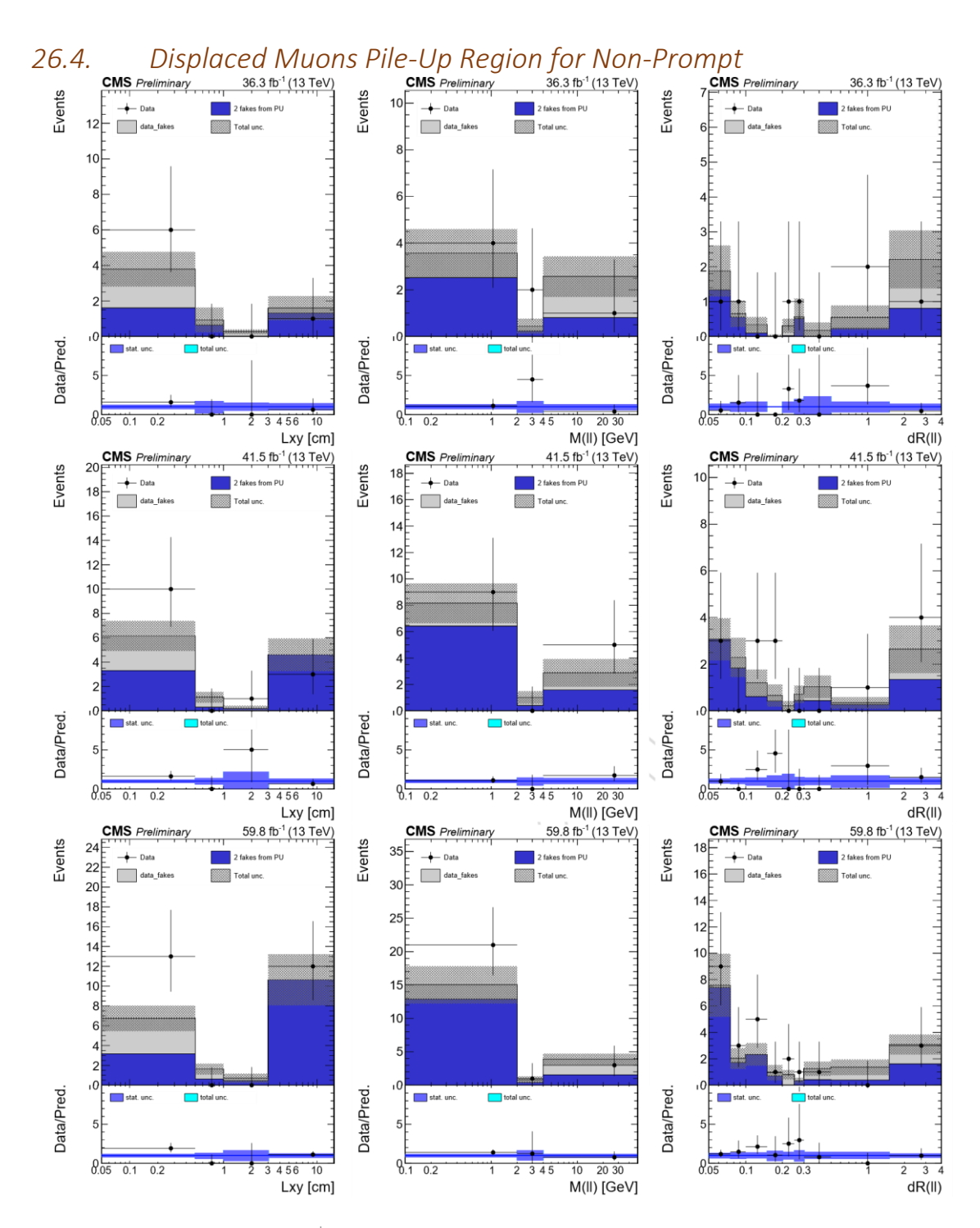


Figure 85: From top to bottom: High p_{T}^{miss} - Inclusive σ_{IP2D} distributions of the Pile-up Region for the displaced muons using 2016, 2017, and 2018 datasets. From left to right: Transverse displacement between PV and SV (L_{xy}), Dilepton invariant mass at SV ($M_{\ell\ell}$), and angle between the 2 leptons ($\Delta R_{\ell\ell}$).

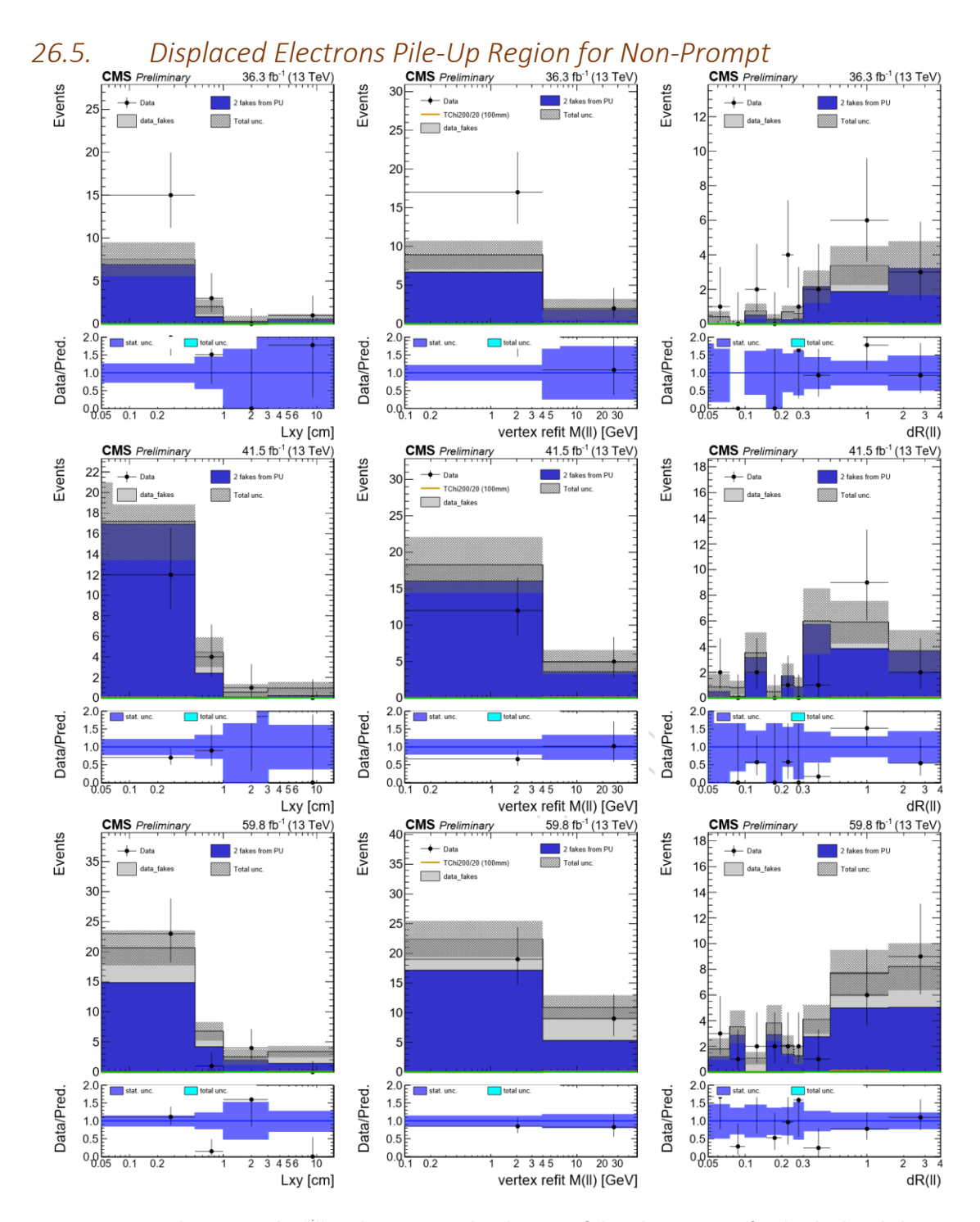


Figure 86: From top to bottom: High p_T^{miss} - Inclusive σ_{IP2D} distributions of the Pile-up Region for the displaced electrons using 2016, 2017, and 2018 datasets. From left to right: Transverse displacement between PV and SV (L_{xy}), Dilepton invariant mass at SV ($M_{\ell\ell}$), and angle between the 2 leptons ($\Delta R_{\ell\ell}$).

27. Prompt Rate Measurements for the Tight-to-Loose method

27.1. Prompt Electrons and Muons

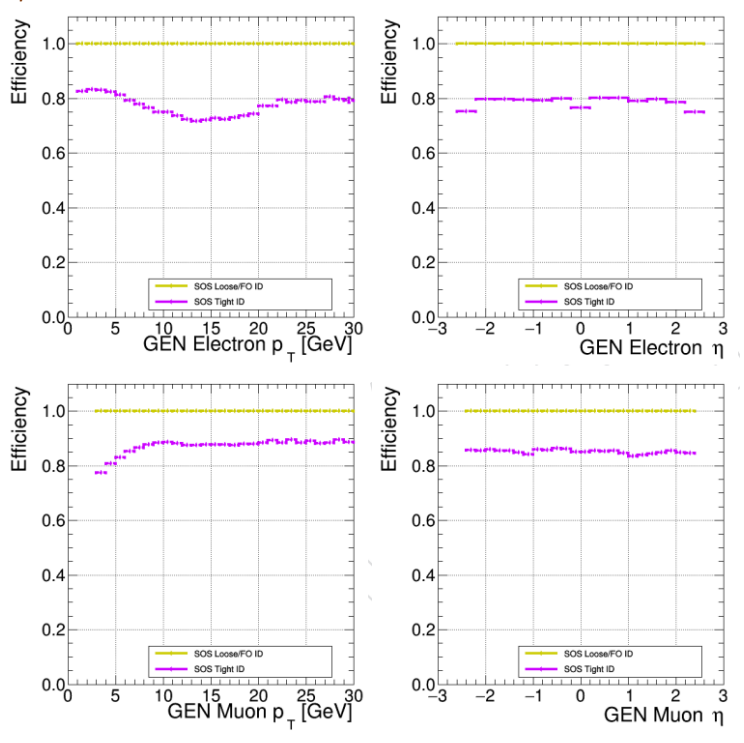


Figure 87: Prompt rates (probabilities for a loose lepton to pass the full TightID) as measured for the definitions in of Muon Tight ID and Electron Tight ID. The measurements have been carried out on leptons from signal events.

References and Citations

- [1] <u>Brüning, O; Klein, M; Myers, S; Rossi, L</u>, 70 years at the high-energy frontier with the CERN accelerator complex, doi: 10.1038/s42254-024-00758-5, Nature Rev. Phys. (2024) **6:** 628-637, https://cds.cern.ch/record/2917069
- [2] <u>Canesse, A; Zimmaro, A; Prelipcean, D; Ricci, D; Di Francesca, D; Lerner, G; Garcia Alia, R; Danzeca, S, Overview of the radiation levels in the CERN accelerator complex after LS2, doi: 10.18429/JACoW-IPAC2023-THPA046, Journals of Accelerator Conferences Website IPAC (2023) 14th: THPA046, https://cds.cern.ch/record/2940603</u>
- [3] CMS Collaboration, CMS Physics: Technical Design Report Volume 2: Physics Performance, ISBN: 978-92-9083-269-0, CERN-LHCC-2006-021, CERN, 2006, https://cds.cern.ch/record/942733
- [4] CMS Collaboration, The CMS tracker system project: Technical Design Report, ISBN: 978-92-9083-124-2, CERN-LHCC-98-006, CERN, 1998, https://cds.cern.ch/record/368412
- [5] <u>Kotlinski, D; Baur, R; Horisberger, R P; Schnyder, R; Erdmann, W; Gabathuler, K</u>, Readout of the CMS pixel detector, doi:10.5170/CERN-2000-010.95, CERN, 2000, https://cds.cern.ch/record/478252
- [6] The LHC experiments Committee, UCG Report on the Phase II Upgrade of the CMS Tracker, CERN-LHCC-2017-024; UCG-023, Geneva, 2017, https://cds.cern.ch/record/2295762
- [7] Weber, H A, The construction of the phase-1 upgrade of the CMS pixel detector, doi: 10.1088/1748-0221/12/C12049, JINST 12 (2017) C12049, https://cds.cern.ch/record/2285254
- [8] CMS upgrades during LS2, 2022, https://home.cern/press/2022/CMS-upgrades-LS2
- [9] Phase 1 Upgrades; CMS at Fermilab, 2017, https://cms.fnal.gov/phase-1-upgrades
- [10] CMS Collaboration, The CMS electromagnetic calorimeter project: Technical Design Report, ISBN: 929-08-3112-21, CERN-LHCC-97-033, CERN, 1997, https://cds.cern.ch/record/349375
- [11] CMS Collaboration, Performance and Operation of the CMS Electromagnetic Calorimeter, doi: 10.1088/1748-0221/5/03/T03010, JINST 5 (2010) T03010, https://arxiv.org/abs/0910.3423v3
- [12] Aspell, P; Barney, D; Bloch, P; Bourotte, J; Domeniconi, J; Peisert, A; Evangelou, I; Kloukinas, K; Kyriakis, A; Loos, R; Loukas, D; Mousa, J; Peron, F; Reynaud, S; Sirunyan, A M; Tournefier, E; Van Hove, A; Zamiatin, N, Results from the 1999 Beam Test of a Preshower Prototype, CMS-NOTE-2000-001, 2000, https://cds.cern.ch/record/687210
- [13] CMS Collaboration, The CMS hadron calorimeter project: Technical Design Report, ISBN: 978-92-9083-109-9, CERN-LHCC-97-031, CERN, 1997, https://cds.cern.ch/record/357153
- [14] <u>Abdullin, S</u> et al., Design, performance, and calibration of the CMS hadron-outer calorimeter, doi: 10.1140/epjc/s10052-008-0756-6, Eur. Phys. J. C (2008) **57**: 653-663, https://link.springer.com/article/10.1140/epjc/s10052-008-0756-6
- [15] Abdullin, S et al., Design, performance, and calibration of CMS hadron-barrel calorimeter wedges, doi: 10.1140/epjc/s10052-008-0573-y, Eur. Phys. J. C (2008) 55: 159-171, https://link.springer.com/article/10.1140/epjc/s10052-008-0573-y
- [16] CMS Collaboration, Performance of the CMS Hadron Calorimeter with Cosmic Ray Muons and LHC Beam Data, doi: 10.1088/1748-0221/5/03/T03012, JINST 5 (2010) T03012, https://arxiv.org/abs/0911.4991v3
- [17] CMS Collaboration, The CMS muon project: Technical Design Report, ISBN: 978-92-9083-121-1, CERN-LHCC-97-032, CERN, 1997, https://cds.cern.ch/record/343814

- [18] CMS Collaboration, CMS Technical Design Report for the Muon Endcap GEM Upgrade, ISBN: 978-92-9083-396-3, CERN-LHCC-2015-012, CERN, 2015, https://cds.cern.ch/record/2021453
- [19] LS2 Report: 144 new muon detectors in CMS, 2020, https://home.cern/news/news/experiments/ls2-report-144-new-muon-detectors-cms
- [20] UPGRADES CMS Bulletin, 2013, https://cds.cern.ch/journal/CMSBulletin/2013/1/Articles/1544508
- [21] <u>Bauer, P</u> et al., UCG Report on the TDR for the CMS Muon System Phase-II Upgrade, CERN-LHCC-2018-005, CERN, 2018, https://cds.cern.ch/record/2304341
- [22] CMS Collaboration, The CMS magnet project: Technical Design Report, ISBN: 978-92-9083-101-3, CERN-LHCC-97-010, CERN, 1997, https://cds.cern.ch/record/331056
- [23] CMS Collaboration, Precise Mapping of the Magnetic Field in the CMS Barrel Yoke using Cosmic Rays, doi: 10.1088/1748-0221/5/03/T03021, JINST 5 (2010) T03021, https://arxiv.org/abs/0910.5530
- [24] CMS Collaboration, CMS TriDAS project: Technical Design Report, Volume 1: The Trigger Systems, ISBN: 929-08-3110-2, CERN-LHCC-2000-038, CERN, 2000, https://cds.cern.ch/record/706847
- [25] CMS Collaboration, CMS Technical Design Report for the Level-1 Trigger Upgrade, ISBN: 978-92-9083-390-1, CERN-LHCC-2013-011, CERN, 2013, https://cds.cern.ch/record/1556311
- [26] CMS Trigger: Lessons from LHC Run 2, 2019, https://ep-news.web.cern.ch/content/cms-trigger-lessons-lhc-run-2
- [27] CMS Collaboration, CMS TriDAS project: Technical Design Report, Volume 2: Data Acquisition and High-Level Trigger, ISBN: 929-08-3111-4, CERN-LHCC-2002-026, CERN, 2002, https://cds.cern.ch/record/578006
- [28] Sert, H, CMS High Level Trigger Performance in Run 2, Conference Report, 27th International Symposium on Nuclear Electronics & Computing, Becici, Budva, Montenegro, 2019, CMS-CR-2019-278, https://cds.cern.ch/record/2712275
- [29] First collisions reconstructed with GPUs at CMS, 2021, https://cmsexperiment.web.cern.ch/index.php/news/first-collisions-reconstructed-gpus-cms
- [30] CERN's LHC Experiments Increase Use of GPUs to Improve Computing Infrastructure, 2022, https://www.hpcwire.com/off-the-wire/cerns-lhc-experiments-increase-use-of-gpus-to-improve-computing-infrastructure
- [31] P. Katsoulis, Development of triggering systems and searches for signatures from theories beyond the standard model with the CMS detector at the LHC, Master Thesis, University of Ioannina, 2019, https://olympias.lib.uoi.gr/jspui/handle/123456789/32271
- [32] [L1 O2O] ESGetToken migration L1CondDBPayloadWriter and O2O unit tests, 2022, https://github.com/cms-sw/cmssw/pull/37602
- [33] P. Binétruy, Supersymmetry Theory, Experiment, and Cosmology, ISBN 978-0-19-850954-7, Oxford University Press, 2006
- [34] Rolbiecki K., Sakurai K., Long-lived bino and wino in supersymmetry with heavy scalars and higgsinos. *J. High Energy Phys.* **2015**, 91 (2015). https://doi.org/10.1007/JHEP11(2015)091
- [35] Allanach B. C., SOFTSUSY: a program for calculating supersymmetric spectra, Computer Physics Communications (2002) **143**: 305-331, doi: 10.1016/S0010-4655(01)00460-X, https://arxiv.org/abs/hep-ph/0104145
- [36] CMS Collaboration, Search for new physics with compressed mass spectra in final states with soft leptons and missing transverse energy in proton-proton collisions at $\sqrt{s}=13~TeV$, CMS-PAS-EXO-23-017, https://cds.cern.ch/record/2930836

- [37] CMS Collaboration, Search for compressed electroweakinos with low-momentum isolated tracks, CMS-PAS-SUS-24-012, https://cds.cern.ch/record/2929520
- [38] CMS Collaboration, Search for supersymmetry in final states with disappearing tracks in proton-proton collisions at $\sqrt{s}=13~TeV$, Phys. Rev. D 109 (Apr, 2024) 072007, doi:10.1103/PhysRevD.109.072007, https://arxiv.org/abs/2309.16823v2
- [39] Recommendations for Systematic Uncertainties HL-LHC (3 fb⁻¹), 2018, https://twiki.cern.ch/twiki/bin/viewauth/CMS/YR2018Systematics
- [40] A. Tews, Search for Electroweakinos Using Two Soft Opposite-Sign Displaced Muons at the CMS Experiment, PhD Thesis, University of Hamburg, 2024, https://inspirehep.net/literature/2777128
- [41] G. Cowan, K. Cranmer, E. Gross, O. Vitells, Asymptotic formulae for likelihood-based tests of new physics, 2013, https://arxiv.org/abs/1007.1727v3
- [42] CMS Collaboration, Simulation of the Silicon Strip Tracker pre-amplifier in early 2016 data, CMS-DP-2020-045, cds.cern.ch/record/2740688
- [43] LHC SUSY Cross Section Working Group, 2024, https://twiki.cern.ch/twiki/bin/view /LHCPhysics/SUSYCrossSections
- [44] CMS Collaboration, The CMS Statistical Analysis and Combination Tool: Combine, Computing and Software for Big Science, doi: 10.1007/s41781-024-00121-4, Computing and Software for Big Science (2024) 8: 19, https://arxiv.org/abs/2404.06614
- [45] CMS Collaboration, Search for supersymmetry in final states with two or three soft leptons and missing transverse momentum in proton-proton collisions at $\sqrt{s} = 13 \, TeV$, doi: 10.48550/arXiv.2111.06296, JHEP 04 (2022) 091, https://arxiv.org/abs/2111.06296
- [46] CMS Collaboration, Muon Reconstruction and Identification Performance with Run-2 data, CERN-CMS-DP-2020-040, CERN, 2020, https://cds.cern.ch/record/2727091
- [47] Bols E; Kieseler J; Verzetti M; Stoye M; Stakia A, Jet Flavour Classification Using DeepJet, doi: 10.1088/1748-0221/15/12/P12012, JINST 15 (2020) P12012, https://cds.cern.ch/record/2730134
- [48] Agarwal G, Jet Energy Scale and Resolution Measurements in CMS, doi: 10.22323/1.414.0652, PoS ICHEP2022 (2022) 652, https://cds.cern.ch/record/2847453
- [49] CMS Collaboration, Pileup mitigation at CMS in 13 TeV data, doi: 10.48550/arXiv.2003.00503, JINST 15 (2020) P09018, https://arxiv.org/abs/2003.00503v2
- [50] <u>Giraldi A</u>, Precision luminosity measurement with proton-proton collisions at the CMS experiment in Run 2, doi: 10.22323/1.414.0638, PoS ICHEP2022 (2022) 638, https://cds.cern.ch/record/2824971